DISS. ETH NO. 23332

FREQUENCY-SWEPT MICROWAVE PULSES FOR ELECTRON SPIN RESONANCE

A dissertation submitted to
ETH ZURICH

for the degree of
DOCTOR OF SCIENCES

presented by
ANDRIN DOLL
MSc in Electrical Engineering and Information Technology
(ETH Zurich)
born 1 October 1984
citizen of Niederweningen ZH, Switzerland

accepted on the recommendation of
Prof. Dr. Gunnar Jeschke, examiner
Prof. Dr. Matthias Ernst, co-examiner

2016

ABSTRACT

Pulsed electron paramagnetic resonance (EPR) is a versatile technique to study specific interactions within a system containing unpaired electron spins. One limitation of the technique is that only a fraction of the entire EPR spectrum can be excited with the monochromatic excitation pulses applied at microwave frequencies. Especially for transition metal ions, this excited fraction can be rather small. As a consequence of this limitation, sensitivity is restricted in a number of relevant EPR experiments. Moreover, multi-dimensional correlation techniques that are well established in nuclear magnetic resonance (NMR) spectroscopy are not commonplace in pulsed EPR.

In order to excite a larger fraction of the EPR spectrum, this work introduces frequency-swept microwave pulses for increasing excitation bandwidth in EPR spectroscopy. Such pulses became available only in recent years thanks to fast arbitrary waveform generators. The focus of this work is on technical aspects as well as on experimental aspects.

Technically, implementation of frequency-swept pulses required construction of dedicated experimental setups. In particular, commercial X- and Q-band spectrometers were extended with incoherent frequency-swept pulses and a dedicated spectrometer providing competitive sensitivity with phase-coherent pulses at either X- or Q-band frequencies was constructed. An important technical restriction when exciting electron spins with frequency-swept pulses is the limited bandwidth of the microwave resonator that is used to couple to the spins. Accordingly, a way to compensate such technical bandwidth limitations by adaptation of the pulse's frequency sweep based on the adiabaticity criterion was developed. This approach could be checked for self-consistency based on linear response theory and the procedure was extended to pulses optimized for frequency-selective excitation.

Experimentally, these pulses were incorporated into a number of existing EPR pulse sequences. Significant sensitivity enhancement of distance measurements between a pair of electron spins was achieved by replacing the incoherent pump pulse in the four-pulse double electron-electron resonance (DEER) pulse sequence by an incoherent frequency-swept pulse. In particular, a three-fold improvement in X-band DEER modulation depth to 24% when pumping a spectrally broad Cu(II) center with a frequency-swept pulse instead of a monochromatic pulse was achieved. For distance measurements between a pair of Gd(III) centers bearing a high spin of $S = 7/2$, similar modulation depths could be achieved at Q band by using two consecutive pulses that pump separate frequency windows.

Due to the multiple energy levels of the $S = 7/2$ spin state, coherence and population transfers within the spin multiplet were considered experimentally and with spin dynamics simulations. In particular, an unwanted coherence transfer due to the pump pulse influenced DEER sensitivity and stimulated the development of a simple and fast procedure to optimize pulse parameters in situ. With respect to population transfer, polarization from unobserved transitions could be transfered to the observed transition by means of frequency-swept pre-polarization pulses. The resulting signal enhancement was up to a factor of three and allowed to determine Gd-Gd distances up to 8.6 nm by pre-polarized four-pulse DEER .

Frequency-swept pump pulses were also examined in systems containing three spins, where the large DEER modulation depth led to a more pronounced signature of three-spin correlations and alleviated its extraction from experimental data.

A general limitation when using frequency-swept pulses in DEER were interference effects related to the extended pulse duration, which could

deteriorate data quality at short inter-spin distances. Accordingly, a novel interference-free pulse sequence (abbreviated as CIDME) that is suited for short distances was developed and verified by a Gd-Gd spacer with 2.1 nm inter-spin distance.

The home-built spectrometer allowed to perform correlation experiments by computing the Fourier-transform (FT) of transient spin echo signals. Thanks to the uniform excitation profile achieved with bandwidth-compensated pulses, the main impact of limited resonator bandwidth on FT spectra was only due to the detection process. Accordingly, the net bandwidth of the FT EPR experiment was enhanced as compared to experiments performed with uncompensated pulses. As a result, FT EPR spectra ranging over several hundreds of MHz could be recorded. Three different types of two-dimensional correlation experiments were implemented, each correlating the FT EPR spectrum to either (i) longitudinal relaxation T_1, (ii) nuclear modulation, or (iii) dipolar modulation.

Correspondence between FT EPR-correlated inversion recovery kinetics of nitroxides and the same kinetics observed with selective pulses required minimization of cross talk in FT EPR spectra due to proton modulations. In particular, the pronounced proton modulations at X-band frequencies induced changes on the order of $\pm 10\%$ in apparent relaxation times. Furthermore, inversion recovery initiated by an adiabatic inversion pulse that inverts the entire spectrum reduced contributions of spectral diffusion between inverted and non-inverted spins. Consequently, longer relaxation times were observed upon an adiabatic inversion pulse than upon a monochromatic inversion pulse.

Nuclear modulations correlated to the EPR spectrum were studied at X and Q band for nitroxides and at X band for an oriented bispicolinate Cu(II) complex. Nitroxides at Q band revealed the proton combination frequency around 100 MHz, whereas the Cu(II) complex showed fundamental nuclear modulation frequencies up to 200 MHz related to the enriched ^{63}Cu nucleus. Such fast modulation frequencies could not be excited efficiently with monochromatic pulses due to limited excitation bandwidth.

Dipolar modulations correlated to the EPR spectrum were recorded at Q band using nitroxide spin pairs. The uniform excitation pulses were incorporated into an existing four-pulse sequence that refocuses the dipolar coupling by a solid echo (abbreviated as SIFTER) in a way that allowed to obtain FT EPR-correlated dipolar spectra. The resultant correlation pattern confirmed the expectation based on the inter-spin geometry of the spin pair. Previously, EPR-correlated dipolar spectra of nitroxides were not accessible by FT EPR techniques, especially not at Q band.

ZUSAMMENFASSUNG

Die gepulste Elektronenspinresonanz (ESR) ist eine vielseitige Methode zur Untersuchung von spezifischen Interaktionen in Systemen mit ungepaarten Elektronenspins. Eine grundlegende Einschränkung dieser Methode liegt jedoch darin, dass monochromatische Mikrowellenpulse nur einen Anteil des gesamten ESR-Spektrums angeregen können. Insbesondere für Ionen von Übergangsmetallen kann dieser angeregte Anteil sehr klein sein. Aufgrund dieser Einschränkung ist die Empfindlichkeit in einigen wichtigen ESR-Experimenten begrenzt. Ausserdem sind mehrdimensionale Korrelationsexperimente, welche sich in der Kernspinresonanz bewährt haben, in der gepulsten ESR nicht weit verbreitet.
Um einen grösseren Anteil des ESR-Spektrums anzuregen, werden in dieser Arbeit Mikrowellenpulse mit zeitvariabler Frequenz in die gepuste ESR eingeführt. Solche Pulse können erst seit einigen Jahren technisch realisiert werden, nachdem schnelle Arbriträrwellenformgeneratoren aufgekommen sind. Der Fokus dieser Arbeit liegt sowohl auf technischen wie auch auf experimentellen Aspekten.
Auf der technischen Seite wurden dedizierte experimentelle Aufbauten zur Implementation von frequenzvariablen Pulsen benötigt. Dazu wurden handelsübliche X- und Q-Band Spektrometer mit inkohärenten frequenzvariablen Pulsen erweitert. Zudem wurde ein Spektrometer mit konkurrenzfähiger Empfindlichkeit aufgebaut, das im X- und Q-band kohärente Pulse erzeugen kann. Eine wichtige technische Einschränkung bei der Anregung von Elektronenspins mit frequenzvariablen Pulsen ist die begrenzte Bandbreite des Mikrowellenresonators, welcher zur Ankopplung an die Spins verwendet wird. Daher wurde eine Methode zur Kompensation dieser Bandbreitenbegrenzung entwickelt, welche die Frequenzvariation des Pulses aufgrund des Adiabatizitätskriteriums anpasst. Die Konsistenz dieses Verfahrens liess sich anhand der linearen Antworttheorie verifizieren und die Methode wurde auf Pulse erweitert, welche für eine frequenzselektive Anregung optimiert wurden.
Auf der experimentellen Seite wurden diese Pulse in eine Vielzahl von bestehenden ESR-Pulssequenzen eingebracht. So konnte für Abstandsmessungen zwischen zwei Elektronenspins eine beträchtliche Empfindlichkeitssteigerung erreicht werden, indem der inkohärente Pumppuls in der Vierpuls-Doppel-Elektron-Elektron-Resonanz-Sequenz (DEER) durch einen inkohärenten frequenzvariablen Puls ersetzt wurde. So konnte im X-Band eine dreifache Erhöhung der DEER-Modulationstiefe auf 24% erreicht werden, indem ein spektral breites Cu(II)-Zentrum mit einem freqenzvariablen Puls anstelle eines monochromatischen Pulses gepumpt wurde. Bei Abstandsmessungen zwischen zwei Gd(III)-Zentren mit jeweils hohem Spin von $S = 7/2$ konnten mithilfe von zwei aufeinanderfolgenden frequenzvariablen Pulsen im Q-Band, welche jeweils unterschiedliche Frequenzbereiche pumpten, vergleichbare Modulationstiefen erreicht werden.
Wegen den vielen Energieniveaus des $S = 7/2$ Spins wurde der Transfer von Kohärenzen und Populationen anhand von Experimenten und Spindynamiksimulationen genauer untersucht. So beeinflusste ein ungewollter Kohärenztransfer augrund des Pumppulses die DEER-Empfindlichkeit. Um diese Empfindlichkeit durch Variation der Pulsparameter zu optimieren, wurde eine schnelle und einfach Prozedur entwickelt. Im Bezug auf Populationstransfer konnte Polarisation von unbeobachteten Übergängen mit frequenzvariablen Pulsen auf den beobachteten Übergang überführt werden. Dadurch konnte eine Signalverstärkung bis zu einem Faktor von 3 erzielt werden, welche die Bestimmung von Abständen bis zu 8.6 nm in vorpolarisierten DEER-Experimenten ermöglichte.

Frequenzvariable Pulse wurden ebenfalls auf Systeme mit drei Spins angewandt, wobei die hohe DEER-Modulationsamplitude zu einer ausgeprägteren Signatur von Dreispinkorrelationen führte, welche wiederum die Extraktion dieser Korrelationen aus experimentellen Daten erleichterte.
Eine wichtige Einschränkung für frequenzvariable Pulse in DEER-Experimenten waren Interferenzeffekte aufgrund der verlängerten Pulsdauer, welche bei kurzen Spindistanzen die Datenqualität verschlechtern könnten. Daher wurde eine neue interferenzfreie Pulssequenz für kurze Abstände entwickelt (mit dem Kürzel *CIDME*) und mit einem Gd-Gd-Modellsystem mit 2.1 nm Spin-Spin-Abstand getestet.
Das selbstgebaute Spektrometer ermöglichte Korrelationsexperimente, die auf der Fourier-Transformation (FT) von Spinechotransienten beruhen. Dank dem uniformen Anregungsprofil von bandbreitenkompensierten Pulsen konnte die Auswirkung der begrenzten Resonatorbandbreite auf FT-ESR-Spektren hauptsächlich auf die Detektion reduziert werden. Somit wurde die effektive Bandbreite von FT-ESR-Experimenten im Vergleich zu Experimenten mit unkompensierten Pulsen vergrössert. Dadurch konnten FT-ESR-Spektren über mehrere hundert Megahertz aufgenommen werden. Drei verschiedene Korrelationsexperimente wurden verwirklicht, welche das FT-ESR-Spektrum zu (i) longitudinaler Relaxation, (ii) Kernspinmodulation, oder (iii) dipolarer Modulation korrelieren.
Um eine Übereinstimmung zwischen ESR-korrelierter Inversionserholungs-Kinetik von Nitroxiden mit derjenigen zu erreichen, die mit selektiven Pulsen beobachtet wurde, musste das Übersprechen in FT-ESR-Spektren aufgrund von Protonenmodulationen minimisiert werden. Insbesondere im X-Band führten solche starke Protonenmodulationen zu Änderungen von $\pm 10\%$ in den beobachteten Relaxationszeiten. Ausserdem reduzierte ein adiabatischer Inversionspuls im Inversionserholungs-Experiment den Beitrag der spektralen Diffusion zwischen invertierten und nichtinvertierten Spins. Entsprechend wurden nach einem adiabatischen Inversionspuls längere Relaxationszeiten beobachtet als nach einem monochromatischen Inversionspuls.
Die Korrelation von Kernspinmodulationen mit dem ESR-Spektrum wurde für Nitroxide im X- und Q-Band und für einen orientierten Cu(II)-picolinat-Komplex im X-Band untersucht. Nitroxide im Q-Band zeigten die Protonenkombinationsfrequenz bei zirka 100 MHz, während der Cu(II)-Komplex fundamentale Kernspinfrequenzen bis zu 200 MHz aufzeigte, welche dem angereichertem ^{63}Cu-Kern zuzuschreiben sind. Solch schnelle Modulationen könnten mit monochromatischen Pulsen aufgrund von deren begrenzter Anregungsbandbreite nicht effizient angeregt werden.
Die Korrelation dipolarer Modulationen mit dem ESR-Spektrum wurde im Q-Band für Nitroxidspinpaare untersucht. Die uniformen Anregungspulse wurden in eine bestehende Vierpuls-Sequenz zur Refokussierung der dipolaren Kopplung eingebracht (mit dem Kürzel SIFTER), sodass FT-ESR-korrelierte dipolare Spektren aufgenommen werden konnten. Das resultierende Korrelationsmuster bestätigte die Erwartungen, die aus der bekannten wechselseitigen Geometrie der beiden Spins resultiert hatten. Bisher waren ESR-korrelierte dipolare Spektren von Nitroxiden mithilfe von FT-ESR-Techniken nicht zugänglich, insbesondere nicht im Q-Band.

CONTENTS

LIST OF FIGURES

LIST OF TABLES

1

INTRODUCTION

Frequency-swept pulses, often referred to as chirp pulses, are used in numerous contexts at microwave frequencies. Most prominently, microwave chirps with durations in the sub-millisecond regime are applied in radar technology to optimize the trade-off between distance range requiring long pulses and distance resolution requiring broad bandwidths [1]. For spectroscopic purposes, however, the pulse duration must be short compared to the decoherence times of the investigated system, which requires pulses with sub-microsecond duration for electron paramagnetic resonance (EPR) spectroscopy. The formation of such pulses necessitates arbitrary waveform generators (AWG) with nanosecond to sub-nanosecond timing resolution that became commercially available in the past few years. As an example, such AWGs were introduced recently into the field of rotational microwave spectroscopy to drastically enhance the signal-to-noise ratio [2]. Typical chirp pulse durations are on the order of 1 μs, whereas the frequency range covered by the pulse is 10 - 20 GHz broad [3]. For a comparison, one would estimate that for EPR spectroscopy, typical decoherence times, line widths and resonator bandwidths require pulses with duration on the order of few 100 ns and frequency range on the order of few 100 MHz.

The primary purpose for implementing chirp pulses in EPR spectroscopy is to enhance the excitation bandwidth. In particular, the monochromatic excitation pulses utilized so far often only excite a part of the entire EPR spectrum. Accordingly, not all spins available in the sample contribute to the detected signal, which is a potential loss of sensitivity. The main aim of this dissertation is therefore to enhance the excitation bandwidth by frequency-swept pulses for improved sensitivity.

At the beginning of this thesis in 2012, there were only few examples in EPR of pulses shaped by AWGs for fast frequency-sweeps or variants including amplitude and frequency modulation. In nuclear magnetic resonance at radio frequencies, on the contrary, frequency-swept pulses had already become well established and widely known for their high-fidelity adiabatic population inversion over large bandwidths and extensions thereof [4]. Even pulses shaped by intricate amplitude and frequency modulation functions derived from optimal control theory had been implemented to tailor the pulse performance according to the experimental requirements [5].

In contrast, for quite a long time, pulse shaping in electron spin resonance was limited to binary amplitude modulation, i.e. switching on and off a monochromatic microwave carrier, as well as coarse-grained stepping of the pulse phase. Besides providing the well-known monochromatic excitation pulses that established pulsed EPR, these capabilities also allowed for more elaborate excitation schemes, such as selective Gaussian-like excitation pulses [6], composite pulses [7], and stochastic excitation [8].

To the best of the author's knowledge, electron spin excitation pulses shaped by an AWG were first demonstrated in 2004 at radio frequencies in the context of electron spin imaging, where bandwidth-compensated sinc pulses have been demonstrated [9]. Just a few years later, a home-built EPR spectrometer employing AWG pulses at X band allowed to implement optimal control approaches in the context of quantum information processing [10, 11]. Adiabatic inversion of electron spin population by a frequency-swept AWG pulse has been first implemented in 2009 at radio frequency [12]. However, it should be noted that force-detected EPR approaches relied on repeated

adiabatic population inversions by frequency modulated microwave pulses at timescales of longitudinal relaxation and mechanical oscillation frequencies since the late nineties [13], which facilitated detection of a single electron spin in 2004 [14].

The first application of AWG pulses in the context of EPR spectroscopy has been demonstrated just at the beginning of this thesis, where pulses derived from optimal control theory revealed enhanced excitation bandwidths as compared to monochromatic pulses at the same power level [15]. Within linear response theory, the authors also demonstrated how experimental bandwidth limitations can be included into the optimization procedure.

Overall, it was mainly due to technological reasons that there were so few applications of shaped pulses in EPR by the beginning of this thesis. Most importantly, the performance and benefits related to frequency-swept excitation pulses were largely unexplored for EPR spectroscopy purposes. For that reason, this thesis represents a major contribution towards these unanswered questions and the obtained results are presented in the following way:

First, Chapter 2 explains the basic theory to understand the presented experiments, where particular emphasis is laid on understanding the spin dynamics of frequency-swept excitation pulses. Then, Chapters 3 to 6 incorporate the four first-author publications that appeared throughout this thesis in chronological order. In particular, Chapter 3 assesses the performance of frequency-swept pulses for inversion purposes on ordinary EPR instrumentation at X band. Compensation of frequency-swept pulses for bandwidth limitations as well as applications to electron-electron distance measurements and inversion recovery are introduced. Chapter 4 then proceeds to phase-coherent X-band pulses from the home-built spectrometer that establish FT EPR with bandwidths of several hundreds of MHz. Initial correlation experiments are also presented, namely nuclear modulation and inversion recovery correlated to the FT EPR spectrum.

Chapter 5 advances towards higher frequencies at Q band, larger excitation bandwidths well beyond 1 GHz, and higher spins $S = 7/2$. In particular, population transfer techniques for sensitivity enhancement using Gd(III) spin labels are introduced. In combination with further refinements in Gd-Gd distance measurements with frequency-swept pulses, unprecedented sensitivity is presented in Chapter 6.

Chapter 7 focuses on sensitivity from an instrumentation perspective. Primarily, this chapter describes the state of the home-built AWG spectrometer at the time of writing, which is capable of both X- and Q-band FT EPR experiments. Furthermore, Section 7.2 assesses whether the presented experiments could be optimized further by optimization of the resonator bandwidth.

Subsequently, Chapter 8 reports on results that are either unpublished or where the author of this thesis contributed by co-authorship or by supervision of student projects. A detailed outline is presented at the beginning of the chapter. In brief, Section 8.1 introduces a novel pulse sequence that is particularly well suited for short distances. A potential application to distance measurements involving three spins is presented in Section 8.2. In order to optimize the performance of frequency-selective pulses, the developed bandwidth-compensation procedure is generalized to amplitude- and frequency-modulated pulses in Section 8.3. In the subsequent Section, two-dimensional correlation experiments that correlate the X- or Q-band FT EPR spectrum to nuclear modulation (Section 8.4.1), longitudinal relaxation (Section 8.4.2), or dipolar modulation (Section 8.4.3) are presented.

The thesis is concluded in Chapter 9 and supporting information related to the first-author publications are found in Appendices A to D, respectively.

2

THEORY

This chapter provides a brief overview on the theory required to understand the data presented within this thesis. Most of the topics covered are treated in much more detail in the numerous textbooks available on magnetic resonance, such as for instance [16–18]. It is only the description of frequency-swept pulses in Section 2.4.2, where the concepts of superadiabaticity [19] and of Landau-Zener-Stückelberg-Majorana theory go beyond the description that is usually encountered in textbooks on magnetic resonance.

2.1 THE SPIN HAMILTONIAN

The relevant static interactions of a paramagnetic system containing unpaired electron spins and surrounding nuclear spins in an external magnetic field are often well described by the Hamiltonian

$$\hat{\mathcal{H}}_0 = \underbrace{\hat{\mathcal{H}}_{\mathrm{EZ}} + \hat{\mathcal{H}}_{\mathrm{NZ}}}_{\text{Zeeman}} + \underbrace{\hat{\mathcal{H}}_{\mathrm{HF}}}_{\text{electron-nuclear}} + \underbrace{\hat{\mathcal{H}}_{\mathrm{ee}}}_{\text{electron-electron}} + \underbrace{\hat{\mathcal{H}}_{\mathrm{ZFS}} + \hat{\mathcal{H}}_{\mathrm{NQ}}}_{\text{high spin}} \tag{2.1}$$

where the first two terms are the Zeeman interactions between the spins and the applied magnetic field, $\hat{\mathcal{H}}_{\mathrm{HF}}$ describes the coupling between electrons and nuclei, $\hat{\mathcal{H}}_{\mathrm{ee}}$ describes (weak) couplings between electrons and the last two terms are interactions specific to electron and nuclear spins with spin quantum numbers $S > 1/2$ and $I > 1/2$, respectively.
The energy levels E_i related to the spin Hamiltonian can be obtained from the Hamiltonian by solving the time-independent Schrödinger equation

$$\hbar\hat{\mathcal{H}}_0 \left|\psi_i\right\rangle = E_i \left|\psi_i\right\rangle \tag{2.2}$$

where $\left|\psi_i\right\rangle$ are the corresponding eigenstates spanning the Hilbert space and the $\hbar$ indicates that the Hamiltonian $\hat{\mathcal{H}}_0$ is specified in units of angular frequencies. Importantly, the spin Hamiltonian contains only spin coordinates, such that spin quantization results in a finite number of energy levels E_i. Nevertheless, static interactions which couple spin coordinates to spatial coordinates, as for instance the spin-orbit coupling, are included in the parameters of the spin Hamiltonian (see also below).
Spectroscopy is based on investigation of transitions between energy levels when driven into resonance by a radiation field at frequency ω_{res}. For the most part, such transitions are observed if the radiation frequency matches the transition energy between two states a and b

$$\Delta E = |E_a - E_b| = \hbar\omega_{\mathrm{res}} \tag{2.3}$$

and if angular momentum is conserved.

2.1.1 *Zeeman interaction*

The Zeeman interaction describes the energy splitting due to an externally applied magnetic field and the magnetic moment related to the spin. For an electron spin, the anisotropic Zeeman interaction is defined as

$$\hat{\mathcal{H}}_{\mathrm{EZ}} = \frac{\mu_{\mathrm{B}}}{\hbar} \vec{B}_0^T \mathbf{g} \vec{\hat{S}} \tag{2.4}$$

where μ_B is the Bohr magneton, $\vec{B}_0$ the vector describing the applied magnetic field, $\mathbf{g}$ the g tensor and $\vec{\hat{S}}$ the vector of electron spin operators ($\hat{S}_x$, $\hat{S}_y$, $\hat{S}_z$). The g tensor contains details on the electron orbitals. For a free electron, the g tensor is isotropic and takes a value of $g_e \approx 2.002319$. For an electron in the relevant ground-state orbital, anisotropy is introduced by the spin-orbit coupling. In general, the g tensor has a complicated relation on the orbitals because spin-orbit contributions from excited states need to be taken into consideration. Organic radicals typically have deviations below 1% from the free electron g_e. Transition metal ions may have fairly large deviations from the free electron g_e.
With an anisotropic g tensor, the magnetic moment, and therefore the energy splitting, depends on orientation. The g tensor defines a coordinate system (x, y, z) based on the principal axes system (PAS) of the g tensor, with principal components g_{xx}, g_{yy}, g_{zz}. The orientation of the magnetic field with respect to the PAS is then determined by the polar angle θ and the azimuthal angle ϕ. The orientation-dependent effective g value becomes

$$g_{\text{eff}}(\theta,\phi) = \sqrt{g_{xx}^2 \sin^2(\theta)\cos^2(\phi) + g_{yy}^2 \sin^2(\theta)\sin^2(\phi) + g_{zz}^2 \cos^2(\theta)} \quad (2.5)$$

At sufficiently large fields, in particular for electron spins $S = 1/2$, the Zeeman interaction is often the dominant interaction (high field approximation). In powder spectra, where all orientations contribute, the principal components of the g tensor thus may be resolved.
For the simplest case, which is a paramagnetic system with one single electron spin $S = 1/2$ in a static field B_0 along the z-axis, the relevant Hamiltonian is determined by

$$\hat{\mathcal{H}}_0 = \omega_S \hat{S}_z \quad (2.6)$$

where $\omega_S = g_e \mu_B B_0/\hbar$ is the resonance frequency of the electron spin and the two energy levels are due to the spin quantization number $m_S = \pm 1/2$. The nuclear Zeeman interaction is formally equivalent, but on the order of three orders of magnitude smaller than the electron Zeeman interaction. The anisotropy in the nuclear Zeeman interaction due to shielding effects is usually not resolvable in EPR spectroscopy, hence

$$\hat{\mathcal{H}}_{\text{NZ}} = \frac{-g_n \mu_n}{\hbar} \vec{B}_0^T \vec{\hat{I}} = \omega_I \hat{I}_z \quad (2.7)$$

where μ_n is the nuclear magneton, g_n the nuclear g factor and $\vec{\hat{I}}$ the vector of nuclear spin operators ($\hat{I}_x$, $\hat{I}_y$, $\hat{I}_z$). The second expression follows for a magnetic field along the z-axis. Gyromagnetic ratios γ_n common in the context of NMR are given by $\gamma_n = g_n \mu_n/\hbar$. In the context of EPR spectroscopy, the nuclear Zeeman frequency ω_I becomes relevant if its magnitude is comparable to the anisotropic part of the hyperfine interaction $\hat{\mathcal{H}}_{\text{HF}}$.

2.1.2 *Electron-nuclear hyperfine interaction*

The hyperfine interaction describes electron-nuclear couplings. For an electron-nuclear spin pair, the interaction is

$$\hat{\mathcal{H}}_{\text{HF}} = \vec{\hat{S}}^T \mathbf{A} \vec{\hat{I}} = \vec{\hat{S}}^T (a_{\text{iso}} \mathbb{1} + \mathbf{T}) \vec{\hat{I}} \quad (2.8)$$

where $\mathbf{A}$ is the hyperfine tensor with isotropic contribution a_{iso} and anisotropy $\mathbf{T}$. There are two sources for the hyperfine interaction, namely direct spatial overlap between the electron wavefunction and the nucleus or through-space dipole-dipole couplings between the electron and the nucleus.
Wavefunction overlap is most relevant for electrons in s orbitals and is described by the isotropic Fermi contact term

$$a_{\text{iso}} = \frac{2}{3} \frac{\mu_0}{\hbar} g_e \mu_B g_n \mu_n |\psi_{\text{electronic}}(0)|^2 \quad (2.9)$$

where μ_0 is the vacuum permeability and $|\psi_{\text{electronic}}(0)|^2$ is the probability to find the electron at the location of the nucleus.
Through space dipole-dipole coupling is most relevant for electrons in non-spherical orbitals, where the elements of the relevant tensor $\mathbf{T}$ are obtained by averaging over the ground-state wavefunction by

$$T_{ij} = \frac{\mu_0}{4\pi\hbar} g_e \mu_B g_n \mu_n \left\langle \psi_{\text{electronic}} \left| \frac{3r_i r_j - \delta_{ij} r^2}{r^5} \right| \psi_{\text{electronic}} \right\rangle \tag{2.10}$$

where r is the electron-nuclear distance and r_i,r_j projections along general coordinates (x, y, z). For highly localized electron wavefunctions, as for instance encountered for some transition metal ions, it may be possible to approximate the electron as a point dipole, which results in

$$\mathbf{T} = \frac{\mu_0}{4\pi\hbar} \frac{g_e \mu_B g_n \mu_n}{r^3} (3\vec{n} \cdot \vec{n}^T - \mathbb{1}) \tag{2.11}$$

where r is the electron-nuclear distance and $\vec{n}$ the direction of the inter-spin vector. In general, however, quantum chemistry computations are required to relate the hyperfine parameters a_{iso} and $\mathbf{T}$ to structural information. The experimental consequences of an anisotropic hyperfine interaction that is on the same order of magnitude as the nuclear Zeeman interaction will be discussed below in Section 2.5.1.

2.1.3 *Weak electron-electron interactions*

Electron-electron interactions are considered to be weak if $\hat{\mathcal{H}}_{\text{ee}} \ll \hat{\mathcal{H}}_{\text{EZ}}$, where the coupling Hamiltonian between two electron spins $\vec{\hat{S}}_1$ and $\vec{\hat{S}}_2$ is given by

$$\hat{\mathcal{H}}_{\text{ee}} = \vec{\hat{S}}_1^T \mathbf{J} \vec{\hat{S}}_2 + \vec{\hat{S}}_1^T \mathbf{D} \vec{\hat{S}}_2 \tag{2.12}$$

and $\mathbf{J}$ is the Heisenberg exchange interaction tensor and $\mathbf{D}$ is the dipolar electron-electron interaction tensor. The former is caused by residual spatial overlap between the wavefunctions of the two electrons, whereas the latter is caused by through-space dipolar couplings.
Within this thesis, only systems where $\hat{\mathcal{H}}_{\text{ee}}$ is dominated by the dipolar contribution are relevant. In the absence of Heisenberg exchange, the wavefunctions of the two electrons are well separated and may often be approximated as point dipoles. This results in a coupling tensor according to Eq. (2.11), where the appropriate magnetic moments of the coupled electrons need to be substituted. Conveniently, the resulting dipole-dipole Hamiltonian is transformed into spherical coordinates, which results in

$$\hat{\mathcal{H}}_{\text{dip}} = \frac{\mu_0}{4\pi\hbar} \frac{g_1 g_2 \mu_B^2}{r^3} (\hat{A} + \hat{B} + \hat{C} + \hat{D} + \hat{E} + \hat{F}) \tag{2.13}$$

with the so-called dipolar alphabet using shift operators $\hat{S}^+$ and $\hat{S}^-$

$$\begin{aligned}
\hat{A} &= \hat{S}_{1z}\hat{S}_{2z}(1 - 3\cos^2(\theta)) \\
\hat{B} &= (\hat{S}_1^+\hat{S}_2^- + \hat{S}_1^-\hat{S}_2^+)\frac{3\cos^2(\theta) - 1}{4} \\
\hat{C} &= (\hat{S}_1^+\hat{S}_{2z} + \hat{S}_{1z}\hat{S}_2^+)\frac{-3\sin(\theta)\cos(\theta)\exp(-i\phi)}{2} \\
\hat{D} &= (\hat{S}_1^-\hat{S}_{2z} + \hat{S}_{1z}\hat{S}_2^-)\frac{-3\sin(\theta)\cos(\theta)\exp(i\phi)}{2} \\
\hat{E} &= (\hat{S}_1^+\hat{S}_2^+)\frac{-3\sin^2(\theta)\exp(-2i\phi)}{4} \\
\hat{F} &= (\hat{S}_1^-\hat{S}_2^-)\frac{-3\sin^2(\theta)\exp(2i\phi)}{4}
\end{aligned} \tag{2.14}$$

where θ and ϕ are the angles that describe the orientation of the inter-spin vector. The prefactor in Eq. (2.13) determines the coupling strength ω_{dd}. Spectroscopic separation of the dipolar electron-electron coupling ω_{dd} is discussed in Section 2.5.2.

2.1.4 *High spin interactions*

For strongly interacting electron spins, as often encountered in transition metal ion complexes, it is more appropriate to describe the interacting electrons by a coupled group spin $S > 1/2$. The corresponding zero-field splitting (ZFS) is expressed as

$$\hat{\mathcal{H}}_{\mathrm{ZFS}} = \vec{\hat{S}}^T \mathbf{D} \vec{\hat{S}} = D(\hat{S}_z^2 - \frac{1}{3}S(S+1)) + E(\hat{S}_x^2 - \hat{S}_y^2) \tag{2.15}$$

where $\mathbf{D}$ is the ZFS tensor with principal components D_{xx}, D_{yy} and D_{zz}. The last expression is the Hamiltonian in the principal axis system, which is parametrized by $D = 3D_{zz}/2$ and $E = (D_{xx} - D_{yy})/2$. The asymmetry parameter E can take values between 0 and $D/3$, where $E = 0$ denotes axial symmetry and $E > 0$ orthorhombic symmetry.
Only systems where $\hat{\mathcal{H}}_{\mathrm{ZFS}} < \hat{\mathcal{H}}_{\mathrm{EZ}}$ and S is a half-integer are relevant within this thesis. In this case, perturbation theory can be used to obtain the corrections to the energy levels of the electron spin. Moreover, the central transition between the $m_S = +1/2$ and the $m_S = -1/2$ energy level has no first-order correction. Within experimental constraints, single-quantum transitions where the angular momentum projection changes by $\Delta m_S = 1$ are most relevant.
A formally equivalent interaction of different origin is the nuclear quadrupole interaction for nuclear spins $I > 1/2$, which is defined as

$$\hat{\mathcal{H}}_{\mathrm{NQ}} = \vec{\hat{I}}^T \mathbf{P} \vec{\hat{I}} \tag{2.16}$$

where $\mathbf{P}$ is the quadrupole tensor. A similar parametrization as for $\hat{\mathcal{H}}_{\mathrm{ZFS}}$ by a splitting parameter and an asymmetry parameter is often used. Since this interaction can become comparable in magnitude to the anisotropic hyperfine interaction, it may be relevant in the context of EPR. In the context of this thesis, this is not discussed further, but concepts that are established in the context of NMR with quadrupolar nuclei will be important in Chapter 5.

2.2 SPIN DYNAMICS

Magnetic resonance phenomena can be described by the time evolution of a spin system under the relevant Hamiltonian $\hat{\mathcal{H}}(t)$, which contains $\hat{\mathcal{H}}_0$ but also additional time-dependent contributions, such as for instance excitation pulses (see Section 2.4). Since the dynamics of a statistical ensemble of quantum systems are of interest in the context of magnetic resonance (mixed states), a description by means of density operators $\hat{\sigma}$ is most appropriate. The mixed state of the spins is therefore represented by

$$\hat{\sigma}(t) = \overline{|\Psi(t)\rangle \langle\Psi(t)|} = \sum_i \sum_j \overline{c_i(t) c_j^*(t)} \, |\psi_i\rangle \langle\psi_j| \tag{2.17}$$

where $c_i(t)$ are the coefficients related to the eigenfunctions $|\psi_i\rangle$ that describe the wavefunction $|\Psi(t)\rangle$ of each pure state, averaged over the ensemble as indicated by the bars. Mixed states are distinguished from pure states by $\mathrm{tr}(\hat{\sigma}^2) < 1$ and $\mathrm{tr}(\hat{\sigma}^2) = 1$, respectively.
The time evolution of the density operator is determined by the Liouville-von Neumann equation

$$\frac{d}{dt}\hat{\sigma}(t) = -i\big[\hat{\mathcal{H}}(t), \hat{\sigma}(t)\big] \tag{2.18}$$

Experimental observables are computed from $\hat{\sigma}(t)$ by taking the expectation value of a Hermitian operator. In particular, the operator $\hat{S}_x$ influences the magnitude of the magnetic moment perpendicular to the applied field, which is usually detected in magnetic resonance and obtained by

$$\langle \hat{S}_x \rangle = \mathrm{tr}(\hat{\sigma}(t) \cdot \hat{S}_x) \tag{2.19}$$

Within this thesis, the software package SPIDYAN (spin dynamics analysis) is often used to compute $\hat{\sigma}(t)$ and relevant expectation values [20]. In these simulations, the time-dependence of $\hat{\mathcal{H}}(t)$ is removed by assuming piecewise constant Hamiltonians within fine-grained time steps.
In the case of a time-independent Hamiltonian, the Liouville-von Neumann equation has the solution

$$\hat{\sigma}(t) = \exp\left(-i\hat{\mathcal{H}}t\right)\hat{\sigma}(0)\,\exp\left(i\hat{\mathcal{H}}t\right) \tag{2.20}$$

where the matrix exponentials are referred to as propagators.
If we consider evolution for a time t under the Zeeman Hamiltonian $\hat{\mathcal{H}}_0 = \omega_S\hat{S}_z$, two important solutions are

$$\hat{\sigma}(0) = \hat{S}_z \xrightarrow{\hat{S}_z(\omega_S t)} \hat{\sigma}(t) = \hat{S}_z \tag{2.21}$$

$$\hat{\sigma}(0) = \hat{S}_x \xrightarrow{\hat{S}_z(\omega_S t)} \hat{\sigma}(t) = \cos(\omega_S t)\hat{S}_x + \sin(\omega_S t)\hat{S}_y \tag{2.22}$$

where notation and calculation according to the product operator formalism is used (see for instance [17, 18]).
The physical interpretation of Eq. (2.21) is that for a magnetic moment initially aligned along the applied magnetic field (z-axis), the Zeeman Hamiltonian has no effect and the experimental observable $\langle\hat{S}_x\rangle$ is zero. For Eq. (2.22), one finds that for a magnetic moment initially along the x-axis, the magnetic moment precesses around the applied field with the frequency ω_S and $\langle\hat{S}_x\rangle$ reveals an experimentally detectable cosine oscillation (Larmor precession).
Due to equilibration processes, spins prefer to align along the energetically favored direction of the applied magnetic field. Hence, Eq. (2.21) applies and no signal is observed in the equilibrium state. Accordingly, it is necessary to excite the spins into a non-equilibrium state to detect the resultant spin precession. A description of excitation pulses is provided in Section 2.4. Moreover, the dynamics of the equilibration processes require a dedicated treatment, which is briefly outlined in Section 2.3.
If the equilibrium populations of the energy levels at a temperature T are of interest, these can be obtained by Boltzmann statistics within the energy levels of the static spin Hamiltonian. For a precession frequency ω_S of 10 GHz, one finds that on the order of one spin out of thousand spins contributes to the detected signal. For NMR, where precession frequencies are smaller, even less spins contribute. In general, this mitigates the sensitivity of magnetic resonance experiments. Also note that the description of spin dynamics often only considers the spins that contribute to the signal, which results in traceless density matrices $\hat{\sigma}(t)$, as for instance in Eqs. (2.21) and (2.22). While this is not strictly according to the definition of the density operator in Eq. (2.17), it eases the analysis of the relevant dynamics considerably.

2.3 RELAXATION

Stochastic processes at finite temperature T are responsible for the thermalization of a non-equilibrium state back to the equilibrium state. If the effective timescales of these processes are on the timescales of the experiment, which happens rather often, the Liouville-von Neumann equation is no longer an exact description of spin dynamics. As has been noted by Bloch [21] in the context of the classical description of the first very NMR experiments, there are two characteristic timescales to be considered for a spin $S = 1/2$, namely the spin-lattice relaxation time T_1 and the spin-spin relaxation time T_2.
In the context here, T_1 is the timescale for the lattice to absorb the energy difference $\hbar\omega_S$ between the two energy levels. The relaxation time T_1 therefore describes the equilibration of spin populations, which corresponds to the component of the magnetic moment along the applied field. One therefore often refers to T_1 as the longitudinal relaxation time. The spin-spin relaxation time T_2 determines the timescale of phase coherence amongst the ensemble

of spins precessing around the applied field, hence the terminology of a transverse relaxation time. As opposed to longitudinal relaxation, thermalization of phase coherence does not necessarily require the lattice to absorb energy and exchange of energy is sufficient. In particular, there is no difference in energy between the states $\hat{\sigma} = \hat{S}_x$ and $\hat{\sigma} = \hat{S}_y$ for $S = 1/2$, whereas the phase of the precessing magnetic moment differs by $\pi/2$.
Within Wangsness-Bloch-Redfield theory [22, 23], it is possible to describe spin dynamics according to the master equation

$$\frac{d}{dt}\hat{\sigma}(t) = -i\big[\hat{\mathcal{H}}(t), \hat{\sigma}(t)\big] - \hat{\Gamma}(\hat{\sigma}(t) - \hat{\sigma}_{\mathrm{eq}}) \tag{2.23}$$

where the second term introduces damping (and coupling) of the components that deviate from the equilibrium $\hat{\sigma}_{\mathrm{eq}}$. The variable $\hat{\Gamma}$ is the so-called relaxation superoperator and contains the decay rates across individual elements of the density matrix. The derivation and formal definition of the relaxation superoperator exceed the scope of this section and is detailed elsewhere (see for instance [24]).
In brief, stochastic modulation of the spin Hamiltonian is introduced by the perturbation Hamiltonian $\hat{\mathcal{H}}_{\mathrm{stochastic}}(t)$. The main approximation is that the timescale of individual stochastic fluctuations (the correlation time) is short compared to the resultant variation in the density matrix (the relaxation time), which is referred to as the Redfield limit. In cases where the temporal (and spectral) correlation characteristics of the stochastic Hamiltonian are known, it is possible to derive models for the relaxation times and obtain insight into dynamics. Within this thesis, such an approach is not performed. It should also be noted that in solid-state EPR experiments, there are additional contributions to loss of phase coherence than transverse relaxation [18], as for instance spin diffusion. It is therefore more convenient to refer to a phase memory time T_{m} that describes the net loss of phase coherence.

2.4 PULSED EXCITATION

2.4.1 *Monochromatic pulses*

A monochromatic pulse oscillating at a frequency ω_{mw} with linear polarization along the x-axis and oscillation phase offset ϕ gives rise to the pulse Hamiltonian

$$\hat{\mathcal{H}}_{\mathrm{Pulse}}(t) = 2\omega_1 \cos(\omega_{\mathrm{mw}} t + \phi)\hat{S}_x \tag{2.24}$$

where ω_1 is the field strength of the pulse, which is related to the peak-to-peak oscillation amplitude of the magnetic field, $4 \cdot B_1$, by $\hbar\omega_1 = g_{\mathrm{e}}\mu_{\mathrm{B}}B_1$. During application of the pulse, the total Hamiltonian in absence of relaxation is therefore

$$\hat{\mathcal{H}}(t) = \hat{\mathcal{H}}_0 + \hat{\mathcal{H}}_{\mathrm{Pulse}}(t) \tag{2.25}$$

The time dependence of the pulse Hamiltonian may be removed by changing to a coordinate system that rotates with a frequency ω_{mw} around the z-axis. To obtain the Hamiltonian in this rotating frame, the Hamiltonian in the static coordinate frame from Eq. (2.25) is transformed into the rotating frame according to

$$\hat{\mathcal{H}}_{\mathrm{rot}} = \hat{\mathcal{H}}' - \omega_{\mathrm{mw}}\hat{S}_z \tag{2.26}$$

$$\hat{\mathcal{H}} \xrightarrow{\hat{S}_z(\omega_{\mathrm{mw}}t)} \hat{\mathcal{H}}' \tag{2.27}$$

where $\hat{\mathcal{H}}'$ is the Hamiltonian rotated about the z-axis and the second term in Eq. (2.26) is due to the rotation of the coordinate system [17].
In general, $\hat{\mathcal{H}}'$ is not time-independent and special consideration is required

to arrive at a time-independent representation. For the pulse Hamiltonian rotated about z, one obtains

$$\begin{aligned}\hat{\mathcal{H}}'_{\text{Pulse}}(t) &= \omega_1(\cos(\phi)\hat{S}_x + \sin(\phi)\hat{S}_y) \\ &\quad + \omega_1(\cos(2\omega_{\text{mw}}t + \phi)\hat{S}_x + \sin(2\omega_{\text{mw}}t + \phi)\hat{S}_y)\end{aligned} \tag{2.28}$$

where the time-dependent part is due to the counter-rotating component, which can be neglected if $\omega_{\text{mw}} \gg \omega_1$. If this is not the case, the off-resonant counter-rotating component results in a Bloch-Siegert phase shift.
For the spin Hamiltonian $\hat{\mathcal{H}}'_0$ rotated about z, time-dependent components arise due to off-diagonal elements in the matrix representation of the spin Hamiltonian. Within the secular approximation, these terms can be neglected if the magnitude of each off-diagonal element is much smaller than the difference between the connected diagonal elements [17]. Here, a spin $S = 1/2$ is considered with $\hat{\mathcal{H}}_0 = \omega_0\hat{S}_z$, such that no special considerations on off-diagonal elements are required. The time-independent rotating frame Hamiltonian results as

$$\hat{\mathcal{H}}_{\text{rot}} = \omega_1(\cos(\phi)\hat{S}_x + \sin(\phi)\hat{S}_y) + \Omega_0\hat{S}_z \tag{2.29}$$

where $\Omega_0 = \omega_0 - \omega_{\text{mw}}$ is the resonance offset. The time evolution of the spin in the rotating frame under this Hamiltonian can be computed according to the Liouville-von Neumann Equation (2.18).
In general, a pulse of duration t_{p} can be understood as a rotation around an effective field ω_{eff} by an angle $|\omega_{\text{eff}}|t_{\text{p}}$, where

$$|\omega_{\text{eff}}| = \sqrt{\omega_1^2 + \Omega_0^2} \tag{2.30}$$

and the orientation of the effective field is determined by the azimuthal phase angle ϕ and by the polar angle θ defined as

$$\theta = \arctan(\omega_1/\Omega_0) \tag{2.31}$$

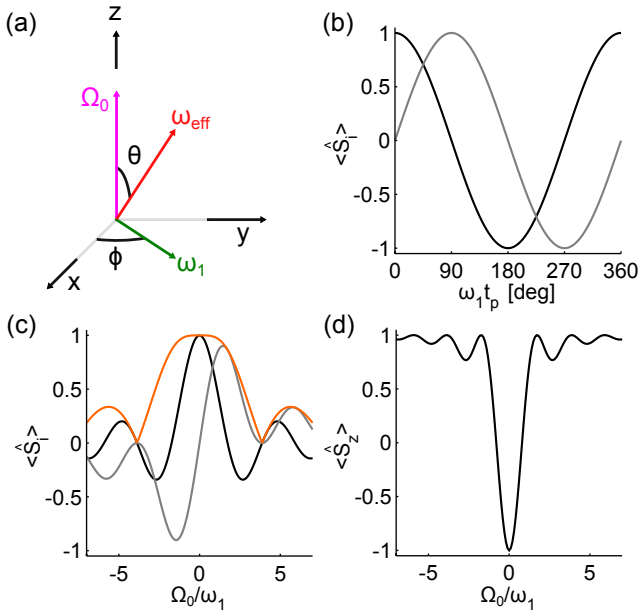

Figure 2.1 – Monochromatic excitation pulses. (a) Illustration of the rotating frame coordinate system with components according to Eq. (2.29). (b) Dependence on flip angle $\omega_1 t_{\text{p}}$ of $\langle\hat{S}_z\rangle$ (black) and $\langle\hat{S}_x\rangle$ (gray) after an on-resonance pulse. (c) $\langle\hat{S}_x\rangle$ (black), $\langle\hat{S}_y\rangle$ (gray) and total coherence $|\langle\hat{S}_x\rangle + i\langle\hat{S}_y\rangle|$ (orange) after a $\pi/2$ pulse as a function of normalized offset Ω_0/ω_1 (d) $\langle\hat{S}_z\rangle$ after a π pulse as a function of normalized offset Ω_0/ω_1. Calculated using matrix rotations.

An illustration of all the relevant quantities and their orientation in the rotating frame is shown in Fig. 2.1a. If the pulse is applied exactly on resonance, $\Omega_0 = 0$ and rotations around the x- or y-axis can be performed by proper choice of ϕ. A spin aligned along z at equilibrium can therefore be rotated around the y-axis according to

$$\hat{S}_z \xrightarrow{\hat{S}_y(\omega_1 t_\mathrm{p})} \hat{S}_z \cos(\omega_1 t_\mathrm{p}) + \hat{S}_x \sin(\omega_1 t_\mathrm{p}) \tag{2.32}$$

Fig. 2.1b shows the expectation values $\langle \hat{S}_z \rangle$ (black) and $\langle \hat{S}_x \rangle$ (gray) after the pulse as a function of the flip angle $\omega_1 t_\mathrm{p}$. By choosing $\omega_1 t_\mathrm{p} = \pi$, the pulse inverts the spin state. For that reason, such a π pulse is often referred to as an inversion pulse. By choosing $\omega_1 t_\mathrm{p} = \pi/2$, the pulse leaves the spin in the coherent superposition state along the x-axis. For that reason, such a $\pi/2$ pulse is often referred to as an excitation pulse.
If the pulse is no longer on resonance, off-resonance effects due to Ω_0 need to be considered. Fig. 2.1c shows the expectation values $\langle \hat{S}_x \rangle$ (black) and $\langle \hat{S}_y \rangle$ (gray) after a $\pi/2$ pulse as a function of normalized offset Ω_0/ω_1. The spin state along x is only realized on resonance. For small offsets, the azimuthal phase ϕ related to the spin state after the pulse depends almost linearly on offset (data not shown). Since a linear dependence of the phase in frequency domain relates to a delay in time domain, the total coherence $|\langle \hat{S}_x \rangle + i \langle \hat{S}_y \rangle|$ shown in orange is of experimental relevance. Total coherence is beyond 0.99 over an offset range of $1.6 \cdot \omega_1$.
For a π pulse, the resultant $\langle \hat{S}_z \rangle$ is shown in Fig. 2.1d. Here, $\langle \hat{S}_z \rangle$ is below -0.54 over an offset range of ω_1. One reason why the $\pi/2$ pulse has a slightly broader bandwidth is its shorter duration t_p for a given ω_1. In any case, it is difficult to achieve an effective bandwidth that is significantly larger than ω_1. Moreover, larger offset frequencies feature pronounced wiggles in the excitation profiles.
It is possible to improve the experimental performance of monochromatic pulses by using a cascade of pulses, so called composite pulses [25]. Both tolerance towards variations in ω_1 as well as effective excitation bandwidth can be improved. It has for instance been shown that composite pulses achieve uniform inversion for offsets well beyond ω_1 [26]. Such pulses will not be treated in detail within this thesis. Interestingly, it is also possible to derive composite pulses for uniform inversion beyond ω_1 based on frequency-swept pulses [27]. Frequency-swept pulses will be discussed in more detail in the following section.

2.4.2 *Frequency-swept pulses*

2.4.2.1 *Frequency-swept excitation and inversion pulses*

Frequency-swept pulses have a time-dependent instantaneous resonance offset $\Omega_\mathrm{i}(t)$. Opposite to monochromatic pulses, it is therefore not possible to remove the time dependence of the pulse Hamiltonian in a rotating coordinate system. Moreover, such pulses usually also have a time-dependent pulse amplitude $\omega_1(t)$, which further complicates a time-independent representation. Thus, the parameters to describe a pulse in a rotating coordinate system introduced in the previous section, namely the effective field ω_eff, the polar angle θ and the azimuthal phase angle ϕ, are all time-dependent. While the time dependence of ω_eff and θ follows directly from their definition in Eqs. (2.30) and (2.31), the time dependence of the phase angle ϕ is due to the instantaneous phase $\phi_\mathrm{i}(t)$ determined by

$$\phi_\mathrm{i}(t) = \phi_0 + \int_0^t \Omega_\mathrm{i}(t')dt' \tag{2.33}$$

where ϕ_0 is a constant phase offset between the frequency-swept pulse and the rotating frame.

For ease of illustration, the time dependence of this phase can be removed by changing to a reference frame with rotation frequency synchronized to the frequency sweep $\Omega_i(t)$ of the pulse. For further reference, this frame is referred to as the accelerated frame. The pulse at a particular time instant is represented as shown in Fig. 2.2a, where the axes labeled x, y, z are the axes of the accelerated frame. The instantaneous offset $\Omega_i(t)$ is along the z-axis and the pulse amplitude $\omega_1(t)$ is along the x-axis, by proper choice of the constant phase offset ϕ_0. The Hamiltonian of the pulse in presence of a static Zeeman interaction is therefore

$$\hat{\mathcal{H}}_{acc}(t) = \Omega_i(t)\hat{S}_z + \omega_1(t)\hat{S}_x \tag{2.34}$$

The type of pulse considered throughout this section has the following form

$$\Omega_i(t) = \Omega_1 + \frac{\Delta\Omega}{t_p} \cdot t \tag{2.35}$$

$$\omega_1(t) = \omega_{1,max} \cdot \begin{cases} \sin\left(\frac{\pi}{2}\frac{t}{t_{rise}}\right) & \text{if } t \leq t_{rise} \\ 1 & \text{if } t_{rise} < t < t_p - t_{rise} \\ \sin\left(\frac{\pi}{2}\frac{t_p - t}{t_{rise}}\right) & \text{if } t \geq t_p - t_{rise} \end{cases} \tag{2.36}$$

The frequency modulation $\Omega_i(t)$ of this pulse describes a linear frequency sweep having a spectral extent of $\Delta\Omega$, starting from Ω_1 to a final frequency Ω_2. The amplitude modulation $\omega_1(t)$ is constant, except for an intentional sinusoidal edge smoothing during t_{rise} (see also below in Fig. 2.2b). Due to the functional form of the frequency modulation, this pulse will be referred to as a linear chirp or a constant-rate chirp throughout this thesis. Note also that in later sections, where actual experiments are involved, it will be more appropriate to describe the pulse in terms of frequencies instead of angular frequencies. These are obtained according to the convention $\nu = \omega/(2\pi)$ and $f = \Omega/(2\pi)$. As an example, the sweep width $\Delta\Omega$ will be referred to as Δf, whereas the field strength ω_1 will be referred to as ν_1.

An illustration of the pulse modulation functions for a spin with resonance frequency centered with respect to the frequency sweep is provided in Fig. 2.2b, with color coding in accordance to panel (a). When translating these modulation functions into the accelerated frame, the effective field $\omega_{eff}(t)$ defines a trajectory from $-z$ to z, crossing the x-axis at $t = t_p/2$. In this way, the effective field passes through resonance, which explains why this pulse belongs to the family of so-called passage pulses.

Exactly this type of passage pulse has been examined previously in [28]. Moreover, it follows the same concept as the WURST pulse (wideband, uniform rate, smooth truncation) introduced later on, which has a different formal definition of $\omega_1(t)$ [29]. Some frequency-swept passage pulses, however, are based on non-linear frequency sweeps [27, 4], as for instance the class of pulses determined by hyperbolic secant and tangent modulation functions [30]. This particular class of pulses is treated in more detail in Section 8.3.1. Importantly, the concepts elaborated in the following can also be applied to pulses having a variable sweep rate.

By assuming a spin with $S = 1/2$ initialized along z and free of any relaxation processes, the spin dynamics under a passage pulse depend on *how slow* the resonance is passed. In the limiting case of a very slow passage, the spin quantization axis follows the trajectory of the effective field adiabatically and is inverted [27]. Adiabatic following of $\omega_{eff}(t)$ formally requires that $[\hat{\mathcal{H}}(t), \hat{\sigma}(t)] = 0$ is fulfilled throughout the entire pulse. From this requirement, it becomes clear why it is important to truncate the amplitude modulation $\omega_1(t)$ to zero at the pulse edges. How well this requirement is fulfilled during the sweep can be quantified by means of the adiabaticity factor [27]

$$Q(t) = \frac{\omega_{eff}(t)}{|\omega_\theta(t)|} = \frac{(\omega_1(t)^2 + \Omega_i(t)^2)^{3/2}}{|\omega_1(t)\dot{\Omega}_i(t) - \Omega_i(t)\dot{\omega}_1(t)|} \tag{2.37}$$

where $\omega_\theta = d\theta/dt$ is the rate of change of the polar angle θ (see also Fig. 2.2a). In particular, the pulse is adiabatic if the variation of the effective field is slow compared to its strength, and therefore $Q(t) \gg 1$.
Here, this condition is most critical on resonance (see also Fig. 2.2d below), where $\omega_{\text{eff}} = \omega_{1,\text{max}}$. At this critical time instant, the adiabaticity factor is

$$Q_{\text{crit}} = \frac{\omega_{1,\text{max}}^2 t_\text{p}}{\Delta\Omega} = \frac{2\pi\nu_{1,\text{max}}^2 t_\text{p}}{\Delta f} \tag{2.38}$$

Typical values for highly efficient adiabatic population inversion are $Q_{\text{crit}} > 5$ [27, 4]. In Fig. 2.2c, two representative spin dynamics simulations with $Q_{\text{crit}} = 5$ (black) and $Q_{\text{crit}} = 2.5$ (gray) are illustrated in the accelerated coordinate system (see caption for details). As can be seen when comparing the precession cone angle around $\omega_{\text{eff}}(t)$ when approaching the $-z$-axis at the end of the pulse, adiabatic following is better fulfilled for the larger adiabaticity factor.
For reference, $\omega_{\text{eff}}(t)$, $|\omega_\theta(t)|$ and $Q(t)$ of the pulse with $Q_{\text{crit}} = 5$ are illustrated in Fig. 2.2d in red, blue and gray, respectively. The effect of the amplitude modulation $\omega_1(t)$ at the pulse edges during t_{rise} is clearly recognized in $Q(t)$. This effect will become significant for spins that are passed in the vicinity of the pulse edges, as discussed further below when taking into consideration the offset dependence of Q_{crit}.
As an interesting side remark, it should be noted that spins are aligned along the transverse plane while passing adiabatically through resonance. A transient precessing signal is therefore induced to the detector. It is this

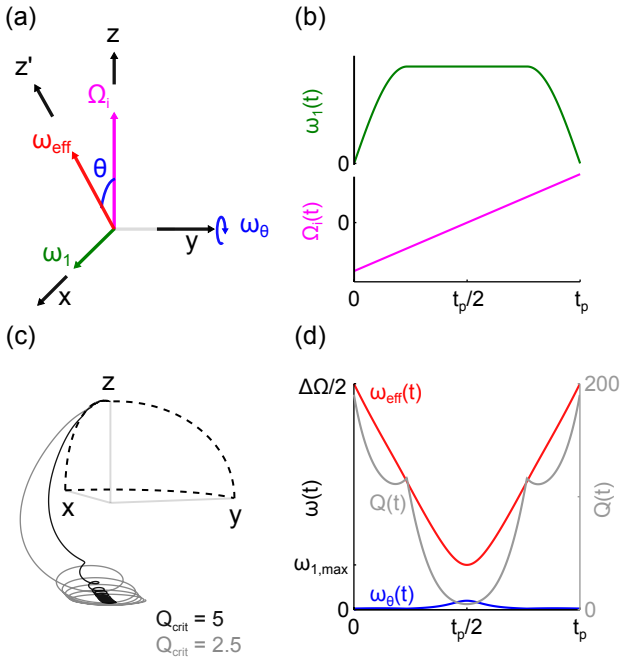

Figure 2.2 – Resonance passage illustrated in different frames. (a) Zeeman and pulse Hamiltonian $\hat{\mathcal{H}}(t)$ illustrated at a particular time instant in the accelerated frame with axes x, y and z and components according to Eq. (2.34). The axis labeled z' indicates the ω_{eff} frame, with components of the Hamiltonian according to Eq. (2.39). (b) Pulse modulation functions $\Omega_\text{i}(t)$ and $\omega_1(t)$ according to Eqs. (2.35) and (2.36) for spin with resonance frequency in the center of the frequency sweep. (c) Spin trajectories simulated using SPIDYAN [20] translated into the accelerated frame with Q_{crit} values as indicated in the plot. The pulse parameters were $t_\text{p} = 128$ ns, $t_{\text{rise}} = 30$ ns, $\Delta f = 0.63$ GHz. The indicated adiabaticities of 5.0 and 2.5 were determined by setting $\nu_{1,\text{max}}$ to either 62.5 MHz or 23.0 MHz, respectively. (d) Time-dependence of $\omega_{\text{eff}}(t)$, $\omega_\theta(t)$ and $Q(t)$ as indicated in the plot. The pulse parameters correspond to $Q_{\text{crit}} = 5$ as described in the caption of panel c.

transient response which was observed in the very first induction-detected NMR experiments of protons by Felix Bloch and coworkers [21, 31]. In these experiments, passage was implemented by the formally equivalent approach of sweeping the magnetic field B_0 through resonance while irradiating continuously at a fixed frequency. This detection principle found a number of applications in earlier NMR experiments [16]. Nowadays, while less common in NMR, it is being developed actively to optimize the SNR of continuous-wave EPR spectroscopy by means of rapid-scan techniques [32].

While the accelerated frame is well suited to illustrate the spin dynamics, further insight into adiabatic passage can be obtained when tilting the coordinate system by the angle $\theta(t)$. In this way, the effective field $\omega_{\text{eff}}(t)$ remains parallel to the new z'-axis throughout the pulse (see Fig. 2.2a). This frame is therefore referred to as the ω_{eff} frame [4]. Moreover, this frame corresponds to the eigenframe of the Hamiltonian in the accelerated frame [19] (see also below). The Hamiltonian in this frame reads

$$\hat{\mathcal{H}}_{\text{eff}}(t) = \omega_{\text{eff}}(t)\hat{S}_{z'} - \omega_\theta(t)\hat{S}_y \tag{2.39}$$

and directly contains the quantities relevant to determine the adiabaticity factor $Q(t)$. The z' label in the $\hat{S}_z$ operator is only introduced to indicate the new reference frame. Since at $t = 0$, z' coincides with the spin quantization axis z for a properly truncated pulse, it is immediately clear that $[\hat{\mathcal{H}}_{\text{eff}}(t), \hat{\sigma}(t)] = 0$ if $\omega_\theta(t)$ is negligibly small compared to $\omega_{\text{eff}}(t)$: It describes a spin-lock to z'. However, for $Q_{\text{crit}} = 5$ where almost perfect population inversion is possible, it is not necessarily clear why spins should remain locked to z' and end up inverted at $-z$. This problem has been addressed by repeated diagonalization of the Hamiltonian, starting from the ω_{eff} frame, which yields so-called superadiabatic frames [19]. This procedure revealed that a pulse with $Q_{\text{crit}} = 5$ does indeed end up inverted at $-z$, but does not strictly follow the trajectory defined by $\omega_{\text{eff}}(t)$. In the ω_{eff} frame, for instance, $\omega_{\text{eff}}(t)$ and $\omega_\theta(t)$ define a new *second-order* trajectory, which is partially followed. As a consequence, the simulated trajectory for $Q_{\text{crit}} = 5$ has a rather distinct excursion towards $-y$ before even passing the xy-plane (see Fig. 2.2c). If the Hamiltonian describing the second-order would be diagonalized again, higher order corrections to the trajectory followed by the spins are obtained. As stated previously in a more general context, such repeated frame diagonalizations diverge at some point [33]. Also note that the second-order correction to the actual trajectory was found independently in a more specific context [34].

An important distinction between adiabatic and non-adiabatic passage can be made in terms of avoided energy level crossings. The eigenvalues of $\hat{\mathcal{H}}_{\text{acc}}(t)$ are shown in Fig. 2.3a, where the solid lines are the two eigenvalues for $Q_{\text{crit}} = 5$ and the dashed lines for $Q_{\text{crit}} = 0$, by setting $\omega_1(t)$ to zero. In the limiting case of $Q_{\text{crit}} = 0$, the energy levels do cross, whereas in presence of a driving field, the energy levels do no longer cross and become separated by $\omega_{1,\text{max}}$. The time evolution of the corresponding eigenvectors of $\hat{\mathcal{H}}_{\text{acc}}(t)$ in the accelerated frame are shown in Fig. 2.3b. Note the equivalence between the eigenvalues and eigenvectors of $\hat{\mathcal{H}}_{\text{acc}}(t)$ with the $\hat{S}_{z'}$ term and $\hat{S}_x$ term of $\hat{\mathcal{H}}_{\text{eff}}(t)$ in Eq. (2.39), respectively.

Resonance passage therefore results in an avoided crossing of energy levels in the eigenbasis of the Hamiltonian. For adiabatic inversion, the populations of the eigenstates remain unchanged throughout the pulse. For non-adiabatic passage on the contrary, the populations are modified due to coupling between the levels while passing the avoided crossing.

Non-adiabatic passage of an avoided crossing has been studied in 1932 by Landau, Zener, Stückelberg and Majorana [36–39]. The different approaches to this problem have been compared in [40], where it has also been suggested to mention all four authors when referring to the results from 1932, instead of only mentioning Landau and Zener. While Landau, Zener and Stückelberg studied the avoided crossing in the context of inelastic atomic scattering, Majorana treated a spin passing through a magnetic field with

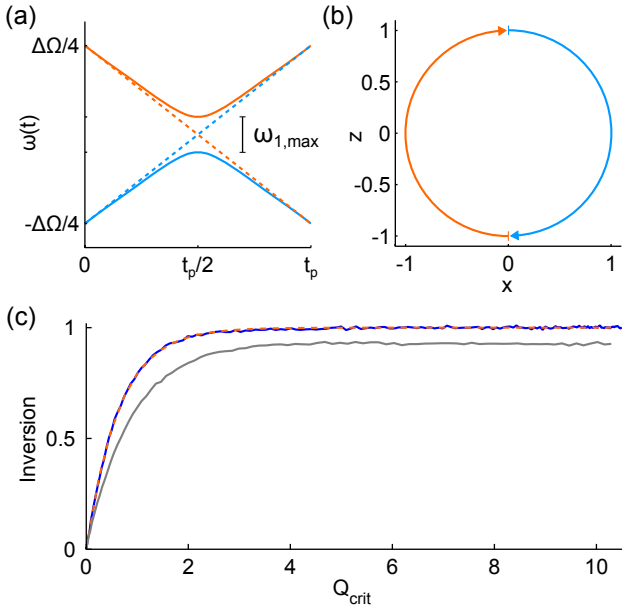

Figure 2.3 – Transition probability when passing through avoided crossing using Landau-Zener-Stückelberg-Majorana theory. (a) Eigenvalues of $\hat{\mathcal{H}}_{\mathrm{acc}}(t)$ discriminated by colors blue and orange. The solid lines are for $Q_{\mathrm{crit}} = 5.0$ according to Fig. 2.2c, whereas the dashed lines are for $Q_{\mathrm{crit}} = 0$ by setting the pulse amplitude $\omega_{1,\mathrm{max}}$ to zero. (b) Trajectory defined by eigenvectors of $\hat{\mathcal{H}}_{\mathrm{acc}}(t)$ illustrated in the accelerated frame. (c) Inversion as a function of Q_{crit} according to theory in Eq. (2.42) (dashed orange) and for two different experiments (solid blue and solid gray). The experiments show the echo-detected inversion of E′-centers in γ-irradiated Herasil achieved by a frequency-swept passage pulse. Adiabaticity was varied by changing the pulse amplitude $\nu_{1,\mathrm{max}}$, while maintaining $t_{\mathrm{p}} = 800$ ns, $t_{\mathrm{rise}} = 50$ ns and $\Delta f = 0.8$ GHz. For a well-defined Q_{crit} value, the passage pulse had a variable sweep rate adapted to the experimental resonator profile (see Section 3.4.4). The data shown in blue were obtained with a small sized (3-mm length, 1-mm diameter) cylinder having long relaxation times. The data shown in gray were obtained with a larger sized (30-mm length, 2-mm diameter) cylinder having shorter relaxation times. The same raw experimental data as in [35] were used for this illustration and further experimental details are found there.

field reversal along one component. In all these cases, it has been shown that for a linear variation of eigenenergies in presence of a time-independent coupling, the probability of a transition from one of the two energy levels to the other obeys an exponential law. Applied to our problem, the transition probability at the avoided crossing for a constant-rate chirp with constant amplitude $\omega_1(t) = \omega_{1,\mathrm{max}}$ can be calculated. In fact, the Hamiltonian in Eq. (2.34) considered here formally resembles the Hamiltonian considered by Majorana [39]. By inserting the appropriate parameters, the Landau-Zener-Stückelberg-Majorana formula for the transition probability at the avoided crossing is

$$P_{\mathrm{LZSM}} = \exp\left(-2\pi\frac{\omega_{1,\mathrm{max}}^2 t_{\mathrm{p}}}{4\Delta\Omega}\right) = \exp\left(-\frac{\pi}{2}Q_{\mathrm{crit}}\right) \tag{2.40}$$

As one would expect for an adiabatic passage, the transition probability P_{LZSM} approaches zero asymptotically when Q_{crit} is increased. Moreover in the limit of $Q_{\mathrm{crit}} = 0$, $P_{\mathrm{LZSM}} = 1$ since the energy levels do cross. For a non-adiabatic passage with intermediate Q_{crit}, the finite transition probability leaves the two eigenstates in a coherent superposition state upon passage.

For a spin along the z-axis before passage, the following relations can be obtained from the Landau-Zener-Stückelberg-Majorana formula

$$\langle \hat{S}_z \rangle = 2 \cdot \exp\left(-\frac{\pi}{2} Q_{\text{crit}}\right) - 1 = \cos\left(\theta_{\text{flip}}\right) \tag{2.41}$$

$$I = (1 - \langle \hat{S}_z \rangle)/2 = 1 - \exp\left(-\frac{\pi}{2} Q_{\text{crit}}\right) \tag{2.42}$$

where θ_{flip} is an equivalent polar flip angle and I is the inversion, describing how well population is inverted. For $Q_{\text{crit}} = 5$ for instance, one obtains $I = 0.9996$, which can be interpreted in the two following (equivalent) ways. First, it means that a single spin is inverted with a fidelity of 99.96%, which corresponds to a flip angle θ_{flip} on the order of 177.7°. Second, one can deduce that for an ensemble of spins, 99.96% of all spins are inverted upon passage. Besides adiabatic inversion at large Q_{crit}, excitation of a coherent superposition state with $Q_{\text{crit}} = 2 \cdot \ln(2)/\pi$ is also of interest. In this case, coherence upon passage is maximized because $\langle \hat{S}_z \rangle = 0$ and $\theta_{\text{flip}} = \pi/2$.
Note that the Landau-Zener-Stückelberg-Majorana transition probability was derived for a constant amplitude $\omega_1(t) = \omega_{1,\text{max}}$. In practice, however, one needs to truncate the amplitude at the pulse edges in some way to drag the spin towards the avoided crossing without causing additional transitions. Only if the pulse edges have a *smooth* truncation, the total transition probability of the pulse can be described by P_{LZSM} at the avoided crossing. For the example considered here, one would also not expect an influence of the pulse truncation on the probability P_{LZSM} itself, so that Eqs. (2.41) and (2.42) provide a valid description. The breakdown of P_{LZSM} at the pulse edges will be discussed below in Fig. 2.4.
The spin dynamics under a passage pulse can therefore be simplified thanks to Landau-Zener-Stückelberg-Majorana theory. Despite the usefulness to describe passage phenomena in magnetic resonance, there are only few appearances found in the corresponding literature, including [41–44]. In order to point out the validity of P_{LZSM}, we briefly take into consideration our own experimental results from [35]. In particular, Fig. 2.3c shows the inversion I as a function of Q_{crit} according to Eq. (2.42) (dashed orange) as well as two experimental datasets (solid blue and solid gray). As is readily seen, one dataset is in remarkable agreement with Landau-Zener-Stückelberg-Majorana theory, whereas the other dataset does not reproduce the expected relationship. In the context here, it is most relevant to point out the differences between the two experimental datasets. Further experimental details are described in the caption and in [35].
Accordingly, the data shown in blue originate from a sample with confined spatial geometry and very long relaxation times. The data shown in gray originate from a sample with loose spatial confinement and relaxation times comparable to the length of the pulse. The experiments therefore differ in two aspects, namely spatial inhomogeneity in $\omega_{1,\text{max}}$ and relaxation times. Both these effects are not considered in Eq. (2.42) and explain the degraded inversion properties of the data shown in gray as compared to the theoretical prediction. In particular, spatial inhomogeneity in $\omega_{1,\text{max}}$ affects the inversion I most significantly in the non-adiabatic regime for moderate flip angles θ_{flip} (see also below in Fig. 2.5). Fast relaxation times, on the contrary, affect the inversion I most significantly in the adiabatic regime. Relaxation, which we so far disregarded in our discussion, can actually only be neglected if the passage is fast compared to relaxation times. This can be expressed mathematically as [16]

$$\omega_{1,\text{max}} \ll T_2 \cdot \Delta\Omega / t_{\text{p}} \tag{2.43}$$

Note that this is the reason why one often finds the term "adiabatic *fast* passage" for adiabatic population inversion. Throughout this thesis, "*fast*" is often omitted because the requirements for incorporation of frequency-swept passage pulses into multi-pulse sequences requires $t_{\text{p}} \ll T_2$, which is equivalent to the above criterion.

Having established an understanding for frequency-swept excitation for a spin with resonance frequency at the center of the frequency sweep, spins with resonance frequency spread throughout the excitation band are considered in the following. Hereto, the critical adiabaticity Q_{crit} is calculated by taking the minimum of $Q(t)$ in Eq. (2.37) as a function of resonance frequency. For the modulation functions considered above in Fig. 2.2b, the resulting offset dependence of Q_{crit} is shown in Fig. 2.4a. As is readily seen, the adiabaticity $Q_{\text{crit}} = 5$ is achieved for a large range of resonance frequencies. Note that the total width of the frequency sweep $\Delta\Omega$ extends over the region where $Q_{\text{crit}} > 0$. The reduction of Q_{crit} in the transition regime is due to the truncation of the pulse edges during t_{rise}. Importantly, there are ways to compute pulse modulation functions that strictly enforce an *offset-independent* adiabaticity throughout the entire excitation window [45, 46]. This concept will become important further on in this thesis, both when compensating for bandwidth limitations in Section 3.4.4 as well as for the pulses with hyperbolic secant amplitude modulation discussed in Section 8.3.

A prediction of the inversion profile based on Eq. (2.42) is shown in blue in Fig. 2.4b. A spin dynamics simulation of the inversion profile is shown in orange. Interestingly, the transition probability P_{LZSM} predicts the inversion profile rather well. Additional transitions due to finite pulse duration and pulse truncation are only visible at the edges of the inversion window. In contrast to this, results for a pulse with an almost instantaneous truncation are shown in Fig. 2.4c. Here, the simulation and the prediction are in considerable disagreement. This is because $[\hat{\mathcal{H}}(t), \hat{\sigma}(t)] \neq 0$ at the *hard* edges of the pulse. As a consequence, the hard edges induce transitions between the eigenstates of the Hamiltonian. The pronounced wiggles in the inversion profile are another indication of hard pulse edges.

The case of coherence excitation with $Q_{\text{crit}} = 2 \cdot \ln(2)/\pi$ is illustrated in Fig. 2.4d. The intended inversion of 0.5 is also here reached for a large range of offsets. Accordingly, frequency-swept passage pulses can achieve coherence excitation and population inversion with an effective bandwidth on the order of $\Delta\Omega$. Note that the $\pi/2$ pulse is a non-adiabatic passage. There are ways to realize adiabatic $\pi/2$ pulses. In particular, one can implement an adiabatic *half passage* by truncation of the pulse at $t = t_{\text{p}}/2$. However, these pulses, including symmetrized composite half passage pulses, provide an effective excitation bandwidth on the order of only $\omega_{1,\text{max}}$ [47] and are therefore not considered explicitly within this thesis.

A well-known property of adiabatic passage pulses is that they are said to be *robust* with respect to experimental imperfections and miscalibration [4, 27]. As discussed above, adiabaticity Q_{crit} quantifies the performance of a passage pulse. For the constant-rate chirp considered here, the parameters of the pulse that determine adiabaticity are t_{p}, t_{rise}, $\Delta\Omega$ and $\omega_{1,\text{max}}$. Imperfections in the field strength $\omega_{1,\text{max}}$ are most relevant and analyzed in the following. Such imperfections originate either from spatial inhomogeneity of the driving field due to the probe-sample geometry or from the dependence of the driving field amplitude on frequency due to bandwidth limitations.

As a measure of robustness, the derivative of $\langle \hat{S}_z \rangle$ with respect to $\omega_{1,\text{max}}$ is considered. The dependence of $\langle \hat{S}_z \rangle$ on Q_{crit} according to Eq. (2.41) is shown in blue in Fig. 2.5, with the upper abscissa showing the equivalent flip angle θ_{flip}. Due to the quadratic dependence of Q_{crit} on $\omega_{1,\text{max}}$, the relevant derivative can be calculated analytically. Its functional shape is indicated by the orange curve in Fig. 2.5. After reaching a minimum in the non-adiabatic regime, the derivative gradually approaches zero when entering the adiabatic regime. Using basic calculus, one finds that $\langle \hat{S}_z \rangle$ is most sensitive to the field strength for $\omega_{1,\text{max}}^2 = \Delta\Omega/(\pi t_{\text{p}})$, which corresponds to $Q_{\text{crit}} = 1/\pi$ and $\theta_{\text{flip}} \approx 77.7°$. At this point, the derivative is

$$\min_{\omega_{1,\text{max}}} \left(\frac{d \langle \hat{S}_z \rangle}{d\omega_{1,\text{max}}} \right) = -2\sqrt{\pi t_{\text{p}}/\Delta\Omega} \cdot \exp(-1/2) \tag{2.44}$$

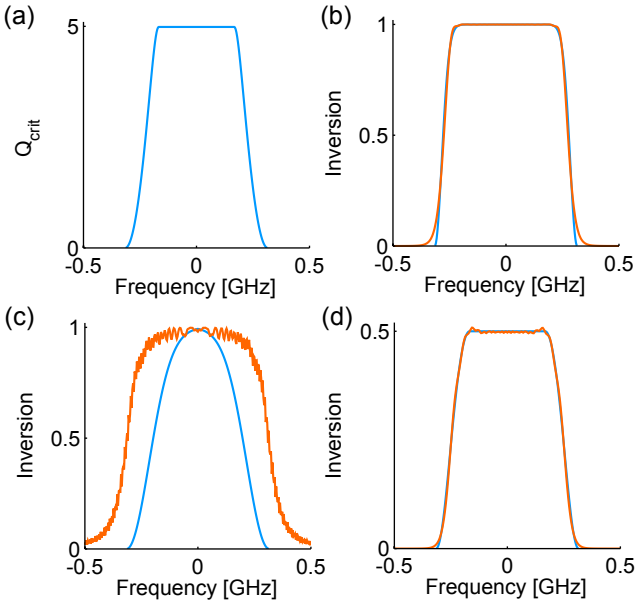

Figure 2.4 – Offset dependence of Q_{crit} and inversion. (a) Offset dependence of Q_{crit} for pulse achieving $Q_{crit} = 5$ at zero offset as defined in the caption of Fig. 2.2c (b) Comparison between theoretically predicted inversion profile using Eq. (2.42) based on Q_{crit} from panel a (blue) and spin dynamics simulation using SPIDYAN (orange). (c) Comparison between theoretical prediction (blue) and simulation (orange) if instead of $t_{rise} = 30$ ns, $t_{rise} = 0.5$ ns is used. (d) Comparison between theoretical prediction (blue) and simulation (orange) if the field strength $\omega_{1,max}$ is reduced to realize a $\pi/2$ pulse with $Q_{crit} = 2 \cdot \ln(2)/\pi$.

and is therefore inversely proportional to the square-root of the sweep rate $\Delta\Omega/t_p$. As an example, the derivative takes on a value of -12.23 ns for $t_p = 128$ ns and $\Delta f = 0.63$ GHz. For a monochromatic pulse, one finds that the derivative of $\langle \hat{S}_z \rangle$ is most significant for a $\pi/2$ pulse and its magnitude is determined by the pulse duration. A monochromatic $\pi/2$ pulse with duration on the order of 12.23 ns has therefore a comparable sensitivity to variations in the field strength than the frequency-swept 77.7° pulse considered above. A monochromatic pulse with shorter duration will be less sensitive to the field strength. However, the frequency-domain excitation profile of a hard pulse will not be as uniform as the profile of the passage pulse shown in Fig. 2.4d.

Overall, adiabatic inversion pulses are almost insensitive to variations in the field strength, whereas non-adiabatic pulses for coherence excitation are

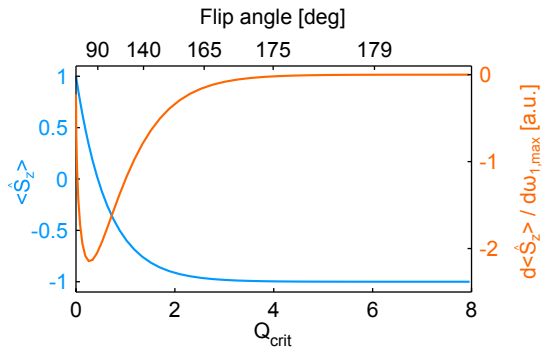

Figure 2.5 – Robustness with respect to variation in field strength by taking the derivative of $\langle \hat{S}_z \rangle$ with respect to $\omega_{1,max}$ as a function of adiabaticity Q_{crit}. The trend of $\langle \hat{S}_z \rangle$ according to Eq. (2.41) is shown in blue, whereas the derivative is shown in orange. The maximum magnitude of the derivative is determined by Eq. (2.44). The upper abscissa indicates the equivalent flip angle θ_{flip}.

less robust. This will be of central importance in the experiments presented further on in this thesis.
Another critical aspect of frequency-swept passage pulses is that different spin packets are passed at different times. For a spin with $S = 1/2$, this results in a frequency-dispersed parabolic phase relation amongst coherently excited spin packets. The formal origin of this parabolic phase is the instantaneous phase $\phi_i(t)$ introduced above in Eq. (2.33). For more complicated spin systems, such as coupled spins or spins with $S > 1/2$, multiple transitions are passed at different times. This can give rise to interference effects, as discussed for instance in [48, 28, 49, 35]. Both the frequency-dispersed parabolic phase and specific interference effects will be analyzed in more detail in the following sections.
An important aspect outside the scope of the present thesis is whether there is further room for improving performance of *robust* broadband pulses by using a different class of pulses than passage pulses. This questions was analyzed within the context of optimal control theory, which allows to compute numerically optimized pulses according to customized restraints [5].
For population inversion using pulse duration comparable to adiabatic pulses, best performance has been achieved with "double" passage pulses, which combine an adiabatic passage at the center of the pulse with a non-adiabatic passage at the pulse edges with hard truncation [50, 51]. Almost the same type of pulse has been proposed previously using a different optimization approach [52]. For this promising class of pulses, it appears as if the non-adiabatic passage at the pulse edges compensates for unwanted transitions at the outer edges of the adiabatic passage. However, the inversion profile of these pulses features pronounced wiggles outside the inversion bandwidth due to the hard pulse truncation [52, 53].
The situation is less clear for coherence excitation, because a parabolic phase relation amongst excited spin packets is usually not preferential for one single excitation pulse. Accordingly, previous studies investigating systematically on fundamental limitations focused on either robust excitation pulses free of any phase dispersion [50, 54, 51] or with a linear phase relation [55]. While a parabolic phase relation is not preferred for one single pulse, it can be refocused over several pulses [56, 57, 35]. A related effect has also been observed when optimizing coherence excitation free of phase dispersion with two concurrent pulses [58]. In particular, each of the two optimal-control pulses resulted in a considerable phase dispersion, which was refocused when combining the pulses together. Given the sensitivity of a non-adiabatic passage pulse to variations in the driving field in Eq. (2.44), one would expect that there is room for improving pulse performance. Nevertheless, it is not yet clear how one single optimum pulse, leaving the excited spins in a non-linear phase relation that can be refocused using several pulses, would look like and how its performance compares with pulses free of any phase dispersion.

2.4.2.2 *Frequency-swept refocusing pulses*

When using a frequency-swept pulse for refocusing of excited coherence, additional aspects need to be taken into consideration. A first aspect has already been mentioned in the previous section, namely the refocusing of the parabolic phase relation amongst the excited spins if coherence was initially generated with a frequency-swept pulse. As a consequence of this, the pulse durations of the involved excitation and refocusing pulses need to fulfill a prescribed relationship [56, 57, 35]. Specific details will be discussed in the following sections, where such pulse sequences are implemented.
A second aspect is related to dynamical Bloch-Siegert phase shifts when applying off-resonance pulses to excited coherence, which is discussed in this section. In particular, the transient phase acquired under a (monochromatic

and amplitude-modulated) pulse far off resonance in the rotating frame may be approximated as [59]

$$\phi_{\text{eff}} = \int_0^{t_p} \omega_{\text{eff}}(t)dt \tag{2.45}$$

and does not necessarily correspond to the phase acquired during t_p by the spins in the absence of the pulse. The phase difference in the presence and absence of the pulse is the experimentally relevant dynamical Bloch-Siegert phase shift [59].

For a frequency-swept pulse, resonance passage renders a closed-form expression of the Bloch-Siegert phase shift difficult. For coherence refocusing with passage pulses, the dynamical phase shift has been first analyzed in [60]. Most importantly, the dynamical phase shift acquired before resonance passage adds up to the dynamical phase shift acquired after passage due to the inversion of coherence order on resonance. One single refocusing pulse does therefore induce an experimentally observable Bloch-Siegert phase shift. In order to compensate this phase shift, two subsequent refocusing pulses are required. The resulting pulse sequence consisting of a $\pi/2$ passage pulse followed by two π passage pulses has been given the acronym ABSTRUSE, which stands for *Adjustable, Broadband, Sech/Tanh-Rotation Uniform Selective Excitation*.

The main advantage of this ABSTRUSE sequence was its improved tolerance with respect to variations in the driving field $\omega_{1,\text{max}}$. In particular, the Bloch-Siegert phase shift was found to depend on $\omega_{1,\text{max}}$. For a spatial dependence of $\omega_{1,\text{max}}$ due to inhomogeneity in the coupling between the sample and the probe, the Bloch-Siegert phase does therefore also depend on space. If one does not compensate the Bloch-Siegert phase shift, the spatial phase dependence will reduce the intensity of the spin echo.

Later on, we found based on simulations and experiments [35] that the Bloch-Siegert phase shift is well modeled by a linear dependence on adiabaticity

$$\Delta\phi_{\text{Bloch-Siegert}} = s_Q \cdot Q_{\text{crit}} \tag{2.46}$$

where s_Q is the relevant scaling factor. The sign of s_Q depends on the direction of the frequency sweep. The magnitude of s_Q depends on the sweep range $\Delta\Omega$ and also shows a non-uniformity across the excited frequency window. In general, the magnitude of s_Q must be computed numerically and a typical value for s_Q for a sweep from below resonance to above resonance is on the order of $s_Q = -3.5$ rad. These findings provided the following insights into refocusing with passage pulses:

When using one single refocusing pulse, there is a trade-off between spatial or spectral inhomogeneity in the Bloch-Siegert phase shift and effective flip angle θ_{flip} according to Landau-Zener-Stückelberg-Majorana theory. On the one hand, the refocusing pulse must invert coherence order, which requires a flip angle θ_{flip} close to π, and therefore a large adiabaticity Q_{crit}. On the other hand, loss of echo intensity due to spatial and spectral variations of the Bloch-Siegert phase shift is minimized by having a small adiabaticity Q_{crit}. Refocusing pulses with pulse amplitude optimized experimentally for maximum echo intensity are therefore often not adiabatic pulses. Note that the spectral variation in the Bloch-Siegert shift is due to the spectral dependence of s_Q. The spatial variation in the Bloch-Siegert shift is due to the quadratic dependence of Q_{crit} on $\omega_{1,\text{max}}$. Accordingly, the spatial phase shift will become larger if the field strength is increased[1].

By using two refocusing pulses, the echo loss mechanisms due to spatial or spectral variations in the Bloch-Siegert phase are largely compensated

[1] If the Bloch-Siegert shift would depend linearly on $\omega_{1,\text{max}}$, as suggested in [60], the spatial phase shift would also increase with the field strength, as opposed to the comment made in the SI of [35].

according to the ABSTRUSE scheme. Experimentally optimized refocusing pulses in this scheme have therefore a larger adiabaticity Q_{crit}. As demonstrated experimentally in [35], the ABSTRUSE scheme may not necessarily result in a larger echo amplitude compared to one single refocusing pulse due to relaxation effects which reduce the equivalent flip angle θ_{flip}.
It is worth mentioning that conceptually similar problems related to coherence combined with resonance passage are encountered in the context of Landau-Zener-Stückelberg interferometry [61]. In this context, a two-level system is passed several times by means of periodic modulation of the energy levels. The so-called Stückelberg phase, which is the phase acquired between successive passages, determines the net transition probability of the subsequent passages. This phase has two contributions. One contribution is due to the dynamic phase ϕ_{i} acquired between the passages, whereas the other contribution is due to the Stokes phase, which is acquired when passing the transition (see also [62]).

2.5 ESSENTIAL PULSE SEQUENCES

2.5.1 *Two-pulse electron spin echo envelope modulation (ESEEM)*

The two-pulse Hahn echo sequence $(\pi/2) - \tau - (\pi) - \tau - (\text{echo})$ refocuses the resonance offset Ω_0 within the excitation bandwidth of the utilized pulses. For a spin $S = 1/2$, the echo decays as a function of the delay τ due to the phase memory time T_{m}. For coupled spin systems, the echo sequence may not refocus the interaction that couples the spins. As a consequence, the echo as a function of τ is modulated by the coupling strength. The case of echo modulations due to dipolar couplings will discussed in Section 8.4.3. Here, the case of an anisotropic hyperfine interaction between an electron spin $S = 1/2$ and a nuclear spin $I = 1/2$ is considered, so that

$$\hat{\mathcal{H}}_0 = \omega_S \hat{S}_z + \omega_I \hat{I}_z + \vec{\hat{S}}^T \mathbf{A} \vec{\hat{I}} \tag{2.47}$$

In order to treat the spin dynamics, a transformation into the rotating frame according to Eqs. (2.26) and (2.27) is preferential. Within the secular approximation, only the terms $A_{zz}\hat{S}_z\hat{I}_z + A_{zx}\hat{S}_z\hat{I}_x + A_{zy}\hat{S}_z\hat{I}_y$ are relevant, which can be transformed into

$$\hat{\mathcal{H}}_{\text{rot}} = \Omega_0 \hat{S}_z + \omega_I \hat{I}_z + A\hat{S}_z\hat{I}_z + B\hat{S}_z\hat{I}_x \tag{2.48}$$

where A is the secular hyperfine coupling and B the pseudosecular hyperfine coupling.
The consequence of B is that the nucleus does no longer quantize along the direction of the external field. The matrix representation of the Hamiltonian is therefore not diagonal and needs to be diagonalized. Most importantly, transformation into the eigenframe will affect the pulse Hamiltonian. In particular, the rotating frame Hamiltonian $\omega_1 \hat{S}_x$ of an on-resonance pulse transforms into

$$\hat{\mathcal{H}}^{\text{trans}}_{\text{Pulse}} = \cos(\eta)\omega_1 \hat{S}_x + \sin(\eta)\omega_1 2\hat{S}_y\hat{I}_y \tag{2.49}$$

with

$$\eta = \frac{1}{2}\left(\arctan\left(\frac{-B}{2\omega_I + A}\right) - \arctan\left(\frac{B}{2\omega_I - A}\right)\right) \tag{2.50}$$

This means that the microwave pulse resonant with the electron spin does not only excite the electron spin transition, but also electron-nuclear spin transitions. In the absence of pseudosecular coupling B, electron-nuclear transitions are forbidden since angular momentum is not conserved. One therefore often refers to excitation of formally forbidden transitions in presence of B. Efficient excitation of forbidden transitions requires B to be on the same order of magnitude as A and ω_I.

A detailed analysis of the spin dynamics of the two-pulse echo sequence is found in [18]. The resulting spin echo has a modulated contribution according to

$$V_{2p}(\tau) = 1 - \frac{k}{4}\left[2 - 2\cos(\omega_\alpha \tau) - 2\cos(\omega_\beta \tau) + \cos(\omega_+ \tau) + \cos(\omega_- \tau)\right] \tag{2.51}$$

with modulation depth

$$k = \left(\frac{B\omega_I}{\omega_\alpha \omega_\beta}\right)^2 \tag{2.52}$$

and nuclear frequencies in the eigenframe

$$\omega_\alpha = \sqrt{\left(\omega_I + \frac{A}{2}\right)^2 + \frac{B^2}{4}} \tag{2.53}$$

$$\omega_\beta = \sqrt{\left(\omega_I - \frac{A}{2}\right)^2 + \frac{B^2}{4}} \tag{2.54}$$

and combination frequencies

$$\omega_+ = \omega_\alpha + \omega_\beta \tag{2.55}$$

$$\omega_- = |\omega_\alpha - \omega_\beta| \tag{2.56}$$

Pseudosecular coupling B therefore results in electron spin echo envelope modulation (ESEEM) by the fundamental nuclear frequencies and combinations thereof. The modulation frequencies are analyzed by Fourier transform of the modulated contribution. Extensions to more complicated spin systems are summarized in [18].
An important case within this thesis is the modulation of the electron spin echo by matrix protons [63]. In this case, the distribution of protons around the electron result in a spread of hyperfine parameters A and B. In a two-pulse ESEEM spectrum, one typically only observes two modulation frequencies, ω_I and $2\omega_I$. Moreover, the spectral contribution at ω_I due to the spread in ω_α and ω_β is broader than the contribution at $2\omega_I$ due to the combination frequency.
There are extensions of ESEEM to multiple pulses, such as three-pulse ESEEM which is free of combination frequencies ω_+ and ω_-, or the two-dimensional HYSCORE sequence which allows to correlate nuclear frequencies ω_α and ω_β. While these sequences are also relevant in the context of frequency-swept excitation pulses [64], the ESEEM experiments shown within this thesis are based on the two-pulse echo sequence.

2.5.2 *Four-pulse double electron-electron resonance (DEER)*

The dipolar coupling between a pair of electron spins is most commonly studied with the four-pulse double electron-electron resonance (DEER) sequence [65], which is illustrated in Fig. 2.6. The pulse sequence consists of a refocused primary echo sequence at a frequency ω_{obs} defined by the pulses ①, ②, and ④ with fixed pulse delays determined by τ_1 and τ_2. A pump pulse applied at an incremented time t at frequency ω_{pump} allows for controlled evolution under the dipolar coupling. Accordingly, the amplitude of the spin echo is modulated as a function of t and the modulation frequency entails information on the coupling strength.
The working principle of this pulse sequence is discussed based on two spins $S_A = 1/2$ and $S_B = 1/2$ with Larmor frequencies ω_A and ω_B coupled by ω_{dd}. By assuming that $|\omega_A - \omega_B| \gg \omega_{dd}$ (weak coupling), the secular approximation yields the rotating frame Hamiltonian

$$\hat{\mathcal{H}}_{rot} = \Omega_A \hat{S}_{Az} + \Omega_B \hat{S}_{Bz} + \omega_{dd} \hat{S}_{Az} \hat{S}_{Bz} (1 - 3\cos^2(\theta)) \tag{2.57}$$

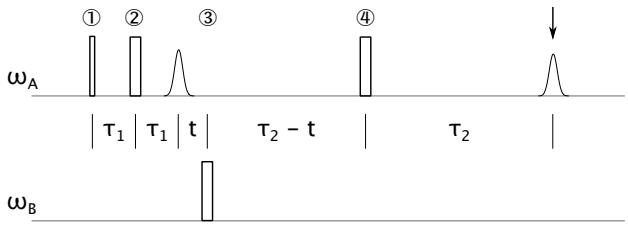

Figure 2.6 – Four-pulse DEER sequence consisting of a refocused primary echo sequence ①-②-④ at ω_{obs} and an inversion pulse ③ at ω_{pump}. Evolution under the dipolar coupling is achieved by variation of the delay t, whereas the pulse delays τ_1 and τ_2 are kept constant. The maximum evolution time is bounded by $\tau_1 + \tau_2$. The length of each pulse is illustrated according to its flip angle of either $\frac{\pi}{2}$ or π. In the actual experiment, the choice of the pulse length depends on various parameters [66].

where the contribution of the dipolar coupling is due to the $\hat{A}$ term in the dipolar alphabet in Eq. (2.14).
The weak coupling Hamiltonian above has four observable transition frequencies: A doublet centered at Ω_A and a doublet centered at Ω_B, each split by $\omega_{split} = \omega_{dd}(1 - 3\cos^2(\theta))$. DEER requires that the observer pulses at ω_A excite the doublet at Ω_A exclusively, while the pump pulse at ω_B has to excite the doublet at Ω_B exclusively. In this case, the refocused primary echo sequence at ω_A in absence of the pump pulse refocuses the dipolar coupling. A change in the pulse delays τ_1 and τ_2 does not result in any echo modulation, except for an altered echo intensity due to the phase memory time T_m. The pump pulse inverts the B spin, such that the local field of the B spin experienced by the A spin is inverted. The pump pulse does therefore *swap* the doublet of the A spin: For an A spin precessing at frequency $\Omega_A \pm \omega_{split}/2$ before the pump pulse, the precession frequency after the pump pulse is $\Omega_A \mp \omega_{split}/2$. The net change in precession frequency due to the pump pulse is therefore $\pm\omega_{split}$. With the timings of the four-pulse DEER sequence, one finds that the spin echo is modulated by

$$V_{4p}(t) = \cos\Big(\omega_{dd}(1 - 3\cos^2(\theta))t\Big) \tag{2.58}$$

Because negative times t can be realized by moving the pump pulse position in front of the primary echo at $2\tau_1$, the zero time of the dipolar evolution can be obtained. Four-pulse DEER is therefore a pulse sequence that yields the dipolar evolution free of a dead time.
This feature is particularly important for the random orientations encountered in glassy frozen solutions of spin pairs. In these cases, only a fraction λ of all spin pairs contribute to the dipolar modulation and there is also a contribution from inter-molecular dipolar couplings. The echo amplitude $V(t)$ is then

$$V(t) = V_0 F(t) B(t) \tag{2.59}$$

where V_0 is the echo amplitude at $t = 0$, $F(t)$ the form factor due to spin pairs, and $B(t)$ a background decay function due to inter-molecular couplings.
The background decay can often be modeled according to a stretched exponential

$$B(t) = \exp\Big(-k\, t^{d_{bg}/3}\Big) \tag{2.60}$$

where k is the decay rate and the stretching exponent d_{bg} is referred to as background dimension. A homogeneous distribution of molecules corresponds to $d_{bg} = 3$, whereas inhomogeneous environments usually result in $d_{bg} \neq 3$ [67].

If all orientations θ of the inter-spin vector contribute equally and are within the weak-coupling limit, the relevant form factor is

$$F(t) = 1 - \lambda + \lambda \cdot \left\langle \cos\left(\omega_{\mathrm{dd}}(1 - 3\cos^2(\theta))t\right) \right\rangle \tag{2.61}$$

where the brackets denote averaging over all orientations. Note that the orientation-averaged modulation corresponds to a Pake pattern in frequency domain.

The systems of interest usually feature a distribution of the inter-spin distance and information on conformational dynamics can be obtained by computing distance distributions based on $V(t)$ [68]. Since extraction of inter-spin distances from time-domain data is an ill-posed problem, the fitting is stabilized by Tikhonov regularization [69, 70]. Depending on the maximum attainable evolution window, which is limited by the phase memory time T_{m}, DEER can provide long-range distance restraints up to 10 nm for structure determination. The lower limit on the attainable distance range is on the order of 1.5 - 2.0 nm and constrained by the bandwidth required to excite the doublet of the A spin and by potential contributions from exchange coupling and spin pairs that are not in weak coupling conditions.

Within this thesis, many situations are encountered where Eq. (2.61) is no longer appropriate. The pump pulse may not excite all orientations uniformly, such that only certain components of the Pake pattern contribute to the dipolar evolution. This effect is referred to as orientation selection and can in principle be an additional source of information [71]. Moreover, the contributing spin pairs may not be in weak coupling conditions, such that the pseudosecular contribution to the dipolar coupling by the term $\hat{B}$ of the dipolar alphabet distorts the signal. This will be of particular relevance for DEER experiments with spins $S > 1/2$, because the raising and lowering operators $\hat{S}^+$ and $\hat{S}^-$ introduce off-diagonal elements that are enhanced as compared to the spin $S = 1/2$ case [72]. Another case where Eq. (2.61) is not necessarily applicable is in the presence of more than one coupled spin partner, which results in multi-spin effects [73].

Overall, the DEER sequence allows for distance determination between electron spins in the nanometer range. The separation of the form factor from the primary signal $V(t)$ and calculation of a distance distribution thereof is a delicate task. Primary data of high quality is therefore crucial, in particular in the context of spin-labeled biomacromolecules. As the reader will recognize in the chapters that follow, sensitivity enhancement in DEER by frequency-swept pulses is an important aspect throughout this thesis.

3

ADIABATIC AND FAST PASSAGE ULTRA-WIDEBAND INVERSION IN PULSED EPR

ABSTRACT

We demonstrate that adiabatic and fast passage ultra-wideband (UWB) pulses can achieve inversion over several hundreds of MHz and thus enhance the measurement sensitivity, as shown by two selected experiments. Technically, frequency-swept pulses are generated by a 12 GS/s arbitrary waveform generator and upconverted to X-band frequencies. This pulsed UWB source is utilized as an incoherent channel in an ordinary pulsed EPR spectrometer. We discuss experimental methodologies and modeling techniques to account for the response of the resonator, which can strongly limit the excitation bandwidth of the entire non-linear excitation chain. Aided by these procedures, pulses compensated for bandwidth or variations in group delay reveal enhanced inversion efficiency. The degree of bandwidth compensation is shown to depend critically on the time available for excitation. As a result, we demonstrate optimized inversion recovery and double electron electron resonance (DEER) experiments. First, virtually complete inversion of the nitroxide spectrum with an adiabatic pulse of 128 ns length is achieved. Consequently, spectral diffusion between inverted and non-inverted spins is largely suppressed and the observation bandwidth can be increased to increase measurement sensitivity. Second, DEER is performed on a terpyridine-based copper(II) complex with a nitroxide-copper distance of 2.5 nm. As previously demonstrated on this complex, when pumping copper spins and observing nitroxide spins, the modulation depth is severely limited by the excitation bandwidth of the pump pulse. By using fast passage UWB pulses with a maximum length of 64 ns, we achieve up to threefold enhancement of the modulation depth. Associated artifacts in distance distributions when increasing the bandwidth of the pump pulse are shown to be small.

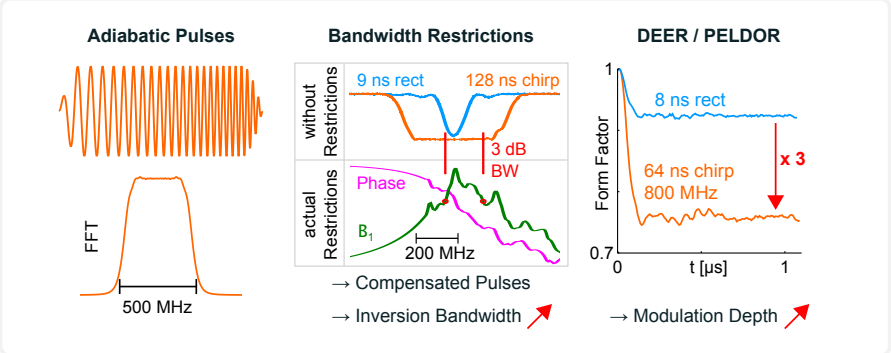

This chapter has been published as [74] and edited for consistency of notation:

A. Doll, S. Pribitzer, R. Tschaggelar, G. Jeschke, Adiabatic and fast passage ultra-wideband inversion in pulsed EPR, J. Magn. Reson 230, 2013, 27-39

where S. Pribitzer provided the MATLAB code for propagation of density matrices (Section 3.3.2) and R. Tschaggelar supported the design of the AWG extension (Section 3.3.1).

3.1 INTRODUCTION

Only a fraction of all electron spins can typically be excited in pulsed electron paramagnetic resonance (EPR) spectroscopy due to the technically constrained excitation bandwidth of rectangular pulses. In fact, the width of the EPR spectrum often exceeds the excitation bandwidth by several multiples, as for instance for transition metal centers with spectral widths above 1 GHz at moderate fields or for nitroxide radicals at high fields. While partial spin excitation is advantageous in order to select particular orientations of spectroscopically resolved anisotropy parameters [75, 76, 71], the constrained excitation bandwidth limits the measurement sensitivity in many EPR experiments [18]. Accordingly, a lot of effort has been invested in the field to enhance the excitation bandwidth:
First, the microwave resonator and the available pulse power at microwave frequencies are key restrictions to the excitation bandwidth of rectangular (hard) pulses, such that a number of optimized microwave resonators and optimized spectrometers have been reported. Recent examples include [77–80] and several earlier contributions are found in [81, 82]. Second, alternative excitations providing larger bandwidths have been investigated, namely composite pulses [7], stochastic excitation pulses for Fourier transform EPR [8], shaped sinc-pulses for EPR imaging at radio frequency [9] and multichromatic rectangular pulses for broadband spin pumping [83]. Third, shaped microwave pulses tailored from optimal control theory (OCT) for increased excitation bandwidth have been demonstrated at X-band frequency [15]. Considering the impact of OCT pulses in nuclear magnetic resonance (NMR) spectroscopy [5], the combination of OCT and EPR is promising and has already shown interesting applications of coherence pathway selection [11, 84] and narrowband control [85] with shaped X-band pulses in the context of quantum information processing.
In order to experimentally realize shaped microwave pulses derived from OCT, fast arbitrary waveform generators (AWG) with up to 1 ns timing resolution to modulate amplitude and phase of a fixed microwave oscillator (LO) have been used. To date, the fastest commercially available AWGs even provide sub-ns timing resolution to directly synthesize microwave pulses, as demonstrated for rectangular pulses [86, 87] and applied in rotational spectroscopy [2].
In this study, an ordinary X-band spectrometer is extended by a 12 GS/s AWG to test the feasibility of ultra-wideband (UWB) inversion by adiabatic or fast passage pulses. Since UWB refers to spectral extent above 0.5 GHz [88], the excitation bandwidth exceeds the bandwidth of current microwave resonators. The aim of this study is therefore to establish compensation techniques of bandwidth effects distorting the excitation pulse and to demonstrate applications where UWB inversion surpasses conventional approaches. For an identification of bandwidth effects due to the entire excitation chain, adiabatic pulses of fairly basic shapes are examined, because these provide simple means of comparing actual experimental performance against simulated performance. As a result, bandwidth limitations and variations in group delay are found to influence inversion performance (*vide infra* adiabaticity). Compensation of those is based on a quasi-linear hardware model obtained upon processing data from transient nutation experiments, because the high power microwave amplifier is strongly nonlinear. The validity of this quasi-linear model is discussed and enhanced inversion performance by pulse compensation is demonstrated experimentally. Then, suppression of spectral diffusion processes by virtually complete inversion of the nitroxide spectrum is shown to prolong longitudinal relaxation times obtained from inversion recovery (IR) experiments, thus allowing for the measurement of intrinsic longitudinal relaxation times by that experiment. Finally, double electron-electron resonance (DEER, also termed PELDOR) experiments with fast passage pulses on a copper-nitroxide complex are presented. Herein,

enhanced modulation depth is shown when pumping the spectrally broad copper center with UWB pulses and observing the nitroxide spins.

3.2 THEORY

3.2.1 *Adiabatic inversion*

Adiabatic inversion by phase and amplitude modulated pulses has been established in NMR since many years. While early implementations made use of frequency swept pulses of constant amplitude [16], later a number of optimized pulse shapes have been developed [27, 45, 4]. A unique property of adiabatic pulses is that the magnetization follows the effective field $\boldsymbol{\omega_{eff}}$ and is relatively insensitive to inhomogeneities in the driving field B_1. The requirement for the magnetization to follow $\boldsymbol{\omega_{eff}}$, expressed via the adiabaticity factor Q, is given by [27]

$$Q = \frac{\omega_{\mathrm{eff}}}{|d\theta/dt|} \gg 1 \tag{3.1}$$

The factor $|d\theta/dt|$ is the instantaneous angular velocity of $\boldsymbol{\omega_{eff}}$. Considering a linear frequency sweep (linear chirp), Q has its minimum at the time when a particular isochromat is on resonance and can be written as [27]

$$Q_{\mathrm{crit}} = \frac{2\pi\ \nu_1^2\ t_{\mathrm{p}}}{\Delta f} \tag{3.2}$$

where ν_1 is the nutation frequency, t_{p} the pulse length and Δf the total sweep width (all frequencies in Hz). UWB inversion performance ($Q_{\mathrm{crit}}\Delta f$) therefore scales quadratically in ν_1, which is limited by the available microwave power and the resonator bandwidth, and linearly in the pulse length t_{p}, which is limited by relaxation or coherence transfer times required by the experiment. All other parameters being equal, UWB inversion performance scales linearly with microwave power.

In addition to a high adiabaticity factor Q, an adiabatic inversion pulse should rotate $\boldsymbol{\omega_{eff}}$ from +z to -z, which is usually fulfilled by smooth tails of the inversion pulse. For the chirped pulses used in this study, the pulse edges were therefore weighted with a quarter period of a sine, whose length is specified separately by t_{rise}. While slightly better suited pulses for frequency-selective adiabatic wideband inversion are found in the literature [45, 46, 19], it should be noted that in an ordinary EPR spectrometer the pulse modulation functions are distorted by a number of hardware imperfections:

The amplitude modulation function is most affected by the saturated traveling wave tube (TWT) amplifier and the bandwidth of the resonator. Such amplitude imperfections have an effect on ν_1 and their impact on the adiabaticity of linear chirps is quantified by Q_{crit} in Eq. (3.2). The phase modulation function is perturbed by the phase response $\beta(f)$ of the excitation chain, which describes the relative phase offset of the driving field with respect to the phase programmed in the AWG. The influence of $\beta(f)$ on the adiabaticity requires separate analysis, which is presented in the following.

3.2.2 *Dependence on group delay*

UWB chirp pulses for adiabatic inversion in EPR raise the relevance and importance of the excitation chain's phase response $\beta(f)$, which, in general, has previously not been considered. In order to simplify the analysis for present consideration, the perturbation of the phase modulation function is modeled by the frequency domain phase response $\beta(f)$ evaluated at the instantaneous frequency f_{i} of the chirp. The analogous procedure is used for the perturbation of the amplitude modulation function by the amplitude response $\nu_1(f)$. Note that such an approximation has its limitations towards

fast chirp rates ($\Delta f/t_p$) and non-smooth amplitude and phase responses, $\nu_1(f)$ and $\beta(f)$. However, our current experimental results based on linear chirps indicate that the actual perturbation of the pulse modulation functions in time domain are approximated to a significant degree.

Accordingly, the influence of $\beta(f)$ is best seen in an accelerated rotating frame synchronized to the unperturbed phase modulation function, as illustrated in Fig 3.1b. If the pulse is not subject to any phase shift β, the observer frame remains in phase with the effective field $\boldsymbol{\omega_{eff}}$. The trajectory of $\boldsymbol{\omega_{eff}}$ is therefore entirely in the $x-z$ plane and the polar velocity ω_α constitutes the angular rate of change $\omega_\theta = d\theta/dt$ of the effective field. Consequently, any phase shift $\beta(f)$ moves $\boldsymbol{\omega_{eff}}$ azimuthally off the $x-z$ plane and reduces the adiabaticity by enhancing $|\omega_\theta|$, which becomes the root sum over the squared polar and azimuthal velocities, ω_α and ω_β.

Note that the construction described above is valid for any phase modulation function. For a linear chirp, the velocities at the time when a particular isochromat is on resonance with the instantaneous frequency f_i are

$$\omega_\alpha = \frac{\Delta f}{\nu_1(f_i)\, t_p} \tag{3.3}$$

$$\omega_\beta = d\beta/df\, \frac{\Delta f}{t_p} = -2\pi\, \tilde{\tau}_g(f_i)\, \frac{\Delta f}{t_p} \tag{3.4}$$

where $\tilde{\tau}_g(f)$ denotes variations in the group delay with frequency and is related to the group delay, which is the negative phase-derivative with respect to angular frequency, via $\tilde{\tau}_g(f) = \tau_g(f) - \tau_g(0)$. Neglect of overall pulse delays, $\tau_g(0)$, prevents the unphysical situation of adiabaticity reduction due to frequency-independent delays in the excitation chain. However, any group delay *variations* undergone by the pulse prior to spin excitation persist and degrade the adiabaticity.

Under idealized conditions, the excitation chain operates linearly and its net excitation bandwidth is defined by the resonator. In this case, the perturbations of the intended pulse modulation functions are completely described by the linear transfer function of the excitation chain. For the simplest possible resonator model, an RLC series circuit, the transfer function is given by its normalized admittance and can be written as

$$H_{id}(f) = \frac{1}{1 + iQ_L(\frac{f}{f_0} - \frac{f_0}{f})} \tag{3.5}$$

where f_0 is the resonance frequency and Q_L the quality factor.

The corresponding phase response $\beta(f)$ and normalized magnitude response $\nu_1(f)$ are shown in Fig. 3.1a for f_0 = 9.5 GHz and Q_L = 100. The maximum group delay is $Q_L/(\pi f_0)$ on resonance. The isochromat at f_0 thus experiences the highest degradation in adiabaticity. As an example, $\nu_\alpha = \omega_\alpha/(2\pi)$, ν_β and ν_θ are shown in Fig. 3.1c for a pulse with t_p = 128 ns and Δf = 630 MHz. For ν_α, high power was assumed, i.e. a length of 8 ns for a π-pulse and therefore ν_1 = 62.5 MHz. Note that the same curves result for pulses with identical chirp rate ($\Delta f/t_p$), such as for instance t_p = 48 ns and Δf = 236 MHz. At the resonance frequency f_0, ν_α has its minimum (12.5 MHz), whereas ν_β has its maximum (16.5 MHz). While Eq. (3.2) would suggest Q_{crit} = 5 in this case, the group delay leads to $Q_{crit} = 3$. For isochromats offset to f_0, the minimum adiabaticity is dominated by ν_α.

Because $\nu_1(f)$ and $\beta(f)$ compete in degrading the adiabaticity, we examined each contribution individually for the case above. We therefore simulated the dependence of the inversion efficiency on the field amplitude ν_1 at the resonance frequency f_0 for chirps (t_p = 128 ns, t_{rise} = 30 ns) that were modified by either $\nu_1(f)$ or $\beta(f)$, or modified by both $\nu_1(f)$ and $\beta(f)$, or not modified. Note that the abscissa in Fig. 3.1d denotes the field amplitude ν_1 relative to its maximum value and all ν_1 values given without a unit in this study are to be understood as such. As can be seen from the results, modification by $\beta(f)$ introduces the largest degradation in ν_1 robustness

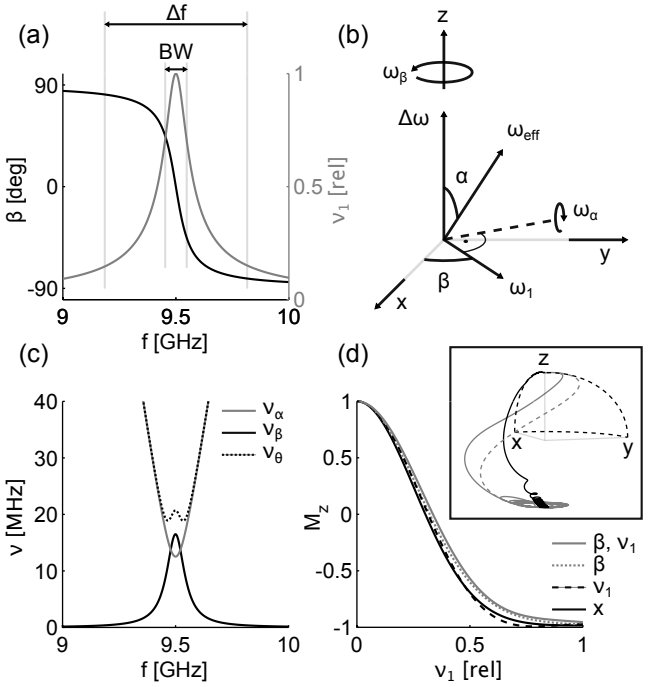

Figure 3.1 – Influence of bandwidth limitations on adiabaticity. (a) Phase $\beta(f)$ and normalized magnitude $\nu_1(f)$ of the idealized transfer function $H_{\mathrm{id}}(f)$, Eq. (3.5). (b) $\boldsymbol{\omega_{\mathrm{eff}}}$ in an observer frame synchronized to the unperturbed phase modulation function of the inversion pulse. $\omega_1 = 2\pi\nu_1$ is the field strength and $\Delta\omega$ the resonance offset. α is due to the unperturbed modulation functions of the pulse, β originates from phase shifts. $\boldsymbol{\omega_\alpha}$ and $\boldsymbol{\omega_\beta}$ are orthogonal. (c) Angular velocity components of $\boldsymbol{\omega_{\mathrm{eff}}}$ in MHz. Chirp parameters t_{p} = 128 ns, Δf = 630 MHz. ν_1 = 62.5 MHz at f_0. At 20 MHz offset from f_0, $\nu_\alpha \approx \nu_\beta$ and starting at 75 MHz offset from f_0, $\nu_\theta \approx \nu_\alpha$. (d) Simulations of $M_z(\nu_1)$ at f_0 for chirps (t_{p} = 128 ns, t_{rise} = 30 ns) modified by either $\nu_1(f)$ (dashed black) or $\beta(f)$ (dotted gray), both of them (solid gray) or none of them (solid black). See Section 3.3.2 for simulation method. Inset in (d) Evolution of the magnetization in an accelerated frame for the unmodified reference chirp (black) and for the chirp modified by both $\nu_1(f)$ and $\beta(f)$ (solid gray). The evolution under the modified chirp follows the projection of $\boldsymbol{\omega_{\mathrm{eff}}}$ onto the magnetization sphere (dashed gray).

and inversion efficiency (gray curves vs. black curves), which both relate to the adiabaticity. Interestingly, modification by solely $\nu_1(f)$ (dashed black) reduces the inversion efficiency but partially enhances the ν_1 robustness compared to the unmodified reference (solid black). The inset in Fig. 3.1d shows the evolution of the magnetization in an accelerated frame for the unmodified reference chirp (solid black) and for the chirp modified by both $\nu_1(f)$ and $\beta(f)$ (solid gray). The evolution under the modified chirp follows the projection of $\boldsymbol{\omega_{\mathrm{eff}}}$ onto the magnetization sphere (dashed gray), which reveals $\beta(f)$ directly for negative gyromagnetic ratio [89]. Due to reduced adiabaticity, the cone angle of precession around $\boldsymbol{\omega_{\mathrm{eff}}}$ is larger for the perturbed chirp (solid gray) than for the unperturbed chirp (solid black). In general, degradation in adiabaticity due to $\beta(f)$ occurs whenever ν_β is comparable to ν_α. Hence, group delay variations can only be neglected if there is sufficient resonator bandwidth compared to ν_1, i.e.

$$2\nu_1 \ll \mathrm{BW} \tag{3.6}$$

where BW denotes the 3 dB bandwidth (f_0/Q_{L}). While this simple condition assumes the transfer function H_{id}, experimental responses are typically not as smooth and can degrade adiabaticity regardless of bandwidth sufficiency. We will discuss such cases in Section 3.4.3 and demonstrate compensation of $\beta(f)$ by adapting the arbitrary waveform.

At this point, it is important to distinguish between the phase distortions discussed above for adiabatic pulses, which arise due to the phase modulation

(chirp) of the pulse, and the phase distortions present for monochromatic rectangular pulses [90, 91]. A monochromatic pulse is purely amplitude modulated and transient phase modulation at the sharp pulse extremities arises due to limited bandwidth and nonlinearity. One consequence is that the inversion efficiency achievable by a single monochromatic pulse is lowered [90]. For an adiabatic pulse on the contrary, the amplitude modulation typically appears smoother than for a rectangular pulse. Even in this case, amplitude modulation is likely to stimulate transient phase modulation and thus perturb the intended spin manipulation. For instance, the amplitude-dependent phase offset of a TWT [92] may lead to such perturbations. Due to the rather complex nonlinear hardware modeling required to treat those phase transients, an explicit treatment was omitted in this study. The same problem occurs for amplitude transients due to amplitude modulation (*vide infra* amplitude compression). In fact, the limitations to compensate transients induced by amplitude modulation based on linear system theory in the presence of nonlinear behavior were already highlighted in [93] in the context of low field NMR.

3.3 MATERIALS AND METHODS

3.3.1 *Instrumentation*

A Bruker Elexsys E680 pulsed EPR spectrometer was extended by an incoherent UWB pulse channel realized with a 12 GS/s AWG (Agilent M8190A). A schematic is depicted in Fig. 3.2. The AWG provides 2 channels with 12 bit vertical resolution, 128 MS memory and waveform sequencing functionality. Pulses from the AWG are upconverted to X-band frequencies by a 8 GHz LO (Agilent E8257D or Nexyn NXPLOS), amplified (Minicircuits ZX60-01412L) and inserted into the +<y> channel of the E680 bridge. The 3 dB cutoff of the UWB channel at 12 GHz is set by the mixer (MITEQ DM0412LW2) and the actual passband is usually centered around 9.3 GHz due to the resonator (Bruker MS3 split-ring that was fully overcoupled). Reflections of the image around 6.7 GHz off the bridge are isolated from the mixer by 10 dB with an X-band isolator (Ferrocom 60B60). The high IF frequencies above 1 GHz enabled by the fast AWG reduce the experimental significance of LO leakage through the upconversion mixer [85] and minimize the impact of IF harmonics, because these move to higher frequencies outside the passband of interest. To operate the same pulse channel on a Elexsys E580 bridge instead of the E680 bridge (see Section 3.4.6), an amplifier with higher power (MEURO MBM0812G2423) was used. When operated at X-band, the two bridges have identical internal signal routing towards the resonator.
Pulse generation is triggered by the Elexsys console (U1 channel) and 1D or 2D sweeps over several pulse waveforms can be performed by proper setup of the AWG sequencer with respect to the actual sweep definition in Bruker's Xepr spectrometer control program. The AWG itself is programmed via MATLAB from a separate host computer and the download time for a sweep over 2048 pulses is currently between 1 and 2 s.

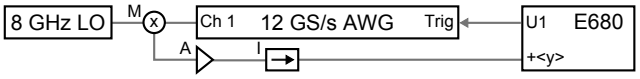

Figure 3.2 – Schematic of incoherent UWB channel. M: mixer, A: amplifier, I: isolator.

The main attenuator of the microwave bridge was always at 0 dB in order to make use of the nominal 1 kW delivered by the power amplifier (Applied Systems Engineering, 117X), whose bandwidth spans from 8 GHz to 12 GHz. Accordingly, observation pulses (t_π = 32 ns) originated from the +/-<x> channels by adjusting the channel-specific attenuators. The reference clocks of the E680 and the AWG were not synchronized, such that a 5.3 ns trigger-

to-output jitter results for the AWG. While this timescale is not relevant for the results presented in this study, the length of the blanking pulse applied to the +<y> channel needed to be prolonged by 8 ns to avoid pulse truncation. Note that one complication upon synchronization of the reference clocks is the time base of the external triggering unit of this particular fast commercial AWG at 12 GS/s, which is longer than the time base of the Elexsys trigger (5.33 ns versus 4 ns). For monitoring purposes, the second AWG channel is acquired by a fast digitizer (SP devices, ADQ412).

3.3.2 *Simulations*

The evolution of the spin density matrix of a two-level system under adiabatic microwave pulses was simulated in Hilbert space. By simulation in a frame rotating with the LO frequency, simulation time steps equal to the actual AWG time steps could be used without introducing significant numerical errors in integration. Because it is computationally inefficient to calculate the pulse propagator in each time step, propagators for single AWG time steps were precomputed for the 4096 possible output levels and stored in tables. Electron spin relaxation was accounted for by damping the elements of the density matrix difference from equilibrium by appropriate factors in each AWG time step. Relaxation times T_1 = 1 ms and T_2 = 2 μs were assumed. All calculations were performed in MATLAB. A detailed account on optimized simulation of arbitrary waveform excitation will be published elsewhere.
The simulation code from above was used to calculate M_z after the adiabatic pulse in Figs. 3.1d, 3.4 and 3.5. Any bandwidth-related distortions of the pulse modulation functions were accounted for by incorporating corresponding frequency-dependent amplitude or phase factors evaluated at the instantaneous frequency f_i of the chirp during the calculation of the digital waveform. Any amplitude compression (see Fig. 3.5d) was accounted for by amplitude-dependent modification of the amplitude modulation function. Time-dependent magnetization trajectories, as illustrated in the inset of Fig. 3.1d, were obtained from the time-dependent spin densities. The transformation from the frame rotating with the LO frequency into an accelerated frame was achieved by multiplying the transverse magnetization component with a complex-valued frequency chirp and low-pass filtering.

3.3.3 *Sample preparation*

TEMPOL was purchased from Sigma and used as received. A 1 mM solution was prepared from a 100 mM stock solution in milli-Q water, by diluting to 2 mM and mixing with glycerol (1:1 in volume). Synthesis of the terpyridine based copper-nitroxide complex was described in [94].

3.3.4 *Inversion sequences*

Several experiments recording longitudinal magnetization due to an incoherent inversion pulse from the AWG were performed on a glassy frozen solution of 1 mM TEMPOL in water/glycerol at 50 K (Sections 3.4.1 - 3.4.5). Inversion pulses were either monochromatic rectangular pulses or chirped pulses with t_{rise} = 30 ns. Unless otherwise stated, the sequence was set up as described in the following two paragraphs:
The signal was detected by a (16-32 ns) Hahn echo detection scheme, which uses coherent 16 ns and 32 ns pulses from the Elexsys bridge with pulse and (initial) recovery delay of 400 ns. In order to cancel offsets and select the longitudinal magnetization component, a [+(+x) -(-x)] phase cycle on the 16 ns pulse was used. The integration time p_g of the echo was 32 ns. In each cycle, the echo intensity was accumulated 10 times at a repetition rate of 116 Hz. The normalized magnetization component M_z was obtained by dividing

the actual echo intensity with the equilibrium echo intensity measured in the absence of an inversion pulse.
The observation frequency f_{obs} was set to the center frequency f_0 of the resonator, where the central line of the nitroxide spectrum was set to be in resonance by adjusting the magnetic field. When monochromatic rectangular inversion pulses were used (transient nutation or IR), the inversion pulses had the same frequency as the observation pulses. When chirped pulses were used, the sweep width Δf was centered with respect to the observation frequency. The chirp thus started at $f_1 = f_{obs} - \Delta f/2$ and ended at $f_2 = f_{obs} + \Delta f/2$.

3.3.5 *DEER experiments*

Four-pulse DEER data of the copper-nitroxide complex were obtained with the sequence $\pm(\pi/2)_{obs} - \tau_1 - (\pi)_{obs} - (\tau_1 + t) - (\pi)_{pump} - (\tau_2 - t) - (\pi)_{obs} - \tau_2 - echo$, where τ_1 = 400 ns, τ_2 = 1200 ns and a time increment for t of 8 ns were used. Observer pulses originating from the +/-<x> channels (16-32-32 ns scheme) were tuned to the central line of the nitroxide spectrum and the pump pulse originating from the AWG was resonant with a part of the copper spectrum. Pump pulses were either monochromatic rectangular pulses or chirped pulses with t_{rise} = 10 ns. The exact pulse frequencies are given in Section 3.4.6. Observation of nitroxide permitted a temperature of 35 K with a repetition rate of 116 Hz. Data was analyzed and regularized using DeerAnalysis2011 [95]. A Tikhonov regularization parameter of 100 was found to be adequate for all data.

3.4 RESULTS AND DISCUSSION

3.4.1 *Spin-detected hardware characterization*

In the following, two procedures are described that were applied to obtain hardware characteristics from transient nutation experiments.
First, knowledge of the spectrometer's transfer function $H(f)$ is essential to model UWB behavior. Due to the saturated power amplifier, however, the excitation chain is nonlinear and a single transfer function $H(f)$ can no longer describe the entire system [96]. Nevertheless, $H(f)$ can be regarded as a quasi-linearization of the nonlinear excitation system with respect to a prescribed input condition, which is termed as a describing function [97]. The input condition that suits the envisaged adiabatic inversion pulses best is a single sinusoidal input of constant full-scale amplitude, because the amplitude is modulated only during the specified time t_{rise} at the pulse edges and is otherwise constant at the full-scale amplitude to maximize pulse power. Such a quasi-linear model describes the excitation chain best, when rise transients at the beginning of the chirped pulse have decayed and when the input pulse has full-scale amplitude.
To obtain $H(f)$ experimentally, transient nutations were measured in the frequency range provided by the Elexsys bridge (9.1 - 9.9 GHz) with a frequency increment of 10 MHz. At each frequency, the central line of the nitroxide spectrum was observed by adjusting the magnetic field and the length of the monochromatic rectangular nutation pulse from the AWG was ramped up to 63.75 ns in 0.25 ns increments. Further details on the pulse sequence are given in Section 3.3.4. Optimization of observer pulse amplitude and phase at each observation frequency as well as phase cycling were here omitted to minimize the overall time of the experiment to typically 2 hours. In doing so, it is important to have the observer pulse amplitude initially set up and optimized in the vicinity of the center frequency of the resonator f_0. Finally, the on-resonance nutation frequency ν_1 was obtained as maximum value of the magnitude of the Fourier transform upon windowing and zero padding the nutation signal to 2^{14} points. Note that off-resonance contributions due

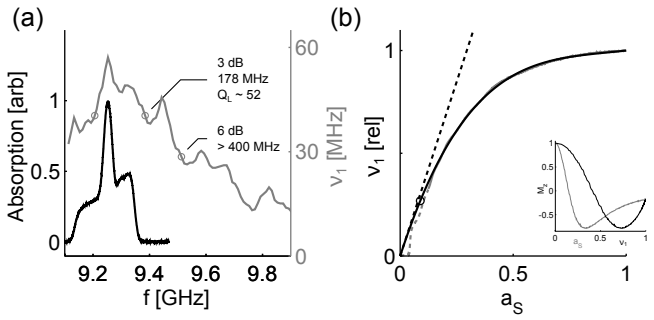

Figure 3.3 – Characterization of high power branch (resonator and TWT amplifier). (a) Magnitude response $\nu_1(f)$ of the spectrometer extracted from transient nutation (gray). 3 dB and 6 dB bandwidth and Q_L as indicated. The maximum ν_1 is 57 MHz at f_0 = 9.253 GHz. The field-swept echo-detected EPR spectrum converted to a frequency axis of 1 mM TEMPOL (black) is indicated for reference. (b) Nonlinearity calibration $\nu_1(a_S)$ performed at f_0 by measuring transient nutation at 1024 distinct digital pulse amplitudes a_S. Primary data (gray) was fitted by a constrained 4th order polynomial (black, 3 fitting parameters). For $a_S < 1/8$, primary data was omitted (gray dashed). The 1 dB compression point with respect to linear behavior (dashed black) is indicated by the black circle at a_S = 0.089. Inset (b) Nonlinearity corrected $M_z(\nu_1)$ (black) for a 12 ns rectangular pulse by correcting $M_z(a_S)$ (gray)

to the actual lineshape modify the initial oscillation period of the nutation signal. In the limiting case of a very broad line, for instance, the nutation signal follows a decaying Bessel function [18], whose initial oscillation period is longer than $1/\nu_1$. In order to obtain the proper ν_1 from the spectral magnitude, a symmetrical window function that rejects the initial part of the nutation signal was used (Dolph-Chebychev window, 100 dB sidelobe attenuation). The resulting $\nu_1(f)$ profile represents the magnitude of $H(f)$ and is shown in Fig. 3.3a (gray). The maximum ν_1 is 57 MHz at f_0 = 9.253 GHz and from the 3 dB bandwidth, a loaded quality factor Q_L of 52 results. The experimental $\nu_1(f)$ has distinct features and differs drastically from the ideal model H_{id} in Eq. (3.5). The origin of those features is located mostly in the high power branch following the amplifier, because amplitude characteristics prior to the power amplifier are compressed by the nonlinearity (see also discussion in Section A.1). The corresponding nitroxide spectrum (1 mM TEMPOL, 50 K) at 0.33 T extends over 260 MHz and is indicated for comparison. Drawbacks of this procedure are that the experiment is time consuming due to the manual frequency and field adjustments and the lack of primary phase information. Because it turned out advisable to measure $\nu_1(f)$ for each time a sample is inserted into the resonator, the measurement would benefit from a fast automatization. With an implementation of this measurement in the Bruker macro language ProDel, a partial automation is provided, but the overall time consumption did not improve much due to the frequency stepping. Pickup coil approaches [15, 93] on the contrary allow for a fast characterization of complex valued transfer functions. However, additional hardware with its own response function needs to be introduced and therefore possibly modifies experimental conditions with respect to the target experiment, especially at higher fields. The nutation experiment directly measures the microwave field experienced by the spins.

Furthermore, a calibration of the nonlinearity that distorts the pulse envelope amplitude a_S allows for prediction or compensation beyond the quasi-linearizing $H(f)$ described above. We therefore characterized the total nonlinearity at f_0 by measuring $\nu_1(a_S)$ in a single 2D sweep, where transient nutation was measured at 1024 different pulse amplitudes a_S. The ν_1 extraction is analogous to the $\nu_1(f)$ measurement described above. Although we here ramped the length of the nutation pulse up to 127 ns in 1 ns increments and used a (64-128 ns) Hahn echo detection scheme, small ν_1 were not re-

solved correctly. We therefore truncated the primary $\nu_1(a_S)$ below $a_S = 1/8$ and fitted a 4^{th} order polynomial constrained by $\nu_1(0) = 0$ and $\nu_1(1) = 1$, which yielded the black curve in Fig. 3.3b. The 1 dB compression point of the full excitation chain at the center frequency f_0 indicated by the black circle is at $a_S = 0.089$. Amplitude modulation by the AWG is therefore compressed substantially and in our case the effective rise time of the adiabatic inversion pulse is significantly shortened. This effect will be accounted for in Section 3.4.3.

The nonlinearity calibration furthermore allows us to obtain $M_z(\nu_1)$, which is depicted for a 12 ns rectangular pulse in the inset in Fig. 3.3b. Accordingly, the distorted $M_z(a_S)$ (gray) transforms into a cosine shaped $M_z(\nu_1)$ (black). We have found that the reverse procedure, i.e. an extraction of $\nu_1(a_S)$ from $M_z(a_S)$ of rectangular pulses is difficult due to the number of fit parameters involved.

Altogether, it should be emphasized that one single quasi-linearizing $H(f)$, whose magnitude $\nu_1(f)$ can be measured by transient nutation, and one single nonlinearity calibration $\nu_1(a_S)$ at one fixed frequency are still not capable of modeling the complete excitation hardware and thus predicting the pulse shape experienced by the spins. This is mainly due to the amplitude compression $\nu_1(a_S, f)$, which varies with frequency f. It is likely that the measurement time required for constructing a complete nonlinear model from transient nutation for each time a sample is inserted is too long for routine measurements. Nevertheless, such a spin-detected model permits verification of models obtained by different methodology, such as for instance a local pickup coil, which is essential to gauge the performance of arbitrarily modulated pulses. For the pulse shapes employed in this study, compression of the amplitude modulation only occurs during t_{rise} at both the rising and falling edges. In this particular case, a single quasi-linearizing $H(f)$, whose magnitude is obtained from transient nutation, is already a suitable approximation that allows for compensation, as demonstrated in the results.

3.4.2 *Spin-detected pulse calibration*

Due to the simple modulation function of a linear frequency sweep, a number of control experiments can be performed to provide insight into the actual inversion profile and to identify effects due to hardware imperfections by comparing to simulations with unperturbed pulses. The experimental conditions were given by $\nu_1(f)$ in Fig. 3.3a and details on the pulse sequence are given in Section 3.3.4. Accordingly, longitudinal magnetization upon adiabatic inversion is detected on the central line of the nitroxide spectrum. First, an experimental calibration of admissible chirp rates ($\Delta f / t_p$) aids the selection of pulse parameters. Because we are interested in the performance of a short UWB pulse, we chose a pulse length of 128 ns, which is much shorter than T_2 (2 μs). In the experiment, we observed M_z at f_0 while varying Δf and keeping the center frequency of the chirp at f_0. The obtained $M_z(\Delta f)$ curve is shown in Fig. 3.4a. Despite the drop in inversion efficiency above 300 MHz due to reduced adiabaticity, Δf = 525 MHz still permits 97% inversion with respect to the observed spins at f_0. Not surprisingly, the 64 ns pulse measured for comparison experiences a more pronounced drop in $M_z(\Delta f)$. For small Δf below 200 MHz, the adiabaticity according to its definition is high, but the flip angle is not 180° when $\Delta f/2$ becomes comparable to ν_1 (see [4]). This explains the corresponding reduction in inversion efficiency. Interestingly, a simulation under idealized conditions (dashed) predicts a much better inversion performance and highlights the importance of pulse perturbations, which is discussed in Section 3.4.3.

Second, the widely appreciated insensitivity to ν_1 of adiabatic inversion pulses was measured by observing M_z at f_0 while ramping the pulse amplitude. The resulting $M_z(\nu_1)$ curve for a 128 ns pulse with Δf = 525 MHz is

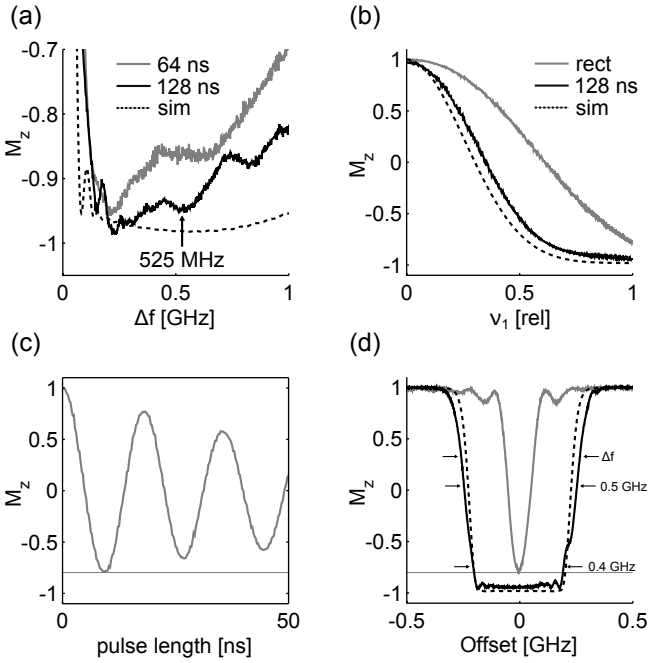

Figure 3.4 – Calibration of inversion pulses. (a) Experimental chirp rate dependence $M_z(\Delta f)$ of the center isochromat at fixed pulse length of 128 ns (black) and 64 ns (gray). The simulation shown (dashed black) neglects pulse imperfections. (b) Experimental ν_1 robustness $M_z(\nu_1)$ of the center isochromat for a 128 ns chirp (black, Δf = 525 MHz) and a monochromatic rectangular 9 ns pulse (gray) as well as an idealized simulation (dashed black). (c) Transient nutation with 0.25 ns time increment for the calibration of the rectangular pulse. Inversion maximum as indicated by the thin gray line. (d) Frequency offset dependence of inversion with respect to center isochromat for a 128 ns chirp (black, Δf = 525 MHz) and a monochromatic rectangular 9 ns pulse (gray) as well as for an idealized simulation (dashed black). The labeled bandwidths are defined between the intersection points of the corresponding arrows and the black curve.

shown in Fig. 3.4b, where the nonlinearity mapping $\nu_1(a_S)$ from Fig. 3.3b has been used. We found the experimental inversion efficiency at the 6 dB points (78%) to be a useful figure, because it can be combined with the 6 dB bandwidth of the resonator (≈400 MHz) to estimate the inversion performance at offset from the resonator peak at f_0. The quantitative accuracy of this 6 dB figure is limited by pulse imperfections: An isochromat exactly at the 6 dB frequency of the resonator experiences different amplitude and phase modulation than the reference isochromat at f_0 with a chirp of half the amplitude. This is because the shape of $\nu_1(f)$ and $\beta(f)$ experienced as $\nu_1(t)$ and $\beta(t)$ is different for each individual isochromat. The adiabaticity with respect to the reference isochromat is therefore altered, even if the pulse amplitude at the reference is scaled accordingly. Nevertheless, we can say that the robustness of the inversion efficiency with respect to ν_1 significantly alleviates the excitation bandwidth limitation of the resonator. Note also that this 6 dB figure is strongly dependent on experimental conditions, $\nu_1(f)$. In fact, we could observe 6 dB figures as high as 86% with the same pulse parameters under best conditions so far (see Fig. A.3c below). As an alternative, 6 dB figures can also be obtained by setting the high power attenuator to 6 dB instead of reducing the amplitude of the digital waveform. This procedure does not require knowledge of $\nu_1(a_S)$.

If $M_z(\nu_1)$ is compared with a simulation under idealized conditions (dashed), the simulation significantly outperforms the measurement. In addition, the experimental $M_z(\nu_1)$ is shown for a monochromatic rectangular 9 ns pulse (gray), which shows lower ν_1 robustness and a lower inversion maximum at zero offset than the chirped pulse. Because $M_z(\nu_1)$ for monochromatic rectangular pulses depends strongly on the pulse length, the underlying transient

nutation curve with 0.25 ns time increment is shown in Fig. 3.4c. Accordingly, a pulse length of 9 ns results in a representative inversion maximum for the rectangular pulse. It is worth mentioning that we observed this advantage in maximum achievable inversion efficiency of chirped pulses over rectangular pulses in all experiments done so far. With respect to ν_1 robustness, however, we observed slightly better performance for rectangular pulses than in Fig. 3.4b, for instance by analyzing nutation traces from the $\nu_1(a_S)$ calibration (see section 3.4.1), which contain $M_z(\nu_1)$ for various t_p. The best robustness, quantified as 6 dB figure, was found to be 43%, which exceeds the 6 dB figure of 35% from Fig. 3.4b. It is supposed that a figure closer to 43% could be achieved by a prolongation of the rectangular pulse to 9.5 ns, which would meanwhile not significantly alter its inversion maximum.
Third, it is interesting to experimentally determine the bandwidth in which the flip angle remains constant at fixed ν_1. We therefore observed M_z at f_0 while varying the center frequency of the adiabatic pulse. In that way, the inversion efficiency of subsequent time slices of the pulse is analyzed. In Fig. 3.4d, M_z against frequency offset is shown for the adiabatic 128 ns pulse with Δf = 525 MHz, as well as for a monochromatic rectangular 9 ns pulse. The advantages of the adiabatic UWB pulse with respect to both inversion bandwidth and inversion efficiency are clearly seen. In fact, the adiabatic pulse has supreme inversion efficiency over almost 400 MHz. As a reference, the maximum inversion achievable with a rectangular pulse is indicated by the thin gray line.
The inversion bandwidth obtained by this measurement should not be confused with the effective inversion bandwidth, which is certainly below the bandwidth found here (400 MHz) due to $\nu_1(f)$. However, coincidence with the 6 dB bandwidth of $\nu_1(f)$ (400 MHz) and the 6 dB figure of 78% predicts a reasonable overall inversion performance. The edges of the inversion band are dependent on the rising and falling edges of the pulse and by flipping the direction of the frequency sweep, start and end transients can even separately be identified. The edge at positive frequency offset is therefore dominated by probe ringing at the end of the pulse. Further discussions as well as a better overlap with simulations are presented in Section 3.4.3.
Overall, these control experiments aid the selection of appropriate pulse parameters from experimental data exclusively. In situations where only little information about pulse imperfections is available, such an experiment driven parameter setup avoids potential performance loss by choosing pulse parameters from simulations which might overestimate the actual performance.

3.4.3 *Group delay compensation*

As derived previously in Section 3.2.2, group delay variations with frequency reduce the adiabaticity of an inversion pulse. Accordingly, the aim of this section is to demonstrate inversion pulses which compensate for group delay variations and thus have enhanced adiabaticity. Because the phase characteristic, and so the group delay variation, is not available from the nutation experiments described in Section 3.4.1, the phase retrieved from the magnitude response $\nu_1(f)$ is used for the group delay compensation. A detailed description of this procedure is found in Section A.1 and the results in the frequency range of interest are summarized in Fig. 3.5: Fig. 3.5a shows the extrapolated magnitude response $\hat{\nu}_1(f)$ (black), which is obtained by combining the measured response $\nu_1(f)$ with the magnitude response $|H_{id}(f)|$ (gray) of the RLC series circuit H_{id} from Eq. (3.5). Fig. 3.5b shows the resulting phase $\hat{\beta}(f)$ reconstructed from $\hat{\nu}_1(f)$ (black). Also shown is the phase reconstructed from $|H_{id}(f)|$ (gray), whose apparent offset to the actual model phase $\angle H_{id}(f)$ (dashed gray) is explained in Section A.1.
The azimuthal velocity $|\nu_\beta(f)|$ according to Eq. (3.4) is shown in Fig. 3.5c for the reconstructed $\hat{\beta}(f)$ (black) and for $\angle H_{id}(f)$ (dashed gray), where a

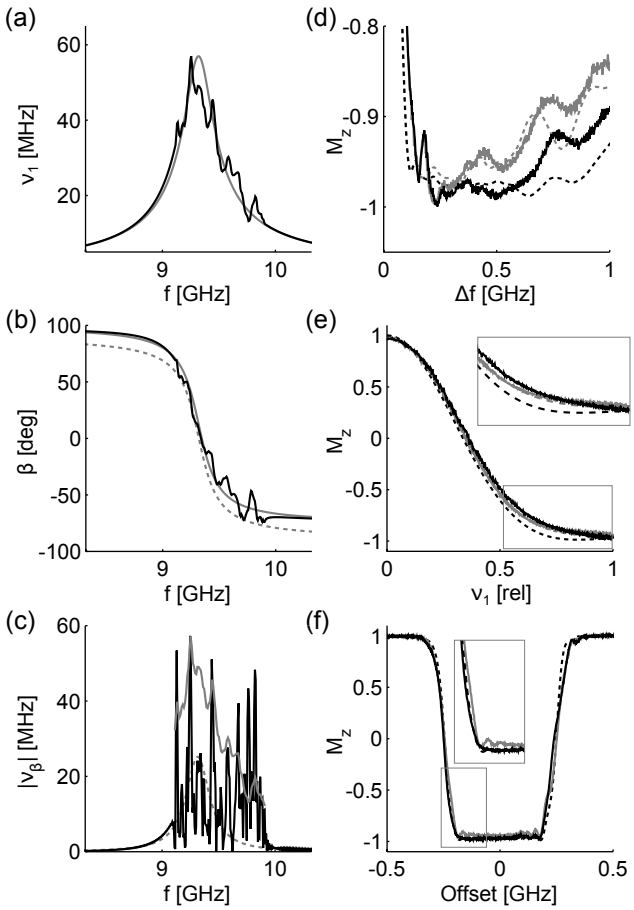

Figure 3.5 – Compensation of group delay variations. (a) Magnitude response $\hat{v}_1(f)$ (black) and $|H_{\mathrm{id}}(f)|$ (gray). (b) Phase $\beta(f)$ reconstructed from $\hat{v}_1(f)$ (black) and $|H_{\mathrm{id}}(f)|$ (gray) as well as original phase of $H_{\mathrm{id}}(f)$ (dashed gray). (c) $|\nu_\beta|$ of $\hat{\beta}(f)$ (black) and $\angle H_{\mathrm{id}}(f)$ (dashed gray) with a chirp rate of (640 MHz / 32 ns). $\nu_1(f)$ (gray) is indicated for reference. (d) $M_z(\Delta f)$ for a 128 ns pulse with (black) and without phase (gray) correction. Simulations accounting for $\nu_1(f)$ (dashed black) and both $\hat{v}_1(f)$ and $\hat{\beta}(f)$ (dashed gray). (e) $M_z(\nu_1)$ for a 128 ns pulse with Δf = 525 MHz with (black) and without phase (gray) correction. Simulations accounting for $\hat{v}_1(f)$ (dashed black) and both $\hat{v}_1(f)$ and $\hat{\beta}(f)$ (dashed gray, mostly below gray curve). (f) Frequency offset dependence of inversion with respect to center isochromat for 128 ns chirp with Δf = 525 MHz with (black) and without phase (gray) correction. Simulation accounting for $\hat{v}_1(f)$ as well as $\nu_1(a_S)$ (dashed black).

chirp rate of (640 MHz / 32 ns) has been used. When comparing to $\nu_1(f)$ (gray), it can be seen that peaks in $|\nu_\beta(f)|$ are associated with pronounced narrowband features in $\nu_1(f)$, thus pointing at the cause of the enhanced group delay variations of $\hat{\beta}(f)$ with respect to $\angle H_{\mathrm{id}}(f)$. An interesting point is the center frequency of the resonator, f_0, because $\nu_1(f_0)$, $\nu_\beta(f_0)$ and $\nu_\alpha(f_0)$ are all comparable for the chosen chirp rate. Accordingly, $Q_{\mathrm{crit}}(f_0)$ is by a factor of $\sqrt{2}$ lower than the value suggested by Eq. (3.2) for any chirp rate. We therefore examined the group delay compensation at the center frequency f_0. A sufficient degree of compensation was achieved by adding the frequency-dependent phase offset of $\hat{\beta}(f)$ during the calculation of the digital waveform.

The adiabaticity improvement is best seen in the $M_z(\Delta f)$ curves, which are shown in Fig. 3.5d for a 128 ns pulse. The inversion efficiency of the compensated chirp (black) is always slightly better than that of the uncompensated chirp (gray, black in Fig. 3.4a). Furthermore, the agreement between experiment (solid) and simulation (dashed) is better than in Fig. 3.4a, because the pulse perturbations were included in the simulation: The compensated chirp has ideally $\nu_\beta = 0$, such that only the amplitude correction $\hat{v}_1(f)$ was

incorporated. The uncompensated chirp was modified by both $\hat{\nu}_1(f)$ and $\hat{\beta}(f)$. Note that the simulation models a 2 level system, whereas the measurement observes an ensemble. It is therefore not possible to quantify the actual degree of compensation from the remaining deviations between experiment and simulation.

The ν_1 sensitivity $M_z(\nu_1)$ for Δf = 525 MHz in Fig. 3.5e reveals that the inversion is only enhanced if the normalized ν_1 is above 0.75 (see inset). It is suggested that the reason for the degraded ν_1 robustness of the compensated pulse is the nonlinearity. Recalling Section 3.4.1, $H(f)$ is a quasi-linearization for sinusoidal input at full-scale amplitude. In the measurement of $M_z(\nu_1)$ however, the amplitude a_S of the AWG waveform is reduced and the quasi-linearization loses its validity. As a consequence, the compensation aims to correct for group delay variations that do not exist at small a_S (overcompensation) and thus explains the reduction in inversion efficiency towards small ν_1. In that sense, a comparison between simulation and experiment is also delicate, because the waveform perturbations at small relative ν_1 are not modeled properly.

The frequency offset dependence of M_z at f_0 is shown in Fig. 3.5f. For the group delay compensation (black), the phase offset $\hat{\beta}(f)$ was added to the digital waveform after shifting its center frequency. In comparison to the uncompensated pulse (gray), the inversion is slightly improved. As shown in the inset, the inversion at negative offset after the rising edge of the pulse also settles earlier to its maximum. For the falling edge at positive offset, probe ringing is predominant. In the depicted simulation (dashed black), $\hat{\nu}_1(f)$ as well as the amplitude compression $\nu_1(a_S)$ from Fig. 3.3b were included. The purpose of including amplitude compression was to highlight the associated shortening of the rise time in an approximative manner. Accordingly, the simulation fits better at the pulse edges than in Fig. 3.4d. As mentioned in Section 3.4.1 however, the application of an accurate nonlinear model that includes rise and fall transients is more demanding and beyond the scope of the current study.

In summary, group delay compensated pulses revealed slightly enhanced performance as compared to uncompensated pulses within the validity of the quasi-linear hardware model. As one would expect, the actual relative improvement when using the proposed compensation technique is strongly dependent on the experimental conditions $\nu_1(f)$ and $\beta(f)$. For the spectrometers and probeheads applied in this work and for the fairly robust chirp pulses, such compensation may be unnecessary in routine measurements. Note however that we never observed reduction in performance for group delay compensated UWB pulses having full-scale amplitude and the effects might be more prominent for other hardware or with other excitation waveforms (see also Fig. A.3).

3.4.4 *Bandwidth compensation*

As discussed in Section 3.4.3, the compensation of group delay variations is achieved in a rather direct manner by addition of a phase offset to the phase modulation function. A compensation of amplitude perturbations by $\nu_1(f)$ on the contrary cannot be achieved in a similar way because the amplitude is bounded. In addition to that, amplitude compression complicates an accurate prediction of the amplitude modulation seen by the spins. Under these conditions, the minimum adiabaticity with respect to a particular isochromat at frequency f is proportional to $\nu_1(f)^2$ for a linear chirp. If however the instantaneous chirp rate is adapted to $\nu_1(f)^2$, all isochromats within Δf can be inverted with the same adiabaticity Q_{ref} (excluding those at the pulse extremities during t_{rise}). This procedure is termed *offset- independent adiabaticity* [45, 46] and the instantaneous chirp rate is given by

$$\frac{\delta f(t)}{\delta t} = 2\pi\ \nu_1(t)^2\ /\ Q_{\text{ref}} \tag{3.7}$$

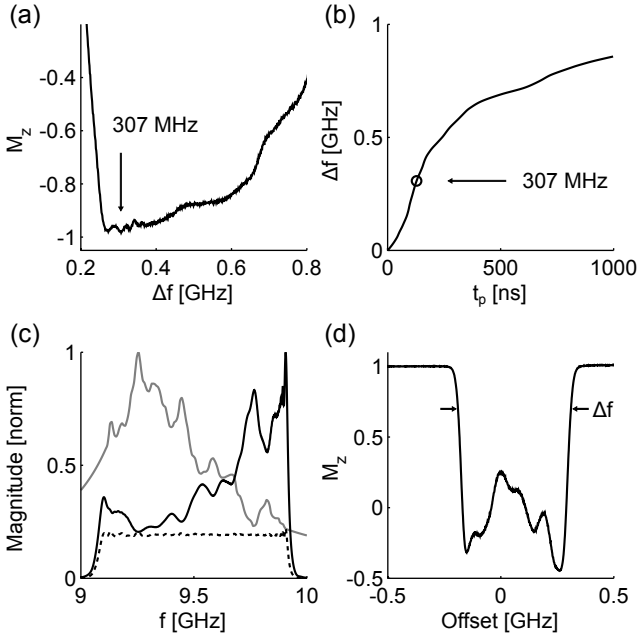

Figure 3.6 – Compensation of amplitude perturbations. (a) Experimental calibration of Q_{ref} at f_0 by incrementing Δf of a 128 ns pulse. Maximum inversion indicated at Δf = 307 MHz. (b) $\Delta f(t_{\mathrm{p}})$ obtained from experimental Q_{ref} calibration. $\Delta f(998\mathrm{ns})$ = 858 MHz. (c) Magnitude of Fourier transformed pulse (black, Δf = 858 MHz) adapted to $\hat{\nu}_1(f)$ (gray). The flat line (dashed gray) depicts their product, which is proportional to the square root of the net energy density delivered by the pulse. (d) Frequency offset dependence of inversion with respect to center isochromat for 241 ns chirp adapted to $\nu_1(f)$. Δf = 0.5 GHz and the pulse amplitude is intentionally reduced to provide only 30% of the maximum ν_1 at f_0, thus revealing features of $\nu_1(f)$. The labeled bandwidth Δf is defined at the intersection between the corresponding arrows and the black curve.

A fundamental difference to previous studies in NMR spectroscopy is, however, that in our case the chirp rate adaptation compensates for bandwidth limitations $\nu_1(f)$ rather than for an intentionally prescribed amplitude modulation function $\nu_1(t)$. As a consequence, the instantaneous frequency $f(t)$ of the adapted chirp needed to be deducted from its inverse

$$t(f) = \int_{f_1}^{f} \frac{Q_{\mathrm{ref}}}{2\pi\, \nu_1(f')^2}\, df' \tag{3.8}$$

where f_1 is the initial frequency of the adapted chirp.
For an appropriate choice of Q_{ref}, we measured $M_z(\Delta f)$ at f_0 for 128 ns long pulses with chirp rate adaptation and group delay compensation, which is shown in Fig. 3.6a. The experimental conditions were given by $\nu_1(f)$ in Fig. 3.3a. Because the initial frequency f_1 was 190 MHz below f_0, $\hat{\nu}_1(f)$ was used for the adaptation. The experimental inversion maximum at Δf = 307 MHz results in Q_{ref} = 4.17, which is obtained from

$$Q_{\mathrm{ref}}(\Delta f) = \frac{2\pi\, t_{\mathrm{p}}}{\int_{\Delta f} \nu_1(f)^{-2}\, df} \tag{3.9}$$

Given Q_{ref}, the time required for a certain sweep width Δf can be calculated and is shown in Fig. 3.6b. Interestingly, the time required for inversion throughout the full range of the spectrometer is below 1 μs and thus much shorter than typical longitudinal relaxation times of electron spins in pulsed EPR. Fig. 3.6c shows that the chirp rate adaptation results in equal distribution of pulse energy throughout the frequency sweep at the level of the spins (dashed black). At the level of signal generation by the AWG on the contrary, the digital waveform has not yet experienced $\nu_1(f)$ (gray) and its spectral magnitude (solid black) highlights the compensation of $\nu_1(f)$. We

also measured the frequency offset dependence of M_z at f_0 for a deliberately attenuated 241 ns pulse, which permits Δf = 0.5 GHz. As this experiment reveals the inversion efficiency at constant ν_1, the fingerprint of the resonator can be identified in Fig. 3.6d. Note that the pulse amplitude needed to be reduced by a factor of 3 for that purpose. At full scale excitation, the inversion efficiency would remain large and mostly constant within the inversion bandwidth.
Overall, bandwidth compensation can overcome the bandwidth limitations $\nu_1(f)$ posed to excitation. Recalling the 6 dB figure used in Section 3.4.2 to estimate the minimum inversion efficiency within the 6 dB bandwidth, bandwidth compensation can in principle achieve a 6 dB figure of 100%. A major limitation is set by the pulse time t_p. In fact, the time required for adiabatic UWB inversion with $Q_{ref} > 4$ was found to be below 1 μs and can compete with typical longitudinal relaxation times. An application to IR using bandwidth compensation is demonstrated in the next section. Inversion pulses that affect coherence transfer on the contrary, such as for instance the pump pulse in four-pulse DEER, are likely to introduce distortions if the pulse time is comparable to the evolution period of the coherence. In these cases, the applicability of bandwidth compensated pulses is severely limited. The four-pulse DEER experiments described in Section 3.4.6 were therefore performed without bandwidth compensation.

3.4.5 *Inversion recovery with adiabatic pulses*

When measuring the decay of longitudinal magnetization, spectral diffusion processes often shorten the apparent relaxation time T_1 with respect to the intrinsic T_{1e} that is related to direct magnetization transfer between on-resonance spins [98, 99]. Several experimental procedures to suppress spectral diffusion contributions have been proposed. One possibility is to apply saturation recovery (SR), where spectral diffusion processes can be equilibrated [100, 101]. Another possibility is to observe IR on a small fraction of the inverted spins [102]. In the limit of complete inversion, however, a reduction in observation bandwidth, and thus a reduction in measurement sensitivity, is not necessary anymore. A related experiment was described in [103], where uniform inversion of a three-line nitroxide spectrum was achieved by a tailored composite pulse. One would expect that the versatility of such an approach is enhanced by applying adiabatic inversion pulses capable of UWB inversion. We therefore sought for changes in apparent T_1 times on TEMPOL at 50 K for a set of adiabatic inversion pulses.
Beforehand, it was interesting to test if any signature of spectral diffusion can be detected by variation in the observation bandwidth when using a monochromatic rectangular inversion pulse of fixed bandwidth. Accordingly, IR traces following a monochromatic rectangular 9 ns inversion pulse were recorded with a (16-32 ns) or a (52-104 ns) Hahn echo detection scheme on the central line of the nitroxide spectrum. While a 32 ns pulse length in the detection scheme was used throughout this study (see Section 3.3.4), 104 ns is applied, for instance, to obtain relaxation-based distance information [104]. As the normalized IR traces in Fig. 3.7a indicate, the longitudinal decay characteristic of the 32 ns (dashed black) and 104 ns (gray) echo signal is identical. In this particular case, we could thus not detect spectral diffusion to nearby spins. When comparing signal levels normalized by the echo integration time p_g, the 32 ns echo signal is 1.77 times stronger than the 104 ns echo signal (data not shown).
To investigate spectral diffusion processes to distant spins, the sweep width Δf of a 128 ns inversion pulse was varied. The experiment is analogous to the measurement of $M_z(\Delta f)$ described in Section 3.4.2, the only difference being that an inversion recovery trace is recorded for each Δf. Inversion recovery traces were measured up to a recovery delay of 15.35 ms, starting at 400 ns with an increment of 10 μs, in 8.8 minutes total measurement time

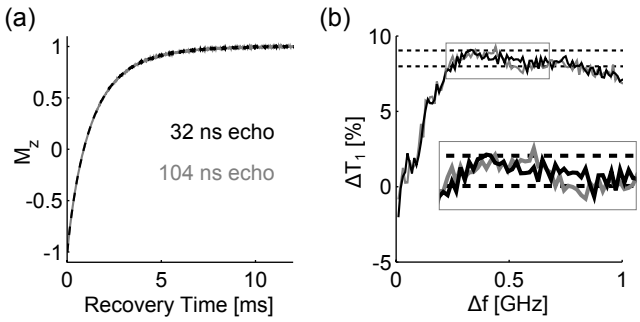

Figure 3.7 – Nitroxide inversion recovery. (a) Normalized recovery traces upon inversion with monochromatic rectangular 9 ns pulse measured with different observation bandwidth by (16-32 ns) (dashed black) and (52-104 ns) (gray) Hahn echo detection scheme. (b) Change in apparent T_1, ΔT_1, versus sweep width Δf with respect to T_1 obtained with a monochromatic rectangular 9 ns pulse for $\tilde{\tau}_g(f)$ compensated (solid black) and uncompensated (solid gray) pulses. The two dashed lines indicate T_1 obtained with bandwidth and $\tilde{\tau}_g(f)$ compensation using Δf = 307 MHz, t_p = 128 ns (lower line, 8%) and Δf = 412 MHz, t_p = 170 ns (upper line, 9%).

each by using a repetition rate of 58 Hz. The increment in Δf was 10 MHz, while keeping Δf centered with respect to the observation frequency. All the data was acquired in a single 2D experiment, including group delay compensated and uncompensated pulses. The apparent T_1 times were obtained as $1/e$-times from a biexponential fit to experimental data, where the first data point has been excluded. Note that even in the absence of spectral diffusion, inversion decay is not a single exponential in glassy solvents due to orientation dependence of relaxation times [105–107]. It is therefore not possible to infer the presence or absence of spectral diffusion from the characteristic of the inversion decay alone. As a reference, T_1 was measured with a monochromatic rectangular 9 ns inversion pulse. Experimental conditions and pulse performances were the same as those presented in Sections 3.4.1 and 3.4.2. Further details on the pulse sequence are described in Section 3.3.4. The change in apparent $T_1(\Delta f)$ with respect to the apparent T_1 measured with the monochromatic rectangular pulse is shown in Fig. 3.7b for group delay compensated (solid black) and uncompensated (solid gray) pulses. Both curves achieve an enhancement in ΔT_1 of 9% for $\Delta f \approx$ 330 MHz. For larger Δf, group delay compensated pulses reveal a slightly more monotonic decay in $\Delta T_1(\Delta f)$ than uncompensated pulses (see inset). It is proposed that the monotonic decay is because the inversion profile $M_z(f)$ of the compensated pulse, which is related to $\nu_1(f)$, is maximal at the observer spins, thus resulting in a gradual decay in net inversion above Δf = 330 MHz. The uncompensated pulse on the contrary has its inversion profile modified by $\tilde{\tau}_g(f)$, which is rather strong at the observation frequency f_0 (Fig. 3.5c). When using a bandwidth and $\tilde{\tau}_g(f)$ compensated chirp with $f_1 = f_0 -$ 190 MHz, Δf = 307 MHz and t_p = 128 ns, ΔT_1 was 8%, which is indicated by the lower dashed line. The maximum enhancement of 9% was attained with $f_1 = f_0 -$ 190 MHz, Δf = 412 MHz and t_p = 170 ns, which is indicated by the upper dashed line.

Based on these results, we conclude that virtually complete inversion of the nitroxide spectrum results in 9% longer apparent T_1 by suppression of spectral diffusion processes. The apparent T_1 times versus Δf suggest that the suppressed diffusion processes transfer inverted spins throughout the whole spectrum. Experimental evidence for such magnetization transfer using pulsed ELDOR is provided in Section A.2. Possible magnetization transfer processes involve, for instance, electron spin exchange due to exchange couplings or relaxation of the nitrogen nuclear spin, which is the more likely of the two under the given conditions [108]. However, an elucidation of the underlying diffusion process based on the available experimental

data at 50 K is not possible and further investigations are beyond the scope of the current study.
Nevertheless, the signature of a weak spectral diffusion process in ΔT_1 allowed for comparison of inversion efficiency with respect to the whole nitroxide spectrum. Because the spectral width of the nitroxide spectrum is below the 6 dB bandwidth of $\nu_1(f)$ (see Fig. 3.3a), the maximum achieved inversion efficiency with linear chirps and bandwidth compensation was experimentally comparable. Towards larger Δf in the UWB regime, modification of nitroxide inversion due to both $\nu_1(f)$ and $\beta(f)$ has been observed. For virtually complete inversion of a spectrum broader than the 6 dB bandwidth of $\nu_1(f)$, adiabatic inversion by bandwidth compensated pulses with sufficient Δf is therefore the method of choice. For inversion of narrower spectra, such as the presented example, the performance of uncompensated pulses can compete with the performance of compensated pulses in a certain range, but setting up a compensated pulse with sufficient Δf is more robust.

3.4.6 *DEER with fast passage pulses*

In the DEER experiment with two dipole-coupled spin ensembles, the dipolar modulation depth is directly related to the inversion efficiency for the pumped spins [109]. When pumping a metal center, the modulation depth is thus often small and limits data quality. For distance information between a broad metal center and a nitroxide radical, one can overcome this limitation by pumping the spectrally narrower nitroxide radical and observing the metal center [94, 68]. For distance information between two metal centers on the contrary, the limitation in inversion efficiency is unavoidable [110]. We thus studied the possible improvement in modulation depth when pumping a metal center by using UWB pulses. As a model system, we chose the terpyridine-based copper-nitroxide complex with an interspin distance of 2.43 nm described and analyzed in [94]. For the purpose of this study, we pumped copper spins with UWB pulses and observed nitroxide spins. Since the dipolar evolution period t_{dip} corresponding to 2.43 nm is 276 ns, the inversion pulse needs to be short compared to this time scale for minimal distortions in DEER data. An enhancement in modulation depth is therefore achieved by trading pulse time t_{p} against sweep width Δf.
To explore what improvement such short UWB pulses can achieve, we compared DEER experiments performed with several (Δf, t_{p}) combinations. We chose the pulse times to be shorter than $t_{\mathrm{dip}}/4$, such that 32 ns, 48 ns, and 64 ns pulses with t_{rise} = 10 ns were examined (without compensation). For each t_{p}, the sweep width Δf was varied from 250 MHz to 900 MHz in 50 MHz steps and each DEER trace was acquired in 50 minutes. The experimental conditions were as shown in Fig. 3.8a. The observer frequency f_{obs} was coincident with the maximum of the nitroxide spectrum (black) at 9.113 GHz and the initial frequency of the chirp was at f_1 = 9.213 GHz, where the copper spectrum is predominant (light gray). As a reference, a monochromatic rectangular 8 ns pump pulse at f_{rect} = 9.313 GHz was used (actual length of digital waveform was 7.7 ns). Further details on the pulse sequence and on data evaluation are described in Section 3.3.5.
The resulting enhancements in modulation depth are shown in Fig. 3.8e. Notably, all (Δf, t_{p}) combinations result in higher modulation depth than that achieved with a monochromatic rectangular 8 ns pump pulse. Enhancement maxima of 2.30, 2.56 and 2.67 are found for (500 MHz, 32 ns), (550 MHz, 48 ns) and (600 MHz, 64 ns), respectively. These experimental optima in Δf at given pulse time t_{p} are all significantly above the 6 dB resonator bandwidth (see $\nu_1(f)$ in Fig. 3.8a). In fact, Δf above 280 MHz implies that the final frequency of the chirp is above the 6 dB point at 9.493 GHz. Nevertheless, maximum inversion efficiency of the broad copper spectrum at given t_{p} is achieved if also those spins above 9.493 GHz are pumped. As a consequence, the adiabaticity for these pulse parameters is low. With Δf = 500 MHz and

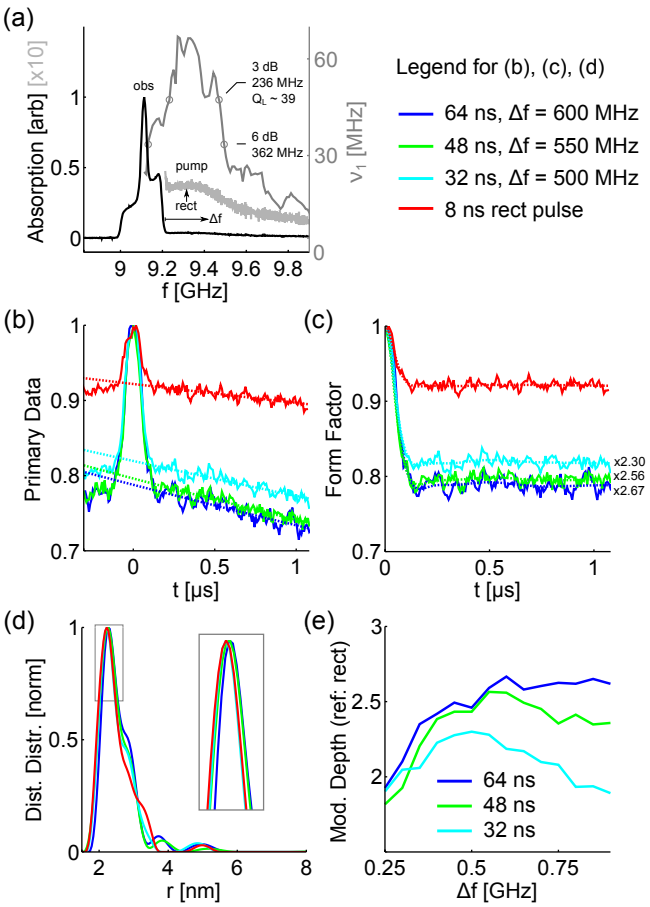

Figure 3.8 – DEER modulation depth enhancement with fast passage pulses. (a) Experimental conditions showing the field-swept echo-detected EPR spectrum converted to a frequency axis of the copper-nitroxide complex, both as is (black) and 10x magnified in the copper region (light gray), and $\nu_1(f)$ (gray). Pulse frequencies as indicated: f_{obs} = 9.113 GHz, f_{rect} = 9.313 GHz, f_1 = 9.213 GHz. The final frequency of the chirp is $f_1 + \Delta f$ (b) Primary DEER traces (solid) for experimental Δf optima and monochromatic rectangular 8 ns reference pump pulse and background fit (dashed), legend on top right (colors online). (c) Experimental (solid) and fitted (dashed) form factors for experimental Δf optima and rectangular 8 ns pulse, legend on top right, enhancement in modulation depth with respect to rectangular 8 ns pulse indicated aside of each trace. (d) Regularized distance distributions for experimental Δf optima and rectangular 8 ns pulse including a zoom in the inset, legend on top right. (e) Enhancements in modulation depths with respect to rectangular 8 ns pulse for Δf varied between 250 MHz and 900 MHz in 50 MHz steps for t_{p} of 64 ns (blue), 48 ns (green) and 32 ns (cyan). Modulation depths were extracted from the last point of the form factor fit.

t_{p} = 32 ns for instance, the adiabaticity Q_{crit} as given in Eq. (3.2) is below 1 where $\nu_1(f)$ is below 50 MHz. Accordingly, we refer to these pulses as fast passage pulses. A distinct feature of these pulses is that a moderate inversion is maintained over a large bandwidth. An adiabatic pulse on the contrary establishes a large inversion over a moderate bandwidth for the case that t_{p} is limited.

Primary DEER data for the experimental Δf optima is shown in Fig. 3.8b (corresponding legend on top right). The reduction in echo amplitude with respect to the monochromatic rectangular pump pulse, which cannot be seen in the figure due to data normalization, was 10% for all three Δf optima, which is small compared to the improvement in modulation depth. The maximum improvement in total detection sensitivity with respect to the monochromatic rectangular pump pulse achieved with the 64 ns pulse is thus 2.40. The corresponding form factors are shown in Fig. 3.8c. Data

obtained with the 64 ns pulse (blue) exhibit an unexpected regular oscillation at $t > 0.75$ μs. We tentatively assign this oscillation to enhanced spectral overlap between the pump and the observer pulse when using the chirped 64 ns pulse, as also indicated by enhanced nuclear modulation. On another spectrometer higher quality data were obtained which do not exhibit these oscillations (see Fig. 3.9a). The corresponding distance distributions are shown in Fig. 3.8d. Overall, the distributions obtained with fast passage pulses are in good agreement with the distribution obtained with the monochromatic pulse (red). On a closer look at the distance peaks (see inset), a slight shift towards longer distances with increasing pulse length can be seen, which is at most 2.2%. An analysis of distance distortions due to UWB pumping, including also orientation selection, is given below on data of higher quality. For further enhancements in modulation depth, we applied group delay compensation and also changed experimental conditions by using an Elexsys E580 spectrometer instead of the E680 we used so far. The details are described in Section A.3. In summary, the most significant improvement resulted from changing experimental conditions, whereas improvements upon group delay compensation were comparably small. The highest achieved modulation depth using a 64 ns UWB pump pulse with Δf = 800 MHz was 24% and therefore three times larger than the highest modulation depth of 8% achieved with a monochromatic rectangular 8 ns pulse. When considering the reduction in echo amplitude associated with this UWB pump pulse, an improvement in total detection sensitivity of 2.47 results. Fig. 3.9a shows the form factor for this 64 ns UWB pump pulse (black), as well as for a reference obtained with a monochromatic rectangular 8 ns pulse measured under the same experimental conditions (gray). Both traces were accumulated for a sufficiently long time (16 h).

For an analysis of related distance distortions due to the 64 ns UWB pump pulse, corresponding experimental dipolar spectra are shown in Fig. 3.9b for the 64 ns UWB pump pulse (solid black) and the monochromatic rectangular pulse (solid gray). Note that the nuclear modulations (14 MHz) clearly visible in the corresponding form factors do not contribute to the dipolar spectrum in the depicted frequency range $|\nu| < 10$ MHz. Also shown is the ratio (black divided by gray) between these spectra (dashed). From this ratio, the modifications of the dipolar spectra introduced by the UWB pump are readily identified: For $|\nu| < 4.7$ MHz, the dipolar spectra are comparable in magnitude. In this region, deviations are mostly due to orientations excited by the UWB pulse, which are not excited by the monochromatic rectangular pulse. As a consequence, the singularity around 2 MHz dominating towards low g values ($g_{||}$, see [94, 111]) is slightly more pronounced with the UWB pump and emerges as a peak in the ratio of the dipolar spectra (see arrows). For $|\nu| > 4.7$ MHz, the dipolar spectrum of the UWB pulse is cut off. This low-pass characteristic originates from continuous transfer of coherence during $t_p = 64$ ns, which smears out fast evolving coherences. In fact, the evolution period of the experimental cutoff at 4.7 MHz is 213 ns, which is 3.3 times t_p. Note that this number is not valid in general, because the cutoff depends not only on excitation time t_p, but certainly also on excitation efficiency in time domain, especially on how excitation initiates and terminates at the edges of the pulse. Regularized distance distributions are shown in Fig. 3.9c. A shift in peak distance of 1.6% is observed, which is in line with the observations in Fig. 3.8d. Recalling the ratio between the experimental dipolar spectra, the observed modification of the distance distribution is mainly due to the suppression of short distances. Contributions due to additional orientations excited are comparably weak.

Overall, we have demonstrated significant improvements in total detection sensitivity by using UWB fast passage pulses when pumping copper. Note that for the particular model system being a copper-nitroxide complex, the achieved modulation depths are unable to compete with typical modulation depths observed in such complexes when pumping nitroxide and observing

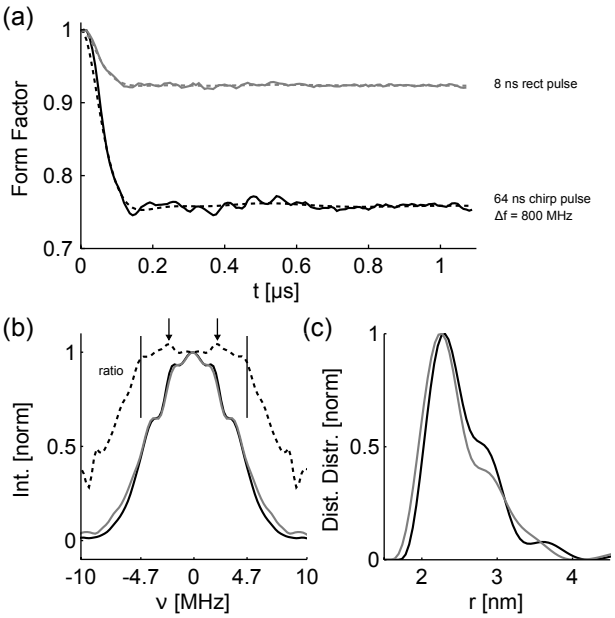

Figure 3.9 – Suppression of large dipolar frequencies by prolonged chirp inversion pulses. (a) Experimental (solid) and fitted (dashed) form factors for a monochromatic rectangular 8 ns pump pulse (gray) and a 64 ns UWB pump pulse (Δf = 800 MHz, black, see also Section A.3) (b) Normalized experimental dipolar spectra for the 8 ns reference pulse (solid gray) and the UWB pump pulse (solid black). The ratio (dashed black) between the two spectra (black divided by gray) is shown to identify low-pass filtering of the time trace due to chirped excitation and excitation of orientations by the UWB pump not excited by the rectangular pulse. (c) Regularized distance distributions corresponding to the 8 ns reference (gray) and the UWB pump (black) revealing the shift to longer distances, mainly due to short distance suppression.

copper [94, 111]. For a metal-nitroxide system, UWB pumping on the metal center thus may not be advantageous compared to pumping on the nitroxide. However, for certain metal centers transverse relaxation at the metal ion may be faster than on the nitroxide in the low-temperature transverse relaxation limit or it may be impossible to attain this limit. To measure long distances in such a metal-nitroxide pair, the nitroxide would be favored as slowly relaxing observer [83]. In distance measurements between copper pairs [110, 112], as well as between pairs of other metal centers, comparable enhancements in modulation depth as observed in this study can be expected when using an UWB pump pulse. Owing to the suppression of short-distance contributions due to the chirped excitation, the pulse length t_p has to be adjusted for the expected distance and the required precision. As demonstrated, even short pulses of 32 ns length can achieve a more than twofold improvement in modulation depth. In situations where orientation selection is critical, UWB pumping may not be the method of choice, but an improvement of the excitation profile by adiabatic inversion may be an option.

3.5 CONCLUSIONS AND OUTLOOK

The presented methodology for efficient ultra-wideband inversion opens up new ways for improving measurement sensitivity and specificity in pulsed EPR spectroscopy. Two possible applications were demonstrated, namely inversion recovery with an adiabatic inversion pulse to suppress spectral diffusion contributions and four-pulse DEER with a fast passage pump pulse to enhance the modulation depth.

One major challenge towards widespread application is the prediction of both the final pulse shape incident at the sample and its effect on the spin system, which critically depends on the accuracy of both the applied hard-

ware model and the spin dynamics simulation. As discussed in this work, the effort required for an accurate hardware model accounting for nonlinearity increases with the complexity of the pulse shape.

In order to facilitate an ordinary quasi-linear hardware model, frequency-swept pulses used in this work had a minimum extent of amplitude modulation. As a consequence, compensation of bandwidth and variations in group delay were achieved by proper modification of the phase modulation function of the pulse. The compensated pulses revealed enhanced performance whenever the amplitude of the pulse agreed to the input condition of the quasi-linear hardware model: a single sinusoidal input having a constant full-scale amplitude. It is worth mentioning that regardless of the additional improvements achieved upon pulse compensation, even uncompensated adiabatic pulses can offer a remarkably large degree of intrinsic bandwidth compensation.

As a next step, the realizability of coherent ultra-wideband excitation and detection will be tested, which demands for development of a dedicated spectrometer. During this process, the aim is to optimize hardware performance and refine hardware modeling up to a precision suitable for prediction of complex manipulations on the spin system.

4

FOURIER-TRANSFORM ELECTRON SPIN RESONANCE WITH BANDWIDTH-COMPENSATED CHIRP PULSES

ABSTRACT

Electron spin echo experiments using chirp pulses at X-band around 9 GHz have been performed with a home-built spectrometer based on an arbitrary waveform generator. Primary echoes without phase dispersion were obtained by employing the Böhlen-Bodenhausen scheme with the refocusing pulse being half as long as the coherence-generating pulse. To account for physical bandwidth limitation by the resonator, the instantaneous sweep rate of the chirps was adapted to the spectrometer's frequency response function, which can be recorded from the sample under study within a few minutes. Such bandwidth-compensated chirp pulses are experimentally shown to achieve an almost uniform excitation bandwidth that exceeds the resonator bandwidth.

This uniform excitation allows for computing frequency-domain spectra by Fourier-transformation (FT) of the echo signal. For a nitroxide in dilute solid solution with a spectral width of 200 MHz, the FT EPR spectrum agrees remarkably well with a field-swept echo-detected EPR spectrum. The overall spectral perturbation for operation far beyond the resonator bandwidth was characterized by acquiring a 700 MHz wide spectral range of a copper(II) EPR spectrum with nearly uniform amplitude with excitation and refocusing pulses of 200 and 100 ns, respectively.

Furthermore, peculiarities were observed in solid-state FT EPR spectra of disordered systems. To understand these peculiarities two-dimensional data sets were acquired that correlate the FT EPR spectrum to inversion recovery or nuclear modulation. The echo envelope modulation experiments reveal echo decay rates increased by enhanced instantaneous diffusion and passage-specific effects in the nuclear modulations. The latter effect can be suppressed by nuclear modulation averaging. Apparent longitudinal relaxation times for a given subset of orientations are influenced by nuclear modulation effects. Proper extraction of orientation-dependent relaxation times thus requires an experimental setup that minimizes the modulations.

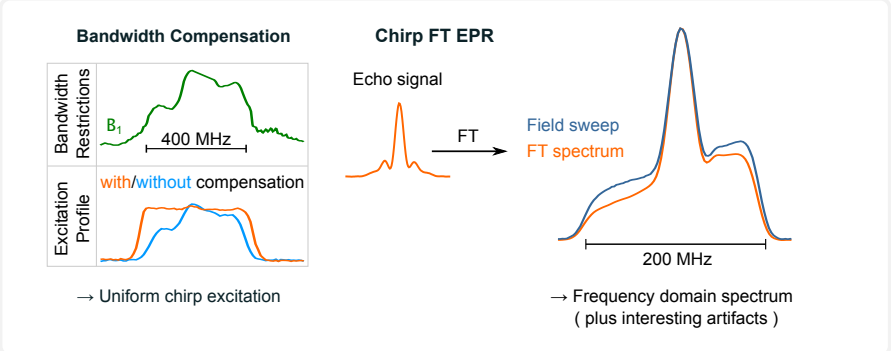

This chapter has been published as [113] and edited for consistency of notation:

A. Doll, G. Jeschke, Fourier-transform electron spin resonance with bandwidth-compensated chirp pulses, J. Magn. Reson. 246, 2014, 18-26

4.1 INTRODUCTION

While Fourier transform (FT) techniques have become the standard for NMR, the situation is quite different in electron paramagnetic resonance (EPR). The main limitation in EPR spectroscopy is that spectral widths exceed the experimentally achievable excitation bandwidth. The solid-state nitroxide spectrum for instance spans over 200 MHz at X-band frequencies around 0.35 T. On an ordinary spectrometer, it is not possible to excite the entire spectrum with monochromatic rectangular pulses. At higher magnetic fields or for transition metal complexes, the situation gets even worse since spectra extend towards the GHz range.

Thanks to extensive optimization of home-built spectrometers [114, 115], a number of FT EPR studies on nitroxides using short and intense pulses could be performed [116–118]. These studies outline possible improvements in resolution and sensitivity by FT EPR techniques. Yet routine application is held back by the particular requirements on spectrometer performance.

This situation is expected to change by using arbitrarily modulated excitation pulses. A key advantage of such shaped pulses over monochromatic pulses is that the instantaneous frequency of the pulse can be varied to achieve a broader excitation bandwidth. Due to the microwave frequencies required for electron spin excitation, an arbitrary waveform generator (AWG) with nanosecond to subnanosecond timing resolution is needed, which became commercially available in the past few years. Shaped pulses well known to the NMR community, namely frequency-swept passage pulses [4] or pulses derived from optimal control theory [5], have thus already been demonstrated for a variety of electron spin excitation schemes (see for instance [11, 12, 15, 74, 119–123]). For FT EPR in particular, optimal control pulses designed for an excitation bandwidth of 200 MHz have been proposed [15].

In this work, we investigate the feasibility of FT EPR with frequency-swept passage pulses, which we refer to as *chirp* pulses. These type of pulses are well known as adiabatic passage (AP) pulses for population inversion on the order of Δf, which is the width of the pulse's frequency sweep [27]. For the FT approach with non-adiabatic fast passage (FP) pulses, the foundations were elaborated with chirp FT NMR [57, 28]: Unlike conventional FT NMR, where the free induction decay is observed, a refocused echo is required for FT spectra with chirps. Furthermore, the non-adiabatic FP excitation and refocusing chirps must have a pulse length ratio of $2:1$. Note that contemporary chirp echo detection schemes in quadrupole NMR often do not rely on a FT and use pulse length ratios different from 2:1 [124, 125].

The complications to implement chirp FT EPR are twofold. First, the impact of the spectrometer hardware on the chirp pulse must be considered [74]. In general, the pulse seen by the spins differs from the pulse digitally programmed in the AWG, which we refer to as the *digital pulse*. Second, spin dynamics differs between experiments with hard monochromatic and chirp pulses [48]. Here, our focus is on the former type of complications in experiments where ultra-wideband (UWB) excitation and detection of coherence is required. Since UWB stands for bandwidths above 500 MHz, we aim for uniform excitation and refocusing of spins over a bandwidth that is larger than the overall physical bandwidth of the spectrometer hardware.

For this task, we will rely on the fairly simple bandwidth-compensated chirp pulses that we proposed previously for UWB population inversion [74]. These compensated chirp pulses feature a numerically tailored rate of change in the pulse's instantaneous frequency and are here referred to as *variable-rate* chirps. As a reference, ordinary non-compensated passage pulses are implemented as *constant-rate* chirps with smoothened pulse edges.

This chapter is organized as follows. In Section 4.2, we describe our home-built AWG spectrometer and the experiments we have performed thereon. Experimental results are presented in Section 4.3: First, we report on excita-

tion profiles for various types of pulses in Section 4.3.1. Second, Section 4.3.2 shows chirp FT EPR spectra of nitroxide, whose spectrum is narrower than the overall physical bandwidth of our spectrometer. Then, a chirp FT EPR spectrum in the UWB regime beyond the overall physical bandwidth is presented in Section 4.3.3. Finally in Section 4.3.4, a three-pulse chirp inversion recovery experiment [126] is implemented. The discussion of our results follows separately in Section 4.4. Complementary details on our experiments are found in the appendix in Chapter B.

4.2 MATERIALS AND METHODS

4.2.1 *Instrumentation*

All experiments were performed on a home-built high-power X-band spectrometer, which employs a heterodyne transceiver with an 8 GHz local oscillator for up- and downconversion combined with broadbanded excitation and detection arms. The resonator used in this work (fully overcoupled Bruker MS3 split-ring) confined the overall 3 dB bandwidth for excitation and detection to roughly 250 MHz around 9.3 GHz. A fast 12 GS/s AWG (Agilent M8190A) generated pulse sequences centered around 1.3 GHz and provided all necessary synchronization triggers.
Resulting spin echoes, oscillating at around 1.3 GHz upon downconversion, were captured and coherently averaged with a 1.5 GS/s digitizer (SP Devices ADQ412). In a subsequent postprocessing step, the digitized echoes were transformed into their analytic representation [127], digitally downconverted to zero frequency and phased in time domain, which resulted in the conventional real and imaginary components acquired in pulsed EPR.
A set of custom MATLAB scripts and executables enabled software control of the spectrometer and data processing. Every experiment was described by means of an event-based data structure, which defined all intended pulses and triggers in combination with an N-dimensional parameter sweep specification. On the basis of this data structure and instrumentational restraints, a set of digital waveforms and corresponding playback instructions were calculated that synthesize the entire experiment on the AWG. Subsequent data transfer to the AWG avoided any reprogramming during an experiment. Once an experiment was started, control was based on counting acquisition events on the digitizer. When cycling of the observation phase was required, it was applied prior to the postprocessing steps related to digital downconversion (see above).
Note that the setup described above experiences on-going development. At the time of publishing this chapter, the spectrometer was not yet optimized for sensitivity and was devoted to studies on model compounds. Further details and comments are given in Section B.1, whereas the state of this spectrometer at the time of writing this dissertation is described in Section 7.1.

4.2.2 *Data evaluation*

Given the real and imaginary components of the echo with proper phase, we either evaluated the zero frequency component, which we refer to as *echo integral*, or the entire FT. In any of the two cases, we used a normalized Chebychev window of 256 points (170 ns) length to mask the echo. The echo integral was then obtained by summation over the real part. For the special case of field-swept echo-detected spectra of nitroxide, 1024 points were used for windowing and summation.
For the FT, we added 256 zero points to the data in time domain. In frequency domain, we applied a linear correction to the spectral phase. The correction was obtained from a linear fit to the spectral phase inside the region from -100 MHz to 100 MHz. The echo spectrum resulted by taking the real part

of the phased-corrected FT. Note that application of a linear phase correction is equivalent to shifting the echo in time domain. Where underlying time domain data is illustrated (see below in Figs. 4.3b and 4.5b), the time shift from the linear phase correction was applied accordingly. Spectral phasing based on the position of the echo maximum and cyclic permutation before the FT led to comparable results at slightly lower time shift resolution, because the spectral phase can encode time shifts below the timestep of the digitizer.

4.2.3 *Hardware characterization*

All necessary calibration of the non-linear excitation arm was based on nutation experiments [74]. The length of the nutation pulse was incremented by 1 ns up to 63 ns. Upon a recovery delay of 500 ns, the observation pulses for the Hahn echo had a length of 16 ns ($\pi/2$) and 32 ns (π), with a delay of 350 ns in between starting pulse flanks.
The field strength ν_1 as a function of the digital pulse amplitude a_S on the AWG, $\nu_1(a_S)$, was calibrated on a grid of 100 points at the resonance frequency of the resonator. A 4^{th} order polynomial fit to $\nu_1(a_S)$, as well as its inverse $a_S(\nu_1)$ truncated at polynomial order 10, eased setup of pulse amplitudes. The obtained calibration curves $\nu_1(a_S)$ were similar to those obtained previously (see Fig. 3.3b).
Amplitude-dependent (magnitude) transfer functions $\nu_1(a_S, f)$ were acquired with frequency steps of 10 MHz over a window of 1 GHz. The magnetic field was co-stepped to retain observation of the spin packet with maximum echo integral. The digital amplitude of the nutation pulse, which influences the shape of the transfer function, was constant throughout the experiment. In the first acquisition, the nutation pulse had always full-scale digital amplitude, which we refer to as $\nu_1(f)$ *at full-scale*. Further transfer functions at different digital pulse amplitudes a_S of the nutation pulse were acquired where needed for pulse compensation at reduced digital amplitude.
The digital amplitude of the frequency-stepped observation pulses was also constant, which lead to attenuation of the echo amplitude as the frequency offset increased. In cases where this attenuation was too strong, smaller 500 MHz frequency windows with adapted observation pulse amplitudes needed to be used.
For all samples used, the acquisition time was roughly 1 min per 100 MHz frequency window. Note that these types of two-dimensional calibration sequences involve many digital waveforms to be synthesized by the AWG. For a 1 GHz frequency window, the total amount of waveform memory is almost 100 MS for each of the two AWG channels (8.3 ms of digital waveforms, 400 MB data in total, 33320 individual waveforms). Our current control software requires an overhead time of 40 s to calculate all these waveforms and transfer them to the AWG.

4.2.4 *Pulse characterization*

For pulse characterization, the influence of pulse parameters on longitudinal magnetization was recorded. The three-pulse sequence was set up as in Section 4.2.3, additionally with a [+(+x) -(-x)] phase cycle on the 16 ns pulse and a specific one-dimensional parameter sweep. Besides parameter sweeps of the pulse to be characterized [74], we also stepped the frequency of the observation pulses. To keep the flip angles of the observation pulses close to their optima at the center frequency of the resonator, digital observation pulse amplitudes were calculated for each observation frequency with help of hardware characteristics $\nu_1(f)$ and $a_S(\nu_1)$. This calculation involved two steps:
First, we computed field amplitudes ν_1 for constant flip angles of observation pulses based on the calibrated amplitude at the center frequency of the resonator and the inverse of $\nu_1(f)$ at full-scale. Second, these field amplitudes

were converted to digital amplitudes by $a_S(\nu_1)$. Due to amplitude dependence of $\nu_1(f)$, pulse amplitudes obtained in this way cannot be optimum at all frequencies, but come at least close to it. Note that in the first step described above, we often deliberately attenuated the calibrated field amplitude by a few percent to avoid overflipping. The frequency-stepped acquisition of echo integrals with and without the pulse to be characterized then resulted in frequency dependent longitudinal magnetization profiles (see below in Fig. 4.2 and in Figs. B.2-B.4). The magnetic field was co-stepped for maximum echo integral.

4.2.5 *Chirp echo pulse sequences*

Each pair of fast passage pulses to generate a chirp echo, FP90 and FP180, had a pulse length ratio of 2:1 [57]. Both pulses had the same frequency modulation $f_i(t)$ scaled by their pulse length. The shape of $f_i(t)$ was determined by the transfer function $\nu_1(f)$ to be compensated, as described in [74]. The sweep width Δf was set to 500 MHz for nitroxide and to 700 MHz for copper(II), always centered at the center frequency of the resonator. Unless otherwise specified, the direction of the frequency sweep was from low frequencies to high frequencies. The tails of the digital pulse envelope $a_S(t)$ were smoothed during 30 ns with a quarter period of a sine. The modulation functions for the pulses applied to nitroxide are illustrated below in Fig. 4.3a. The pulse amplitudes were optimized as described in Section B.3. Note that when referring to the digital pulse amplitude of a chirp pulse, this corresponds to the maximum value of the digital pulse envelope $a_S(t)$.
Unless an echo decay was measured, the FP180 refocusing pulse always followed 408 ns after the beginning of the FP90 pulse. In order to compare chirp echoes to Hahn echoes with hard pulses, the hard refocusing pulse followed earlier by a time $\Delta\tau$ for an evolution time equal to the evolution time of the chirp echo. For chirp echoes, the evolution time $2\tau(f)$ was obtained from $2\tau(f)$ = 816 - $\Delta t(f)$, where $\Delta t(f)$ is the time when the FP90 pulse hits f. For Hahn echoes, we used 2τ = 816 + t_π - $2\Delta\tau$, where t_π is the length of the hard refocusing pulse and $\Delta\tau$ the shift in pulse timing mentioned above.
A [+(+x) -(-x)] phase cycle on the FP90 pulse combined with a [+(+x) -(+y) +(-x) -(-y)] exorcycle [128] on the FP180 pulse was applied. For nitroxide, chirp echoes were acquired with 40 accumulations per point. Where an echo decay was measured by variation of the inter-pulse delay, we acquired 10 accumulations per point. For copper(II), we used 400 accumulations per point.
Three-pulse chirp IR of nitroxide was measured by putting a 128 ns variable-rate AP pulse in front of the FP90 pulse. The recovery delay was incremented from 1 μs to 40 ms in 256 logarithmic steps. Each data point was accumulated 20 times and a fixed relaxation delay of roughly 40 ms followed upon the observation pulses. For comparison, the same IR experiment was observed with frequency-stepped Hahn echoes using 5 accumulations per point. The frequency-stepped observation pulses were programmed as described in Section 4.2.4 and combined with the eight-step phase cycle from above. The frequency step size was 10 MHz within a 200 MHz window for sufficient data points. The T_1 times were extracted as 1/e-times from 3rd order polynomial fits to the logarithm of normalized decay functions.
IR experiments were also acquired with different inter-pulse delays between the observation pulses. For chirp observation pulses, the same acquisition parameters as described above were used. For monochromatic observation pulses, the number of accumulations per point was increased to 15.

4.2.6 *Sample preparation*

TEMPOL was purchased from Sigma-Aldrich and used as received. A 1 mM solution was prepared from a 100 mM stock solution in Milli-Q water,

by diluting to 2 mM and mixing with glycerol (1:1 in volume). Unless indicated otherwise, this sample was used for nitroxide experiments. A 100 μM solution was obtained by further dilution. Experiments on nitroxide were performed at 50 K and with a repetition rate of 100 Hz. For IR experiments, the repetition rate was lower and ranged from 25 Hz to 12.5 Hz.
A 1 mM solution of the hexaquo copper(II) complex was prepared by dilution of copper(II) chloride dihydrate (Sigma-Aldrich) into a water-glycerol mixture (1:1 in volume). All experiments on the hexaquo copper(II) complex were performed at 20 K with a repetition rate of 500 Hz.

4.3 RESULTS

4.3.1 *Flip angles for different pulses*

In order to contrast AP and FP pulses, we recorded the flip angle of a constant-rate chirp against its field strength ν_1. The chirp pulse had a length of 128 ns and its frequency sweep Δf was 500 MHz, centered with respect to the resonator. The inversion efficiency obtained at the center frequency of the resonator is shown in Fig. 4.1. The minimum adiabaticity related to constant-rate chirps is indicated in the upper abscissa. In the AP regime, which heuristically applies for $Q_{\text{crit}} > 5$ [27], a flat inversion plateau was reached. In the FP regime, the flip angle was always below π and depended on ν_1. A $\pi/2$ pulse was obtained for $Q_{\text{crit}} = 0.7$, which we refer to as FP90 pulse.

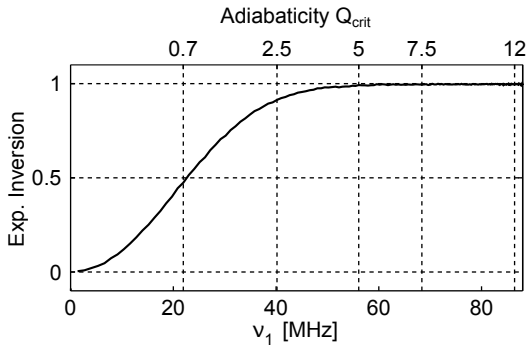

Figure 4.1 – Experimental inversion versus field strength ν_1 for a 128 ns constant-rate chirp with Δf = 500 MHz. Corresponding adiabaticity $Q_{\text{crit}} = 2\pi\nu_1^2 t_{\text{p}}/\Delta f$ indicated in the upper abscissa. The equilibrium echo integral for normalization was obtained in absence of the chirp pulse.

The frequency offset dependence of flip angles is influenced by the (magnitude) transfer function $\nu_1(f)$ of the entire excitation chain. Due to non-linear devices therein, transfer functions depend on digital pulse amplitudes a_{S}. Such transfer functions were measured at four different pulse amplitudes (Fig. 4.2a). The characteristic of the employed resonator with 250 MHz bandwidth showed up in all four curves. In fact, the bandwidth denotes the frequency range within which the coupling to the spins is higher than 71% of its peak value. As is seen in the depicted transfer functions, operation outside this bandwidth still permits a coupling above roughly 50% of the peak value over the entire frequency range shown in the figure. Note that the curve at smallest digital amplitude suffered from significant noise contributions at large frequency offset.
Under these experimental conditions, the frequency dependence of flip angles was measured for passage pulses and monochromatic hard pulses. In the actual experiment, we measured the normalized residual longitudinal magnetization upon the pulse, which is the cosine of the flip angle. The pulses under test were either set up for population inversion or for coherence excitation. Three kinds of pulse shapes were tested: Monochromatic

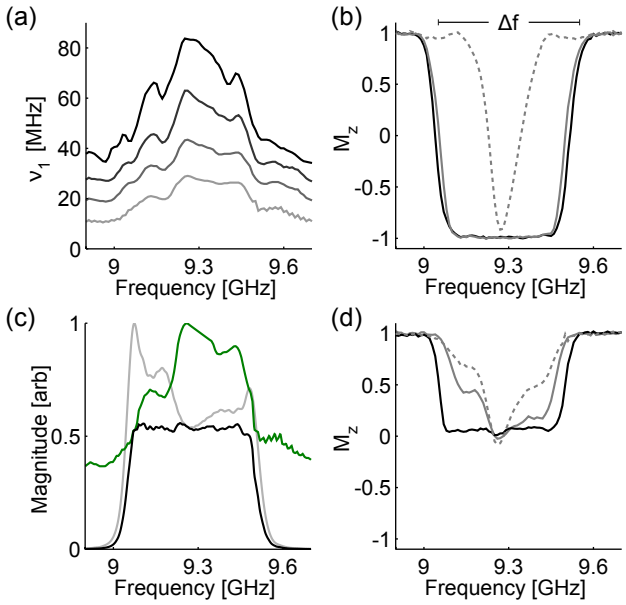

Figure 4.2 – Frequency dependence of normalized residual longitudinal magnetization upon 128 ns long AP and FP pulses with Δf = 500 MHz. (a) Experimental conditions $\nu_1(f)$ measured with the four digital pulse amplitudes a_S = [0.99, 0.44, 0.27, 0.15] for the nutation pulse. (b) π pulse realized with variable-rate chirp (black), constant-rate chirp (solid gray) and hard pulse (dashed gray, 5.5 ns). The variable-rate chirp compensated for $\nu_1(f)$ at full-scale amplitude. (c) Fourier transform magnitude of the digital pulse with variable-rate chirp (light gray), which compensated for the illustrated transfer function $\nu_1(f)$ (green). The product of these two curves shows the Fourier transform of the pulse seen by the spins (black). $\nu_1(f)$ was measured with the digital pulse amplitude of the FP90 pulse (see Section B.3 for optimization protocol). (d) $\pi/2$ pulse realized with variable-rate chirp (black), constant-rate chirp (solid gray) and hard pulse (dashed gray, 2.75 ns). The variable-rate chirp corresponds to the one shown in panel (c).

rectangular pulses, constant-rate chirps and variable-rate chirps. The latter pulses had their chirp rate adapted to an experimental $\nu_1(f)$ profile obtained at an appropriate digital pulse amplitude a_S [74].

The constant-rate AP pulse, which is the pulse from Fig. 4.1 at full-scale, created an almost flat inversion over 350 MHz (solid gray in Fig. 4.2b). The variable-rate AP pulse resulted in a similar profile with a modified transition region at the edges of the inversion band (black in Fig. 4.2b). In comparison to the AP pulses, the hard pulse with a length of 5.5 ns (dashed gray in Fig. 4.2b) had reduced inversion efficiency and bandwidth.

For coherence excitation with FP pulses, the calculation of the variable-rate FP90 pulse is illustrated in Fig. 4.2c. The transfer function $\nu_1(f)$ obtained at a reduced pulse amplitude (green) was used for the adaptation of the chirp rate. The resulting digital pulse, whose FT is shown in light gray, led to an almost flat distribution of pulse energy at the level of the spins (black). The digital pulse modulation functions of this pulse are illustrated in Fig 4.3a. The actual protocol for setting up pulse amplitudes is given in Section B.3.

Residual longitudinal magnetization upon $\pi/2$ pulses is shown in Fig. 4.2d. The variable-rate FP90 pulse from above displayed almost perfect flipping of the magnetization into the xy plane over 350 MHz (black), whereas the constant-rate FP90 pulse (solid gray) and a 2.75 ns long hard pulse (dashed gray) showed non-uniform excitation profiles. When we used a variable-rate FP90 pulse that compensated for $\nu_1(f)$ at full-scale, a less uniform excitation was observed (see dashed black in Fig. B.4a).

4.3.2 *Chirp echo of nitroxide*

For chirp echoes, we used the variable-rate FP90 pulse from Section 4.3.1 for coherence excitation. The refocusing pulse, which we refer to as FP180 pulse, therefore needed to be 64 ns short. The optimization of pulse amplitudes is detailed in the Section B.3 and the resulting pulse modulation functions $a_S(t)$ and $f_i(t)$ are shown in Fig. 4.3a. The FP90 pulse passed the nitroxide spectrum (indicated by the gray area in Fig. 4.3a) in 52 ns. An ordinary Hahn echo with optimized digital pulse lengths of 2.75 ns and 5.5 ns served as a reference.

Real (solid curves) and imaginary parts (dashed curves) in time domain are shown in Fig. 4.3b for the chirp echo (black) and the Hahn echo (gray). In comparison to the Hahn echo, the chirp echo had a 29% larger peak amplitude and a higher bandwidth. Corresponding echo spectra are shown in Fig. 4.3c, using the same color code as Fig. 4.3b. The related spectral phases are shown in Fig. 4.3d. The absence of significant parabolic phase dispersion in the chirp echo indicated successful refocusing. Note that the spectral phase of the chirp echo did not show much influence on whether an exorcycle or an alternating two-step phase cycle was used for the FP180 pulse (data not shown).

Interestingly, the chirp echo spectrum resembled the expected nitroxide spectrum quite well (see below). The Hahn echo spectrum did not provide sufficient bandwidth for the shoulders of the nitroxide spectrum (see up-arrows in Fig. 4.3c). However, the echo integral of the chirp echo was reduced to 94% of the Hahn echo integral, as seen by comparing the zero frequency components (see down-arrow). We found that this reduction was due to differences in echo decay times: The chirp echo decayed faster than the Hahn echo. At a concentration of 100 μM, the echo decay times of chirp and Hahn echoes were comparable (see Fig. B.6).

Note that even though all spin packets refocus at one specific time, the total evolution time among different spin packets is not the same. The underlying reason is that evolution initiates at the time when the FP90 pulse becomes

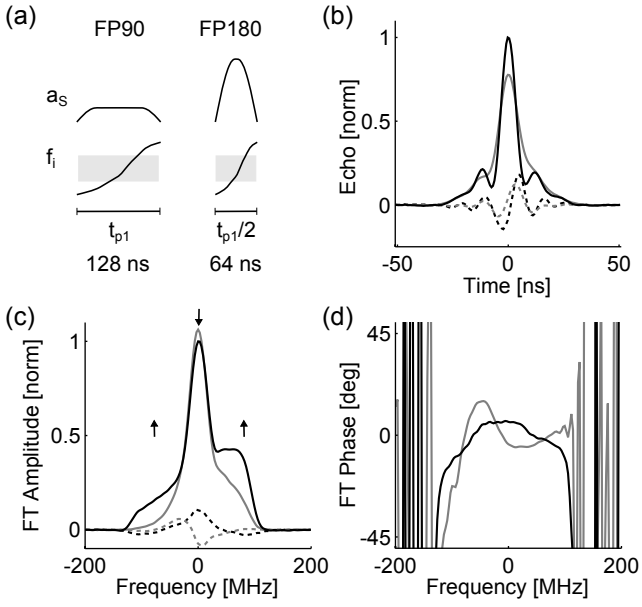

Figure 4.3 – Chirp echo of nitroxide. (a) Digital modulation functions $a_S(t)$ and $f_i(t)$ for the FP90 and FP180 pulse. The gray area denotes the spectral extent of the nitroxide spectrum. (b,c) Real part (solid lines) and imaginary part (dashed lines) of chirp echo (black) and Hahn echo (gray) in time domain (b) and frequency domain (c). The arrows in (c) indicate the performance of the chirp echo relative to the Hahn echo (up-arrow: better performance, down-arrow: worse performance). (d) Frequency domain phase of chirp echo (black) and Hahn echo (gray).

resonant, which was determined by the frequency modulation $f_i(t)$ of the FP90 pulse (Fig. 4.3a). Here, the maximum difference in evolution time was 52 ns, which lead to significant distortions in chirp echo spectra. This was best observed when chirp echo spectra were recorded with different inter-pulse delays. Fig. 4.4a shows such spectra along the abscissa versus evolution times of the central nitroxide line. Note that FT along the second dimension can provide a 2D FT EPR/ESEEM spectrum. As is readily seen, the nuclear modulation pattern had a phase shift, which increased with frequency. For a frequency offset of $\pm$100 MHz, the phase displacement in nuclear modulation was found to be 34 ns, based on FT along the second dimension. The passage time of the FP90 pulse based on the frequency modulation $f_i(t)$ for this frequency window was 33 ns, which agrees to the 34 ns above within experimental uncertainty. Interestingly, the spectral phase showed a dependence on the inter-pulse delay (see Fig B.5a), which was also observed with hard pulses (data not shown).
In order to remove such frequency-encoded nuclear modulations from chirp echo spectra, spectra were averaged over one nuclear modulation period. In Fig. 4.4b, this averaged chirp echo spectrum (solid black) is compared to the conventional field-swept spectrum converted to a frequency axis (light gray). The ratio between these two spectra (dashed black) shows the overall perturbation of the chirp echo spectrum. The transfer function $\nu_1(f)$ at full-scale (green) indicates that the perturbation was to a large extent due to the detection efficiency of the employed resonator. Actual flip angles of FP90 and FP180 pulses, which also perturb chirp echo spectra, are shown in Fig. B.4.
Chirp echoes were also measured with constant-rate chirps. The corresponding spectra showed more pronounced perturbation than those presented above due to non-uniform excitation (see Fig. B.7).

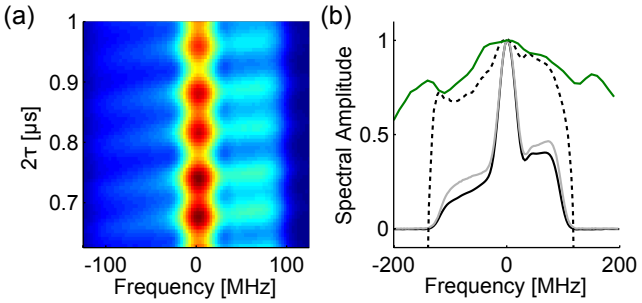

Figure 4.4 – Offset-dependent evolution time and comparison with field-swept spectrum. (a) Chirp echo in frequency domain measured for different evolution times 2τ, where τ is the evolution time of the central nitroxide line between the two pulses. (b) Chirp echo in frequency domain averaged over one nuclear modulation period (solid black) and conventional field-swept echo-detected spectrum converted to a frequency axis (light gray). The ratio between the two spectra (dashed black) shows the perturbation of the chirp echo spectrum, which appears to be dominated by the resonator that is indicated by $\nu_1(f)$ obtained at full-scale (green).

4.3.3 *Chirp echo of copper(II) ions*

Chirp echoes of copper(II) ions were acquired to gain further insight into hardware-induced perturbations of chirp echo spectra. The field position was therefore adjusted to a g-value of 2.36, where the copper(II) spectrum was almost flat within 200 G (see inset in Fig. 4.5a). Under these conditions, the hexaquo copper(II) complex can be considered as a model for an inhomogeneously broadened line with infinite width. Optimization of FP90 and FP180 pulses with Δf = 700 MHz resulted in pulse lengths of 200 ns and 100 ns, respectively (see Fig. B.4).

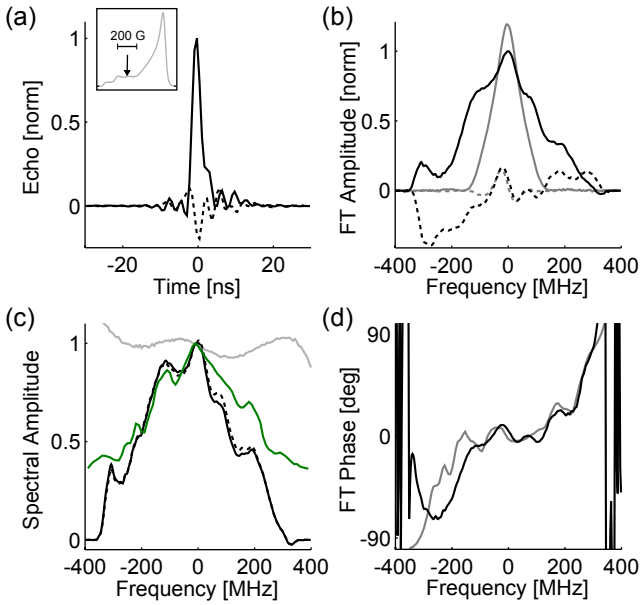

Figure 4.5 – UWB chirp echo of copper(II). (a) Real part (solid) and imaginary part (dashed) of chirp echo in time domain. Field-swept echo-detected spectrum (light gray) and observation position (arrow) indicated in the small inset. (b) Real part (solid lines) and imaginary part (dashed lines) of chirp echo (black) and Hahn echo (gray) in frequency domain. (c) Chirp echo in frequency domain averaged over several nuclear modulation periods (solid black) and conventional field-swept echo-detected spectrum converted to a frequency axis (light gray). The ratio between the two spectra (dashed black) shows the perturbation of the chirp echo spectrum, which appears to be dominated by the resonator that is indicated by $\nu_1(f)$ obtained at full-scale (green). (d) Frequency domain phase of chirp echo (black) and approximative instrumental phase (gray), which is twice the phase $\hat{\beta}(f)$ reconstructed from $\hat{\nu}_1(f)$ obtained at full-scale (see Section A.1 for details).

The resulting chirp echo in time domain was a short transient with its main peak confined within 7 ns. Fig. 4.5a shows both real (solid) and imaginary components (dashed). In Fig. 4.5b, the chirp echo spectrum (black) is compared to a Hahn echo spectrum (gray). The Hahn echo spectrum was acquired with optimized digital pulse lengths of 2.75 ns and 5.5 ns. The Hahn echo spectrum had a full width at half maximum of 109 MHz and a steep decay, whereas the chirp echo spectrum gave a signal over almost the entire 750 MHz detection window of the digitizer. Despite the much smaller bandwidth of the Hahn echo, its zero frequency component was 19% stronger than for the chirp echo. In analogy to our results with nitroxide, we found a faster echo decay for the chirp echo as compared to the Hahn echo (data not shown).

Due to the 200 ns long FP90 pulse, the chirp echo spectrum was substantially affected by nuclear modulation (see Fig. B.5c). Upon nuclear modulation averaging (solid black in Fig. 4.5c), the spectrum underwent apparent changes for negative frequency offsets. Fig. 4.5c also shows the comparison with the field-swept spectrum (light gray). Because of the almost flat field-swept spectrum, the ratio between the spectra (dashed black) did not deviate much from the chirp echo spectrum. The chirp echo spectrum shape was therefore mainly due to experimental artifacts. The dominating contribution was the characteristic of the resonator, which is approximated by $\nu_1(f)$ at full-scale (green). Note also that the FP90 and FP180 pulses had only moderate excitation uniformity, when compared to the results with nitroxide in Section 4.3.2 (see Fig. B.4).

Besides distortions in the line shape, chirp echo spectra on copper(II) also appeared with a rather distorted phase. The spectral phase associated to Fig. 4.5b is shown in black in Fig. 4.5d. Unlike our observations on nitrox-

ide, we did not observe strong changes in the spectral phase of copper(II) upon nuclear modulation averaging (see Fig. B.5b). The overall instrumental phase accumulated by the chirp echo was approximated by taking twice the phase $\hat{\beta}(f)$ reconstructed from $\hat{v}_1(f)$ obtained at full-scale, as described previously [74]. As shown in Fig. 4.5d, this approximate instrumental phase (gray) and the spectral phase of the echo shared common features, especially for positive frequency offsets.

4.3.4 *Chirp IR*

In order to resolve the anisotropy in longitudinal relaxation of nitroxide [105], we performed IR with chirp pulses. The inversion pulse was a variable-rate AP pulse, as shown previously in Fig. 4.2b. The pair of FP pulses for the chirp echo followed the inversion pulse upon a logarithmically stepped recovery delay. For comparison, the relaxation anisotropy was also observed using frequency-stepped Hahn echoes.

When we used FP90 and FP180 pulses as described in Section 4.3.2, the characteristic *W-shape* of the relaxation anisotropy could easily be identified by just looking at echo spectra versus recovery delay (compare Fig. 4.6a). Upon comparison to conventional Hahn echo data, however, we observed discrepancies in the decay characteristic. Closer inspection revealed that these discrepancies depend on the evolution time τ of the central nitroxide line in between the FP90 and FP180 pulse.

The decay characteristic obtained with the same τ as in Section 4.3.2 is shown in Fig. 4.6a. The echo spectra along the abscissa were all normalized by the equilibrium echo shape, which was obtained by averaging the last 10 data points (recovery delays between 27 ms and 40 ms). T_1 times were extracted as $1/e$-times from polynomial fits to the logarithm of the decay function. The ratio between T_1 times obtained with chirps and Hahn echoes is indicated by the black curve in Fig. 4.6b. Except for the ratios at offset frequencies of 90 MHz and 100 MHz, the deviations in T_1 were below $\pm 3\%$. For an observation scheme with the above mentioned evolution time τ prolonged by 15 ns on the contrary, the deviations in T_1 were significantly larger, as indicated by the gray curve in Fig. 4.6b. Relaxation appeared considerably faster at offset frequencies of ± 30 MHz (ΔT_1 of -8.9% and -7.4%). At an offset frequency of -10 MHz, relaxation appeared slower (ΔT_1 of 6.8%).

Note that at the 15 ns longer τ value, the reduction of the spin echo due to nuclear modulations was close to its maximum. Experimentally, this τ

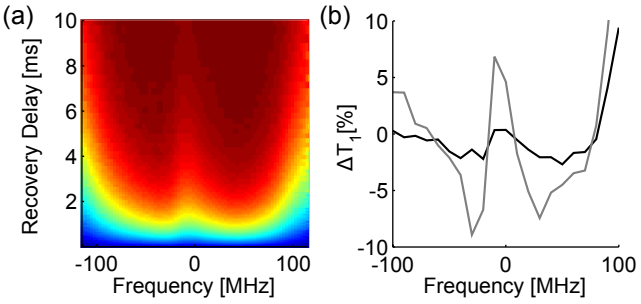

Figure 4.6 – Chirp inversion recovery of nitroxide. (a) Normalized chirp echo spectra versus recovery delay observed with FP90 and FP180 pulses from Section 4.3.2. The equilibrium spectrum for the normalization was obtained by averaging the last 10 data points, which had recovery delays between 27 ms and 40 ms. (b) Ratio in T_1 times obtained as $1/e$-times from chirp echo and Hahn echo data (chirp echo T_1 divided by Hahn echo T_1). The black curve corresponds to the data shown in panel a). The gray curve corresponds to data obtained with a 15 ns longer evolution time in between the FP90 and FP180 pulse. The resolution along the frequency axis is 10 MHz due to the frequency step size of the Hahn echo.

value was implemented by flipping the direction of the frequency sweep of all involved passage pulses. A more direct approach is to record IR data for a set of inter-pulse delay offsets $\Delta\tau$, as shown in Fig. 4.7. In order to include several nuclear modulation periods, $\Delta\tau$ was incremented up to 150 ns in steps of 6 ns. The resulting percentage variation in T_1 times (right inset) was periodic in $\Delta\tau$ and in line with nuclear modulations observed at the central frequency (left inset). T_1 times extracted at $\Delta\tau = 0$ served as a reference to calculate the indicated percentage change. The blue areas indicate where relaxation appeared faster, whereas the red areas indicate slower relaxation. Two distinctive features can be identified:
First, at those $\Delta\tau$ where the echo modulation was maximum, the shape of ΔT_1 was comparable to the gray curve in Fig. 4.6b: faster relaxation at ± 30 MHz, slower relaxation at -10 MHz. The higher spectral resolution in Fig. 4.7 actually reveals four peaks within this region at frequencies of -26, -8, 20 and 32 MHz. Second, the shoulders of the spectrum had large variation in T_1. At these positions, the $\Delta\tau$ times of maximum variation in ΔT_1 also coincided with maximum modulation of the echo at the corresponding offset frequency (data not shown). In order to see how these changes in T_1 influence the decay characteristic, a set of normalized echo spectra for two different $\Delta\tau$ times is given in Fig. B.8d.
At a frequency offset of -26 MHz, where we obtained large modulations in T_1 with $\Delta\tau$ using chirp echoes, the same experiment was observed with Hahn echoes. The resulting change in T_1 as a function of $\Delta\tau$ with the Hahn echoes was on the order of 4% and thus more than a factor of two smaller than for the chirp echoes (see Fig. B.8a,b). The T_1 times were actually the same for those $\Delta\tau$, where nuclear modulation was at its minimum. Interestingly, the nuclear modulations observed with Hahn echoes at this particular frequency offset were also less pronounced than with chirp echoes (see Fig. B.8c). At this frequency offset, T_1 times obtained with chirp or Hahn echoes therefore deviated where the observation scheme lead to a reduced echo amplitude due to nuclear modulation.

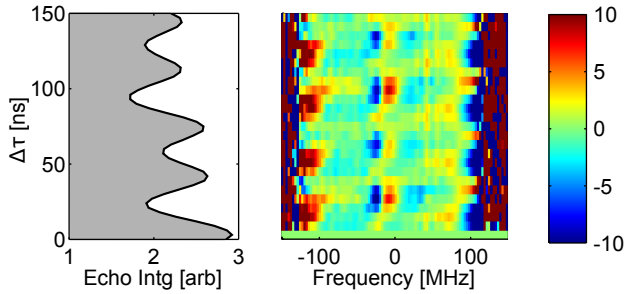

Figure 4.7 – Dependence of T_1 times extracted from chirp echo spectra on inter-pulse delay. The left inset shows the nuclear modulation observed on the center of the nitroxide spectrum. $\Delta\tau$ is the offset of the inter-pulse delay with respect to the timing described in Section 4.2.5. The right inset shows the variation of T_1 times versus frequency offset and $\Delta\tau$. The increment for $\Delta\tau$ was 6 ns. The color coding on the right hand side indicates the percentage change in T_1 times in relation to T_1 times for $\Delta\tau = 0$. Blue areas denote faster relaxation. Red areas denote slower relaxation.

4.4 DISCUSSION

4.4.1 *Excitation uniformity of passage pulses*

Based on our results in Section 4.3.1, we conclude that best spectral excitation uniformity is achieved with variable-rate chirps that compensate for bandwidth limitations of the spectrometer. The reason behind this is that the pulse compensation maximizes the frequency window, for which the

adiabaticity factor remains constant.
This concept is known as *offset-independent adiabaticity* and the majority of passage pulses applied in NMR achieve such offset-independent adiabaticity to a large extent. A strict independence on offset is often not guaranteed due to the pulse modulation functions at the pulse edges. One exception that shows a strict offset-independence is the hyperbolic secant pulse in its non-truncated form, which is well known for its frequency selectivity [45, 46]. Note however that all these pulses assume a flat transfer function $\nu_1(f)$, which is often not well fulfilled in pulsed EPR due to limited bandwidth of the resonator. In such cases, the implications of using non-compensated pulses depend on whether one wants to invert population or excite coherence:
For population inversion, a highly uniform inversion may be achieved for any passage pulse of sufficient adiabaticity (see Fig. 4.2b). This is due to the well known robustness of adiabatic pulses with respect to the driving field ν_1, which can be recognized by the vanishing derivative of the inversion efficiency with respect to both ν_1 and adiabaticity in Fig 4.1. The main advantage of compensated variable-rate AP pulses is that for adiabatic inversion over a certain frequency window, the pulse length can be reduced [74].
For coherence excitation on the contrary, uniform excitation may *only* be achieved with compensated FP pulses. For any FP90 pulse, the derivative of the flip angle with respect to both ν_1 and adiabaticity is fairly large (see for instance Fig. 4.1 or [28, 129]). Unlike a non-compensated AP pulse, a non-compensated FP pulse therefore has no intrinsic robustness towards $\nu_1(f)$. Pulse compensation does not alter this lack of robustness: Variable-rate FP90 pulses remain sensitive to spatial field inhomogeneities inside the resonator or inaccuracies in the transfer function $\nu_1(f)$. To the best of our knowledge, adiabatic plane rotations [47, 130, 4] provide ν_1-insensitive coherence excitation based on passage pulses, however at the expense of spectral excitation uniformity.
In order to make use of the presented variable-rate pulses in both the AP and FP regime, one should be aware of their limitations:
First, the pulse compensation works only for sufficiently smooth transfer functions $\nu_1(f)$ due to simplified treatment of pulse dynamics [74]. Pronounced narrowband features in the transfer function $\nu_1(f)$, such as standing waves in the microwave excitation arm, should therefore be minimized. Whether a given $\nu_1(f)$ is smooth enough can actually be judged from the FT of the pulse as seen by the spins, which is the product between the FT of the digital variable-rate chirp and $\nu_1(f)$ (black in Fig 4.2c). Further information is given in Section B.2, together with data where experimental conditions were not suitable for pulse compensation.
Second, the sinusoidal smoothing of the pulse edges is a critical factor (see [28]), which is applied without any formal connection to the calculated frequency modulation $f_\mathrm{i}(t)$. The parameter that determines the time scale of the pulse smoothing, t_rise, therefore may require optimization where frequency selectivity is important. We often skip this step and use a fixed t_rise of 30 ns. In principle, one could incorporate the amplitude smoothing into the calculation of the frequency modulation $f_\mathrm{i}(t)$ for improved selectivity, which however requires some consideration of compression of the pulse amplitude due to non-linear devices in the spectrometer.
Third, coherence excitation with a single FP pulse may result in multiple quantum coherence due to spin-spin coupling [48]. As such interference effects can be avoided by means of a passage that is fast with respect to the coupling, it is presumed that a spectrometer which can provide short and intense FP pulses is advantageous.
Despite the mentioned shortcomings, the performance of these fairly simple variable-rate chirps is promising for coherence excitation in the UWB regime. While there is still room for improvement with respect to compensation of passage pulses for limited bandwidth, the sensitivity to spatial

inhomogeneities in ν_1 may pose a performance limitation. For such cases, it is expected that better performance could be achieved by numerically optimized pulses [131] with dedicated bandwidth compensation [15, 85].

4.4.2 *Chirp echoes*

In contrast to the situation during excitation, compensation of limited bandwidth is not possible during detection. As seen in the results, this leads to apparent distortions in experimental chirp echo spectra. In other words, one does not only acquire the wanted frequency domain response of the spin system under study, but also that of the spectrometer's electrical network topology. To quantify these unwanted distortions, one needs to consider the transfer function from the signal induced by the spins inside the resonator to the digitizer. In the present work, an experimental characterization of this detection transfer function was omitted. Instead, the experimentally obtained excitation transfer function $\nu_1(f)$ at full-scale was used to approximate the detection transfer function. The justification of such an approximation is as follows:
On our spectrometer, the resonator imposes the dominant bandwidth limitation. If only the spectrometer's hardware is considered, one would therefore expect excitation and detection transfer functions to be very similar. This argument also holds for the inductively coupled spin system, since this kind of coupling to the spins is reciprocal [132].
Accordingly, experimental chirp echo spectra are in the best case only distorted by the detection transfer function. Any further distortions are due to imperfections of the excitation pulses or due to peculiarities of the spin system. In order to maintain a high sensitivity, these distortions should be minimized. In the best experimental chirp echo spectrum obtained of nitroxide (see Fig. 4.4b), there is indeed only slight attenuation of the spectrum beyond that dictated by the resonator. In the UWB spectrum of copper(II) (see Fig. 4.5c), distortions are more pronounced. From the available experimental data, we find two hardware-related sources for such distortions:
First, the excitation profile of the FP180 refocusing pulse is not as uniform as the FP90 excitation pulse (see Fig. B.4). This is because the FP180 pulse requires a larger digital amplitude than the FP90 pulse and is shorter by a factor of two. The shorter pulse length leads to more pronounced artifacts at the pulse edges [133] and a less accurate pulse compensation. The larger digital amplitude of the FP180 pulse leads to further problems in the compensation, because the FP180 pulse compensates for the transfer function seen for the FP90 pulse of lower amplitude, which differs from the actual one.
Second, transfer functions also result in a phase shift that perturbs the spectral phase and thus reduces the amplitude of the echo spectrum. Since the excitation pulses are not compensated for any phase shifts, the phase shifts related to excitation and detection add up to an overall instrumental phase. The agreement between instrumental phase and spectral phase observed for copper(II) in Fig. 4.5d is quite remarkable. Whenever such an agreement is achieved, the quality of UWB chirp echo spectra can be improved significantly by a correction with this instrumental phase. Note however that there are several reasons why the agreement could be poor in practice:
First, the approximated instrumental phase may be inaccurate. Second, additional phase shifts may be introduced in between excitation by the FP90 pulse and echo formation. Possible sources are for instance spin-spin couplings [48, 28] or inhomogeneities in ν_1 [130]. In fact, we found phase shifts due to nuclear modulation in nitroxide FT spectra for both chirp pulses (Fig. B.5a) and hard pulses. These are presumably due to admixture of forbidden electron-nuclear transitions, which introduce coupling between remote frequency components (see [116, 134, 135] and Section 4.4.3).
In principle, the overall instrumental phase could be considered in the calcu-

lation of excitation pulses. Since the resonator phase adds up twice, these pulses would excite the spins with the inverse resonator phase. We currently do not see much reason for such a *double compensation* of the phase. Only in cases where the phase perturbation results in considerable reduction of pulse adiabaticity [74], a compensation of the excitation phase could be required. Note however that in such a situation, the spectrometer anyway may not yield the performance required for FT spectra with a minimum amount of distortions (see Section B.2).

Besides the hardware-related distortions, one should note that excitation with chirp pulses is different from excitation with hard pulses. The presence of nuclear modulation along the frequency axis in chirp echo spectra is one example that could readily be observed in the results (see Fig. 4.4b) and accounted for by nuclear modulation averaging. For distortions related to interference during passage [48], it appears that these are too small to be distinguished from hardware-related distortions in chirp echo spectra presented in Sections 4.3.2 and 4.3.3. We expect that there are different sample and pulsing conditions under which such effects will be more prominent.

A related point is the faster decay of the chirp echo (see Fig. B.6), which is presumably due to enhanced instantaneous diffusion caused by the larger bandwidth of the chirp echo (see [98, 136]). This faster decay is thus related to the echo bandwidth and not specific to chirp excitation.

In summary, we note that there is an inevitable perturbation of chirp echo spectra by the resonator. As a consequence, a quantitative interpretation of FT line shapes on a routine basis is presumably too involved and field sweep approaches may still be preferable for that. However, in pulsed EPR experiments, the echo spectra add an additional dimension to the experiment. In such experiments, the actual shape of the echo spectrum may be normalized by a reference to ease identification of changes in the echo. Any static distortions present in the echo spectra are removed by such a normalization. One such example is orientation selection of nuclear modulations (see also 2D FT EPR [116]) and another one the chirp IR experiment discussed in the following section.

4.4.3 *Chirp IR*

The chirp IR experiments in Section 4.3.4 reveal possible peculiarities that could arise with passage pulses. It is in principle not surprising that there can be a dependence between the relaxation characteristic and the nuclear modulation imposed on the observer echo because of admixture of forbidden transitions in FT spectra [116, 134, 135]. The resulting relaxation characteristic is rather complicated and a quantification is beyond the scope of the present work.

Empirically, our current results suggest that it is advisable to observe chirp IR experiments using an inter-pulse delay where nuclear modulation is minimized. Since the evolution time throughout the spectrum varies according to the frequency modulation $f_i(t)$ of the FP90 observation pulse, it is not possible to fulfill this for all excited spins simultaneously. For some offset frequencies, an uncertainty in T_1 times thus needs to be accepted.

In ordinary IR experiments, where soft rectangular observation pulses are used [102], nuclear modulations are usually suppressed due to reduced observation bandwidth. This would also partially explain the smaller nuclear modulation depth observed with the rectangular observation pulses (Fig. B.8c).

In general, the impact of nuclear modulation on T_1 is unlikely to be known a priori. The size of the uncertainty in T_1 therefore cannot be predicted. Since we calibrated the uncertainty of our nitroxide experiments (Fig. 4.7), we conclude that it is possible to obtain T_1 times of fairly sufficient accuracy within the significant part of the nitroxide spectrum. The deviations at the far shoulders of the spectrum, where the signal in any case gets rather small,

can be tolerated and considered separately where really necessary. Note that on a spectrometer with lower excitation power and bandwidth, this may not be the case anymore due to longer pulses needed.
Along the same line, the requirement for minimum nuclear modulation throughout the spectrum gets more difficult to fulfill in the UWB regime, where the passage time of the FP90 pulse is prolonged. In the chirp refocusing scheme utilized in this work [57], the FP90 pulse has actually a rather low power to allow for the shorter FP180 pulse. Alternative chirp refocusing schemes that allow for FP90 pulses of higher power [124], and thus of shorter length, may be advantageous for such purposes.

4.5 CONCLUSIONS

Our work demonstrates that it is possible to achieve uniform spin excitation beyond the overall physical bandwidth of the spectrometer. To the best of our knowledge, the presented bandwidth-compensated chirps so far provide the most viable approach for such excitation. The associated experimental *overhead*, namely the in situ characterization of actual hardware perturbations with the sample under study inserted, is rather moderate on a modern AWG spectrometer.
For FT EPR, these pulses minimize the overall impact of physical bandwidth limitations on experimental FT spectra. As a consequence, the net detection bandwidth is increased compared to previous FT EPR approaches with monochromatic pulses [115] and broader spectra can be acquired within a single shot. The absolute limitations of this approach in terms of signal-to-noise ratio and dynamic range remain to be investigated.
Aside from this technical feasibility of chirp FT EPR, which still leaves room for improvement on pulse performance and instrumentation, a key challenge for spectroscopic application is imposed by spin dynamics. In particular, our results point to rather intricate effects due to nuclear modulation in FT spectra of powders, which are partially triggered by the frequency-swept excitation. Our current activities include disentanglement of such effects.
Yet another complication are short T_2 times, as encountered for liquids at room temperature. If chirp pulses are used in this regime, their duration may become comparable to T_2. Accordingly, one would expect more stringent limitations for chirp pulses applied to such systems than for the short and intense rectangular pulses demonstrated previously [115].

5

SENSITIVITY ENHANCEMENT BY POPULATION TRANSFER IN GD(III) SPIN LABELS

ABSTRACT

In order to enhance echo signals observed with selective pulses, equilibrium populations of the energy levels of $S = 7/2$ Gd(III) spin labels are rearranged with frequency-swept passage pulses. To transfer population from as many energy levels as possible, the 2 μs long passage pulses range over more than 1 GHz. Application of this technique at Q-band frequencies to three different Gd(III) complexes and spin dynamics simulations reveal large signal enhancements beyond 100% for Gd(III) complexes with zero-field splitting parameters below 1 GHz. For complexes with larger splittings, experimental enhancements are on the order of 90%. Moreover, population transfer is combined with distance measurements on a model system with a pair of Gd(III) ions. As a result, a signal enhancement of 85% is achieved without inducing changes in the obtained distance information. Besides this enhancement by population transfer, a dipolar modulation depth of 9% is demonstrated, which results in a total enhancement of 3.3 with respect to data obtained with monochromatic rectangular pulses. The limitations of the population transfer technique are discussed. In particular, the extraordinary broad pulse bandwidths caused heating effects and pulse distortions, which constrain the pulse length and thus the achievable signal enhancement.

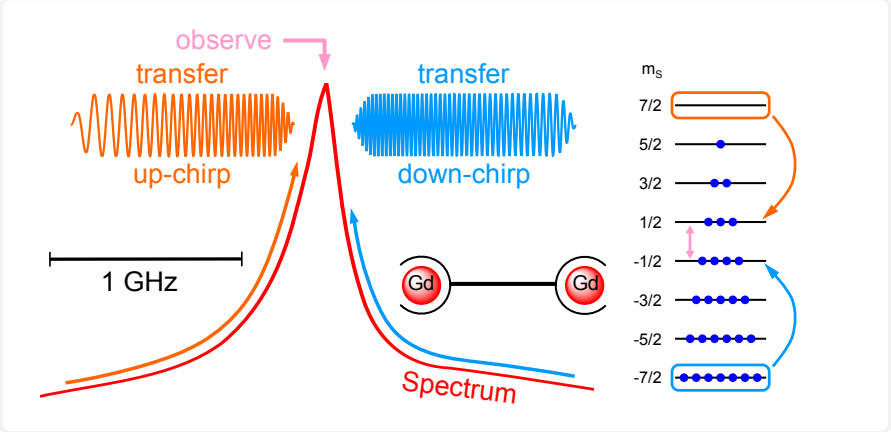

This chapter has been published as [137] and edited for consistency of notation:

A. Doll, M. Qi, S. Pribitzer, N. Wili, M. Yulikov, A. Godt, G. Jeschke, Sensitivity enhancement by population transfer in Gd(III) spin labels, Phys. Chem. Chem. Phys. 17, 2015, 7334-7344

where M. Qi and A. Godt synthesized the Gd-rulers (Section 5.3.1.1), S. Pribitzer provided the MATLAB code for propagation of density matrices (Section 5.3.4) and initial simulation routines. N. Wili incorporated numerical perturbation theory and contributed to the optimization of the chirp pump pulse in Section 5.4.3 (see also Chapter 6). M. Yulikov provided routines and expertise to model Gd(III) spectra and propagation of density matrices in the laboratory frame.

5.1 INTRODUCTION

Pulsed EPR spectroscopy has found broad application in measurement of nanometer distances in disordered systems via the dipolar spin-spin interaction [68, 138]. In the most common approach, pairs of nitroxide-based spin labels are attached to specific sites of a biomacromolecule for obtaining pairwise distance information. The approach has also been applied to different spin labels and paramagnetic cofactors.

One recently introduced spin label is based on the Gd(III) ion [139], which bears a high spin of $S = 7/2$. Accordingly, these labels feature a zero-field splitting (ZFS) that leads to fairly broad EPR spectra. Out of all seven single-quantum transitions, the central $1/2 \leftrightarrow -1/2$ transition (CT) is the most relevant transition for Gd(III)-based distance measurements, since its spectral width is the least affected by the ZFS.

While there is an ongoing effort to resolve all possible peculiarities due to the ZFS with respect to distance determination, a number of studies has already proven this approach to be especially well suited for magnetic fields above 1 T [140]. The particular advantages of Gd(III) at high fields, as compared to nitroxide labels, are the absence of orientation selection, the higher transition moment for selective excitation, and faster longitudinal relaxation times. Another advantage is the stability of Gd(III) under reducing conditions, which recently facilitated distance measurements inside cells [141, 142]. Since spin concentrations in labeled biosystems may be in the lower μM range and access to distances beyond 6 nm is desirable, sensitivity is a critical factor to be considered [143].

In this work, we address one specific sensitivity aspect of experiments on such $S = 7/2$ systems, namely the circumstance that primarily one of the seven transitions contributes to the observed signal, whereas the other six transitions remain mostly unobserved. In the majority of cases, this observed transition will be the CT. The experiment thus does not use the polarization available on the six other transitions. Towards higher fields and lower temperatures, equilibrium polarization is larger for the lower lying unobserved transitions, at the expense of polarization on the relevant CT. Since this problem arises in many kinds of experiments on half-integer high-spin systems, in particular also for quadrupolar nuclei, a solution was proposed a while ago: Population transfer to redirect unobserved polarization to the CT [144–146].

For efficient population transfer to the CT, frequency-swept passage pulses in the adiabatic regime are required [145]. While such pulses have a long history in NMR spectroscopy [27, 4], the appearance of passage pulses in EPR spectroscopy is rather recent thanks to the availability of fast waveform generators [74, 119, 113, 147]. One challenge for the application of such arbitrarily shaped pulses in EPR is the finite resonator bandwidth, which prompted various pulse compensation techniques [15, 74, 122, 93]. For passage pulses in particular, uniform excitation beyond the resonator bandwidth has been demonstrated [74, 113].

Instead of a frequency-swept chirp pulse, passage can also be realized by a monochromatic pulse combined with a fast field-sweep. The technical challenge related to fast field-sweeps are transient eddy currents [148]. Using this technique, a proof-of-principle demonstration of electron spin population transfer on Mn(II) ions with $S = 5/2$ was performed [149]. The longitudinal relaxation time of Mn(II) allowed for pulse durations of several hundreds of microseconds. For Gd(III), however, longitudinal relaxation would restore thermal equilibrium during such long pulses.

In this work, we aim for population transfer in Gd(III) by combining state-of-the-art high-power Q-band instrumentation [150] with ultra-wideband (UWB) pulse shaping. We start in Section 5.2 by giving a brief description of the basic theory. For a more detailed theoretical description, the interested reader is referred to corresponding review literature on quadrupole

NMR [146] and references therein. In Sections 5.2.1 and 5.2.2, spin dynamics simulations of population transfer in a single crystal as well as in a powder are presented. These simulations intend to introduce the reader to the actual experimental situation, where powder spectra extend over several GHz. The simulation method, together with all necessary experimental methods and investigated samples, is described in Section 5.3.
Experimental results including discussion are presented in Section 5.4. First, key experimental characteristics which influence the polarization enhancement are described (5.4.1). Then, the role of the Gd(III) ZFS parameters is examined by studying the population transfer in three different Gd(III) complexes (5.4.2). Finally, the population transfer experiment is combined with the four-pulse DEER experiment for sensitivity enhancement of Gd(III) distance measurements (5.4.3).

5.2 THEORY

For systems with effective spin greater than 1/2, the (second-order) zero-field splitting (ZFS) Hamiltonian is given by

$$\hat{\mathcal{H}}_{\mathrm{ZFS}} = \vec{\hat{S}}^T \mathbf{D} \vec{\hat{S}} \tag{5.1}$$

with $\mathbf{D}$ being the traceless ZFS tensor with principal components D_{xx}, D_{yy} and D_{zz}, parametrized by $D = 3D_{zz}/2$ and $E = (D_{xx} - D_{yy})/2$. The asymmetry parameter E can take values between 0 and $D/3$, where $E = 0$ denotes axial symmetry and $E > 0$ orthorhombic symmetry. For present consideration, the effective Hamiltonian contains only ZFS and Zeeman terms for a single (half-integer) spin $S > 1/2$. If the ZFS parameters D and E are small compared to the Zeeman splitting ω_0, perturbation theory may be applied to derive energy levels. Analytical formulas for energy levels derived up to third-order perturbation based on irreducible tensor expressions of Eq. (5.1) were reported elsewhere [151, 152].
In the high-temperature approximation $kT/\hbar \gg \omega_0 \gg D$, the population differences between adjacent energy levels have a constant value ΔN, such that the polarization P_0 is the same for all transitions. The population difference between the lowest energy level and the highest energy level is therefore $2S \cdot \Delta N$. For ω_0 = 35 GHz and T = 10 K, there is actually a slight preference of the lower energy levels, which is neglected to simplify the present analysis (see also Section C.6).
These equilibrium populations may be manipulated by means of selective population inversion: A π pulse applied to the transition $m_s \leftrightarrow m_s - 1$ leads to a polarization increase on the neighbor transitions, $m_s + 1 \leftrightarrow m_s$ and $m_s - 1 \leftrightarrow m_s - 2$, from P_0 to $2P_0$. By combining several selective population inversions [145], the maximum polarization achievable on one particular transition is $2S \cdot P_0$. This means that the population difference between the lowest and highest energy level can be transferred to any transition, notably also to the CT, which is the most relevant transition from an experimental point of view.
In an $S = 5/2$ system, for instance, maximum polarization on the CT would be achieved as follows [145]: First, inversion of the $5/2 \leftrightarrow 3/2$ transition is followed by inversion of the $3/2 \leftrightarrow 1/2$, polarizing the CT to $3P_0$. Second, the $-3/2 \leftrightarrow -5/2$ and $-1/2 \leftrightarrow -3/2$ transitions are inverted one after another, polarizing the CT to $5P_0$ (see Fig. 1 in [145] for illustration).
Frequency-swept passage pulses are well suited for inverting connected transitions one after another, because each transition is passed at different times in the correct order. To treat the individual passages through the transitions as selective population inversions, some conditions need to be met [48]: First, the frequency spacing between connected transitions needs to be large compared to the driving field amplitude. Second, population inversion is only achieved if the transitions are passed adiabatically.
A convenient measure of the adiabaticity of the passage is the (minimum)

adiabaticity factor, which can be calculated from the parameters of the passage pulse. Adiabaticity factors above 5 provide an almost perfect population inversion [27, 4]. The most important restrictions on adiabaticity are relaxation, necessitating short pulses, and technical aspects, such as the available power and bandwidth. With typical D values on the order of 1 GHz, broad frequency sweeps beyond the available resonator bandwidth, which is usually on the order of 100 MHz, are required. Two representative examples are given in the following.

5.2.1 *Population transfer for single orientation*

An $S = 7/2$ system with axial ZFS (D = 400 MHz, E = 0 MHz) and the ZFS axis oriented perpendicular to B_0 has its transition frequencies within $\pm$1.2 GHz around the Larmor frequency of ω_0 = 34.35 GHz. To polarize the CT to $4P_0$, an adiabatic passage pulse, which sequentially inverts all three satellite transitions in either the upper or the lower half of the spectrum, is required. Using a resonator with resonance frequency at ω_0, quality factor of 110 (312 MHz 3 dB bandwidth) and shortest π pulse on the CT of 4.5 ns, a 2 μs chirp pulse ranging from $f_1 = -1.275$ GHz to $f_2 = -0.1$ GHz relative to ω_0 has sufficient adiabaticity. The time-dependent amplitude and frequency of this chirp pulse inside the microwave resonator are shown in Fig. 5.1a. The influence of the microwave resonator is best observed in the amplitude function $\nu_1(t)$, which increases as the frequency progresses towards the center frequency of the resonator. In order to keep the flip angle of the chirp pulse constant, the curvature in the pulse's time-frequency profile has been computed for an offset-independent adiabaticity factor [74]. With the transition moment of the CT, an adiabaticity factor of 5.1 is achieved. On satellite transitions, this factor is lowered according to the corresponding transition moment. The outermost transition for instance experiences 66% of the driving field experienced by the CT, which results in an adiabaticity

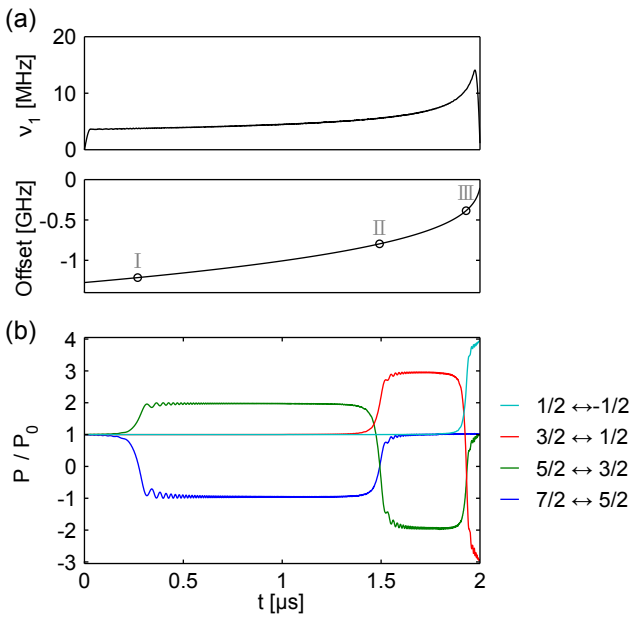

Figure 5.1 – Population transfer simulation for $S = 7/2$ with axial ZFS (D = 400 MHz, E = 0 MHz) and the ZFS axis perpendicular to B_0. (a) Time-dependent amplitude $\nu_1(t)$ (top) and frequency (bottom) of chirp pulse inside a resonator with quality factor 110 and 4.5 ns π pulse on the CT at 34.35 GHz. The chirp sweeps from -1.275 GHz to -0.1 GHz and was calculated for an adiabaticity factor of 5.1 on the CT. The circles indicate when the I: $7/2 \leftrightarrow 5/2$, II: $5/2 \leftrightarrow 3/2$ and III: $3/2 \leftrightarrow 1/2$ transitions are resonant. (b) Simulated evolution of polarization under the chirp for the relevant transitions. Color legend on the right-hand side. For the CT, the polarization achieved with this pulse is 3.96.

factor of 2.2. Under these conditions, the adiabaticity factors for the multi-quantum transitions passed by the pulse are negligible [49, 153], such that these transitions can be excluded from the analysis. The circles indicate those times, when the I: $7/2 \leftrightarrow 5/2$, II: $5/2 \leftrightarrow 3/2$ and III: $3/2 \leftrightarrow 1/2$ transitions are passed.
The simulated evolution of polarization for the relevant transitions under this pulse is shown in Fig. 5.1b. At I, the $7/2 \leftrightarrow 5/2$ transition (blue) is inverted, which polarizes its neighbor transition $5/2 \leftrightarrow 3/2$ (green). As a consequence of the fairly small adiabaticity factor of 2.2 on that particular transition, oscillatory patterns [154] upon I due to nutation around the effective field are readily recognizable. At II, the $5/2 \leftrightarrow 3/2$ transition is inverted to almost $-2P_0$, which polarizes its neighbor transitions $3/2 \leftrightarrow 1/2$ (red) to $3P_0$ and $7/2 \leftrightarrow 5/2$ back to equilibrium. At III, the equivalent process polarizes the CT (cyan) to $3.96P_0$, which is close the theoretical maximum.
For systems with larger D, such a *one-sided* population transfer could no longer achieve a polarization of $4P_0$, since the outermost transition is no longer within the range of the chirp pulse. The start frequency of the chirp pulse may be lowered - this does however reduce adiabaticity and thus the overall transfer efficiency.

5.2.2 *Population transfer for powder average with distributed ZFS parameters*

Orthorhombic $S = 7/2$ systems with distributed ZFS parameters and powder averaging over all orientations better describe actual experiments on Gd(III) complexes in glassy frozen solution than the axial case considered in Section 5.2.1 above. In the example case here, a Gaussian distribution of D values with μ_D = 1.2 GHz and σ_D = 0.24 GHz was assumed and sampled by 10 points within $\pm$0.6 GHz. The distribution in E values was calculated according to [155] $P(E/D) = E/D - 2(E/D)^2$ and sampled with 15 points. An orientational grid with a step size of 4.5° for polar and azimuthal angles θ and ϕ was used.
The spectrum of all single-quantum transitions of the above ZFS obtained with perturbation theory is shown in Fig. 5.2a (black), with the frequency axis defined relative to the Larmor frequency ω_0 = 34.35 GHz. The central peak in the middle is due to the CT, which is influenced by the ZFS through second-order terms only, whereas the almost featureless background is due to the satellites, which exhibit first-order broadening by the ZFS.
On such a system, it is experimentally not possible to selectively observe the CT of the entire ensemble. First, there are technical limitations in terms of excitation and detection bandwidth. Second, also satellite transitions contribute at the position of the central line. In order to account for the former effect, only a subset of the entire ensemble was considered for the simulation. This simulation subset was determined by those parameter configurations, whose CT frequencies lie within $\pm$75 MHz around ω_0. Out of all possible configurations, 41% belong to this subset and the colored curves in Fig. 5.2a represent the related transitions, according to the color legend on the bottom right. The outermost satellites are not shown and a magnified view based on finer grids is shown in Fig. C.12.
The chirp pulse for the population transfer ranges from $f_1 = -1.348$ GHz to $f_2 = -0.124$ GHz relative to ω_0 (see orange arrow), which is small compared to the broad spectrum. In fact, the $3/2 \leftrightarrow 1/2$ transition dominates within the range of the chirp. Using a resonator with resonance frequency at ω_0, quality factor of 110 and shortest π pulse on the CT of 4.6 ns, the adiabaticity factor is 4.1 for the CT and 3.8 for the $3/2 \leftrightarrow 1/2$ transition.
The simulated polarization of the CT achieved with the chirp for the D values under consideration are shown in Fig. 5.2b. For each D value, the polarization represents an average over orientations and E values which belong to the simulation subset. The data indicate that smaller D values can be polarized better. Polarizations above $2P_0$ actually suggest that transitions beyond the

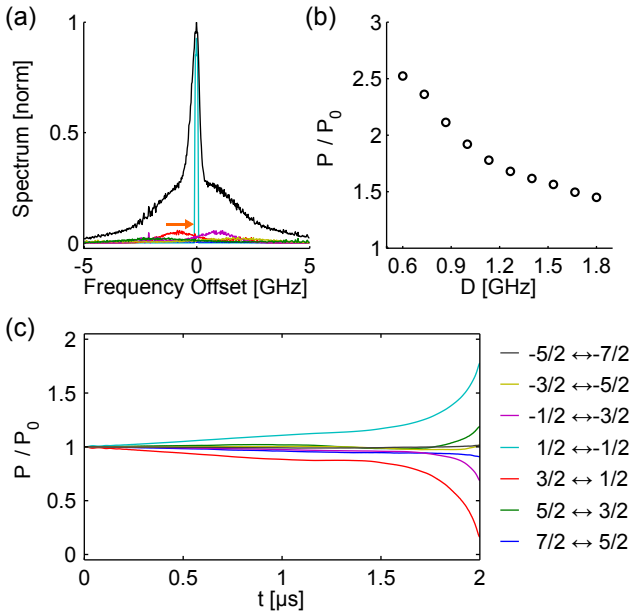

Figure 5.2 – Population transfer simulation for a powder with distributed ZFS parameters at ω_0 = 34.35 GHz. For powder averaging, the step size in θ and ϕ was 4.5°. A Gaussian distribution of D values (μ_D = 1.2 GHz and σ_D = 0.24 GHz) was modeled with 10 points within ±0.6 GHz. For each D value, the distribution in E values was calculated according to [155] $P(E/D) = E/D - 2(E/D)^2$ and sampled with 15 points up to $E = D/3$, excluding E = 0. (a) Spectrum of single-quantum transition frequencies (black) obtained with perturbation theory [151, 152] for frequency offsets of ±5 GHz relative to ω_0 with 24 MHz step size. The cyan curve depicts that fraction of the CT (41%), which is resonant within ±75 MHz. The colored curves depict the satellite transitions of this simulation subset. Color legend on the bottom right, outermost satellites not shown. The orange arrow indicates the frequency range of the chirp pulse from −1.348 GHz to −0.124 GHz. (b) Simulated polarization of the powder- and E-averaged subset of the CT achieved with the chirp pulse at various D values. The resonator was modeled with quality factor 110 and 4.6 ns π pulse on the CT at 34.35 GHz. The chirp pulse was calculated for an adiabaticity factor of 4.1 on the CT. (c) Simulated evolution of powder- and ZFS-averaged polarization under the chirp for the simulation subset. Color legend on the right-hand side. For the CT, the polarization achieved with the pulse is 1.78, which corresponds to the weighted average of polarization in panel (b).

$3/2 \leftrightarrow 1/2$ transition are inverted, which is more likely for small D. Note however that mean polarization below $2P_0$ obtained for larger D does not exclude transfer of population from the $+5/2$ level to the $+1/2$ level of the CT (see also Fig. C.13b). In analogy to the previous example in Section 5.2.1, a chirp of extended sweep range on the order of the spectral width could not provide sufficient adiabaticity due to limitations in excitation power and bandwidth.

The simulated evolution under the chirp averaged over the entire simulation subset is shown in Fig. 5.2c, with color legend for the transitions on the right. Due to the distributed parameters, individual steps during the evolution can not be identified. For the CT, the polarization achieved with the chirp is $1.78P_0$. Because the polarization of the $3/2 \leftrightarrow 1/2$ transition has the largest reduction upon the chirp, the population was transferred to large parts via this transition. A reduction on the $-1/2 \leftrightarrow -3/2$ transition is also observed, which is due to the orientation dependence of the ZFS. The time evolution for the individual D values can be found in Fig. C.14.

This particular example with ZFS and pulse parameters, which are close to experimental ones, indicates that polarization on the order of $2P_0$ may be achieved experimentally. For a combination of two chirps on each side, an-

other improvement by P_0 to $3P_0$ should be possible. Experiments confirming these trends are reported below in Section 5.4.

5.3 MATERIALS AND METHODS

5.3.1 *Sample preparation*

5.3.1.1 *Gd-spacer-Gd*

The syntheses of Gd-ruler $\mathbf{1_3}$ and $\mathbf{2_2}$ (Fig. 5.3) will be reported elsewhere. A 5 mM solution of Gd-ruler $\mathbf{1_3}$ in D_2O (pH 8.0, containing 28 mM NaCl) and a 5 mM solution of Gd-ruler $\mathbf{2_2}$ in D_2O (pH 7.0, containing 30 mM NaCl and ca. 0.5 mM F_3CCO_2H/F_3CCO_2Na) were diluted with D_2O and glycerol-d_8 (1:1 in volume) to give the solutions with a concentration of 600 μM and 200 μM, respectively, that were used for the EPR experiments.

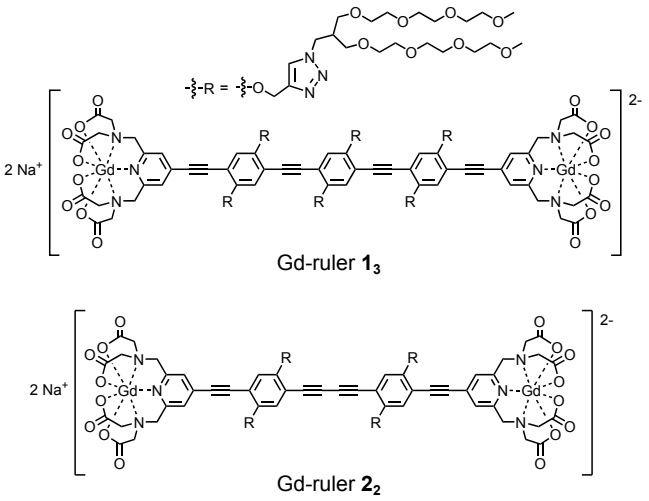

Figure 5.3 – Structures of Gd-ruler $\mathbf{1_3}$ and Gd-ruler $\mathbf{2_2}$. In both compounds two Gd(III)-PyMTA complexes are connected via a rodlike spacer which keeps the Gd(III) ions at a distance of about 3.4 nm and 3.0 nm in case of Gd-ruler $\mathbf{1_3}$ and Gd-ruler $\mathbf{2_2}$, respectively. The limited flexibility of the spacer ensures a narrow distance distribution between the two Gd(III) ions [156, 157]. The branched oligo (ethyleneglycol) side chains ensure a good solubility in water/glycerol.

5.3.1.2 *DOTA and DTPA complexes*

According to the reported procedure [158] a stock solution of Gd(III)-DTPA complex (DTPA = diethylenetriamine pentaacetate) with a concentration of 26.7 mM and a stock solution of Gd(III)-DOTA complex (DOTA = 1,4,7,10-tetraazacyclododecane-1,4,7,10-tetraacetate) with a concentration of 40 mM were prepared. Both stock solutions were diluted with a 1:1 mixture in volume of water/glycerol so as to obtain the solutions with a concentration of 200 μM that were used for the EPR experiments.

5.3.2 *Instrumentation*

A commercial Bruker Elexsys E580 Q-band spectrometer was extended with an incoherent UWB pulse channel based on a 12 GS/s AWG (Agilent M8190A). The spectrometer itself was power-upgraded by a 200 W amplifier and operated with a home-built resonator optimized for over-sized samples, as described elsewhere [150]. The home-built resonator was over-coupled to quality factors of 110, whereas experiments on nitroxides with this spectrometer are typically performed with quality factors around 300 [150]. For the lower quality factors used here, it was no longer possible to identify

the resonance frequency based on the power reflected from the resonator. Consequently, over-coupling to quality factors below 300 was achieved by monitoring the Hahn echo amplitude while adjusting the coupling iris.
The AWG extension was similar to a previously described extension for an Elexsys X-band spectrometer (see Section 3.3.1). Changes to the previous extension were only made in terms of hardware connectivity, as described in Section C.1. The operational bandwidth of the AWG extension was on the order of 2.5 GHz. It is worth mentioning that there are some complications associated with the operation at such broad bandwidths, mostly related to spurious frequencies due to mixers and saturated amplifiers (pulse distortions). As a consequence of these, it was not always possible to operate the 200 W power amplifier at its maximum saturated output power, which resulted in field strengths reduced to roughly 75% of the maximum possible. For further information on these technical issues, the interested reader is referred to Section C.2.

5.3.3 *Pulse sequences*

Unless explicitly indicated otherwise, all experiments were performed at 10 K using a repetition time of 342 μs.

5.3.3.1 *Resonator profiles*

The frequency dependence of the driving field amplitude $\nu_1(f)$ was obtained from nutation experiments performed at various observation frequencies [74, 113]. The observation frequencies were stepped from 33.5 to 34.9 GHz by increments of 25 MHz. At each observation frequency, the magnetic field was adjusted to the central line of the spectrum and a transient nutation experiment was performed. The nutation pulse originated from the UWB channel with pulse length incremented up to 63 ns in 1 ns steps at maximum pulse amplitude. Upon a recovery delay of 5 μs, a Hahn echo was generated by a 16 ns ($\pi/2$) and a 32 ns (π) pulse with 400 ns delay between leading edges. The apparent nutation frequencies obtained upon data processing [74] were primarily due to the field strength experienced by the CT, whose first-order transition moment is 4 times the transition moment of an $S = 1/2$ system.
The experiment was fully automated using the Bruker macro language ProDel and only required 3.5 minutes when using 10 shots per point. It is worth mentioning that on the Elexsys spectrometer at Q band, stepping of the observation frequency takes a fraction of a second due to the synthesizer employed for upconversion. As a consequence of that, such frequency stepped experiments completed much faster than for the previously reported AWG extension operated in X band [74].

5.3.3.2 *Population transfer*

To study the population transfer as a function of chirp and sample parameters, Hahn echoes with and without pre-polarization pulses were recorded. For echo generation, 16 ns ($\pi/2$) and 32 ns (π) pulses with 400 ns delay between starting pulse flanks and a $[+(+x) - (-x)]$ phase cycle on the $\pi/2$ pulse were used. The population transfer chirp started 5 μs before the observation pulses. In those cases where two pre-polarization pulses were used, the two chirps were sequentially combined with a delay of 300 ns between the pulses. The first pulse started 7.3 μs before the observation pulses. For the pre-polarization chirps, the following parameters are important:
Typical pulse lengths were 1 - 2 μs, where 2 μs was the most used length. The trailing edges of the chirps were sinusoidally smoothened on a timescale of 30 ns [28, 74]. The sweep range of the chirp was always defined relative to the observer frequency of the Hahn echo pulses, with start and end frequencies of the chirp referred to as f_1 and f_2, respectively. Representative values

were $f_1 = \pm 1.2$ GHz and $f_2 = \pm 0.1$ GHz, depending on whether up-chirps ($f_1 < f_2$) or down-chirps ($f_1 > f_2$) were used. Since the observer frequency was always centered at the resonator center frequency during these experiments, the chirp frequencies also denote the frequency offset with respect to the microwave resonator. Furthermore, unless the magnetic field was swept during the experiment, chirp frequencies denote the frequency offset with respect to the central line of the Gd(III) spectrum.
Unless explicitly mentioned otherwise, the chirp pulses were designed for an offset-independent adiabaticity factor by calculating the frequency modulation according to the frequency dependence of the driving field, $\nu_1(f)$, as described previously [74]. Since chirps extended far outside the frequency range of experimental $\nu_1(f)$ (see Section 5.3.3.1), a model based fit to experimental data was used for the calculation of the frequency modulation. The model was based on an idealized resonator frequency profile, which can be mathematically described as

$$\nu_{1,\mathrm{fit}}(f) = \nu_{1,\mathrm{max}} \left| \left(1 + iQ_\mathrm{L}\left(\frac{f}{f_0} - \frac{f_0}{f}\right)\right)^{-1} \right| \tag{5.2}$$

where $\nu_{1,\mathrm{max}}$ is the field strength at the center frequency f_0 of the resonator and Q_L the quality factor of the resonator. The 3 dB bandwidth is determined by f_0/Q_L. Representative values were $\nu_{1,\mathrm{max}}$ = 30 - 40 MHz, f_0 = 34.35 GHz and Q_L = 110, resulting in a bandwidth of 312 MHz.

5.3.3.3 *Pre-polarized DEER*

For four-pulse DEER experiments on Gd-ruler $\mathbf{1_3}$ and Gd-ruler $\mathbf{2_2}$, the pulse sequence $\pm(\pi/2)_\mathrm{obs} - \tau_1 - (\pi)_\mathrm{obs} - (\tau_1 + t) - (\pi)_\mathrm{chirp} - (\tau_2 - t) - (\pi)_\mathrm{obs} - \tau_2 - echo$ was used, where τ_1 = 400 ns, τ_2 = 4500 ns and the time increment for t was 8 ns. The observation pulses had a length of 12 ns and the observation frequency was placed on the central line of the Gd(III) spectrum [143]. The chirp pump pulse had a length of 192 ns and ranged from $f_1 = -0.8$ GHz to $f_2 = -0.3$ GHz. The frequency modulation of the chirp was based on the model fit of the resonator (see Section 5.3.3.2) and resulted in an adiabaticity factor of 2, taking into account the transition moment of the CT. The pulse edges were sinusoidally smoothened during 10 ns. To combine DEER with pre-polarization, two sequentially combined pre-polarization chirps with a gap of 300 ns preceded the DEER pulse sequence by 7.3 μs.
Experimental data were processed using the software DeerAnalysis [95]. For distance distributions obtained by Tikhonov-regularization, a regularization parameter of 1 was used.

5.3.4 *Simulations*

The spin dynamics simulations in Sections 5.2.1 and 5.2.2 were computed in MATLAB by propagation of density matrices for $S = 7/2$ under a chirp pulse. The simulation was performed in a frame rotating at a frequency 3 GHz below the Larmor frequency. To include ZFS parameters in the rotating frame, the spin Hamiltonian in the laboratory frame was diagonalized by perturbation theory using analytical formulas derived up to third-order perturbation [151, 152]. Since the $\hat{S}_x$ operator for the pulse Hamiltonian was represented without consideration of the actual ZFS parameters, first-order expressions for the transition moments applied. Notably, EPR powder spectra calculated with third-order transition frequencies and first-order transition moments, such as the one shown in Fig. 5.2a, compared remarkably well to spectra obtained with explicit eigenvalues and transformation of $\hat{S}_x$ into the eigenframe (see also Fig. C.12b). Fitting the experimental spectra with this approach requires further refinements. For reference, a comparison to an experimental spectrum is shown in Fig. C.13a.
To calculate matrix propagators, time steps equal to the AWG time steps

were used (83.3 ps). For reasons of computational efficiency, the propagators were pre-computed for the 4096 possible amplitude levels used to describe the chirp pulse and stored in lookup tables [74]. Special care needed to be taken where ZFS transition frequencies were outside the Nyquist range of the simulation (0 - 6 GHz). In these cases, unwanted excitation of outer transitions due to aliasing was observed. Such effects were avoided by setting the elements related to transitions outside the Nyquist range in the $\hat{S}_x$ operator for the pulse Hamiltonian to zero.
Resonator profiles were included in the simulation by convolution of the chirp pulse with the impulse response function of an idealized resonator. Since the chirp itself was calculated in a rotating frame, the real-valued laboratory frame impulse response function of the resonator was converted into a complex-valued impulse response function in the rotating frame. The laboratory frame impulse response function was calculated from its frequency domain equivalent defined in Eq. (5.2), according to the methods described in Section A.1.
The initial state of the density matrix was set to $\hat{S}_z$ and the evolution of polarization of all transitions under the pulse was extracted from the density matrix. On a Dell precision T3600 computer, the propagation of the density matrix under a 2 μs chirp took 2 seconds, which included pre-computation of propagators. Averaging over orientations and ZFS parameters was performed in parallel on six cores of the processor, taking into account weighting factors related to orientation and ZFS parameters. The simulation shown in Section 5.2.2 required averaging over 24799 configurations and took 4 hours in total.

5.4 RESULTS AND DISCUSSION

5.4.1 *Optimization of chirp pulses*

In the experimental approach, the parameters of the two chirp pulses on each side of the spectrum needed to be optimized for the best possible polarization enhancement. To explain this procedure, Fig. 5.4a shows the EPR spectrum of Gd-ruler $\mathbf{1_3}$ in frequency units (red) along with the experimentally obtained resonator frequency profile $\nu_1(f)$ (brown). The latter is complemented with a fit (blue) based on Eq. (5.2) with a quality factor of 110 and 4.6 ns π pulse on the CT at 34.35 GHz, which implies a bandwidth of 312 MHz.

5.4.1.1 *Positioning of end frequency*

In the first optimization step, the end frequency f_2 of the chirp pulse was varied, while keeping the sweep width fixed at 750 MHz and the pulse length at 1.5 μs. The outcome of this experiment is shown in Fig. 5.4b for both up-chirps (orange) and down-chirps (blue). The ordinate shows the normalized intensity I/I_0 of the Hahn echo observed on the central line (dashed vertical line) of the Gd(III) spectrum. To a large part, this intensity represents polarization on the CT. Contributions from polarization on satellite transitions, however, cannot be excluded. The abscissa depicts the end frequency f_2 of the chirp.
In those regions, where the intensity is above 1, the chirp pulse polarized the observed spins. In regions with intensity below 0, the chirp pulse had spectral overlap with the observed spins and therefore lead to inversion of the observed spins, in addition to population transfer. In fact, the slope in these inverted regions is due to population transfer[3]. The frequency positioning of the chirps for maximum signal enhancement (black open circles) is indicated by the arrows. In addition to the optimum f_2 values (-124 MHz and 142 MHz), this experiment provides further insight:
First, it appears to be advantageous to place the chirp pulses as close as

[3] On a spin 1/2 system, there was no such slope (see Fig. 3.4d)

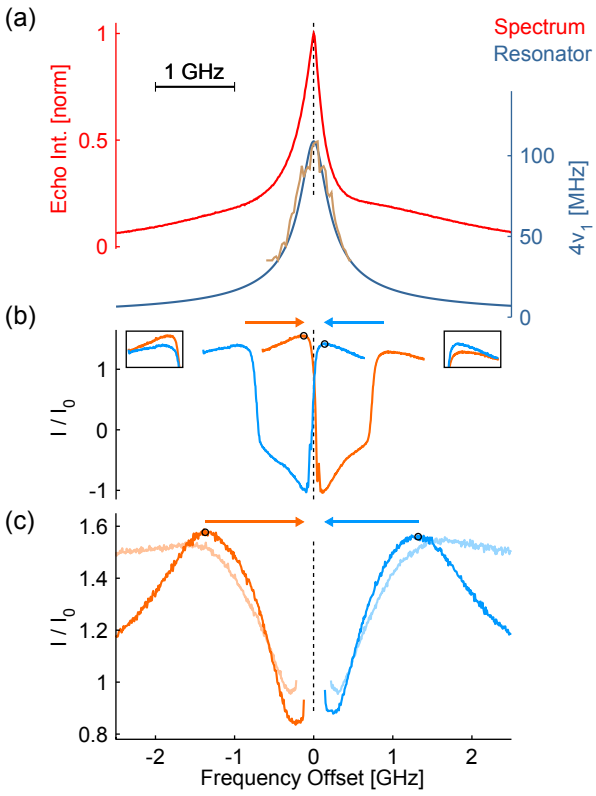

Figure 5.4 – Dependence of polarization enhancement of central line on chirp frequency range. The position of the central line is indicated by a dashed vertical line in all panels. (a) Top: Field-swept echo-detected spectrum of Gd-ruler $\mathbf{1_3}$ cast in frequency scale (red). Bottom: Resonator profile with quality factor 110 and 4.6 ns π pulse on the CT at 34.35 GHz (blue) fitted to experimental $\nu_1(f)$ data (brown). (b) Polarization as a function of f_2, the end frequency of the chirp, for 750 MHz up-chirps (orange) and down-chirps (blue) with t_p = 1.5 μs. The black circles indicate f_2 for maximum enhancement. The two arrows depict the sweep width and direction that led to maximum enhancement. In the insets, the curves are horizontally displaced to compare the influence of the sweep direction at fixed sweep width on each side of the central line. (c) Polarization as a function of f_1, the start frequency of the chirp, at fixed end frequencies f_2 for up-chirps (orange) and down-chirps (blue) with t_p = 2 μs. The end frequencies f_2 corresponded to the optima shown in panel (b). The black circles indicate f_1 for maximum enhancement. The two arrows depict the sweep width and direction that lead to maximum enhancement. The light orange and light blue curves with slightly lower enhancement were obtained with constant-rate chirps with end frequencies $f_2 = -0.22$ GHz and $f_2 = 0.218$ GHz, respectively.

possible to the observed spins to be polarized. For the given ZFS parameters, this is mainly due to the resonator bandwidth: The further away the chirp is from the center, the lower the coupling to the spins, which results in a reduction of the pulse's adiabaticity factor. For close spectral proximity between the chirp pulses and the observed spins, the edge truncation of the chirp pulse is critical.

Second, the data reveal the contribution of outer satellite transitions beyond the $\pm 3/2 \leftrightarrow \pm 1/2$ transitions. For this purpose, the curves were horizontally displaced and overlapped in the insets on each side of the spectrum. In this view, polarization enhancements between up-chirps and down-chirps with exactly the same frequency coverage can be compared. In the inset on the left hand side, for instance, up-chirps resulted in more polarization than down-chirps. Taking into consideration the level ordering, it is only the up-chirp which can transfer population from levels beyond one of the immediate neighbors of the observed transitions. The down-chirp on the contrary sweeps in the opposite direction and can only polarize the observed

spins via inversion of one immediate neighbor transition. The extra polarization achieved with the up-chirp thus originated from population beyond the immediate neighbor transitions of the observed spins. Here, these neighbor transitions were to a good approximation the $\pm 3/2 \leftrightarrow \pm 1/2$ transitions. The inset on the right hand side can be treated in an analogous manner. Considering the actual echo intensities, one finds that roughly 30% of the polarization brought by the chirp pulse originated from outer satellites. Their contribution is therefore significant, even though the 750 MHz chirp pulse extended only over a small fraction of the broad Gd(III) spectrum. Supporting simulations are shown in Fig. C.13b.

5.4.1.2 *Positioning of start frequency*

In the second optimization step, the start frequency f_1 of the chirp pulse was varied. The pulse length was set to 2 μs and for the end frequencies, the values optimized as described above were used. The resulting echo intensities are shown in Fig. 5.4c for both up-chirps (solid orange) and down-chirps (solid blue). The experiment started with $f_1 = f_2$, such that the end points of the curves at the center of the figure denote the optimized end frequencies. Maximum polarization enhancements of 58% and 56% was achieved for $f_1 = -1.348$ GHz and $f_1 = 1.3$ GHz, respectively, as indicated by the black open circles. For start frequencies beyond these points, the adiabaticity factor of the pulse was no longer sufficient. In fact, the adiabaticity factors on the CT for best enhancement were 4.1 for the up-chirp and 4.9 for the down-chirp. These factors represent rough figures only, since they were calculated from the model based fit to the resonator frequency profile $\nu_1(f)$ (see Fig. 5.4a and Section 5.3.3.2). Notably, these optimized chirp pulses extended over roughly 2.6 GHz, which is far beyond the bandwidth of the resonator. Possible complications from operation in this regime are discussed in Sections C.2 and C.3 (pulse distortions and sample heating).
The same optimization procedure was also performed with constant-rate chirps (light orange and light blue), whose adiabaticity factors depend on $\nu_1(f)^2$. With these pulses, optimized end frequencies were further away from the observed spins. The maximum enhancement was slightly lower, but the reduction beyond the optimum was less steep than for chirp pulses calculated for offset-independent adiabaticity. The reason is that even for such broad sweep widths, the constant-rate chirp can retain a fairly sufficient adiabaticity for smaller offset frequencies, where the coupling to the spins is stronger. The variable-rate chirp on the contrary trades its integral performance for uniform excitation [74].

5.4.2 *Pre-polarized field-sweep spectra*

In the experiments described above, we focused on enhancing the polarization on the central line of the Gd(III) spectrum. Certain experiments may require pre-polarization of other regions in the spectrum. For this purpose, we acquired the entire spectrum with a field-sweep combined with pre-polarization pulses.
Fig. 5.5a shows field-swept spectra pre-polarized with up-chirp (orange), down-chirp (blue) and sequential combination of both (green). The sweep width and direction of the chirp pulses in the field domain are indicated by the arrows on the top left. The black curve was obtained without pre-polarization and serves as a reference for equilibrium. Over a range of 16 mT, the signal pre-polarized from both sides was stronger than the peak equilibrium signal.
Using the equilibrium reference, the relative intensities I/I_0 as shown in Fig. 5.5b were obtained. In this representation, it is readily seen that the signal enhancement increased when moving either to the left hand side (up-chirps) or to the right hand side (down-chirps) of the central line of

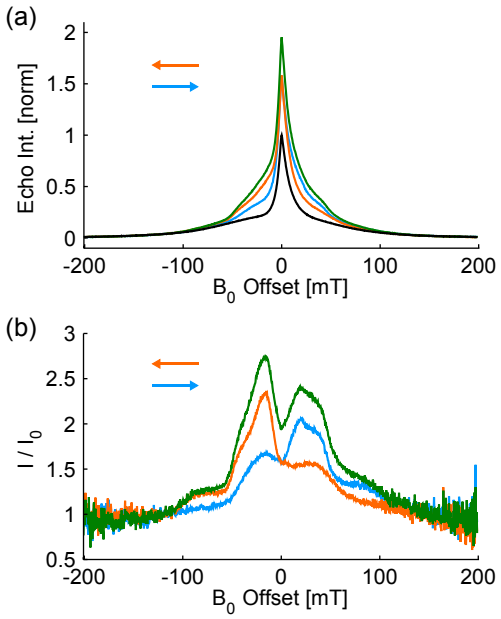

Figure 5.5 – Population transfer to other transitions by field-sweep for Gd-ruler $\mathbf{1_3}$. (a) Echo-detected field-sweep pre-polarized with up-chirp (orange), down-chirp (blue) and sequential combination of both (green) as well as equilibrium reference obtained without pre-polarization (black). The optimized sweep width of the chirp (see Fig. 5.4c) in the field domain is indicated by the arrows on the top left. (b) Field dependence of polarization normalized to equilibrium reference for up-chirp (orange), down-chirp (blue) and sequential combination of both (green).

the spectrum. For field offsets around -16 mT, for instance, the up-chirp achieved an enhancement of 130%, which raised up to 175% for the combined pulses.

The reason for higher enhancements in the region around the central line is due to the orientation dependence of the ZFS. Since the CT is narrow compared to the other transitions, the pre-polarization pulse can invert this transition quite well, which makes efficient population transfer via multiple transitions more likely. Considering again the region around -16 mT, one possible transfer pathway is from the m_s = 3/2 to the m_s = -1/2 level, which polarizes the $-1/2 \leftrightarrow -3/2$ transition. One should, however, remain cautious about interpreting the peak at -16 mT as the maximum of the $-1/2 \leftrightarrow -3/2$ sub-spectrum: There are contributions from other transitions to the observed signal and the finite sweep width of the chirp pulses imprints additional features to these spectra. One particularly apparent feature is the drop in the enhancement around roughly ± 50 mT, where the chirp pulse was no longer able to invert the CT and thus polarize (at least) its immediate neighbors. Furthermore, beyond roughly ± 100 mT, the spacing between transitions became larger than the sweep width of the pulse, such that the enhancement dropped to 0%.

The comparably higher signal enhancements for satellite transitions in the vicinity of the CT may allow for alternative detection schemes in experiments involving Gd(III). Yet, one particular drawback on these satellite transitions is the faster relaxation. To examine this issue, echo-detected field-sweep spectra were recorded with inter-pulse delay between observation pulses prolonged to 7 μs. This inter-pulse delay mimics the long evolution times of coherence on Gd(III) transitions that is typical for DEER experiments. The results are shown in Fig. C.8 and revealed a relative loss in polarization on the order of 15% for the $\pm 3/2 \leftrightarrow \pm 1/2$ transitions. For transitions beyond the $\pm 3/2 \leftrightarrow \pm 1/2$ transitions, an enhancement could no longer be observed. As a consequence for experiments that require long coherence evolution times, detectable polarization enhancements for observation outside the FWHM

of the central line may be reduced due to relaxation. In fact, the majority of distance measurements between Gd(III) pairs involve observation just outside the FWHM of the central line [143, 140].

5.4.2.1 *Pre-polarization of different Gd(III) complexes*

In the following, pre-polarized spectra of different complexes are presented, namely of Gd-DOTA and Gd-DTPA. For Gd-DOTA, echo-detected spectra as well as normalized intensities I/I_0 are shown in Fig. 5.6a and b, respectively, using the same coloring as in Fig. 5.5. For Gd-DTPA, the data are presented in the same way in Fig. 5.6c and d. The experimental conditions for Gd-DOTA in terms of resonator frequency profiles $\nu_1(f)$ were almost identical to those of Gd-PyMTA (Gd-ruler $\mathbf{1_3}$). For Gd-DTPA, the field strength was 13% stronger at a comparable bandwidth. The chirp pulses were optimized according to the description in Section 5.4.1.
For Gd-DOTA, polarization enhancements were in general higher than for Gd-PyMTA. The enhancement of the central line was 187% and for field offsets around −12 mT, the enhancement was even beyond 200%. Since the experimental conditions between Gd-PyMTA and Gd-DOTA were very similar, these higher enhancements were due to the smaller ZFS for Gd-DOTA, which resulted in better spectral coverage of the chirp. The central line can be identified in Fig. 5.6b and was enhanced by more than 100%, independent on the sweep direction of the chirp. The trend towards larger enhancements for smaller ZFS observed in the powder simulations in Section 5.2.2 is thus confirmed experimentally. The D values for Gd-DOTA are actually on the

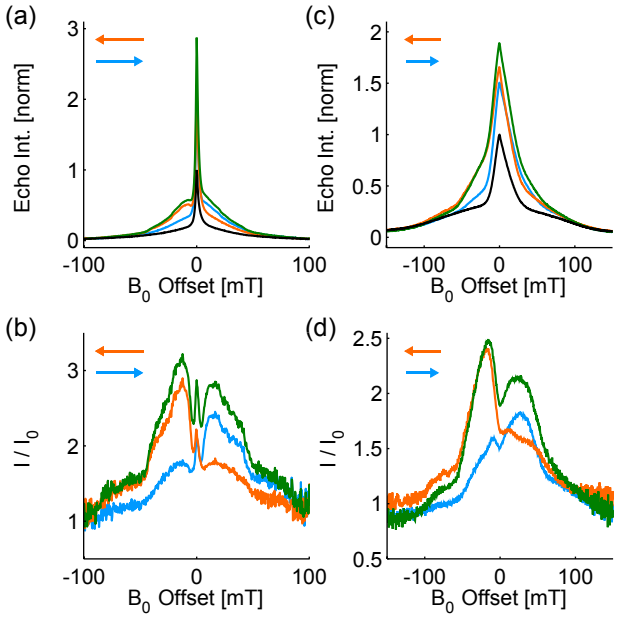

Figure 5.6 – Pre-polarized field-sweep on different Gd(III) complexes. (a) Echo-detected field-sweep of Gd-DOTA pre-polarized with up-chirp (orange), down-chirp (blue) and sequential combination of both (green) as well as equilibrium reference obtained without pre-polarization (black). The sweep width of the 2 μs long chirps in the field domain is indicated by the arrows (f_1 = −1.192 GHz to f_2 = −0.088 GHz and f_1 = 1.17 GHz to f_2 = 0.106 GHz). (b) Pre-polarized field-sweep of Gd-DOTA normalized to equilibrium reference for up-chirp (orange), down-chirp (blue) and sequential combination of both (green). (c) Echo-detected field-sweep of Gd-DTPA pre-polarized with up-chirp (orange), down-chirp (blue) and sequential combination of both (green) as well as equilibrium reference obtained without pre-polarization (black). The sweep width of the 2 μs long chirps in the field domain is indicated by the arrows (f_1 = −1.356 GHz to f_2 = −0.116 GHz and f_1 = 1.206 GHz to f_2 = 0.11 GHz). (d) Pre-polarized field-sweep of Gd-DTPA normalized to equilibrium reference for up-chirp (orange), down-chirp (blue) and sequential combination of both (green).

order of 600 MHz [155, 159], where the simulations showed enhancements beyond 100% (see Fig. 5.2b).
For Gd-DTPA, D values are on the order of 1.5 GHz [155, 160], such that the ZFS is larger than for Gd-PyMTA, which has D values on the order of 1.2 GHz (see Fig. C.13a). The enhancement of the central line was 89% and for field offsets around -18 mT, the enhancement was 147%. Here, these values cannot directly be compared to Gd-PyMTA due to the higher field strength ν_1. Furthermore, the down-chirp showed a significant reduction mechanism, as seen for instance for field offsets below -100 mT. Reduction mechanisms other than sample heating are described in Section C.2. As a consequence, the polarization achieved with the up-chirp was slightly higher for Gd-DTPA, whereas the polarization achieved with the down-chirp was slightly higher for Gd-PyMTA. In any case, one would not expect a very large difference between Gd-PyMTA and Gd-DTPA from the simulation in Section 5.2.2.

5.4.3 *Pre-polarized distance measurements*

In this section, pre-polarization is combined with the four-pulse DEER sequence [65] using a chirp pump pulse for increased excitation bandwidth [74, 119]. One would expect a twofold advantage from using chirp pulses for distance measurements: Signal enhancement by pre-polarization and enhancement of the modulation depth by using a chirp pump pulse. Notably, there are two differences to previous approaches for using a chirp pump pulse for increased modulation depth on a broad (transition metal ion) spectrum [74, 119]. First of all, the S = 7/2 spin of Gd(III) may lead to reduction of the observer echo due to the application of the pump pulse [160]. The spin system therefore introduces an additional constraint on how the chirp pump pulse has to be set up. The solution of this problem is not part of the present work and will be published elsewhere (see Chapter 6). Here, we note that the four-pulse DEER scheme with a chirp pump as presented below yielded a performance which was close to the optimum that we could achieve on our spectrometer for Gd-ruler $\mathbf{1_3}$.
A second aspect is that previous experiments were performed on compounds labeled orthogonally with nitroxide and a transition metal ion, Cu(II) [74] or Co(II) [119]. For these metal-nitroxide systems, the modulation depth for a chirp pump pulse on the metal while observing nitroxide was smaller than for an ordinary pump pulse on the narrower nitroxide spectrum while observing the metal [74]. In the Gd-ruler investigated here, pump and observer spins have both a fairly broad spectrum. Accordingly, there are no such alternate routes to enhance the modulation depth - unless one changes to higher fields and implements a RIDME experiment that relies on longitudinal relaxation to flip the *pump* spins [161].
The primary DEER data without pre-polarization are shown in gray in Fig. 5.7a. The chirp pump pulse was 192 ns long with frequencies $f_1 = -0.8$ GHz and $f_2 = -0.3$ GHz. For the transition moment of the CT, this pulse had an adiabaticity factor of 2. The ordinate was normalized by the maximum echo intensity obtained with this experiment. The same experiment performed with the pre-polarization pulses from Section 5.4.1 resulted in the black curve, which was enhanced by 85%.
At the very beginning of the pre-polarized DEER signal, an unexpected falling edge can be identified. This transient was due to the heating by the up-chirp discussed in Section C.3.1. The inset on the right hand side of Fig. 5.7a compares the initial part of the two curves. As can be recognized, this initial transient decayed before the maximum of the DEER signal was reached. A more detailed discussion of this decay is found in Fig. C.6, where the strategies to minimize such heating transients are described.
In Fig. 5.7b, the form factors for the pre-polarized (black) and the ordinary chirp data (gray) are shown. In both cases, the modulation depth was on the order of 9%. Similar modulation depth was achieved at Q band by pumping

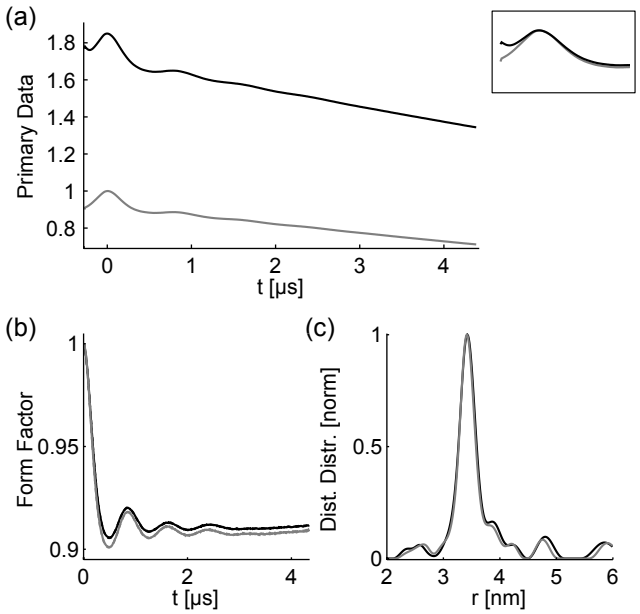

Figure 5.7 – Pre-polarized DEER experiments on Gd-ruler $\mathbf{1_3}$ using a 192 ns long chirp pump pulse ($f_1 = -0.8$ GHz to $f_2 = -0.3$ GHz). (a) Primary data obtained with pre-polarization to 1.85 (black) and without pre-polarization (gray). The inset on the right-hand side shows the initial part of the two curves on top of each other. (b) Form factors with (black) and without (gray) pre-polarization showing modulation depths on the order of 9%. (c) Regularized distance distributions with (black) and without (gray) pre-polarization.

the central line of the Gd(III) spectrum with an 8 ns pulse using an over-coupled normal sample diameter dielectric resonator [79]. In the present study, these 9% were achieved by a *reversed* scheme, where the pump pulse is applied to the spectrally broad satellites off the central line. As the time-domain data suggest, the distance information was rather unaffected by the pre-polarization pulses. The corresponding regularized distance distributions in Fig. 5.7c confirm this. As one would expect for Gd-ruler $\mathbf{1_3}$, the distance distributions peak around a distance of 3.4 nm. Complementary pre-polarized DEER experiments are shown in Figs. C.10 and C.11, including data obtained with Gd-ruler $\mathbf{2_2}$. Also for these experiments, the distance information upon pre-polarization was preserved.

A control experiment with a monochromatic 9 ns pump pulse with an offset of -300 MHz is shown in Fig. C.9. In fact, the echo signal obtained with the monochromatic pump pulse was 25% larger than the echo signal obtained with the chirp pump pulse, but the modulation depth was only 4%. The signal enhancement achieved by the chirp pump pulse was thus 80%. In the combined experiment, the net increase in sensitivity was therefore 3.33, which corresponds to an acceleration in measurement time by one order of magnitude. Such an improvement is especially important for the measurement of longer distances or at reduced spin concentrations.

In all distance measurements reported here, the maximum of the Gd(III) spectrum was observed at the center frequency of the resonator, which corresponds to an optimized experimental scheme on its own [143]. Often, however, the available power and bandwidth do not allow for applying this scheme [140]. As our data suggest, this optimized scheme can be implemented successfully on a spectrometer with high power and bandwidth, and sensitivity can be further enhanced with chirp pulses in the UWB regime.

5.5 CONCLUSIONS AND OUTLOOK

Our investigation has proven the potential for sensitivity enhancement with Gd(III) spin labels by population transfer. For the three experimentally in-

vestigated complexes Gd-DOTA, Gd-PyMTA and Gd-DTPA, the relevant central line of the spectrum could be enhanced by more than 80%. The largest signal enhancements were actually achieved with Gd-DOTA, which had the smallest ZFS parameters amongst the compared complexes, and thus the best spectral overlap with the two ultra-wideband chirp pulses.

In fact, spectral coverage of the chirp pulses is a key factor for experimental performance. Generally, spectral coverage scales with the time available for excitation, whose ultimate limit is set by relaxation. The actual scaling between pulse length and excitation bandwidth critically depends on the available power and bandwidth. In our experiments, this relaxation limit could not be reached due to additional technical constraints. In particular, the 2 μs pulses employed in this work provided a reasonable compromise between signal enhancement by population transfer and signal reduction by (i) sample heating due to the pulses and (ii) pulse distortions resulting in unwanted excitation of the spins to be polarized. The experimental performance could thus be improved further by alleviating such specific technical issues.

A rather convenient aspect of the pre-polarization technique is the ease of combination with existing pulse sequences. In principle, any echo signal detected on a Gd(III) spin label can be enhanced by pre-polarization, as successfully demonstrated for distance measurements between Gd(III) ions. Notably, this type of pre-polarized DEER measurement can be adapted for distance measurements between non-identical spin labels, namely Gd(III) ions and nitroxides [162, 163], or for RIDME type of experiments at higher fields [161]. If other types of high-spin systems are considered for pre-polarization, one has to keep in mind that population is only transferred effectively for a subset of orientations and ZFS parameters. For systems which exhibit orientation selection, this may complicate data analysis.

One important further step of this sensitivity enhancement technique is the application at higher fields, where a very large fraction of the equilibrium polarization resides on unobserved transitions. An advantage of higher fields may be the narrowing of the Gd(III) central transition and the larger resonator bandwidth for a given quality factor. However, power in the millimeter-wave regime is often orders of magnitude below the powers applied here at Q-band frequencies. High-field spectrometers with extraordinary high power and bandwidth [77] or with multi-mode resonators [78] are expected to circumvent this limitation.

6

GD(III)-GD(III) DISTANCE MEASUREMENTS WITH CHIRP PUMP PULSES

ABSTRACT

The broad EPR spectrum of Gd(III) spin labels restricts the dipolar modulation depth in distance measurements between Gd(III) pairs to a few percent. To overcome this limitation, frequency-swept chirp pulses are utilized as pump pulses in the DEER experiment. Using a model system with 3.4 nm Gd-Gd distance, application of one single chirp pump pulse at Q-band frequencies leads to modulation depths beyond 10%. However, the larger modulation depth is counteracted by a reduction of the absolute echo intensity due to the pump pulse. As supported by spin dynamics simulations, this effect is primarily driven by signal loss to double-quantum coherence and specific to the Gd(III) high spin state of $S = 7/2$. In order to balance modulation depth and echo intensity for optimum sensitivity, a simple experimental procedure is proposed.
An additional improvement by 25% in DEER sensitivity is achieved with two consecutive chirp pump pulses. These pulses pump the Gd(III) spectrum symmetrically around the observation position, therefore mutually compensating for dynamical Bloch-Siegert phase shifts at the observer spins. The improved sensitivity of the DEER data with modulation depths on the order of 20% is due to mitigation of the echo reduction effects by the consecutive pump pulses. In particular, the second pump pulse does not lead to additional signal loss if perfect inversion is assumed. Moreover, the compensation of the dynamical Bloch-Siegert phase prevents signal loss due to spatial dependence of the dynamical phase, which is caused by inhomogeneities in the driving field. The new methodology is combined with pre-polarization techniques to measure long distances up to 8.6 nm, where signal intensity and modulation depth become attenuated by long dipolar evolution windows. In addition, the influence of the zero-field splitting parameters on the echo intensity is studied with simulations. Herein, larger sensitivity is anticipated for Gd(III) complexes with zero-field splitting that is smaller than for the employed Gd-PyMTA complex.

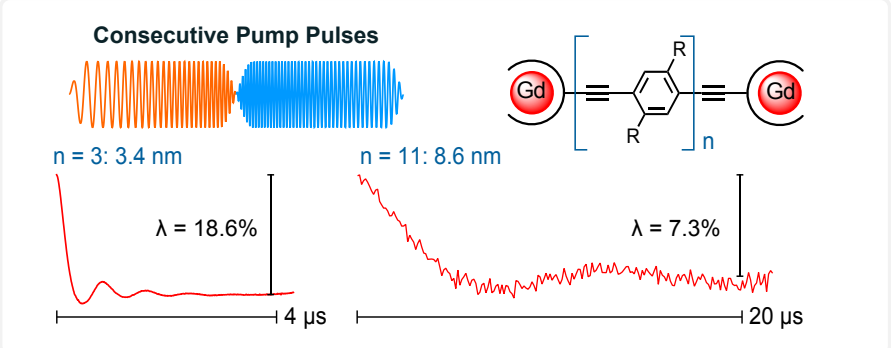

This chapter has been published as [164] and edited for consistency of notation:

A. Doll, M. Qi, N. Wili, S. Pribitzer, A. Godt, G. Jeschke, Gd(III)-Gd(III) distance measurements with chirp pump pulses, J. Magn. Reson. 259, 2015, 153-162

where M. Qi and A. Godt synthesized the Gd-rulers (Section 6.2.1.1) and calculated the expected distances (Section D.6.4). S. Pribitzer provided the MATLAB code for propagation of density matrices (Section D.8.1). N. Wili drafted initial simulations and contributed to the measurement and analysis of the data presented in Section 6.3.1 and Fig. 6.4.

6.1 INTRODUCTION

EPR-based distance determination using Gd spin labels is becoming an important alternative to the common approach based on nitroxide spin labels [140]. The majority of experiments to date rely on the four-pulse DEER (double electron-electron resonance) sequence to access distance information between a pair of Gd(III) centers [139]. Modifications of this approach involve the use of non-identical spin labels, in particular a Gd(III) center and a nitroxide [162, 163], as well as different experimental schemes, such as relaxation-induced dipolar modulation (RIDME) [161] or continuous-wave EPR [165].

Distance measurements involving Gd spin labels have been successfully demonstrated on a number of systems, including model compounds, peptides, nanoparticles, proteins and DNAs [72, 166–170, 160, 159, 158, 171–176]. Moreover, a promising biochemical property of Gd spin labels is the stability under reducing conditions, which recently enabled Gd-Gd distance measurements of peptides and proteins embedded in cellular environments [141, 142].

Because Gd(III) ions are in an $S = 7/2$ high spin state, high magnetic fields above 1 T are required to diminish unwanted contributions from the zero-field splitting (ZFS) to the obtained distance information [72]. Unlike with nitroxides at high magnetic fields, there is no pronounced orientation selection for Gd spin labels, which eases data analysis for the case of Gd-Gd distance measurements. However, there is one specific limitation in Gd-Gd DEER, namely that the dipolar modulation depth λ is only on the order of a few percent due to the broad EPR spectrum. This disadvantage is partially compensated by the large echo signal V_0, which facilitates a large DEER sensitivity $\eta = V_0 \cdot \lambda$. In particular, the sensitivity of ordinary Gd-Gd DEER is optimized by observation of the central $1/2 \leftrightarrow -1/2$ transition (CT) at the central peak of the spectrum and pumping the satellite transitions [143].

In this work, we investigate how Gd-Gd DEER experiments can be improved with chirp pump pulses synthesized by an arbitrary waveform generator (AWG). A key advantage of arbitrarily shaped pulses is the improved excitation bandwidth, as demonstrated in a number of recent studies [15, 74, 119, 113, 147, 137, 35, 64]. For chirp pulses, pulse performance can be quantified by the critical adiabaticity factor Q_{crit} using the Landau-Zener equation [35]. Moreover, limitations in excitation bandwidth imposed by the resonator can be compensated by adaptation of the frequency sweep of the chirp pulse to the resonator profile, which establishes ultra-wideband (UWB) EPR [74, 113].

We have demonstrated recently that the sensitivity of Gd-Gd DEER can be enhanced by rearranging the equilibrium populations and by using a chirp pump pulse (see Chapter 5). The focus of this previous study was on the long and intense chirp pulses required for efficient population transfer over frequency ranges beyond 1 GHz. In the present work, we elaborate further on the pump pulse. In principle, the DEER pump pulse should have a large adiabaticity factor for efficient inversion, which also requires long and intense pulses. However, experiments on $S = 1/2$ spins have shown that interference prohibits the use of long chirp pulses in four-pulse DEER [74, 119]. The key subject of this work is to identify and eventually alleviate additional limitations specific to the Gd(III) high-spin state with respect to chirp pump pulses.

The chapter is organized as follows. In Section 4.2, the compounds used in this study, i.e. the Gd-rulers $\mathbf{1_n}$ of the type Gd-spacer-Gd with the Gd-

PyMTA complex as the spin label, and experimental details are described. Experimental results and discussions follow in Section 6.3. First, we show that optimization of the modulation depth is not necessarily sensitivity optimization, since the pump pulse also has a distinct influence on the echo intensity V_0 (Section 6.3.1). Then, a rather simple experimental procedure for sensitivity optimization is presented and potential complications related to multi-quantum excitation by the pump pulse are addressed (Section 6.3.2). In Section 6.3.3, we use spin dynamics simulations to study the intensity of the (unmodulated) DEER echo V_0 as a function of pulse and ZFS parameters. Further on, we show how sensitivity is improved even further with two consecutive chirp pump pulses (Section 6.3.4). Finally, the new methodology is tested with Gd-rulers having long Gd-Gd distances up to 8.6 nm in Section 6.3.5. At several instances, we refer to the supporting information in Appendix D for related in-depth information and further discussions.

6.2 MATERIALS AND METHODS

6.2.1 *Sample preparation*

6.2.1.1 *Gd-rulers*

The syntheses of Gd-rulers $\mathbf{1_n}$ with $\mathbf{n}$ = {3, 5, 7, 9, 11} (see Fig. 6.1) will be published elsewhere. The stock solutions of Gd-ruler $\mathbf{1_3}$, $\mathbf{1_5}$ and $\mathbf{1_7}$ had concentrations of 5 mM in D_2O (pH 8.0), containing 28 mM, 38 mM and 30 mM NaCl, respectively. The stock solutions of Gd-ruler $\mathbf{1_9}$ and $\mathbf{1_{11}}$ had concentrations of 2 mM in D_2O (pH 8.0), containing 20 mM NaCl. For the EPR experiments, the stock solutions were diluted with D_2O and glycerol-d_8 (1:1 in volume). For Gd-ruler $\mathbf{1_3}$, 20 μl of a solution with a concentration of 600 μM was used. For all the other Gd-rulers, the sample volume was 40 μl with a concentration of 50 μM. In the case of Gd-ruler $\mathbf{1_3}$, also different

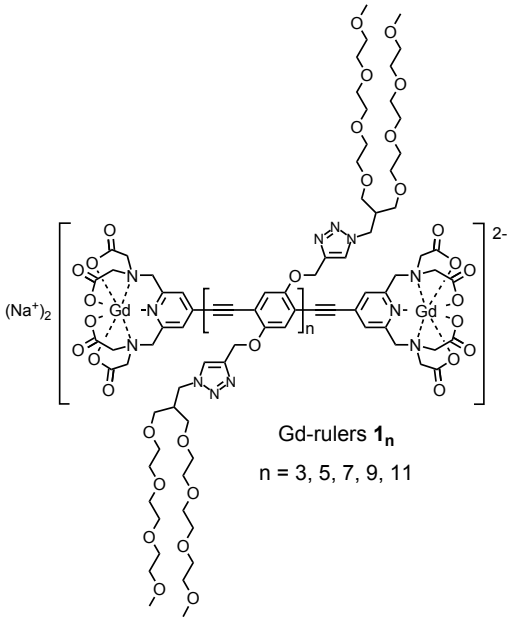

Figure 6.1 – Structures of Gd-rulers $\mathbf{1_n}$ with $\mathbf{n}$ = {3, 5, 7, 9, 11}. In all compounds two Gd(III)-PyMTA complexes are held at distance by a rodlike spacer. The number $\mathbf{n}$ determines the number of the repeating unit poly(*para*-phenyleneethynylene). For the set of $\mathbf{n}$ used in this study, the expected distances are 3.4 nm, 4.7 nm, 6.0 nm, 7.2 nm and 8.5 nm, respectively (see Section D.6.4). The stiffness of the spacer supports a narrow distance distribution between the two Gd(III) ions [156, 157]. Solubility in water/glycerol is made possible by the branched oligo(ethyleneglycol) side chains.

concentrations were prepared. These concentrations are found in Fig. D.12, where the actual concentration study is presented.

6.2.1.2 *Gd(III)-DOTA complex*

According to the procedure reported in [158], a stock solution of Gd(III)-DOTA complex (DOTA = 1,4,7,10-tetraazacyclododecane-1,4,7,10-tetraacetate) with a concentration of 40 mM was prepared. The stock solution was diluted with a 1:1 mixture in volume of water/glycerol to obtain the solution with a concentration of 200 μM that was used for the EPR experiments.

6.2.2 *EPR experiments*

All experiments were performed on a customized Bruker Elexsys E580 Q-band spectrometer [150] with a previously described extension by a 12 GS/s AWG (Agilent M8190A) [137]. The temperature was 10 K and the repetition rate of the pulse sequences was 342 μs in the case of Gd-ruler $\mathbf{1_3}$ and 716 μs for all the other Gd-rulers. An exception is the acquisition of resonator profiles $\nu_1(f)$ based on transient nutation experiments, which were all acquired at a repetition time of 342 μs. The timing and sequence parameters for these transient nutation experiments were identical to the ones described previously in [137].

6.2.2.1 *Four-pulse DEER*

In order to record the DEER signal $V(t)$, the pulse sequence $\pm(\pi/2)_{\mathrm{obs}} - \tau_1 - (\pi)_{\mathrm{obs}} - (\tau_1 + t') - (\pi)_{\mathrm{chirp}} - (\tau_2 - t') - (\pi)_{\mathrm{obs}} - \tau_2 - (\mathrm{echo})$ was used, where all observation pulses had a length of 12 ns and the time t' was incremented by Δt. The chirp pulses originated from the AWG and the relevant pulse parameters are described further below. Due to the chirp pulse, there was a time-shift between the time t' of the pulse sequence and the actual dipolar evolution time t. This time shift varied with the pulse parameters and depended most critically on the total length of the pulse. In this work, typical offsets between t' and t were on the order of 0.8 times the pulse duration. Note that this offset is determined by the frequency sweep and flip angle of the chirp pulse, as well as by the lineshape of the pumped spins. For Gd-ruler $\mathbf{1_3}$, the timings were τ_1 = 400 ns, Δt = 8 ns, and τ_2 = 4.5 μs or 6 μs. For Gd-ruler $\mathbf{1_5}$, we used τ_1 = 2 μs, τ_2 = 15 μs and Δt = 40 ns. For Gd-ruler $\mathbf{1_7}$, $\mathbf{1_9}$ and $\mathbf{1_{11}}$, the timings were τ_1 = 1 μs, Δt = 100 ns and τ_2 = 18 μs, 20 μs and 22 μs, respectively. For reference, an illustration of the pulse sequence with τ_1 = 400 ns, τ_2 = 4.5 μs and t' = 40 ns is shown in Fig. D.22.
For pre-polarized DEER experiments [137], two chirp pulses, with pulse duration of 2 μs each, preceded the above DEER sequence. The time gap between the two pre-polarization pulses was 300 ns and the time gap between the last pre-polarization pulse and the DEER sequence was 3 μs. The number of shots per point was 1000×2 in these experiments.
DEER data were processed with the software DeerAnalysis [95]. Regularization parameters for the five Gd-rulers were 1, 1, 10, 100 and 100, respectively. Details on the separation of the background signals are provided in Section D.6.3.

6.2.2.2 *Parameters of chirp pulses*

For the chirp pulses used in this work, we refer to the start and end frequencies of the frequency sweep as f_1 and f_2, respectively. The (absolute) difference between f_1 and f_2 defines the sweep width Δf. Accordingly, we specify the frequency range of a chirp pulse by Δf and f_2. Unless the sweep direction is explicitly indicated, $f_1 = f_2 - \Delta f$. In all instances, the end frequency f_2 is specified relative to the observation frequency f_{obs}. Hence, f_2 also denotes the closest nominal frequency spacing between the observation

frequency and the pump frequency. In brief, f_2 is also referred to as frequency spacing between pump and observation frequencies. A typical value for this offset is -300 MHz. The deviations between the nominal frequency spacing and the actual frequency spacing are discussed in the SI (see Fig. D.3).
Moreover, almost all chirp pulses used in this work take into consideration the resonator profile $\nu_1(f)$ [74]. Here, we consider idealized resonator profiles parametrized by the quality factor Q_L, the resonance frequency f_0, and the field strength ν_1. Representative parameters are $Q_L = 110$, $f_0 = 34.3$ GHz and $\nu_1 = 40$ MHz. The frequency range and resonator parameters define the actual form of the pulse's frequency sweep function and also yield the adiabaticity factor Q_{crit}. Due to the various transition moments related to Gd(III) ions, the adiabaticity is only indicated for the CT and referred to as Q_{CT}. Note that due to the idealized resonator profiles, the given adiabaticity factors are not as quantitative as in our work at X-band frequencies [35]. Nevertheless, Q_{CT} scales linearly with the pulse length t_p and quadratically with ν_1 for a given frequency range.
The edges of all chirp pulses are smoothened with a sine function parametrized by t_{rise}. For chirp pump pulses, we used $t_{rise} = 10$ ns, whereas for pre-polarization pulses, we used $t_{rise} = 30$ ns.

(Intentional page break)

6.3 RESULTS AND DISCUSSION

6.3.1 *DEER with a single chirp pump pulse*

The performance of distance measurements with a single chirp pump pulse was evaluated with Gd-ruler $\mathbf{1_3}$, whose echo-detected EPR spectrum cast in frequency scale is shown in red in Fig. 6.2a. The black dashed vertical line at the center denotes the position of the central line. Also shown in blue is the frequency response of a resonator with parameters f_0 = 34.27 GHz and Q_L = 120 fitted to experimental $\nu_1(f)$ data (brown).
In order to study the influence of the frequency positioning of the pump pulse relative to the observed A spins, we monitored the amplitude V_0 of the DEER echo ($V(t)$ at t = 0) as a function of the frequency offset between observation and pump frequencies. The frequency offset was varied by adjusting the end frequency f_2 of the chirp pulse, while keeping the other parameters fixed (Δf = 750 MHz, t_p = 128 ns). The real and imaginary components of V_0 are shown in Fig. 6.2b, where the normalization V_{ref} is the echo amplitude obtained in absence of the pump pulse. The data reveal a gradual reduction of V_0 as the chirp pulse approaches the A spins. Furthermore, the phase of the echo is gradually shifted due to a dynamic Bloch-Siegert phase [177]. When considering the magnitudes of the echoes (data not shown), the reduction of the echo V_0 to 75% and 50% of V_{ref} was at a frequency offset of -500 MHz and -260 MHz, respectively.
Given the significant reduction of V_0 by the pump pulse, the experimental DEER sensitivity $\eta = V_0 \cdot \lambda$ was examined for a variety of parameters of the pump pulse. In total, 42 pump pulses with a frequency offset f_2 of either -300 MHz or -400 MHz were tested. Four representative frequency ranges are indicated by the orange arrows in Fig. 6.2a. A collection of raw DEER data is found in Fig. D.1a, together with further information on the actual parameters of these 42 pulses. Interestingly, the obtained echo amplitudes V_0 and modulation depths λ show a correlation (see Fig. 6.2c). The benefit of large modulation depth λ is therefore offset by a smaller echo amplitude V_0, such that maximum modulation depth does not necessarily result in maximum sensitivity.
Further correlations were obtained when taking into consideration the adiabaticity factor of the pump pulse on the central transition, Q_{CT}. This factor quantifies the adiabaticity of the pump pulse and unifies all essential pulse parameters in one single parameter [35, 27, 4]. As is seen in Fig. 6.2d, the echo amplitude V_0 decreases as the adiabaticity of the pump pulse increases. Such a scaling can be explained by coherence transfer to unobserved multiquantum coherence due to inversion of the A spin's neighbor transitions (see also Section 6.3.3 and [160, 35]). The two round circles in the figure with gray color correspond to data obtained with Δf = 250 MHz. In this case, the performance of the pulse cannot be quantified solely by its adiabaticity, because edge effects become significant if $\Delta f/2$ is comparable to the field strength ν_1 of the passed transition [27].
In addition, also λ and Q_{CT} correlate in a sense that λ increases with adiabaticity (see Fig. D.1c). Since adiabaticity relates to the inversion efficiency of the pumped B spins, this result is not surprising and not specific to the high spin state of Gd(III). One would expect a similar scaling behavior for distance measurements between S = 1/2 spins.
For the DEER sensitivity $\eta = V_0 \cdot \lambda$, the competition between echo reduction and modulation depth results in optimum sensitivity for adiabaticities Q_{CT} on the order of 1 - 2 (see Fig. 6.2e). In this regime, the pump pulse cannot be considered as an adiabatic pulse and therefore does not provide a perfect population inversion. Note that for distance measurements between a Gd(III) center and a nitroxide, a related result was obtained for the optimum flip angle of a monochromatic pump pulse [158].
The found correlations may be used to set up DEER experiments with close

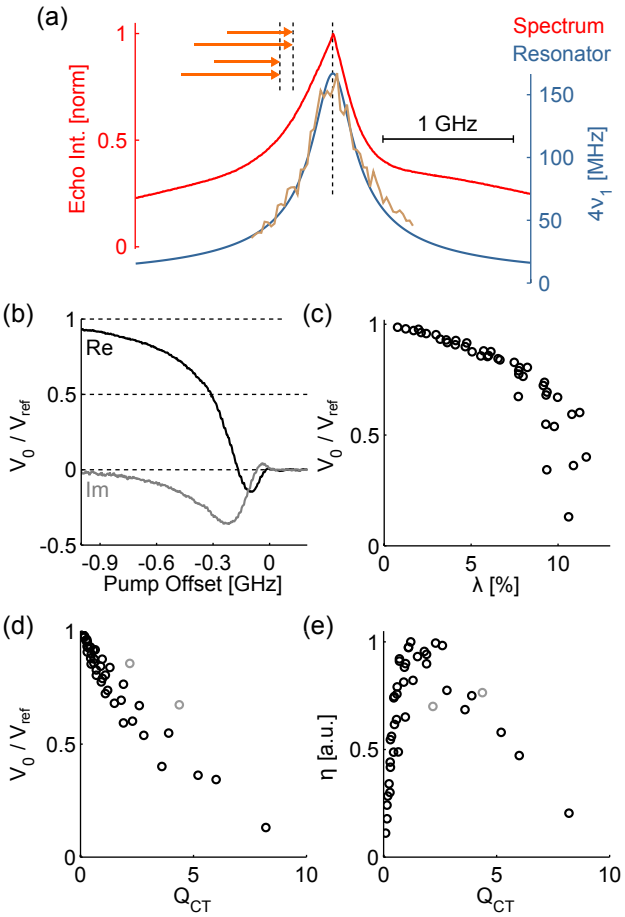

Figure 6.2 – Performance of a single chirp pump pulse. (a) Top: Field-swept echo-detected spectrum of Gd-ruler $\mathbf{1_3}$ cast in frequency units (red). Bottom: Resonator profile with quality factor 120 and maximum ν_1 of 41.7 MHz at 34.27 GHz (blue) and experimental $\nu_1(f)$ data (brown). The orange arrows indicate four relevant frequency positions of chirp pulses having Δf = [500, 750] MHz and f_2 = [−300, −400] MHz. (b) Real (black) and imaginary (gray) components of V_0 as a function of the pump offset frequency f_2 for a 128 ns long chirp with Δf = 750 MHz. The normalization V_{ref} was obtained in absence of the pump pulse. (c) Normalized echo intensity V_0 versus modulation depth λ obtained from 42 experimental datasets, each having different parameters for the chirp pump pulse. (d) Normalized echo intensity V_0 versus adiabaticity factor Q_{CT} of the chirp pulse on the CT for the 42 experimental datasets. The gray circles correspond to chirp pulses with Δf = 250 MHz. (e) DEER sensitivity $\eta = V_0 \cdot \lambda$ versus adiabaticity factor Q_{CT} of the chirp pulse on the CT for the 42 experimental datasets with the same color coding as in inset d.

to optimum sensitivity. For instance, one could determine the sweep width Δf, which results in an optimum adiabaticity Q_{CT} for a fixed offset $f_2 = -300$ MHz and pulse length t_{p}. This procedure does not require any calibration of the pump pulse, except the measurement of experimental $\nu_1(f)$ data to quantify adiabaticity. The DEER experiment with Gd-ruler $\mathbf{1_3}$ in [137] was set up in such a way. In general, however, these correlations are only valid for the ZFS parameters of the Gd-PyMTA label of Gd-ruler $\mathbf{1_3}$ at Q-band frequencies and for the set of pulse parameters sampled by the 42 experiments presented above. Entirely different scaling between modulation depth and echo reduction may apply for compounds labeled with different Gd(III) complexes, or for pulses with different parameters, in particular for a different frequency offset f_2 with respect to the observation frequency.

6.3.2 *An experimental shortcut to optimize sensitivity*

As discussed in the previous section, sensitivity optimization critically depends on the relative scaling between the modulation depth λ and the echo amplitude V_0. In this section, a fairly simple experimental procedure to maximize DEER sensitivity in situ is presented.

While the echo amplitude V_0 can be obtained directly from a single data point at $t = 0$, an accurate extraction of λ requires several data points. However, dipolar modulation leads to a reduction of the echo amplitude $V(t)$ for $t > 0$ due to both inter- and intra-molecular contributions. One can therefore obtain qualitative information on the actual λ by comparing $V(t)$ at $t = 0$ and at a later time t_r. This procedure requires only two data points and results in the *two-point parameters* $\lambda_{2P} = 1 - V(t_r)/V_0$ and $\eta_{2P} = V_0 - V(t_r)$. For the 42 datasets of the previous section, we found rather good correlation between these *two-point parameters* and the actual λ and η, independent on whether t_r = 1 μs or t_r = 4 μs was chosen (see Fig. D.1d,e).

Sensitivity can thus be optimized in situ by searching the maximum of η_{2P}: First, a pulse length t_p is chosen which is short enough for the expected distance. Second, η_{2P} is recorded while changing both the sweep width Δf and the end frequency f_2, thus optimizing the frequency positioning of the chirp pulse (see Section D.1). In this way, we obtained modulation depths beyond 10% with 128 ns long chirp pulses.

The best dataset of Gd-ruler **1**$_3$ from the previous section is shown in black in Fig. 6.3. The form factor in panel (a) shows a modulation depth of 10%. Optimization of η_{2P} resulted in the gray curve with modulation depth of 13% and a 24% improvement in η. The pulse parameters at this sensitivity optimum were Δf = 900 MHz and f_2 = −75 MHz. In agreement with the results of the previous section, the pump pulse had a reduced inversion efficiency ($Q_{CT} = 2$).

While the distance distributions in panel (b) are in good agreement, the form factor of the optimized pulse shows two spikes around t = 4 μs (see arrows). These artifacts are due to residual coherence excitation of the A spins by the pump pulse and typical for small frequency offsets $|f_2|$ between pump and observer pulses ($f_2 = -75$ MHz). Here, these artifacts could in principle be suppressed by digital filtering of the DEER data. However, in situations where such a small offset $|f_2|$ is not admissible, the pulse parameters which maximize η_{2P} up to a given minimum offset may be used instead. Moreover, the consecutive chirp pulses presented below in Section 6.3.4 do typically not require such small offsets.

Besides possible shortcomings due to residual excitation of A spins by the pump pulse, optimization of η_{2P} in high-spin systems may select pulse parameters which lead to higher harmonics of dipolar frequencies by inducing

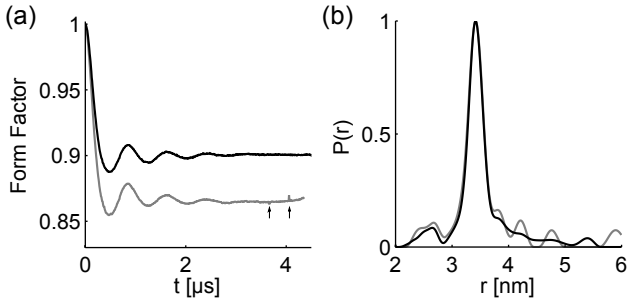

Figure 6.3 – DEER form factor (a) and regularized distance distribution (b) of Gd-ruler **1**$_3$. Black: 128 ns chirp pump pulse with Δf = 500 MHz, f_2 = −300 MHz and $Q_{CT} = 2.6$, which results in V_0/V_{ref} = 0.67 and λ = 9.9%. Gray: 128 ns chirp pump pulse with Δf = 900 MHz, f_2 = −75 MHz and $Q_{CT} = 2.0$, which results in V_0/V_{ref} = 0.62 and λ = 13.3%. The arrows denote spikes from a coherent pump pulse effect.

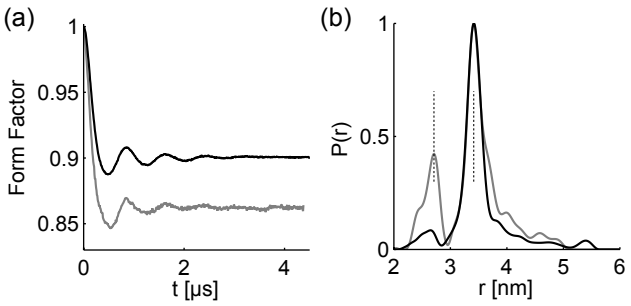

Figure 6.4 – Excitation of dipolar harmonics with chirp pulses. DEER form factor (a) and regularized distance distribution (b) of Gd-ruler $\mathbf{1_3}$. Black: same data as in Fig. 6.3. Gray: 64 ns chirp pump pulse with constant-rate frequency sweep over Δf = 600 MHz and f_2 = −300 MHz. To achieve large adiabaticities, the resonator was down-shifted by 500 MHz with respect to the illustration in Fig. 6.2a. For the strongest experimental ν_1 of 150 MHz for the CT, the adiabaticity Q_{CT} is 15.

$|\Delta m_S| > 1$ flips of the B spins. An example dataset is shown in gray in Fig. 6.4, together with the reference data in black from Fig. 6.3 above. The form factor in panel (a) shows a larger modulation depth for the higher harmonic data. In the distance distributions in panel (b), an additional peak due to the second harmonic is observed ($|\Delta m_S| = 2$). The vertical dashed black line indicates the position of the peak distance at 3.41 nm as well as the position of the second harmonic distance peak at 2.71 nm. In the distance domain, these two positions are related by a multiplication factor of $2^{-1/3}$. Under our current experimental conditions, we could only observe such distinct harmonics for pulses with extraordinary high adiabaticity factors $Q_{\mathrm{CT}} > 5$. These were achieved by application of the pump pulse at the resonator maximum, which enforced observation of the central line outside the resonator bandwidth, thus severely reducing the sensitivity η. However, for cases where (i) multi-mode resonators are used and (ii) echo reduction effects at large adiabaticity factors are tolerable, $|\Delta m_S| > 1$ excitation with chirp pulses may become more prominent. Further data is found in Section D.2, including a significant narrowing of distance distributions which resembles RIDME data recorded with Gd-ruler $\mathbf{1_3}$ [161].

6.3.3 *Dependence of echo intensity on ZFS splitting*

In this section, the echo reduction effect is studied using spin dynamics simulations of the A spins. In particular, these simulations give insight into the behavior with respect to the ZFS parameter D to predict the sensitivity of Gd(III) complexes with different D values. Detailed information on the simulation method is found in Section D.8.1.

At first, the validity of our simulation approach was tested by comparison to experimental data. Experimentally, the normalized DEER echo amplitude V_0/V_{ref} was recorded as a function of the frequency offset between observation and pump frequencies, as described above in Fig. 6.2b. Here, the pulse length t_{p} was 192 ns and the sweep width Δf was 850 MHz. The experimental data for real (black) and imaginary (gray) components are shown by the solid lines in Figs. 6.5a and b for Gd-ruler $\mathbf{1_{11}}$ that contains Gd-PyMTA and for a solution of Gd-DOTA complex, respectively.

The simulated data points are illustrated by the circles in Figs. 6.5a and b. As is readily seen, the simulations agree to the overall trend in experimental data. In particular, the excursion of the imaginary component due to a dynamical Bloch-Siegert phase shift [177] is comparable. When comparing the real component, simulated data show a stronger reduction effect.

The stronger reduction effect is observed even better when comparing the corresponding magnitudes in Fig. 6.5c. Here, data related to Gd-PyMTA and Gd-DOTA spin labels are shown in black and gray, respectively, and

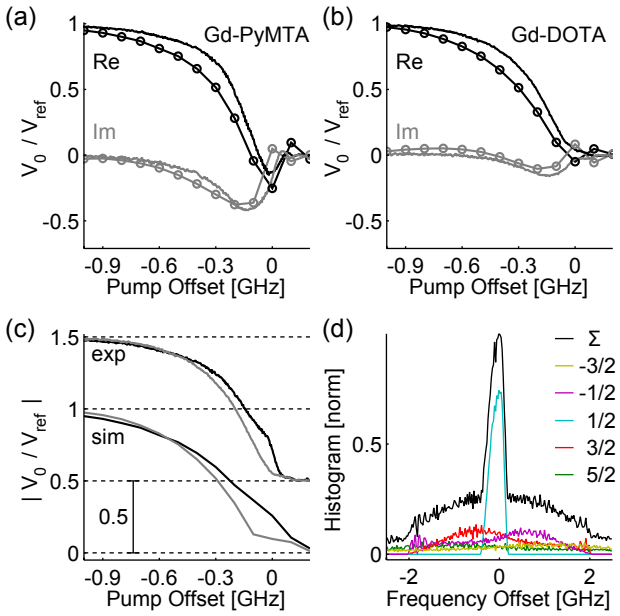

Figure 6.5 – Simulation and measurement of echo reduction related to Gd-PyMTA and Gd-DOTA spin labels. (a,b) Real (black) and imaginary (gray) components of V_0/V_{ref} related to Gd-PyMTA (a) and Gd-DOTA (b) as a function of the pump offset frequency f_2 for a 192 ns long chirp with Δf = 850 MHz. Simulated data points are indicated by circles. (c) Corresponding magnitude of V_0/V_{ref} related to Gd-PyMTA (black) and Gd-DOTA (gray). Top: Experimental measurements. Bottom: Simulations. See Fig. D.27b for simulation of a $S = 1/2$ spin. (d) Histogram of transition frequencies for $S = 7/2$ with D = 1 GHz averaged over polynomial E distribution and over orientation (see [155]) with $15 \times 20 \times 20$ points, respectively. The legend indicates the color of the transitions $m_S \leftrightarrow m_S - 1$ and of the sum Σ. The outermost satellite transitions are not shown and the step size for computing the histogram is 24 MHz.

simulated data are vertically offset below experimental data. Distinct features at experimentally relevant offsets $f_2 < 0$, such as the point where the magnitudes related to Gd-PyMTA and Gd-DOTA cross or the points where the magnitudes are 50%, appear horizontally displaced by roughly 100 MHz. For the phase of V_0/V_{ref} (see Fig. D.27a), a displacement of roughly 50 MHz to the same direction can be observed, which could be explained by an overestimation of the pulse amplitudes in the simulations. In general, the precision of such a simulation depends on how well the orientation-averaged spin dynamics of the Gd(III) centers and the field amplitudes inside the microwave resonator can be modeled. For our present purposes, the overall reproduction of experimental data by our simulations is considered to be sufficient.

As seen in Fig. 6.5c, the reduction of the echo intensity V_0/V_{ref} is more pronounced for Gd-DOTA ($D < 1$ GHz) than for Gd-PyMTA (mostly $D >$ 1 GHz). In the context of distance measurements between Gd(III) centers and nitroxides with monochromatic pulses, comparison of V_0/V_{ref} between Gd-DOTA and Gd-DTPA ($D > 1$ GHz) also revealed a stronger relative reduction effect for Gd-DOTA than for Gd-DTPA [158].

Since the echo V_{ref} in absence of the pump pulse itself depends strongly on D, the absolute echo intensity V_0 in the presence of the pump pulse is required to calculate the DEER sensitivity $\eta = V_0 \cdot \lambda$. For this purpose, V_0 and V_{ref} were simulated for a broad range of D values from D = 0.15 GHz to D = 2.5 GHz. Here, each D value corresponds to an average over orientations and a polynomial distribution of E values (see [155]), as indicated in Fig. 6.5d for D = 1 GHz. The frequency offset f_2 between pump and observer frequencies was kept fixed at −300 MHz. Note that a Gaussian weighting over ten different D values was used above in the simulations related to

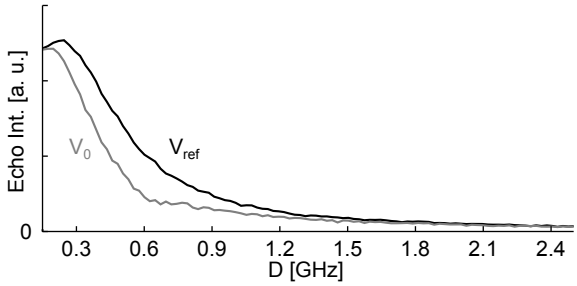

Figure 6.6 – Simulation of echo integral as a function of D in the presence (V_0, gray) and absence (V_{ref}, black) of a 192 ns long Δf = 850 MHz chirp pulse with offset $f_2 = -300$ MHz. See Section D.8.1 for further details on simulations.

Gd-PyMTA and Gd-DOTA spin labels.

Fig. 6.6 shows the results for the simulation of V_0 and V_{ref}. Due to the second order broadening of the CT, the DEER echo V_{ref} in absence of the pump pulse is larger for smaller D values. The monotonic increase in V_{ref} towards small D stops for $D < 0.4$ GHz, which results in a turnover of the V_{ref} curve at the smallest considered D values. Further information on the origin of this effect is found in the SI (see Fig. D.25).

As a consequence of the dependence of V_{ref} on D, the DEER echo V_0 in presence of the pump pulse is also larger for smaller D values. The echo reduction from V_{ref} to V_0 is strongest at D = 0.6 GHz and almost vanishes at the extremities for very small or very large D values (see Fig. D.24). The strong reduction effect at D = 0.6 GHz is due to spectral coverage of the A spin's neighbor transitions by the pump pulse. Hence, inversion of the neighbor transitions results in coherence transfer to double-quantum coherence, which does not contribute to the observed echo in the DEER experiment [160]. At the smallest D of 0.15 GHz, the neighbor transitions occupy (by first order) a frequency range of $\pm$0.3 GHz (compare Fig. 6.5d), such that spectral coverage by the pump pulse goes to zero and $V_0 \approx V_{\text{ref}}$. For large $D > 2$ GHz, the neighbor transitions are broadened to more than 8 GHz, which also results in negligible echo reduction. Based on our simulations, we could not identify any reduction mechanism other than spectral overlap with neighbor transitions, unless the pump pulse has direct spectral overlap with the observed A spins or spatial inhomogeneity of the driving field ν_1 is assumed (see Section D.8.2).

Notably, the scaling of the relative effect V_0/V_{ref} and the absolute intensity V_{ref} can readily be understood qualitatively. When observing the central line of the Gd(III) spectrum, the echo signal V_{ref} arises mainly due to CT contributions, which exhibit second order broadening. In this case, the echo reduction is primarily driven by spectral overlap between the pump pulse and the neighbor transitions of the CT, which exhibit first order broadening. Loosely speaking, a bisection of D therefore enhances the relative echo reduction effect by a factor of two and the absolute intensity by a factor of four, given that pump and observation parameters are unchanged. Using this simplified viewpoint, one realizes that absolute sensitivity improves towards smaller D. Clearly, the actual scaling depends on the pump and observation parameters. An experimentally relevant example is the bisection of $D = 1.2$ GHz to $D = 0.6$ GHz, as these are close to the mean values for Gd-PyMTA and Gd-DOTA, respectively. Here, our simulation showed an enhancement of the relative echo reduction effect by 1.7 and an enhancement of the absolute intensity by 3.8 when going from D = 1.2 GHz to D = 0.6 GHz.

Based on the simulations, a larger relative DEER sensitivity η for Gd(III) complexes with ZFS parameters that are smaller than for Gd-PyMTA, such as for instance Gd-DOTA, is anticipated. Because the modulation depth λ itself is not included in the simulations, an experimental evaluation of η for smaller ZFS is required. In any case, one would expect that for a given inversion

profile of the pump pulse, the narrowing of the satellite transitions at smaller D values results in a larger modulation depth λ. Nevertheless, there are other critical factors that influence the experimental DEER sensitivity. In particular, the environment of the spin label determines the phase memory time T_m and may also influence the echo reduction effect. When comparing experimental DEER data of different Gd(III) complexes in different environments, advantages of smaller ZFS parameters therefore may be offset by the changes induced by the environment.

6.3.4 *Consecutive chirp pulses*

Instead of one single chirp pump pulse, the pump pulse may be split into two consecutive chirp pulses of half the total pump pulse duration t_p that pump the Gd(III) spectrum on both sides. In order to investigate the effects associated to these consecutive chirps, data obtained with one single chirp pulse is compared to data obtained with the same single chirp pulse followed by a second one of equal duration, but frequency positioning mirrored at the observation frequency: An up-chirp that sweeps from f_1 to f_2 is therefore followed by a down-chirp that sweeps from $-f_1$ to $-f_2$. At first, we consider the echo reduction V_0/V_{ref}. Then, we turn to the modulation depth λ.
The echo reduction V_0/V_{ref} is shown in Fig. 6.7a. The black curve represents single pulse data and is identical with the experimental data of Gd-ruler $\mathbf{1_{11}}$ in Fig. 6.5c. The gray curve was obtained with the two consecutive pump pulses. Interestingly, a comparable echo intensity is observed at frequency offsets $|f_2|$ on the order of 100 to 200 MHz. The added pulse therefore does not necessarily result in a smaller echo. This can be explained by double-quantum coherence generation by the first pulse: If the first pulse perfectly inverts the A spin's neighbor transition with the lower resonance frequency, single-quantum coherence is fully converted to unobserved double-quantum coherence. The second pulse inverts the neighbor transition with the higher resonance frequency in the same way and converts the double-quantum coherence further to triple-quantum coherence (see Fig. D.26 for illustration). Consequently, the second pulse does not lead to any further coherence loss in this idealized case. In practice the inversion by the pump pulses is not perfect, such that one would expect some additional loss by the second pulse. In fact, large offset frequencies $|f_2|$ show a rather pronounced loss due to the second pulse, because the adiabaticity at such large offsets is not sufficient for population inversion (see also Fig. D.7).
Interestingly, the second pulse results in a larger echo at very small offset frequencies $|f_2| < 120$ MHz, which indicates the compensation of an echo reduction mechanism at small offset frequencies. For pulses with smaller sweep widths Δf, compensation is even more apparent (see Fig. D.6b). The generation of triple-quantum coherence described above cannot explain such

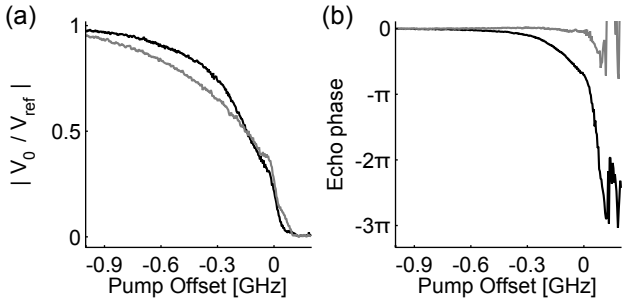

Figure 6.7 – Echo intensity with consecutive pump pulses as a function of the pump offset frequency f_2 with Δf = 850 MHz and t_p = 192 ns. (a,b) Magnitude and phase of V_0/V_{ref} of Gd-ruler $\mathbf{1_{11}}$ obtained with one single pump pulse (black) and consecutive pump pulses (gray). The black curve is also shown in black in Fig. 6.5c.

a compensation. One possibility is the mutual compensation of the Bloch-Siegert phase due to symmetry of the pump frequency windows: The phase of the echo for a single pump pulse is shown in black in Fig. 6.7b. Addition of the second pulse almost fully compensates the Bloch-Siegert phase.
As supported by simulations in the SI (see Fig. D.27 and Section D.8.2), the aforementioned compensation mechanism can be explained by spatial inhomogeneity of the driving field ν_1. In this case, the Bloch-Siegert phase induced by one single pulse becomes spatially distributed and partially dephases the spatially averaged echo. Application of the second pulse largely cancels the spatial dependence of the Bloch-Siegert phase, which increases the echo intensity. Note that such a compensation of Bloch-Siegert phase in presence of spatial inhomogeneity is highly reminiscent of the *ABSTRUSE* echo refocusing scheme with chirp pulses [35, 60]. Since the inhomogeneity in our microwave resonator is not known precisely, it is difficult to quantify the significance of the proposed compensation mechanism. However, we could not identify any other compensation mechanism that is supported by our spin dynamics simulations. Alternative compensation mechanisms would therefore most likely be related to spin couplings which are not considered in our simulations.
The influence of consecutive chirps on DEER data, and in particular on the modulation depth λ, is shown in Fig. 6.8. The form factors $V(t)/V_0$ are shown in panel (a) for the up-chirp (orange), the down-chirp (blue) and the consecutive chirps (green). The parameters of the chirp pulses used here were t_p = 128 ns, Δf = 625 MHz and $|f_2|$ = 300 MHz. With the consecutive chirps, the achieved modulation depth of 17% is almost the sum of the modulation depth of the individual pulses, 10% and 9%. The loss of 2% may be due to the longer overall pulse duration with the consecutive chirps, therefore causing interference of the dipolar evolution (see also Section D.3). Notably, the same experiment performed with shorter pulses shows a much smaller loss of 0.6% in the modulation depth (see Fig. D.11c).
The distance distributions computed from the data in panel (a) are shown in panel (b) using the same color coding. All the distributions are in reasonable agreement. Notably, pumping both sides of the spectrum does not induce $\Delta m_S > 1$ flips of the pumped spins (compare Fig. 6.4). Excitation of dipolar harmonics with chirp pulses is either related to the level connectivity of the inverted transitions or to the direct excitation of forbidden multi-quantum transitions passed by the chirp pulse [49, 153], thus requiring large adiabaticity factors and a large field strength ν_1 (see also Section D.2).
For a fair comparison of sensitivity with one single chirp and consecutive chirps, the overall pulse duration needs to be the same. Fig. 6.9 shows form factors (a) and distance distributions (b) of data obtained with one single

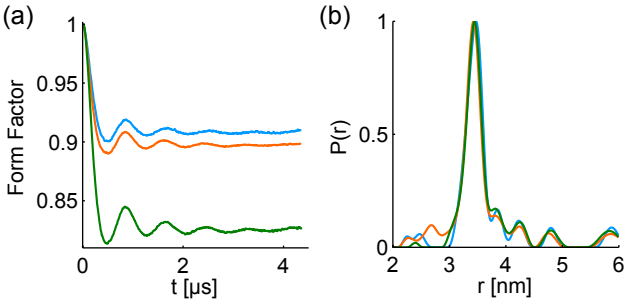

Figure 6.8 – Modulation depth enhancement with consecutive pump pulses with 128 ns length each, Δf = 600 MHz and $|f_2|$ = 300 MHz. Orange curves obtained with a single up-chirp, blue curves with a single down-chirp, and green curves with consecutive up- and down-chirp. (a) Form factor with modulation depths of 10% (orange), 9% (blue), and 17% (green). (b) Regularized distance distributions. The normalized echo intensities V_0/V_{ref} are 0.54 (orange), 0.72 (blue), and 0.54 (green). The primary DEER signals are shown in Fig. D.11a.

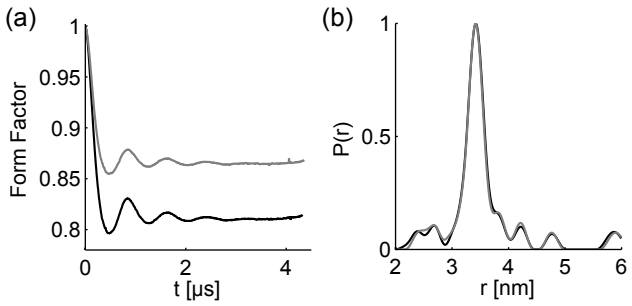

Figure 6.9 – Comparison of sensitivity-optimized DEER form factor (a) and regularized distance distribution (b) of Gd-ruler **1₃**. Black: Consecutive pulses with 128 ns total duration, Δf = 550 MHz, $|f_2|$ = 150 MHz and $Q_{CT} = 3.0$, which results in V_0/V_{ref} = 0.55 and λ = 18.7%. Gray: One single pump pulse with 128 ns duration, Δf = 900 MHz, $f_2 = -75$ MHz and $Q_{CT} = 2.0$, which results in V_0/V_{ref} = 0.62 and λ = 13.3%. Identical data as in Fig. 6.3.

chirp (gray) and consecutive chirps (black). The single chirp data are the same as the data shown above in Fig. 6.3. For the consecutive chirps, optimization of η_{2P} (see Fig. D.2) resulted in the pulse parameters Δf = 550 MHz and $|f_2|$ = 150 MHz, and therefore in an adiabaticity factor on the CT of 3. As compared to the single pump pulse, the broader combined pump frequency window and the larger adiabaticity factors of the consecutive pulses explain the increase in the modulation depth from 13.3% to 18.7%. By taking into consideration the echo intensities V_0/V_{ref}, the addition of the second pump pulse results in an enhancement of the sensitivity η by another 25%.
Moreover, the frequency spacing f_2 between pump and observation at optimum η_{2P} is larger than for a single pump pulse. In this way, proximity problems such as residual excitation of the A spins by the pump pulse or potential deviations from the weak coupling limit of the dipole interaction [72, 175] are alleviated. Another point worth mentioning is that there is no significant overhead in setting up the experiment with consecutive chirps. The parameters of the two pulses are related by symmetry and are optimized concurrently when maximizing the *two-point sensitivity* η_{2P}.
In summary, the consecutive chirp pulses constitute the most sensitive realization of DEER measurements between pairs of Gd(III) ions that we could achieve so far. As with any four-pulse DEER experiment with chirp pulses, the approach has a shortcoming at short distances due to the extended pulse duration of the pump pulse. Previously, we could faithfully obtain a distance distribution with a mean distance of 2.5 nm with a 64 ns pulse on a different system [74]. Five-pulse DEER techniques are considered to be free of this limitation [119]. Due to the high-spin state of Gd(III) ions and the adiabatic pulses required for five-pulse DEER, however, we would expect significant complication in implementing such a scheme. In any case, the shorter dipolar evolution windows required to measure distances below 2.5 nm alleviate sensitivity issues. The situation is opposite when determining long distances: Durations of chirp pulses become short compared to dipolar frequencies and longer dipolar evolution windows require high sensitivity.
Besides possible distortions due to the duration of chirp pulses, the ultra-wideband frequency windows of the pump pulses may influence the obtained distance information. While orientation selection effects in Gd-Gd distance measurements are not significant [140], contributions of the ZFS may be altered [72, 175]. For further reference, an overview over the subtle differences in distance distributions obtained with Gd-ruler **1₃** is provided in Fig. D.14.
In cases where chirp pump pulses are not admissible and monochromatic pump pulses are used, it is worth mentioning that the concepts elaborated in this study can be translated to monochromatic pulses. In particular, we demonstrate in Section D.7 how consecutive monochromatic pump pulses can be optimized in situ to achieve a sensitivity that is surprisingly competi-

tive to chirp pulses. As a result, consecutive monochromatic pump pulses optimized with sub-nanosecond timing reach a modulation depth of 12% at $V_0/V_{ref} = 0.7$, which corresponds to a sensitivity that is 83% of the best result with consecutive chirp pulses. Instead of two consecutive monochromatic pulses, a single multi-frequency pulse as demonstrated in [83] might also be able to reach a similar performance.

6.3.5 *Application to long distances*

Small dipolar couplings related to spins at a long distance require long coherent observation windows, and therefore a high sensitivity. For that purpose, consecutive chirp pump pulses in combination with pre-polarization pulses [137] are applied for distances beyond 6 nm. At first, the modulation depth achieved with Gd-ruler **1**$_7$ is analyzed (6 nm). Fig. 6.10a shows form factors obtained with a dipolar evolution window determined by $\tau_2 = 10$ μs (gray) and $\tau_2 = 18$ μs (black). The phase memory time T_m on the order of 9 μs explains the larger noise contribution of the data with the prolonged observation window (see Fig. D.13a). In fact, the data with $\tau_2 = 18$ μs was acquired 18 times longer than the data with $\tau_2 = 10$ μs.
A peculiar feature of the data in Fig. 6.10a is the difference in the modulation depth. For the shorter time window, the modulation depth is beyond 20%, whereas for the longer time window, the modulation depth is reduced to 15%. Further data is provided in Fig. 6.10b, where the dependence of the two-point parameter λ_{2P} on the delay τ_2 is shown. Accordingly, prolongation of the observation window results in a reduction of the modulation depth. In a previous study, it has been shown that this reduction mechanism does not only depend on τ_2, but also on temperature [168].
In order to gain further insight into the origin of this effect, we studied the dependence on τ_2 of both λ_{2P} and the echo signal V_0/V_{ref} at various concentrations. The data and descriptions are found in Section D.4 and are summarized as follows: First, no pronounced concentration dependence was observed, such that inter-molecular interactions can be excluded. Second, V_0/V_{ref} changed only marginally with τ_2 as compared to the changes in λ_{2P} with τ_2. The efficiency of refocusing the dipolar coupling, which evolves twice during the time interval τ_2 if $t = 0$, is therefore not significantly influenced by τ_2. Accordingly, τ_2-dependent dipolar dephasing mechanisms related to unwanted spin flips can be excluded.
One such mechanism is related to residual spin flips of unobserved spins by the observation pulses, which introduces additional dipolar evolution pathways [178]. Given the large frequency separation between pumped and observed spins, one would expect a majority of these additional evolution pathways to be negligible. Another mechanism is related to stochastic flips of

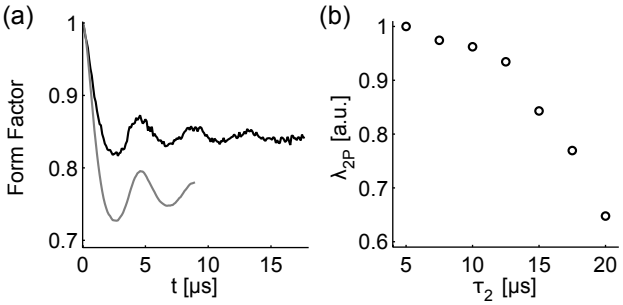

Figure 6.10 – Loss of modulation depth for long evolution windows studied with Gd-ruler **1**$_7$ (6 nm). The consecutive pump pulses each have $t_p = 192$ ns, $\Delta f = 700$ MHz and $|f_2| = 225$ MHz. (a) Form factors obtained with $\tau_2 = 18$ μs (black) and $\tau_2 = 10$ μs (gray). The modulation depths are on the order of 26% and 15%, respectively. See Fig. D.12a for primary DEER signals. (b) Normalized λ_{2P} as a function of τ_2.

the pumped spins by longitudinal relaxation (see also [168]). With the short longitudinal relaxation times encountered in Gd(III) complexes, one would actually expect such a τ_2-dependent dephasing mechanism to be relevant. Our investigations made so far could not fully elucidate the reason for the reduction of the modulation depth at prolonged τ_2 delays and further experiments are required. A relaxation driven mechanism appears most plausible, as also suggested by the temperature dependence of this effect [168]. Moreover, we expect this effect to be specific to high-spin Gd(III) ions, as we are not aware of such a reduction effect in distance measurements between nitroxides. The consequences of the reduction of λ for long time windows are twofold: First, it causes an additional reduction in sensitivity η. Nonetheless, the most stringent reduction in η at long τ_2 remains the small echo signal V_0. Second, the altered apparent λ at long τ_2 may complicate quantitative analysis of the inter-molecular background decay.

A series of long-distance measurements on three different Gd-rulers is shown in Fig. 6.11. Data obtained with Gd-ruler $\mathbf{1_7}$ (6 nm), Gd-ruler $\mathbf{1_9}$ (7.2 nm), and Gd-ruler $\mathbf{1_{11}}$ (8.5 nm), are shown in green, orange, and blue, respectively. As is already seen in the primary data in panel (a), dipolar oscillations are observed up to the longest distance, where τ_2 was set to 22 μs. At the beginning of each curve, a short decay is observed which is an artifact related to the pre-polarization pulses used in these experiments [137]. Here, pre-polarization doubled the echo signal V_{ref} (see Section D.5). The background decay in the primary data has been extracted according to the description in Section D.6.3. In the form factors in panel (b), modulation depths for the distances beyond 6 nm (orange and blue) are reduced to values below 10%. The significant differences in apparent modulation depths may also be related to the choice of pulse parameters (see Section D.1.2.2). The regularized distance distributions in panel (c) constitute well-defined distance peaks.

The dipolar evolutions windows used here allow to extract mean distances as well as the width of the distance distribution [179]. Mean distances predicted

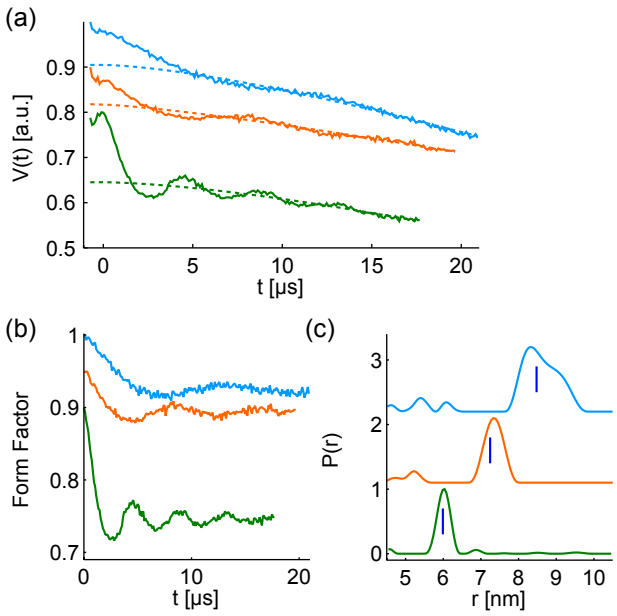

Figure 6.11 – DEER results for long distances using consecutive chirp pulses with 384 ns total duration and pre-polarization for Gd-ruler $\mathbf{1_7}$ (green), $\mathbf{1_9}$ (orange) and $\mathbf{1_{11}}$ (blue). (a) Primary DEER signals $V(t)/V_0$ acquired with 258, 195 and 158 scans, respectively. (b) Form factors with modulation depths on the order of 15% (green), 6% (orange) and 8% (blue). (c) Regularized distance distributions with mean distances of 6.0 nm, 7.3 nm and 8.6 nm, respectively. The blue vertical lines indicate mean distances of 6.0 nm, 7.2 nm and 8.5 nm calculated by taking the bending of the spacer into account (See Section D.6.4). All data are illustrated with vertical offset and parameters of the chirp pulses are given in Table D.2.

by taking the bending of the spacer into account [175] are shown by the blue vertical lines underneath the distance peaks (see Section D.6.4). Mean distances extracted from the experimental distributions (see caption and Section D.6.3) are slightly longer than the predicted distances. The deviation is up to 1.6% and presumably due to approximations in distance prediction and experimental uncertainty. In comparison to recent experiments at W-band [175], we notice apparent differences for the long Gd-ruler $\mathbf{1}_{11}$. These are discussed in Section D.6.3.
Interestingly, all the distance distributions presented in Fig. 6.11c appear symmetric. As previous experiments on structurally closely related nitroxyl-spacer-nitroxyl dissolved in ortho-terphenyl have shown, the bending modes of these compounds result in an asymmetric distribution [156, 157]. Since the shape of the distance distributions in Fig. 6.11c may contain artifacts and broadening due to insufficient length of the dipolar evolution window, we used Gd-ruler $\mathbf{1}_5$ with a 4.7 nm distance for a fully resolved distance distribution. For reference, the data is shown in Fig. D.15 and also does not reveal the asymmetric fingerprint found for nitroxyl-spacer-nitroxyl in ortho-terphenyl. We tentatively attribute the absence of a pronounced asymmetry in our data to the longer persistence length at the glass transition temperature of the D_2O/glycerol solvent.

6.4 CONCLUSIONS

In summary, chirp pump pulses significantly improve Gd-Gd DEER sensitivity. To the best of our knowledge, modulation depths on the order of 20% combined with sensitive observation at the maximum of the Gd(III) spectrum were previously not feasible with conventional DEER techniques. This sensitivity improvement is expected to be of importance for biophysical studies, where low concentration, reduced labeling efficiency and proton-containing environments are commonplace.
Moreover, the complication of finding suitable chirp pulse parameters to reach the sensitivity optimum is eliminated by means of a simple and fast setup protocol. According to this protocol, the only critical pulse parameter that remains to be adjusted is the length of the pump pulse, which needs to be adapted to the expected distance range. Importantly, the applicability of this protocol is not limited to Gd-Gd DEER.
The main limitation related to the high-spin state of Gd(III) is the inverse relation between the modulation depth λ and the echo intensity V_0. As demonstrated in our work, consecutive pump pulses partially alleviate this limitation. Another strategy is to employ a Gd(III) complex with ZFS parameters optimized to the experiment. In this respect, our spin dynamics simulations predict better DEER sensitivity for ZFS parameters smaller than the ones of the employed Gd-PyMTA label. Experimental variation of the ZFS by means of different ligands for the Gd(III) ion may also resolve the currently not fully understood aspects, such as the loss of the modulation depth at long evolution windows or other potential limitations of Gd-Gd DEER.
Important further considerations on Gd-Gd DEER with chirp pulses include the experimental performance at higher fields, where microwave power is reduced, and a comparison to alternative techniques, such as the RIDME technique.

7

SENSITIVITY CONSIDERATIONS

This chapter provides a description of the home-built AWG spectrometer at the time of writing this thesis and its performance (Section 7.1). A photograph of the main part with a Q-band microwave resonator connected is illustrated below in Fig. 7.1. Further in this chapter, the influence of the resonator quality factor Q_L on FT-EPR experiments and Gd-Gd distance measured is taken into consideration (Section 7.2).

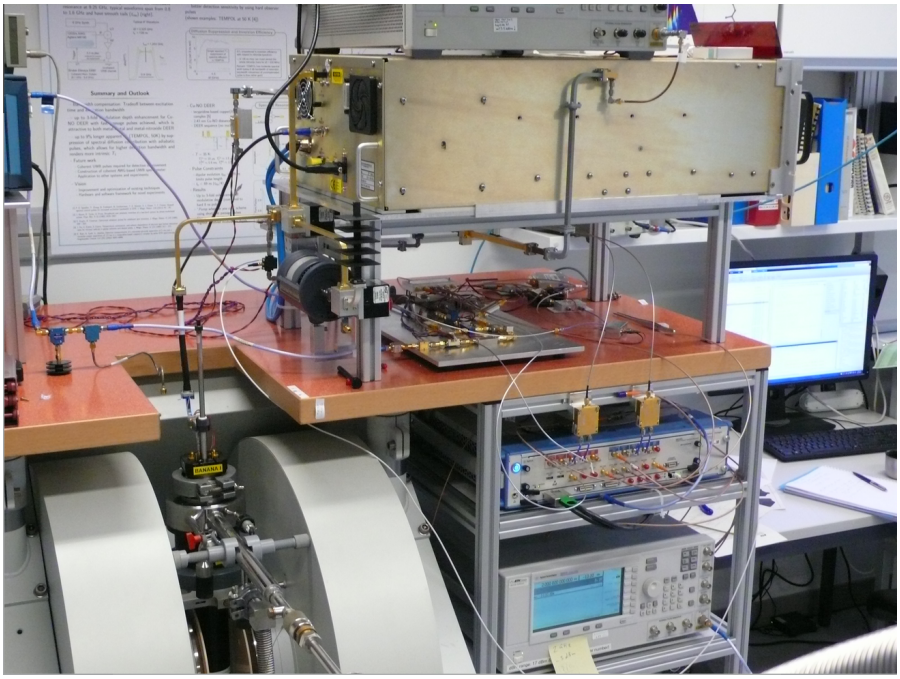

Figure 7.1 – Photograph of the main part of the home-built spectrometer. A schematic description follows in Section 7.1. Knowing the scheme of the spectrometer, the reader may recognize some of the devices on this picture. In particular:
The magnet containing a Q-band resonator within a flow-through cryostat is situated on the bottom left.
The large enclosure at the top-right with visible backside connectors is the high-power amplifier for Q-band microwave pulses. At the same height, a part of the X-band power amplifier is just visible on the left by the blue enclosure.
The X-band transceiver is mounted on a steel plate and situated below the Q-band power amplifier on the red table. The Q-band transceiver is built around the power amplifier, therefore distributed and not recognizable as a whole in this illustration.
Underneath the red table, the device with the blue frame and the numerous cables connected is the AWG. There are also two microwave synthesizers, one clearly visible below the AWG and another one visible in parts above the Q-band power amplifier. The one above the power amplifier provides the LO frequency for Q-band operation. For the synthesizer situated below the AWG, its microwave signal is merely of auxiliary purpose. A 10 MHz reference clock signal that serves as time reference originates from this synthesizer.
The workstation for controlling the spectrometer is on the right-hand side.

7.1 PERFORMANCE OF THE HOME-BUILT SPECTROMETER

7.1.1 *Description of the apparatus*

Up to the time of writing of this thesis, the home-built spectrometer presented in Chapter 4 underwent several upgrades. In the current state, experiments can be performed either at X band or at Q band. The core layout of the spectrometer operated in X band is shown in Fig. 7.2. The related components are listed in Table 7.1. In this configuration, the instantaneous detection bandwidth of 1 GHz covers the frequency window from 9 GHz to 10 GHz. The key layout of the spectrometer is due to the two mixers (M_1 and M_2) for frequency translation, which is referred to as a heterodyne transmitter/receiver layout. Accordingly, the (digital) input and output signals of the spectrometer are oscillating at an intermediate frequency (IF), which is translated to the desired microwave frequency by mixing with a local oscillator (LO).

To illustrate the frequency translation scheme and the role of the filters, an overview is provided in Fig. 7.3. The abscissa illustrates the microwave frequency relative to the LO frequency f_{LO}, which is fixed to 8 GHz at X band. An idealized resonator profile (green) defines the relevant frequency range. The instantaneous detection bandwidth of 1 GHz is indicated by the detection window shown in orange. Note that the digitizer has a Nyquist frequency of 1 GHz and is used to detect signals in the 1 GHz to 2 GHz frequency range. The detected signals are therefore deliberately folded down into the Nyquist window of the digitizer, which is an acquisition concept often referred to as *subsampling*.

The response of the high-pass filters F_1 and F_2 is illustrated on the top of Fig. 7.3. The role of these filters is to suppress the unwanted difference frequencies ($f_{LO} - f_{IF}$) in the lower mixing sideband from the wanted sum frequencies ($f_{LO} + f_{IF}$) in the upper mixing sideband for up- and down-conversion. For up-conversion, sideband suppression by F_1 is important to reduce spurious intermodulation products in the non-linear excitation arm (see Section C.2 for a detailed discussion). For down-conversion, sideband suppression by F_2 is important to reject noise contributions from the lower sideband. In fact, introduction of the filter F_2 improved the SNR of the spectrometer by 50%.

The filters F_3 and F_4 acting on the down-converted IF signal are illustrated in the bottom of Fig. 7.3. Note that the response of these IF filters has been translated up to microwave frequency for ease of illustration. These filters reject contributions in the down-converted signal that lie outside the relevant 1 GHz to 2 GHz frequency window. These filters therefore condition the analog signal for subsampling by the digitizer.

In some cases, one wants to exactly center the detection window with respect to the microwave resonator. This typically requires a change of the LO frequency by roughly $\pm$200 MHz. In these situations, a synthesizer can be connected instead of the fixed 8 GHz LO frequency source.

Having identified the frequency translation scheme of the spectrometer, the reader may recognize in Fig. 7.2 some of the core components that are present in any pulsed EPR spectrometer. These are (i) a 1 kW high-power microwave amplifier in the excitation arm (A_2), (ii) a circulator to separate excitation from detection (C_1), and (iii) a low-noise microwave amplifier (A_3) having a gain on the order of 30 dB with passive and active protection (L_1 and S_1). The high-power amplifier and the active protection switch are gated by one trigger signal each from the AWG (blue lines). Note the additional gating of switches S_2 and S_3, which allows for an optional further amplification on the order of 30 dB of the down-converted IF signal. Gating of hardware therefore requires three digital triggers from the AWG. The fourth (and last available) trigger provided by the AWG is used to trigger the digitizer. Coherence between excitation and detection is guaranteed by locking all frequencies to

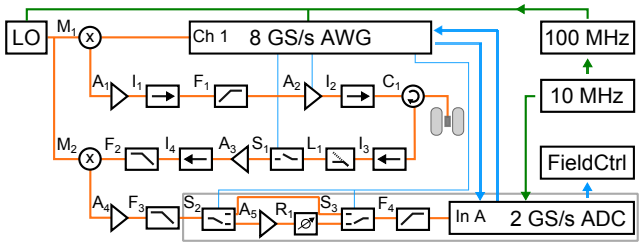

Figure 7.2 – Layout of the home-built AWG spectrometer showing the main signal path (orange), hardware triggers with controlled timing (blue), and clock signals (green). With respect to the layout shown previously in Fig. B.1, the gray box on the bottom indicates the changes made with respect to the older design. Moreover, an additional high-pass filter F_2 for image rejection was introduced before the down-conversion by M_2. The components for operation in either X or Q band are listed in Table 7.1 and 7.2. Microwave attenuators with fixed attenuation levels, for instance to level the LO amplitude, are not shown in the scheme.

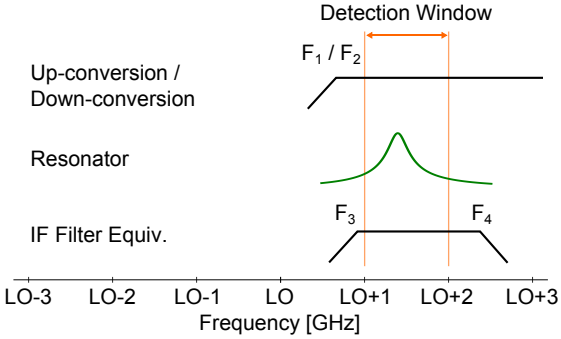

Figure 7.3 – Frequency conversion and filtering scheme in the home-built spectrometer. The abscissa denotes the microwave frequency relative to the LO frequency. At X band, the LO frequency is fixed at 8 GHz. At Q band, the LO frequency is adjustable within 33 GHz - 36 GHz. The effective 1 GHz detection window of the digitizer is indicated by the two orange vertical lines. (Top) Response of the microwave high-pass filters F_1 and F_2 to select the upper sideband for up- and down-conversion. (Middle) Resonator profile (green) indicating the relevant frequency range. The resonator parameters are $Q_L = 40$ and $f_0 = 9.4$ GHz. (Bottom) Response of the IF filters F_3 and F_4, up-converted to microwave frequency for illustration purposes.

a 10 MHz reference (clock signals indicated by green lines).
Different microwave components are used in Q-band operation, but the signal routing is very similar to the one shown in Fig. 7.2. The only significant difference in signal routing is that the up-conversion of AWG pulses is performed with an IQ mixer instead of a single mixer (M_1). As a consequence of that, two channels of the AWG in quadrature phase relation are required. The components that are specific to Q-band operation are shown in Table 7.2. With the LO frequency being tunable, the instantaneous detection bandwidth of 1 GHz can be adjusted within the frequency window from 33 GHz to 36 GHz. An adjustable frequency window is important at Q band, because there is a considerable spread in operation frequencies due to the different resonator designs and sample properties. One drawback of this adjustable frequency window is, however, that the high-pass filters F_1 and F_2 with fixed cutoff frequencies are no longer suitable. For up-conversion, such a filter is in principle not needed due to the IQ mixer (as discussed in more detail in Section C.2). For down-conversion, however, the absence of F_2 results in noise contributions originating from the lower sideband.
The spectrometer hardware at X and Q band is complemented by script-based control software executed on a host computer running MATLAB. To circumvent performance limitations and restrictions of vendor-supplied hard-

ware drivers for MATLAB, optimized driver interfaces for the AWG and the digitizer were developed by using C/C++ driver libraries and compilation into MATLAB, which yields so-called *MEX files*.

Label	Device
AWG	Agilent M8190A with options 002, 12G, AMP, SEQ, FSW, 02G Ch 1 is the AMP output
ADC	SP Devices ADQ412-4G PCIe
FieldCtrl	Bruker E32
M_1, M_2	MITEQ M0812
I_1, I_3, I_4	Meuro CIS080120F
I_2, C_1	RYT Ind. 300190
F_1, F_2	Minicircuits VHF-8400
F_3	Minicircuits SLP-2400
F_4	Minicircuits SHP-900+ (or SHP-600+ with lower cutoff)
A_1	Minicircuits ZX60-01412L
A_2	Applied Systems Engineering TWT 117X
A_3	Meuro MLB0812G3013
A_4	Minicircuits ZX60-V62
A_5	Herotek AF01-6362513B
S_1	Meuro SPST00518N6
S_2, S_3	Minicircuits ZASWA-2-50DR
R_1	Minicircuits ZX76-15R5-PP-5+
L_1	Meuro MLT080120T15
LO	Nexyn NXPLOS-0800-03615 (8 GHz)
CLK	Nexyn NXOS-PLXO-100-03593 (10 MHz $\rightarrow$ 100 MHz) Agilent E8257D 10 MHz RefClk (Master for ADC and all derived clocks) (Synth. also used to vary f_{LO} by $\pm$200 MHz)

Table 7.1 – Component listing for Figure 7.2 and instrument clocking scheme (CLK) when operated in X band

Label	Device
AWG	IQ pairs from Ch 1 and Ch 2 are the differential outputs converted to single-ended by two Picosecond 5310A Balun
M_1	IQ mixer assembled of Marki ML1-1040LS mixer (2x) Marki QH-0444 quadrature hybrid Marki PD-0140 combiner
M_2	Marki ML1-1040LS
I_1, I_4	Raditek Rad-34-36-K1
I_3	Wenteq F3336-3450-10
C_1	Wenteq F3836-3450-03
A_1, F_1, F_2, I_2,L_1	not connected
A_2	Applied Systems Engineering TWT 187KA with preamplifier 3J GAC-333620KF
A_3	3J LNAC-333630KF
S_1	Herley F9014-9
LO	Agilent E8257D frequency-doubled by Marki ADA1020 (33 GHz - 36 GHz) (not locked to the 10 MHz reference)

Table 7.2 – Components specific to Q-band operation. Components in Figure 7.2 that are not listed in this Table are the same as in Table 7.1.

Before starting an experiment, the entire pulse sequence is compiled and pre-loaded to the AWG. At the time of writing, the performance mentioned previously in Section 4.2.3 still describes the state of the art for pulse sequence compilation and transfer to the AWG. In particular, the nutation sequence to characterize resonator profiles is a three-pulse sequence with pulse parameters varied over a 2D grid with a size of 64×100 and requires on the order 20 seconds each for compilation and data transfer. At some instants, large phase cycles combined with large dimensions resulted in impractical compilation times up to 5 minutes.

In the near future, the transfer time to the AWG will be cut down dramatically by further optimization in the AWG driver. In particular, the current driver loads one waveform after another to the AWG instead of all waveforms at once, which is a significant overhead when transferring thousands of waveforms from the host computer to the AWG. Moreover, the compilation procedure awaits a speed-up by a more efficient handling of phase cycling and eventually also by compiling the sequence parallel on several processors. Note, however, that even at the current state such long compilation and transfer times are related to pulse sequences that acquire data during a long time period. Since the experiment can be run almost continuously at the requested repetition time (see also below), the *long* compilation time is not a significant overhead on the timescale of the entire experiment.

Once an experiment is started, the following scheme is repeated for each data point (see also Section B.1): (i) A hardware trigger issued from the digitizer to the AWG initiates the generation of the pulse sequence that corresponds to the actual data point. (ii) The AWG repeats this pulse sequence as specified by the number of accumulations per point. The pulse sequence of the AWG includes the four triggers for hardware gating as well as for the digitizer. (iii) A background process on the control computer recognizes that the digitizer averaged all accumulations and gathers the data. Upon success, the digitizer sends the hardware trigger to advance the AWG to the next data point, which corresponds to step (i) of the next data point. If the experiment requires a step in the magnetic field for the next data point, the digitizer releases another hardware trigger for the field controller before advancing the AWG to the next data point after an intentional delay of 20 ms.

Using this scheme, it is only the data transfer of averaged transients from the digitizer to the computer which may introduce a waiting time during the experiment, unless the magnetic field is swept. When acquiring transients with a length of 8192 data points, this transfer delay is below 1 ms and therefore not significant for repetition rates below 1 kHz. The reason why this delay became shorter than the value stated previously in Section B.1 is due to the replacement of an USB-based digitizer by a PCIe-based digitizer.

The control software handles the repeated transfers of averaged transients in a background process. The user can gather the acquired data from the background process, also during acquisition. However, when acquiring large datasets, there is a considerable amount of data accumulated within the background process. The copy of acquired data from the background process to the user workspace in MATLAB can therefore result in delays beyond the repetition time of the experiment. These user-requested data copies are, however, performed at most within a few seconds. Once the data is available in the MATLAB workspace, the post-processing steps as described in Section 4.2.2 are performed.

At the time of writing this thesis, there were three people that knew how to operate the spectrometer at X band, excluding the author of this thesis. The ease of use in terms of setting up and running experiments and overall productivity appeared to be adequate. However, switching between X-band and Q-band operation requires to exchange a few connections in the main signal path as well as in the control path. A printed circuit board (PCB) to automate switching by means of microwave relays and distribution of trigger signals has been developed. The incorporation of this PCB for automated

switching will be accomplished by a number of modifications in the control software to ease handling of the dual-frequency spectrometer.

7.1.2 *X-band sensitivity*

In order to test the detection sensitivity of the AWG spectrometer at X band, an approach similar as reported in [180] was followed. In particular, the authors used a γ-irradiated quartz cylinder having 2 mm diameter and 10 mm length, where the radiation dose was exactly 1 kGy. Single shot echoes obtained with this sample on various spectrometers allowed to compare detection sensitivities. In particular, the noise level related to this sample was above the quantization noise of common 8-bit digitizers and resulted in signal-to-noise ratios (SNR) on the order of 25 [180].
In our lab, we had available a γ-irradiated Herasil cylinder with 2 mm diameter and 4.7 mm length, irradiated at a nominal dose of 10 kGy. The sample used in this context thus had a higher radiation dose and different quartz properties than the sample used in [180]. We therefore do not intend to compare our results to the results reported in [180], but compare the SNR obtained with the home-built spectrometer to the SNR obtained with our newest commercial Bruker Elexsys E580 spectrometer, which was bought in 2008 and represents the current state of the art for commercial pulsed EPR spectrometers, at both X and Q band.
The experiments were first performed on the commercial spectrometer. Subsequently, the resonator (Bruker MS3) with the sample still inserted was transferred to the AWG spectrometer to perform the experiments thereon. No attempts were made to adjust the quality factor of the resonator to the narrow EPR spectrum. In fact, a comparison of the excitation profile $\nu_1(f)$ between the two spectrometers under broadband conditions was also of interest.
The resulting profiles $\nu_1(f)$ for the AWG spectrometer (orange) and for the commercial spectrometer (blue) are shown in Fig. 7.4a. The larger power achieved by the AWG spectrometer is due to the short path lengths between the high-power amplifier and the resonator, and due to the absence of a variable attenuator after the high-power amplifier. It also appears that the quality factor Q_L in the AWG spectrometer was slightly lower than in the commercial spectrometer. Such differences are not surprising when taking into consideration variations in output impedances among the two spectrometers. The frequencies of maximum ν_1 were chosen to conduct the spin echo experiments.
Hahn echoes were formed by pulses with durations of 16 ns and 32 ns, where the pulse amplitudes were calibrated by means of transient nutation. We have chosen to digitize a long transient with 4 μs duration, where the echo was centered at a position of 1 μs. The inter-pulse delay was set to 1.5 μs. FT magnitudes of one single echo obtained with the AWG spectrometer (orange) and the commercial spectrometer (blue) are shown in Fig. 7.4b. Up to a small frequency shift, the spectra recorded on both spectrometers are equivalent. The echo signals were relatively small and required analog conditioning prior to digitization. On the commercial spectrometer, the low-noise amplifier (LNA) was activated and the IQ pairs carrying the echo signal were amplified further by 28 dB and low-pass filtered at a 200 MHz cutoff frequency (6 dB). On the AWG spectrometer, the down-converted IF signal was amplified by 18 dB.
For studying noise, the FT magnitudes within the entire detection range are of interest. For this purpose, the normalized energy densities on a logarithmic scale are shown in Fig. 7.4c, where 0 dBc corresponds to the maximum intensity of the echo. To minimize noise contributions to this reference intensity, it was extracted from 200 echo transients. Note that the relevant frequency range spans over 1 GHz in both cases. On the AWG spectrometer, a single (real-valued) signal was acquired with a sampling rate of 2 GSa/s.

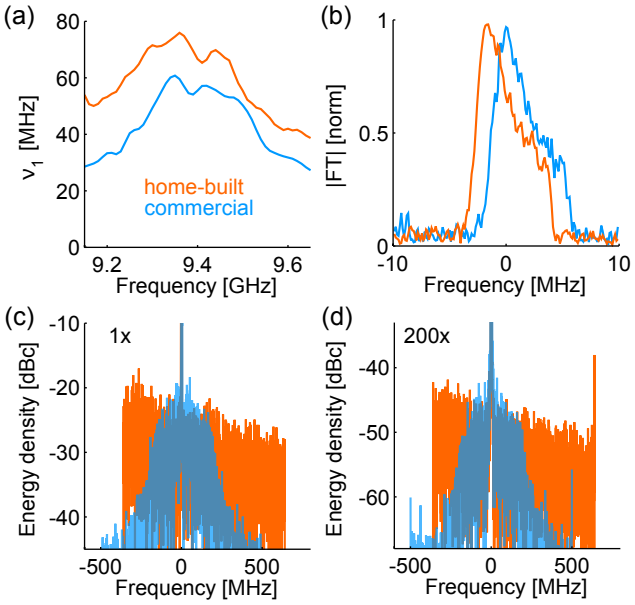

Figure 7.4 – Comparison of detection sensitivity at X band between the AWG spectrometer (orange) and a commercial Bruker Elexsys E580 spectrometer (blue). The sample was a cylinder (2 mm diameter, 4.7 mm length) of γ-irradiated Herasil (10 kGy). The resonator was a Bruker MS3 split-ring resonator. (a) Resonator profiles $\nu_1(f)$ obtained with AWG spectrometer (orange) and with commercial spectrometer (blue). The Hahn echoes were observed at the corresponding maxima, which were at 9.36 GHz and 9.35 GHz, respectively. (b) Magnitude FT of one single spin echo transient obtained with pulses of 16 ns and 32 ns duration having an inter-pulse delay of 1.5 μs. The transient had a duration of 4 μs, where the echo was centered at 1 μs. On the commercial spectrometer, the receiver had a *microwave amplifier* switched on and a *video gain* of 30 dB. On the AWG spectrometer, the attenuator R_1 was set to 12 dB. (c) Energy density of the same echo transient in logarithmic scale, where the reference level (0 dBc) corresponds to the maximum of the spectrum. (d) Energy density of 200 averages of the echo transient in logarithmic scale, where the reference level is again the maximum of the spectrum. The y-axis of this panel has been shifted by $20 \cdot \log_{10}(\sqrt{200}) \approx 23$ dB.

On the commercial spectrometer, an IQ pair, in other words a complex-valued signal, was acquired with a sampling rate of 1 GSa/s. The only post-processing step applied to the raw data from the AWG spectrometer was a digital down-conversion (including computation of the analytic signal by the Hilbert transform [127]), such that the zero-frequency shown on the abscissa coincides with the excitation frequency of 9.36 GHz.

The most apparent difference in the energy densities is the narrower bandwidth for the commercial spectrometer (blue) due to the 200 MHz low-pass filter. The AWG spectrometer on the contrary acquired noise within the entire 1 GHz detection window of the digitizer. The curvature in the AWG spectrometer noise floor (orange) was mainly due to the high-pass filter F_3, whose filter response was *folded up* into the relevant detection window (see also Fig. 7.3). Around zero frequency, the noise floor of the commercial spectrometer was larger.

It is at hand that if the SNR in time-domain of the data shown in panel (c) is evaluated, the AWG spectrometer performs worse due to the broad spectral noise contributions. However, if the AWG data is digitally conditioned by an equivalent low pass filter with 200 MHz cutoff frequency (6 dB), the SNR of the AWG spectrometer is better by 24% (14.2 vs 11.4). Due to the curvature of the noise floor, the SNR obtained with the AWG spectrometer does depend on the actual detection frequency at IF. In this sense, we draw the conservative conclusion that both spectrometers yield comparable sensitivity for acquiring small signals at X band with single shot measurements.

In order to test coherent averaging, 200 individually acquired echo transients were averaged and the resulting energy densities are shown in Fig. 7.4d. The ordinate has been shifted by 23.01 dB with respect to the ordinate shown in panel (c). This shift corresponds to the reduction in noise floor level that one expects if 200 echo transients are coherently averaged. As is readily seen when comparing panels (c) and (d), both spectrometers reproduce the expected reduction in noise floor. The small peak above the noise floor at the highest frequency of the AWG spectrometer is a DC offset folded up to the relevant detection window.

Note that this does not tell anything about the long-time stability of the phase [180]. In this respect, it should be emphasized that the long-term stability of the AWG spectrometer at X band is determined by the stability of the 10 MHz reference clock and of the frequency locking of derived clocks to this reference. In the commercial spectrometer on the contrary, a free-running microwave source, which has a reduced frequency stability, is used. However, the commercial spectrometer features compensation lines to minimize the impact of frequency drifts on echo phase. In the AWG spectrometer, such a compensation line was not installed. Nevertheless, when probing the echo phase in 5 minute intervals for a prolonged time interval of a full day, the peak-to-peak phase deviation with the AWG spectrometer was within $\pm 7^\circ$ 2 hours after the spectrometer has been switched on. Note that this stability required that the 10 MHz reference has been running for few hours before switching on all other parts of the spectrometer. Otherwise, the phase may not be stable due to the instabilities in device-internal phase locking within the AWG and the digitizer. Best mutual coherence between the sampling clocks of excitation and detection is actually achieved if these clock signals at microwave frequencies of 8 GHz and 2 GHz are deduced from phase-locked dielectric microwave oscillators rather than from a reference oscillator at lower frequency. In the future, this will be implemented by using the 8 GHz microwave oscillator that is already used as LO for up- and down-conversion.

Another factor that adds to the sensitivity for long acquisition times is related to interrupts in acquisition due to data transfer and reprogramming of hardware. In this respect, the AWG spectrometer is superior to the commercial spectrometer, in particular for FT EPR purposes where the entire echo transient is required. While the commercial spectrometers have an adequate data acquisition speed when a single point or a boxcar integration of the echo transient is requested, this is not the case if the entire echo transient needs to be digitized. In fact, a delay beyond one second has been observed repeatedly when acquiring echo transients - single shot or multiple averages per transient - with commercial spectrometers, even with a newer model acquired in 2015 in another laboratory. On our commercial spectrometer, the 200 individual echo transients recorded to test coherent averaging required more than 5 minutes of acquisition time. This long delay is mostly a software issue awaiting correction, since the actual transfer times are much faster. This can for instance be recognized when monitoring the echo transient in real-time during optimization of pulse parameters with the Bruker control software.

Altogether, the sensitivity of the AWG spectrometer at X band competes rather well with the sensitivity of commercial spectrometers. If one would want to further enhance the SNR, the following aspects are important. First, the components in the microwave front-end of the receiver are key for a good SNR. The noise characteristics of the utilized LNA are characterized by a nominal noise figure of 1.3 dB. The components prior to the LNA, namely the protection switch S_1 and limiter L_1, have insertion losses on the order of 1.8 and 0.9 dB, respectively. The passive limiter turned out to be very important when examining long high-power pulses and shall never be removed. Determining the SNR with and without the limiter made only a difference of 8%. With respect to the utilized active switch, it must be noted that it is specified to switch from 10% to 90% transmission in 50 ns, which

resulted in approximatively 100 ns to switch the receiver from 0% to 100%. With hard pulses, this switch was turned on 50 ns after the falling flank of the last pulse, resulting in a rather long dead-time of 150 ns. While a short dead-time was not important throughout this thesis, a switch with similar transmission characteristics but ten times faster switching time (HP 33144A) is available to reduce the dead-time below 100 ns.
A second important aspect for the SNR comes after the microwave LNA, where one needs to make sure that down-conversion and detection do not capture noise outside the signal bandwidth of interest. In the AWG spectrometer, this is achieved with filters, as has been explained and illustrated in Fig. 7.3. The filter F_2 for instance rejects noise from the lower microwave sideband and resulted in an SNR improvement on the order of 50%. Note that sideband rejection is also possible with an IQ mixer for down-conversion of detected echoes, as implemented in the commercial spectrometer.

7.1.3 *Q-band sensitivity*

Exactly the same procedure as at X band was applied at Q band. The resonator used here was a home-built design that accepts sample tubes with 3 mm outer diameter [150]. Fig. 7.5a shows the resonator profiles $\nu_1(f)$ obtained with the AWG spectrometer (orange) and with the commercial spectrometer (blue). The quality factor was on the order of 250. The spikes around the central position observed in the commercial spectrometer were reproducible and due to reflections in the microwave path. The AWG spectrometer has a very short microwave path between the amplifier and the resonator, which explains the higher power and the absence of spikes due to reflections in $\nu_1(f)$. Note that similar to X band, there is no microwave attenuator after the 200 W Q-band amplifier. At Q band, one can however switch to an alternate pathway between high-power amplifier and resonator, which contains a variable microwave attenuator.
As expected, the echo signal at Q band was much higher than at X band. When acquiring the echo with exactly the same pulse sequence as at X band, amplification needed to be reduced. Accordingly, the LNA of the commercial spectrometer was switched off and the down-converted IQ signals were amplified by 24 dB. For the AWG spectrometer, the amplifier A_5 was bypassed. The energy densities for one single echo are shown in Fig. 7.5b. The noise floor obtained with the AWG spectrometer (orange) had a similar curvature as at X band, because it was determined by the filter F_3. The noise floor obtained with the commercial spectrometer was more flat than at X band. This is because the analog noise level was hidden below the quantization level of the 8-bit digitizer. Note that for the AWG spectrometer, a 12-bit digitizer is used, which has a much higher dynamic range.
If even larger echo signals would be measured, one would expect that the relative noise floor level of the AWG spectrometer is reduced according to the echo amplitude. For the commercial spectrometer on the contrary, one would expect that the relative noise floor stays at this level, even for larger signals. The larger dynamic range of the AWG spectrometer therefore results in a better SNR for large echo signals.
In order to compare the noise floor due to the analog components, the echo signal was reduced by setting the inter-pulse delay to 5 μs. On the commercial spectrometer, the echo was acquired by switching on the LNA and amplifying the down-converted IQ signals by 6 dB. On the AWG spectrometer, the amplifier A_5 was still bypassed. For a single acquisition, the energy densities are shown in Fig. 7.5c. The characteristic curved noise floor of the AWG spectrometer can also in this case be recognized. For the commercial spectrometer, the noise floor was shaped by the 200 MHz filter, as has been observed in the previous section when acquiring a small signal at X band. As opposed to the situation at X band, the noise level of the AWG spectrometer was above the noise level of the commercial spectrometer. If the echo

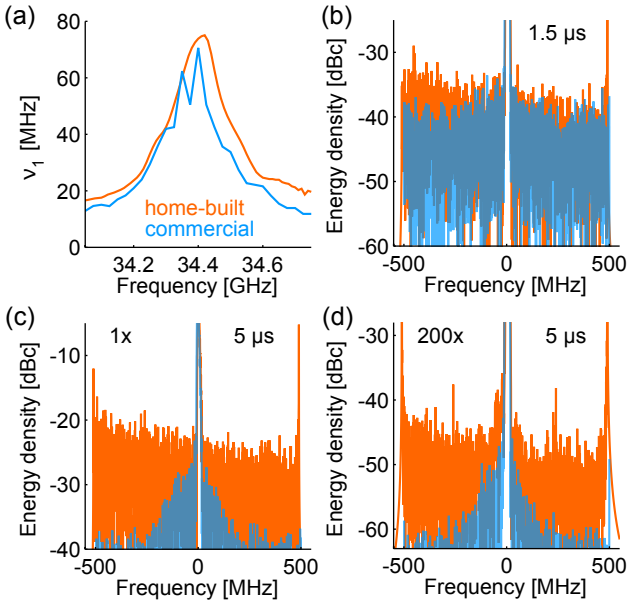

Figure 7.5 – Comparison of detection sensitivity at Q band between the AWG spectrometer (orange) and a commercial Bruker Elexsys E580 spectrometer (blue). The sample was a cylinder (2 mm diameter, 4.7 mm length) of γ-irradiated Herasil (10 kGy). The resonator was a home-built design described in [150]. (a) Resonator profiles $\nu_1(f)$ obtained with AWG spectrometer (orange) and with commercial spectrometer (blue). The Hahn echoes were observed at the corresponding maxima, which were at 34.41 GHz and 34.4 GHz, respectively. (b) Energy density of one single echo transient in logarithmic scale, where the reference level (0 dBc) corresponds to the maximum of the spectrum. The spin echo transient was obtained with pulses of 16 ns and 32 ns duration having an inter-pulse delay of 1.5 μs. The transient had a duration of 4 μs, where the echo was centered at 1 μs. On the commercial spectrometer, the receiver had a *microwave amplifier* switched off and a *video gain* of 24 dB. On the AWG spectrometer, the amplifier A_5 was bypassed. (c) Energy density of one single echo transient with inter-pulse delay set to 5 μs. The AWG spectrometer had the same receiver settings, whereas the commercial spectrometer had a *microwave amplifier* switched on and a *video gain* of 6 dB. (d) Energy density of 200 averages of the echo transient with an inter-pulse delay set to 5 μs. The y-axis of this panel has been shifted by $20 \cdot \log_{10}(\sqrt{200}) \approx 23$ dB.

transient obtained with the AWG spectrometer is digitally conditioned by an equivalent low pass filter with 200 MHz cutoff frequency (6 dB), the SNR of the commercial spectrometer is better by 75% (64.8 vs 37.2).

Note that by measuring the two-pulse echo decay, a slightly slower decay was observed on the AWG spectrometer than on the commercial spectrometer. At the inter-pulse delay setting of 5 μs, the echo on the AWG spectrometer was larger by 1.7 dB than on the commercial spectrometer. Hence, the noise floor of the AWG spectrometer illustrated in Fig. 7.5c needs to be up-shifted slightly. The reason for the different decay times is not clear. Due to the local concentration of E′ centers in our sample, instantaneous diffusion effects are significant. For identical decay characteristics on both spectrometers, we have set up the amplitudes of the $\pi/2$ and π pulse with transient nutation. Clearly, comparison of sensitivity at Q band would favor a sample with a smaller spin concentration or volume.

The energy density when averaging 200 individual echo transients is shown in Fig. 7.5d. The noise floors appear almost as expected. For the AWG spectrometer, however, signatures of unwanted signal correlations are observed. At a frequency of -500 MHz, for instance, a strong peak is encountered. This is due to an artifact of the digitizer at half the sample frequency. Since one does usually not cross the borders of the Nyquist zone, this artifact is not a severe limitation. However, sampling of the acquisition trigger provided by

the AWG has the same artifact at half the sample rate. The time resolution of the acquisition trigger therefore needed to be set to 1 ns. Otherwise, at the maximum possible time resolution of 0.5 ns for this trigger signal, there was a bi-stability in the phase of subsampled echo transients.

Further unwanted peaks in the noise floor in Fig. 7.5d are observed at ± 250 MHz, which corresponds to the quarter sampling frequency of the digitizer. Note that these small artifacts appear due to the small signal amplitude at the digitizer. In fact, the echo amplitude at $\tau = 5$ μs was only 6% of the full scale amplitude of the digitizer. We could suppress the peaks at ± 250 MHz in two ways, namely by ten-fold amplification of the down-converted signal with A_5 or by locking the digitizer sampling rate with an external 2 GHz microwave carrier rather than deriving it internally from the 10 MHz reference clock. The only artifact visible in Fig. 7.5d that is currently not well understood is the increased noise within ± 100 MHz around the center. It is probably also related to the small signal level at the digitizer, but further experiments are required for clarification.

Overall, the AWG spectrometer can not yet compete with the sensitivity of the commercial spectrometer at Q band, for the case that small signals need to be acquired. It is worth mentioning that the microwave front-ends of the AWG spectrometer and the commercial spectrometer are almost the same. In particular, both spectrometers have the same active protection switch followed by low noise amplifiers of similar performance. There is therefore not much room for improvement at the front-end. However, as mentioned above, there is no filter F_2 prior to down-conversion at Q band. At X band, this filter improved the SNR by 50%. At Q band, we would expect an even larger improvement, because all components in the Q-band receiver have broad bandwidths, including the down-conversion mixer. Noise contributions in the lower sideband therefore couple rather well to the down-conversion mixer.

In order to incorporate a down-conversion filter with a fixed cutoff frequency for noise rejection, the architecture of the spectrometer at Q band needs to be modified. In particular, a two-stage up- and down-conversion would enable better rejection of the lower sideband, a so-called superheterodyne transmitter/receiver layout. In the first stage, the echo signal is down-converted from Q band to X band. In this case, the lower sideband has a frequency separation on the order of 19 GHz and can be rejected effectively by a Q-band filter. The frequency of the LO for this first down-conversion step can be adjusted to select the appropriate Q-band frequency window. The second down-conversion step is then from X band to the frequency window centered at 1.5 GHz to be digitized using a fixed 8 GHz LO. Rejection of unwanted noise contributions in this second step can be implemented with the same filters as in the X-band receiver.

By changing to a superheterodyne architecture, not only improvements in detection sensitivity are expected, but also improvements in excitation characteristics. In fact, the current design relies on a single-stage up-conversion of AWG pulses to Q band with an IQ mixer. A very important aspect during up-conversion is that a pulse output by the AWG with one single instantaneous frequency remains a *single frequency* pulse at Q band. Otherwise, the non-linearity of the high-power amplifier will inter-combine the different frequency components and create unwanted residual excitations. These new excitations are termed as spurious tones caused by intermodulation distortion. A more detailed explanation is given in Section C.2.

In the current setup, a rather significant excitation that formally corresponds to the second harmonic of the AWG output frequency was observed (data not shown). The actual origin of this frequency component is due to a third-order mixing process between the intended Q-band pulse and the leakage of the LO through the mixer. In a two-step up-conversion, the significance of this spurious tone would only depend on the leakage of the LO through the first mixer, which translates the AWG pulses to X band. Due to improved

tolerance of X-band mixers with respect to device imperfections as compared to Q-band mixers, the spurious tone of interest would be less significant. In fact, our efforts in minimizing intermodulation distortion for the population transfer experiments at Q band relied on two-stage up-conversion and the spurious tone discussed here was not significant in these experiments (see Section C.2). For the current design of the Q-band spectrometer with single-stage up-conversion, the optimized schemes for Gd-Gd DEER presented in Chapters 5 and 6 are therefore not feasible. However, for Q-band FT EPR, the spurious excitation tone will not be a problem. In fact, the second harmonic of the AWG output lies outside the relevant excitation/detection window between 1 and 2 GHz. Moreover, these spurious second-harmonic pulses will fall onto a frequency range where the coupling $\nu_1(f)$ is reduced. Accordingly, these two aspects are the exact opposite to the situation encountered in Gd-Gd DEER experiments. Q-band FT EPR with nitroxides will be presented in Sections 8.4.2 and 8.4.3.

7.2 RESONATOR PROFILE FOR BEST SENSITIVITY

7.2.1 *Influence of resonator coupling*

In the experiments performed so far, the resonator has always been overcoupled to keep the quality factor of the resonator small and therefore maximize its bandwidth. Moreover, when comparing new methodologies with chirp pulses to established techniques with ordinary pulses, we have always compared the techniques at exactly the same resonator conditions $\nu_1(f)$. Indubitably, overcoupling appears as a reasonable approach for broadband excitation pulses. Nevertheless, it is not clear whether these fixed conditions provided the optimum sensitivity for the investigated experiments. For this purpose, the role of the resonator coupling is studied in this section.
Experimentally, the loaded quality factor Q_L of a microwave resonator can be adjusted by means of impedance transformation with a coupler at the interface between the resonator and the feedline. For the X-band resonator used throughout this work (Bruker MS3), for instance, this is achieved by adjusting the position of a coupling antenna. Resonator profiles $\nu_1(f)$ for five different antenna positions are shown by the solid lines in Fig. 7.6a. As is readily seen, the coupling conditions do not only influence resonator bandwidth, but also the central resonance frequency f_0 and the peak amplitude $\nu_{1,\max}$. In order to extract the relevant parameters, experimental data were fitted by least-square minimization of the deviation to the idealized model (see also Eq. (5.2))

$$\nu_{1,\text{fit}}(f) = \nu_{1,\max}\left|\left(1 + iQ_L\left(\frac{f}{f_0} - \frac{f_0}{f}\right)\right)^{-1}\right| \tag{7.1}$$

The fitted profiles are shown by the dashed lines in Fig. 7.6a (see caption for parameters).

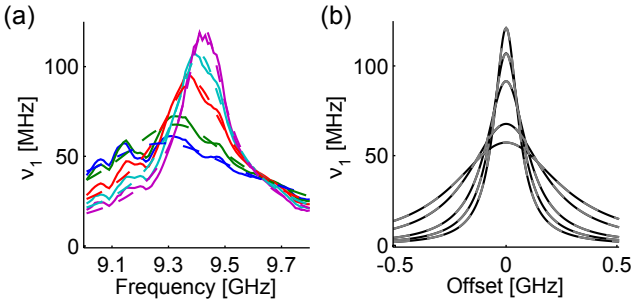

Figure 7.6 – Coupling coefficient to model the resonator response. (a) Experimental $\nu_1(f)$ profiles obtained at five different coupling conditions (solid lines). The data were obtained at room temperature using γ-irradiated Herasil in a Bruker MS3 cavity. The dashed lines are fits of Eq. (7.1) to experimental data using the parameters $Q_L = [16, 23, 41, 56, 73]$, $\nu_{1,\max} = [57, 68, 92, 107, 121]$ MHz and $f_0 = [9.28, 9.32, 9.38, 9.41, 9.43]$ GHz, respectively. (b) Fits from panel (a) replotted as a function of resonance offset (black) and resonator profiles computed with Eq. (7.4) using $Q_{L,H} = 1620.3$, $\nu_{1,H} = 409.2$ MHz and $\beta = [202, 143, 78, 57, 44]$, respectively. The parameters $Q_{L,H}$ and $\nu_{1,H}$ at critical coupling were estimated using $Q_L = [16, 73]$ and $\nu_{1,\max} = [57, 121]$ MHz. The coupling coefficients β were calculated using Eq. (7.2).

A general mathematical approach to describe the (lossless) impedance transformation by the coupler has been provided in [181]. In particular, a coupling coefficient β_c needs to be introduced. The relevant resonator parameters are then

$$Q_L = \frac{2 \cdot Q_{L,H}}{1 + \beta_c} \tag{7.2}$$

$$\nu_{1,\max} = \nu_{1,H}\frac{2\sqrt{\beta_c}}{1 + \beta_c} \tag{7.3}$$

where $Q_{L,H}$ and $\nu_{1,H}$ are the resonator parameters at critical coupling, where the impedance of the resonator is matched to the impedance of the feedline. In terms of the coupling coefficient, critical coupling is achieved for $\beta_c = 1$. In the overcoupled case, the impedance of the resonator seen by the feedline is reduced and the coupling coefficient β_c is greater than 1 [181].
To test whether the coupling coefficient is appropriate for our experimental conditions at X band, $Q_{L,H}$ and $\nu_{1,H}$ were calculated from the extracted parameters Q_L and $\nu_{1,max}$ with the lowest and highest Q_L. As a result, $Q_{L,H} = 1620.3$ and $\nu_{1,H} = 409.2$ MHz were obtained. The value of $Q_{L,H}$ was then used to calculate coupling coefficients β_c for the three datasets at intermediate Q_L based on Eq. (7.2). Self-consistency could then be checked by comparing $\nu_{1,max}$ extracted from these three datasets to the prediction based on β_c and Eq. (7.3). The good agreement between these three value-pairs is illustrated in Fig. 7.7b. The resonator characteristics obtained by fitting experimental data are shown in black. The characteristics determined by $Q_{L,H}$, $\nu_{1,H}$ and β_c are indicated by the dashed gray lines and virtually coincide with the fitted data.
The coupling coefficient therefore provides a useful way to model the resonator characteristics $\nu_1(f)$ under various coupling conditions. Note that the values for $Q_{L,H}$ and $\nu_{1,H}$ were here obtained at room temperature. At cryogenic temperatures and maximum overcoupling, larger values for Q_L and $\nu_{1,max}$ have usually been observed. Typical parameters were $Q_L \approx 40$ and $\nu_{1,max} \approx 80$ MHz.
For convenience, $\nu_{1,fit}(f)$ can be rewritten in terms of β_c, which yields

$$\nu_{1,fit}(f) = 2 \cdot \nu_{1,H} \sqrt{\beta_c} \left| \left(1 + \beta_c + i Q_{L,H} \left(\frac{f}{f_0} - \frac{f_0}{f} \right) \right)^{-1} \right| \tag{7.4}$$

The influence of the resonator characteristics on sensitivity will be studied using this formula. In this context, it is important to note that $\nu_{1,fit}(f)$ does not only model the (idealized) excitation characteristics, but also the (idealized) detection characteristics due to the principle of reciprocity [132].
Furthermore, we are here only interested in the dependence of the coupling strength ν_1 to the spins as a function of frequency offset f and coupling coefficient β_c. In principle, there are many other aspects that influence the coupling strength. The coupling strength $\nu_{1,max}$ at the center frequency of the resonator depends, for instance, on resonator and sample geometry and operation frequency [181–183].

7.2.2 *FT EPR with nitroxides*

Optimum resonator parameters for FT EPR with nitroxides at X and Q band are estimated in the following. There are two key assumptions in our optimization procedure. First, we assume that magnitude and phase responses are compensated entirely during excitation. Spins are therefore excited by compensated passage pulses with an uniform flip angle and the resonator only needs to taken into account for echo detection. Second, a measure for sensitivity needs to be defined. Here, we are interested in maximizing the echo amplitude, such that we define sensitivity as the real part of the integral of the nitroxide spectrum multiplied by the resonator profile. The optimum resonator profile can be computed by maximizing the sensitivity measure over a set of resonator parameters.
In the actual calculation, only the relative scaling of the resonator profile is of relevance. The coupling strength $\nu_{1,H}$ in Eq. (7.4) was therefore set to unity. For $Q_{L,H}$, only results with a value of 1500 will be shown. Calculations performed with $Q_{L,H} = [1000, 2000]$ yielded equivalent scaling behavior and findings. The remaining parameters to be optimized in Eq. (7.4) were β_c and f_0.
The profile $\nu_{1,fit}(f)$ optimized in this way at X band is shown in Fig. 7.7a in orange. This profile is parametrized by $\beta_c = 24.84$ and $f_0 = 9.5$ GHz, which

results in Q_L = 116 and a 3 dB bandwidth of 82 MHz. The real and imaginary components of the nitroxide spectrum are shown by the solid gray and dashed gray curves, respectively. Here, the real and imaginary components were calculated by multiplication of the real-valued nitroxide absorption spectrum with the complex valued resonator response phase-corrected for zero delay. For simplicity, such a delay correction was not performed during the optimization of resonator parameters.

A resonator profile that represents the typical experimental parameters at X band with Q_L = 40 is shown in blue. For this case, the real and imaginary components of the nitroxide spectrum are shown in solid black and dashed black, respectively. By integration of the real components of the nitroxide spectra, a 1.33 fold improvement in echo amplitude is estimated when changing from Q_L = 40 to Q_L = 116.

Using the same color coding, results at Q band are shown in Fig. 7.7b. Here, the optimum profile (orange) is parameterized by β_c = 9.94 and f_0 = 35 GHz, which results in Q_L = 274 and a 3 dB bandwidth of 128 MHz. For experimental parameters used at Q band (see Section 8.4.2), the profile shown in blue has a quality factor Q_L = 120. Integration of the nitroxide spectra predicts a 1.27 fold improvement in echo amplitude when changing from Q_L = 120 to Q_L = 274.

Sensitivity for FT EPR with nitroxides, as defined here by the maximum echo amplitude, could therefore be improved by using larger quality factors Q_L.

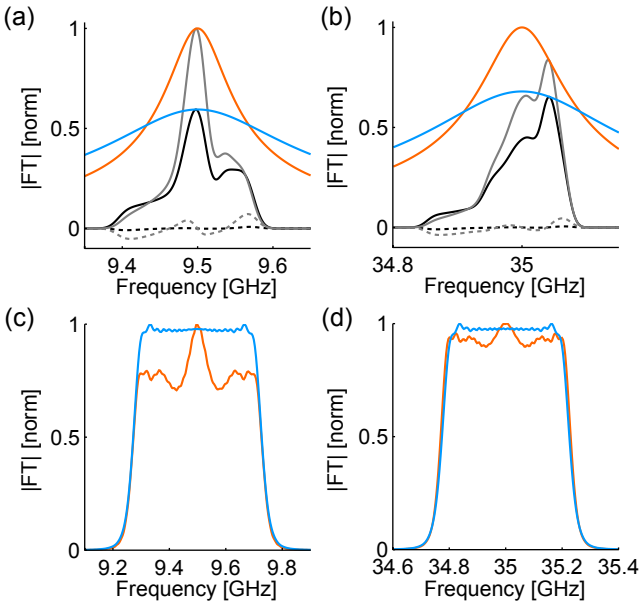

Figure 7.7 – Optimization of resonator profile for FT EPR with nitroxides. (a) Magnitude $\nu_1(f)$ of optimized profile at X band with Q_L = 116 (orange) together with real (solid gray) and imaginary (dashed gray) components of nitroxide absorption spectrum convoluted by resonator during detection. Also shown is the magnitude $\nu_1(f)$ representing typical experimental conditions with Q_L = 40 (blue) and the corresponding components of the detected spectrum (black). (b) Optimized resonator profile at Q band with Q_L = 274 (orange) and profile representing typical experimental conditions with Q_L = 120 (blue). The components of the detected nitroxide spectrum are indicated with the same color coding as in panel (a). For both X and Q band, the absorption spectra were calculated using the software EasySpin [184, 185]. For the calculations, the principal values of the g tensor were [2.008 2.006 2.002] and the principal values of the collinear A tensor were [20 20 90] MHz. Convolution broadening by 20 MHz was applied to spectra. (c) FT magnitudes of compensated pulses convoluted by resonator with Q_L = 40 (blue) and with Q_L = 116 (orange) at X band. (d) FT magnitudes of compensated pulses convoluted by resonator with Q_L = 120 (blue) and with Q_L = 274 (orange) at Q band. For panels (c) and (d), the compensated pulse was parametrized by t_p = 128 ns and Δf = 0.5 GHz centered at f_0.

The related reduction in resonator bandwidth results in a larger discrepancy between experimental FT EPR spectra and the actual shape of the spectrum. In particular, the enhanced sensitivity is due to increased coupling $\nu_1(f)$ at the center of the resonator at a less significant expense of reduced coupling at the shoulders.
Given these findings, the key assumptions underlying the optimization procedure need to be reconsidered. In particular, sensitivity has been defined as the maximum amplitude of the echo. In this way, there is no preference of certain parts of the spectrum other than the actual shape of the spectrum. Different spectral weightings may apply if certain parts of the spectrum entail different information than others. This is for instance the case if FT EPR is used to study effects related to spin orientation. The low-frequency shoulder of the Q-band nitroxide spectrum, for instance, uniquely encodes spin orientations along the z axis of the nitroxide principle axis system (see also Fig. 8.19 below). For such studies, the attenuation of this shoulder by the resonator may need to be minimized, which would result in a different measure of sensitivity and in a different resonator optimum.
The second key assumption was the compensation of magnitude and phase when exciting the spins. Here, it must be noted that we usually only compensate the magnitude $\nu_1(f)$ for FT EPR. If the experimentally approved encoding of the resonator phase into FT EPR spectra due to excitation pulses would be considered (see Fig. 4.5d and SI of [35]), slightly different results may be obtained for the optimum resonator parameters. However, a more severe drawback related to the assumption of uniform excitation pulses is the limited ability to compensate narrow-band features (see Section B.2).
For reference, the self-consistency check of the pulse compensation method is illustrated in Figs. 7.7c and d for X and Q band, respectively. Here, the blue curves represent the FT magnitude of a compensated pulse with t_p = 128 ns and Δf = 500 MHz convoluted by the resonator profile with the lower quality factor, which correspond to the profiles shown in blue in panels (a) and (b). The flat plateau in the FT magnitude approves that the resonator is largely compensated. The situation is different for the optimized resonator profiles with the larger quality factors (orange). Here, the simplified treatment of signal dynamics underlying the compensation method is no longer accurate, especially for the X-band profile. The non-uniform flip angle of the excitation pulse would therefore most likely fail to experimentally reproduce the signal enhancements of 1.33 and 1.27 predicted above. A more general compensation method would therefore be required to operate under the optimized coupling conditions $\nu_1(f)$ derived in this section.

7.2.3 *Gd-Gd distance measurements*

In the Gd-Gd distance measurements described in Sections 5 and 6, a refocused echo was formed with 12 ns pulses at the center of the resonator profile, while pump pulses were applied at the shoulders of the profile. To get an idea about the role of the quality factor Q_L, its influence on observation pulses and pump pulses are considered separately.
To study the observation pulses, a refocused echo sequence with 12 ns pulses for various resonator parameters was simulated using the software package SPIDYAN [20]. SPIDYAN already incorporates convolution of excitation pulses by an idealized resonator profile parametrized by Q_L and f_0. As a spin system, a broad spectrum with $S = 1/2$ was considered, such that the spectral width of the FT of the echo was determined by the excitation bandwidth of the three involved 12 ns pulses. The center frequency of the resonator was set to $f_0 = 34.4$ GHz. Note that the pulse duration was prolonged within the simulation due to ringing effects with the hard pulses. It has been verified by an independent SPIDYAN simulation that a hard pulse with nominal duration of 12 ns and nominal flip angle of π remained a π pulse exactly at the center of the resonator for the Q_L values considered here.

The dependence of the maximum amplitude of the simulated refocused echo on Q_L is illustrated by the dashed gray line in Fig. 7.8a. In order to also simulate echo detection with the resonator, the simulated echo transients were convoluted by the same resonator profile as the one used for excitation, which affected the echo amplitudes as indicated by the solid gray line in Fig. 7.8b. Up to this point, the coupling coefficient β_c was not taken into consideration, which explains the drop in echo amplitude when narrowing the excitation bandwidth of the pulses with Q_L. By assuming $Q_{L,H} = 1500$, a coupling coefficient β_c was obtained for each simulated quality factor Q_L. The relative scaling of the coupling strength $\nu_{1,max}$ with β_c could therefore be determined using Eq (7.3). While the relative scaling of $\nu_{1,max}$ is not relevant for excitation, because the pulse amplitude can be adjusted accordingly, it directly influences the detection efficiency. By rescaling the simulated echo amplitudes by $\nu_{1,max}$, the detected echo amplitude could be estimated (black in Fig. 7.8a).

As is readily seen in the resulting curve, an optimum quality factor on the order of 450 is predicted. With this quality factor, the excitation bandwidth of the 12 ns pulses is already reduced considerably, as is indicated by the dashed gray curve. In the typical experiment at Q band, the quality factor was on the order of 120. Accordingly, an enhancement in echo amplitude by a factor on the order of 1.35 is predicted when increasing the quality factor from 120 to 450.

To study the effect of the quality factor on the pump pulse, the adiabaticity Q_{CT} for a pulse with $t_p = 100$ ns and $f_2 = -250$ MHz relative to the observation frequency was calculated. The result is illustrated in Fig. 7.8b, where lines of constant adiabaticity Q_{CT} are indicated as a function of the quality factor Q_L and the sweep width Δf.

The curve labeled with $Q_{CT} = 0.25$ is for instance relevant for population transfer, because it corresponds to $Q_{CT} = 5$ for a 2 μs long pulse as used in pre-polarization experiments. From this line, one can extract that Δf is reduced by a factor of 1.8 from 1.3 GHz to 725 MHz, if Q_L is increased from 120 to 450 for a 2 μs long inversion pulse. It is difficult to predict the actual implication of the smaller Δf for pre-polarization. Clearly, one would expect that pre-polarized echo amplitudes at $Q_L = 450$ are no longer larger by a factor of 1.35 than pre-polarized echo amplitudes at $Q_L = 120$. If an

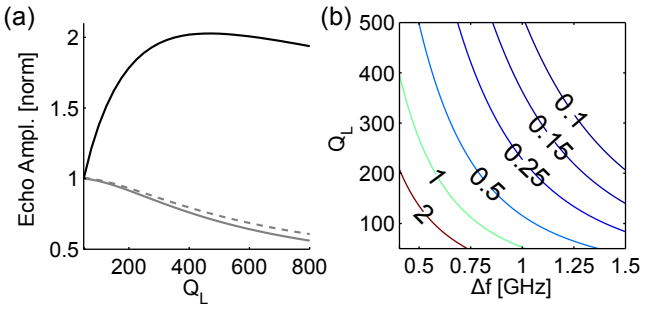

Figure 7.8 – Optimization of resonator profile for Gd-Gd distance measurements. (a) Dependence of refocused echo amplitude on Q_L (dashed gray) by simulation of the pulse sequence $(\pi/2) - \tau_1 - (\pi) - \tau_1 + \tau_2 - (\pi) - \tau_2 - (\text{echo})$ using SPIDYAN with nominal duration of 12 ns for the three monochromatic pulses. Echo formation was by considering a feature-less spectral distribution of $S = 1/2$ (with proper apodization at the edges of the simulated spectrum). To account for the resonator bandwidth during detection, the simulated echo transients were convoluted by the resonator response calculated within SPIDYAN, which attenuated echo amplitudes further (solid gray). The effect of β_c was incorporated by assuming $Q_{L,H} = 1500$ and multiplication of the echo amplitudes according to $\nu_{1,max}$ using Eq. (7.3), which provided an estimate of the detected echo amplitude (black). (b) Contour lines of adiabaticity Q_{CT} of compensated pulses as a function of Q_L and Δf for $t_p = 100$ ns and $f_2 = -250$ MHz with respect to the observation frequency.

experimentally feasible polarization enhancement of 100% is assumed for Q_L = 120, the polarization enhancement for Q_L = 450 needs to be at least 48% for a larger echo. In this case, population transfer only needs to be half as effective at the higher quality factor. The pre-polarized echo for the higher quality factor thus might still be larger than the echo at the smaller quality factor. However, the sweep width Δf of DEER pump pulses is also reduced when increasing the quality factor, such that DEER sensitivity may no longer be significantly superior with Q_L = 450.

While the situation at the Q_L optimum for the observation pulses may not lead to significant improvements, intermediate Q_L are still an interesting option. Importantly, an enhancement in echo amplitude on the order of 1.3 is predicted when going from Q_L = 120 to Q_L = 300, whereas Δf for a 2 μs inversion pulse is only reduced by a factor of 1.45. The value of Q_L = 300 is of particular relevance, because such a quality factor is implemented rather easily with the home-built Q-band resonators available in our labs [150], whereas operation at Q_L = 120 requires considerably more experience of the experimenter.

From the considerations in this section, we anticipate slightly better sensitivity for Gd-Gd distance measurements when working with $Q_L > 120$. It is difficult to make exact predictions based on the simplified modeling within this section. It does, however, appear appropriate to conduct further Gd-Gd DEER experiments with quality factors around 300, which are easier to implement.

8

EMERGING TECHNIQUES

This chapter presents unpublished results or results where the author of this thesis contributed by co-authorship or by supervision of student projects. At first, Section 8.1 presents a new pulse sequence that is advantageous for measuring short distances in several aspects. By testing the new sequence with Gd-rulers at short distances, these experiment complement the studies with Gd-rulers with long distances in Chapters 5 and 6.
In Section 8.2, the large DEER modulation depths achieved by chirp pump pulses are applied to a model system containing three spins, namely one Gd(III) center and two nitroxides. In such a case, mutual geometrical correlations between the three spins dominate experimental data and can be extracted rather efficiently from several datasets acquired at different modulation depths. These experiments have been performed in the context of the master thesis of Bettina Basel [186] conducted from April until September 2014.
Section 8.3.1 extends the bandwidth compensation procedure to hyperbolic secant pulses for frequency selective excitation. Incorporation of these pulses into SPIDYAN as well as comparison of selectivity amongst different classes of pulses has been performed within the semester thesis of Andreas Dounas conducted in Spring 2015.
FT EPR correlation experiments are presented in Section 8.4. First, extraordinary fast nuclear modulation frequencies are correlated to an ultra-wideband X-band FT EPR spectrum in Section 8.4.1. These fast modulation frequencies originate from the ^{63}Cu nucleus directly at the site of the Cu(II) center, which introduces a pronounced anisotropic hyperfine coupling. These data represent a part of the results published recently in [64].
Second, the Q-band FT EPR capabilities of the home-built spectrometer are highlighted in Section 8.4.2. The performed experiments are in exact correspondence to the FT EPR experiments on nitroxides at X band presented in Chapter 4. Accordingly, this section concludes in comparing EPR-correlated relaxation times at X band and at Q band.
Third, Q-band FT EPR is applied to dipole-dipole coupled pairs of nitroxides. On the one hand, Section 8.4.3.1 provides an introduction to chirp FT EPR in systems exhibiting dipolar coupling. At this instance, previous considerations on chirp-specific interference in such systems based on spin dynamics simulations [35] are recapitulated in an experimental context. On the other hand, Section 8.4.3.2 introduces a variant of the four-pulse SIFTER experiment with chirp pulses that allows for EPR-correlated dipolar spectroscopy at Q-band.

8.1 CIDME: SHORT DISTANCES MEASURED WITH LONG CHIRP PULSES

8.1.1 *Introduction*

The four-pulse DEER experiment in combination with a chirp pump pulse causes interference of the dipolar evolution, which can only be avoided if the pump pulse is short compared to the timescales of the dipolar frequencies. One option to overcome this limitation on pulse length is to use multiple pump pulses for refocusing the frequency-dispersion introduced by the chirp [119]. However, DEER with multiple pump pulses entails unwanted dipolar evolution pathways, which complicates data analysis considerably [187, 188]. In this section, a new pulse sequence that is free of interference and free of unwanted dipolar evolution pathways is introduced. The main idea for avoiding interference is to *freeze* dipolar evolution while applying the chirp pump pulse. This can be achieved by introducing a $(\frac{\pi}{2}) - T - (\frac{\pi}{2})$ block into the four-pulse DEER sequence, as shown in the top row of Fig. 8.1a. In particular, the first $\frac{\pi}{2}$ pulse at ③ projects and translates electron coherence to electron poplarization, while the second $\frac{\pi}{2}$ pulse at ④ restores the projected electron coherence for generation of the relevant echo that is marked with an arrow (see also below in Section 8.1.2). During the waiting time T, there is therefore no contribution from coherent evolution of the electron spin to the echo of interest. If a pump pulse is applied during the interval T, the reversal of coherent dipolar evolution takes place at the unique time instant ④ when coherence is restored. The consecutive chirp pulses shown in the bottom row of Fig. 8.1a do therefore not cause interference and can have pulse lengths beyond the dipolar evolution period.

Notably, the sequence described above without AWG pulses corresponds to the dead-time free RIDME sequence [189], where the acronym RIDME stands for *relaxation-induced dipolar modulation enhancement* [190]. In RIDME, longitudinal relaxation during the time interval T flips the coupled spin and reverses the dipolar evolution of the observed spins at ④. The time interval T should therefore be on the order of the longitudinal relaxation time of the unobserved B spins. Accordingly, the experimental conditions for RIDME, most critically the temperature, need to be optimized with respect to the properties of the spin pair under investigation. A major difference of RIDME as compared to DEER is that the modulation depth does not depend on pulse excitation bandwidth, which is favorable for distance measurements involving transition metal ions with broad spectra. A number of recent examples are summarized in [191]. Due to the similarity to RIDME, the new pulse sequence with the AWG pulses is termed *chirp-induced dipolar modulation enhancement*, which is abbreviated as CIDME.

The performance of CIDME is tested at Q band with Gd-spacer-Gd compounds, in particular with Gd-rulers $\mathbf{1_n}$ described in Section 6.2 with a concentration of 50 μM. RIDME experiments at W band with this type of ruler have been reported previously [161]. The apparent differences and similarities between RIDME and CIDME are illustrated in Fig. 8.1b. The black curve corresponds to a CIDME experiment obtained with one single chirp of 128 ns duration, whereas the gray curve corresponds to a RIDME experiment obtained with T = 10.128 μs (see caption for details). Both curves feature dipolar and nuclear modulations: The fast modulation corresponds to deuterium nuclei. The slow modulation is due to the 3.4 nm distance between the two Gd centers. An apparent difference between the two curves is the steeper signal decay in the RIDME data. This decay is due to relaxation processes during the long T interval on the order of 10 μs for the RIDME data. In general, an important decay mechanism during T is spectral diffusion due to coupled nuclei [189]. For the case of Gd-Gd RIDME, an accurate model for this decay is part of ongoing research [161]. Since CIDME has shorter T intervals, such contributions to the background decay are less important and are not considered in detail within this context.

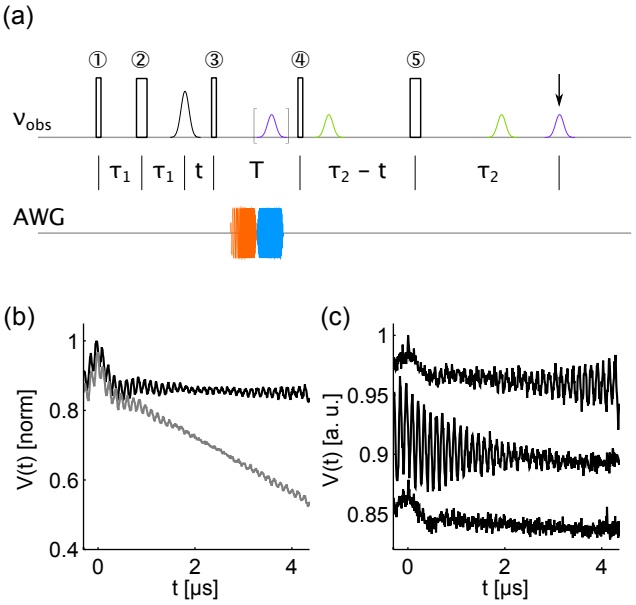

Figure 8.1 – Basic features of the CIDME experiment. (a) Pulse sequences showing the five observer pulses and two consecutive chirp pulses during the interval T. The length of the observer pulses is illustrated according to their flip angles of either $\frac{\pi}{2}$ or π. The magnitudes of important echoes are indicated by the Gaussian curves. The detected echo is due to a virtual echo (violet). The refocused stimulated echo (green) is removed by the phase cycle described in [189]. (b) Comparison between CIDME (black) and RIDME (gray) at Q band using Gd-ruler $\mathbf{1_3}$. Observer pulses had pulse lengths of 12 ns and 24 ns and were timed according to τ_1 = 400 ns and τ_2 = 4.5 μs, with delays T = 228 ns and T = 10.128 μs for CIDME and RIDME, respectively. The time t was incremented by 8 ns. The pump pulse for CIDME was parameterized by Δf = 800 MHz, f_2 = −250 MHz, t_p = 128 ns and t_{rise} = 10 ns. (c) Removal of nuclear modulations in RIDME/CIDME by summing up eight datasets with increment in τ_1 (top), with increment in τ_2 (middle), and with increment in both τ_1 and τ_2 (bottom). The increments for modulation averaging were 28 ns. Here, there was no pump pulse during the delay T = 228 ns.

Nuclear modulations in RIDME are removed by either changing to higher fields where modulations are diminished or by division of two measurements obtained under different conditions [189, 191]. Here, the nuclear modulations are suppressed by summing up data with different delays τ_1 and τ_2, which is conceptually similar to nuclear modulation averaging employed in DEER. RIDME traces (T = 228 ns) with different approaches for nuclear modulation averaging are shown in Fig. 8.1c. The top trace was obtained by averaging over τ_1, which cancels nuclear modulations that evolve between ① and ③. However, the obtained data still exhibit pronounced nuclear modulation towards the end of the curve. These modulations can be removed by averaging over τ_2 (middle). Simultaneous averaging of both τ_1 and τ_2 (bottom) therefore allows for rather good suppression of nuclear modulation artifacts. With nuclear modulation removed, a dipolar modulation of a few percent remains in the data. In a CIDME experiment, where time intervals T can range up to 1 μs, a small fraction of the dipolar modulation is therefore caused by relaxation. However, the modulation-averaged trace also reveals artifacts at $t = 0$ as well as at $t = \tau_2 - \tau_1 = 4.1$ μs. These are presumably due to improper cancellation of the refocused stimulated echo due to non-ideal phase cycling.

8.1.2 *Echo reduction and pump-observer separation*

While echo decay mechanisms driven by relaxation during long intervals T are less important for CIDME than for RIDME, loss mechanisms induced by the pump pulse need to be considered. For Gd-Gd DEER with a chirp pump pulse, coherence transfer due to inversion of the observed A spin's neighbor transitions was found to be an important reduction mechanism (see Section 6.3.3). For CIDME, a similar effect driven by population transfer has been predicted. For ease of discussion, the presentation of experimental data precedes the details on this population transfer mechanism.

For a direct comparison of the echo reduction effects in DEER and CIDME, the dependence of $|V_0/V_{\mathrm{ref}}|$ on the offset between pump and observer is shown in Fig. 8.2a. The experiments were performed according to the description in Section 6.3.1 using a 128 ns long chirp with $\Delta f = 750$ MHz. The gray curve is the DEER echo reduction and resembles the data shown previously in Fig. 6.5c. In particular, the gradual loss of echo intensity V_0 when the pump pulse approaches the observed spins is observed. Due to the sweep width $\Delta f = 750$ MHz of the chirp pulse, echo reduction for offsets $f_2 < -100$ MHz is primarily due to the aforementioned coherence transfer. If the pump pulse has spectral overlap with the observed spins, the echo is entirely lost. Different results are obtained with the CIDME sequence, which are illustrated by the black curve. First, a gradual loss in echo intensity is also observed, but it is less pronounced than with DEER. Second, spectral overlap with the observed spins is feasible. In fact, the pump pulse inverts the observed A spins, which changes the sign of the relevant refocused virtual echo. The increase in echo magnitude $|V_0/V_{\mathrm{ref}}|$ when the pulses have spectral overlap is therefore due to a zero crossing.

Note that the CIDME experiments showed a dependence of the echo reduction on the sweep direction of the pump pulse. In particular, additional wiggles in $|V_0/V_{\mathrm{ref}}|$ have been observed if an up-chirp was applied (data not shown). All pump pulses in CIDME therefore had an inverted sweep direction with respect to the sweep direction used in DEER, unless explicitly indicated otherwise. Hence, each CIDME pump pulse was swept away from the CT, while each DEER pump pulse was swept towards the CT. Another important aspect that is not visible in the plot is intensity of the echo V_{ref} in absence of the pump pulse, which was here reduced by a factor of 2.6 when changing from DEER to CIDME.

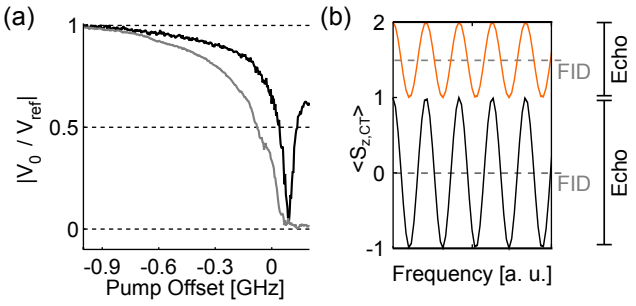

Figure 8.2 – Echo reduction in CIDME experiments. (a) Dependence of $|V_0/V_{\mathrm{ref}}|$ on frequency offset for a 128 ns long chirp with $\Delta f = 750$ MHz for the CIDME sequence (black) and for the DEER sequence (gray). The observer pulses had durations of 12 ns and 24 ns and the experiment was performed in the same way as described in Section 6.3.1. (b) Polarization grating on the CT due to projection of coherence by the $\frac{\pi}{2}$ pulse at ③ before (black) and after (orange) inversion of one neighbor transition by the pump pulse. The black vertical rulers on the right indicate the oscillation amplitude of the grating, which results in a phase-converging stimulated echo and a phase-diverging virtual echo once the grating is projected back by the $\frac{\pi}{2}$ pulse at ④. The dashed vertical lines denote the amplitude of a FID released at ④.

In order to understand the experimental observations for the CIDME sequence, one needs to elaborate further on the spin dynamics of the $(\frac{\pi}{2}) - T - (\frac{\pi}{2})$ block. The projection and translation of phase-diverging coherence at ③ results in an oscillatory polarization pattern, which is referred to as a polarization grating [18]. For phase-diverging coherence on the CT, the translated pattern is illustrated by the black curve in Fig. 8.2b. The oscillation frequency of the grating is determined by the delay to the preceding refocusing position, which is here the time t. The grating encodes the projection of transverse magnetization along one axis. The projection does therefore not preserve the sign of the coherence order. If any coherent and stochastic interactions during T are neglected, the grating remains unchanged and coherence is restored at ④. Since the grating cannot carry any information on the sign of the coherence order, this generates both a phase-converging stimulated echo as well as a phase-diverging virtual echo. The magnitudes and (hypothetical) positions of these echoes are indicated in green and violet around ④ in Fig. 8.1a. Only one half of the initial coherence is therefore detected in the CIDME experiment, which is the main reason for the observed difference by a factor of 2.6 between DEER and CIDME echoes V_{ref}.

Echo reduction in CIDME is due to population transfer acting on the polarization grating. If the pump pulse inverts only one of the neighbor transitions, one finds the up-shifted grating with half the oscillation amplitude illustrated in orange in Fig. 8.2b. Unlike in DEER, where inversion of one neighbor transition eliminates the echo, the echo in CIDME is only reduced by a factor of two. With a single pump pulse, CIDME has therefore half the echo reduction than DEER. The experimental result in Fig. 8.2a is in rather good agreement with this for offsets below -100 MHz. The dependence of the echo reduction on sweep direction in CIDME is probably also related to population transfer effects.

With pump pulses of smaller sweep width Δf, DEER echo reduction entails an additional loss mechanism due to spatial inhomogeneity of the Bloch-Siegert phase shift (see Sections 6.3.4 and D.8.2). In CIDME, there is no Bloch-Siegert shift due to the pump pulse, both in theory and in experiment. As a consequence, the same kind of echo reduction experiment performed with sweep widths Δf of 500 MHz and 300 MHz showed less than half the echo reduction for CIDME than for DEER in those regions where the additional loss mechanism for DEER was expected (data not shown).

A different result is obtained if two consecutive pump pulses are used. In the limiting case of perfect population inversion of both neighbor transitions, one finds that the polarization grating on the CT is lost. In fact, inversion of both neighbor transitions results in $\langle \hat{S}_{z,\mathrm{CT}} \rangle = 3$, which is due to the population difference between the $+3/2$ and the $-3/2$ energy level at thermal equilibrium. Within this limiting case of perfect population inversion of both neighbor transitions, echo reduction in DEER and CIDME is the same. However, one has usually a reduced inversion efficiency on each of the neighbor transitions in an experiment with consecutive pulses. When measuring the echo reduction $|V_0/V_{\mathrm{ref}}|$ with consecutive pulses, CIDME still had less echo reduction than DEER, but the difference was smaller than a factor of two (data not shown).

8.1.3 *Modulation depth and dipolar harmonics*

Since CIDME allows for longer pulses and for overlap between pump and excitation frequencies, modulation depth in CIDME can be rather large. The achievable modulation depth as well as an eventual control of higher harmonics of the dipolar frequency are of interest under these conditions. For one such example, time-domain CIDME data and the regularized distance distribution are shown in blue in Fig. 8.3. The pump pulse had a duration of 512 ns and covered a range of $\Delta f = 1.9$ GHz. Because this pulse was centered at the observation frequency, an adiabaticity Q_{CT} on the order of 4.3 has

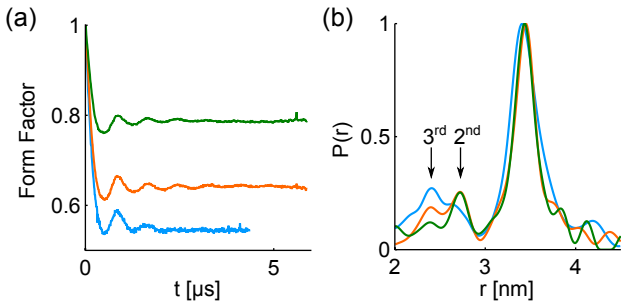

Figure 8.3 – CIDME data obtained with long pump pulses for large modulation depths. The pulse parameters were t_p = 512 ns and Δf = 1.9 GHz centered with respect to the observation frequency (blue) and t_p = 1 μs, Δf = 1 GHz and f_2 = −250 MHz (orange and green). Here, all pulses swept the frequency upwards. For the green dataset, the static field B_0 was reduced by 16 mT. The resulting signal loss was compensated by a longer acquisition time and by also using the pump pulse for pre-polarization. (a) Background corrected form factor (b) Regularized distance distribution using a regularization parameter of 1.

been achieved. For such a large frequency range, one would expect that a significant number of B spins in the states $m_S = \pm 3/2$ are flipped three times by the pump pulse and undergo a total change of $\Delta m_S = 3$. The resulting third harmonic of the dipolar frequency will lead to a contribution in distance domain at around 2.35 nm. There is some hint of such a contribution in the distance distribution extracted from this experiment (blue).
Another set of experiments (orange and green) was performed with a 1 μs long up-chirp with Δf = 1 GHz and f_2 = −250 MHz, which achieved an adiabaticity Q_{CT} on the order of 7.7. The experiment shown in green was obtained by observation of the central peak of the Gd spectrum, which represents the usual B_0 setting in these experiments. For the experiment shown in orange, the static field B_0 was reduced by 16 mT in order to pump the central peak of the Gd spectrum. This corresponds to the field position, where population transfer experiments yielded the largest signal enhancement for an up-chirp (see Fig. 5.5). The larger modulation depth of the orange curve is therefore due pumping of the central peak of the Gd spectrum. It should be noted that this is not an optimum approach for a CIDME experiment. In fact, the data shown in orange was acquired 20 times longer than the data shown in green and was additionally enhanced by population transfer with the same pulse as the CIDME pump pulse. Interestingly, the differences in the distance distributions between these two approaches are very small. In particular, the relative intensities of the peaks due to the second harmonic at 2.7 nm are comparable. There is only a small difference in the peaks due to the third harmonic at 2.35 nm.
Altogether, the data shown in Fig. 8.3 approve that fairly large modulation depths are possible with the CIDME experiment. The largest modulation depth achieved with CIDME is actually due to the ability to observe and pump the central peak of the Gd spectrum at the same time. Such a settling is not possible in DEER, as a pump pulse resonant with the A spins would change the refocusing position of the DEER echo. In the CIDME sequence, a pump pulse that is resonant with the A spins does only invert the phase of the relevant virtual echo, but does not have an effect on the refocusing position of the virtual echo. This leads to the interesting hypothesis that a coupled spin pair that lies completely within the observation bandwidth takes the role of both A and B spins: The first spin changes its resonance frequency by the dipolar coupling due to inversion of the second spin, whereas the second spin changes its frequency due to inversion of the first spin. However, such spin pairs will most likely not contribute to the CIDME modulation, because spin pairs lying completely within the observation bandwidth have different refocusing properties (see Section 8.4.3.1). In any

case, it is clear that a pump pulse with spectral overlap leads to a narrower separation between pump and observation frequency windows than with a pump pulse without spectral overlap. As a consequence, spin pairs which are not in weak coupling conditions contribute and introduce unwanted distortions to the dipolar spectrum [72, 175]. Notably, the data obtained with the centered pump pulse (blue) showed the least number of oscillations in the time domain and the broadest peak in distance domain in comparison to the other data in Fig. 8.3. Further experiments towards this direction will be presented below in Section 8.1.5.
For the second important aspect, namely the presence of dipolar harmonics, the presented CIDME experiments exhibit less harmonic content than RIDME experiments performed with the same Gd-ruler [161]. For Gd-centers with smaller ZFS, these effects may become more pronounced and more controllable, because the pump pulse covers a larger fraction of the Gd-spectrum. In any case, we would not expect that CIDME could be applied to explicitly excite certain higher harmonics while suppressing others. Such experiments would be of interest, since suppression of the fundamental frequency would be advantageous to acquire longer distances.

8.1.4 *Comparison with DEER*

With the longer pulses in CIDME and a less severe echo reduction, it is a tempting question whether CIDME can outperform DEER despite the loss of a factor of two in V_{ref} due to the polarization grating. For this purpose, we optimized both CIDME and DEER using $\eta_{2\mathrm{P}}$ as described in Sections 6.3.2 and D.1. The main outcome from this optimization was that CIDME with consecutive pump pulses achieved a larger sensitivity than CIDME with a single pump pulse. Note that only pump pulses which have no considerable overlap with the A spins were considered, because overlap is problematic for short distances (see Section 8.1.5 below). For two consecutive pump pulses with 64 ns duration each, we found good performance for both DEER and CIDME with Δf = 500 MHz and an offset of 200 MHz between pump and observer. The DEER and CIDME results are illustrated in blue and orange in Fig. 8.4, respectively. When going to longer pulse length, an asymptotic improvement in CIDME performance was observed based on $\eta_{2\mathrm{P}}$. Two consecutive 512 ns long pulses with Δf = 1150 MHz and an offset of 450 MHz between pump and observer have therefore been tested with CIDME. The data obtained with these pulses are shown in green in Fig. 8.4.
By comparing the DEER and CIDME data obtained with the same pump parameters (blue and orange), the modulation depth with CIDME was larger. There are several reasons for this. First, there is a contribution to the dipolar modulation due to longitudinal relaxation of a few percent, as shown in the bottom of Fig. 8.1c. Second, the dipolar evolution about the zero time $t = 0$ is different for DEER than for CIDME, as seen in the vertically displaced $V(t)$ curves in Fig. 8.4a. The DEER signal has a smooth curvature around $t = 0$, as one would expect for the dipolar signal, which is composed of cosine functions. Note that due to the low pass filtering of the dipolar signal by the chirp, frequency components from some orientations of the molecule may be missing, which could in principle reduce the apparent modulation depth in DEER. The CIDME signal on the contrary features an artificial spike at $t = 0$, which does enhance V_0 and results in a larger apparent modulation depth.
However, the larger modulation depth in CIDME is compensated by the smaller echo intensity V_0, which can even be recognized by comparing the noise level in the form factors in panel (b). In fact, the CIDME echo amplitude V_0 was 45% of the DEER echo amplitude. Importantly, the relevant distance peak at 3.4 nm extracted from the CIDME and DEER data is indistinguishable.
With the longer pulse duration (green), a considerable improvement in modulation depth was achieved. However, the apparent modulation depth strongly

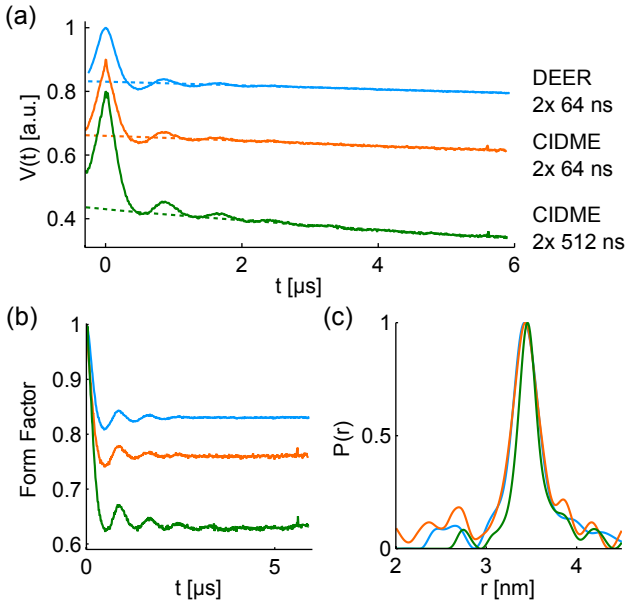

Figure 8.4 – Comparison between DEER data and CIDME data using consecutive pump pulses with t_p = 64 ns, Δf = 500 MHz and an offset of 200 MHz (blue and orange, respectively) as well as with t_p = 512 ns, Δf = 1150 MHz and an offset of 450 MHz (green). (a) Primary data (solid lines), normalized and vertically offset for better visibility, together with background fits (dashed). The echo amplitudes V_0 were 1.0, 0.45 and 0.35 for blue, orange and green, respectively. (b) Background-corrected form factors. (c) Distance distributions obtained with a regularization parameter of 1.

depended on the background correction of primary data. Here, the background was fitted starting from t_{bg} = 912 ns by a stretched exponential that corresponds to a the dimensionality of the background d_{bg} = 3.3. For such a choice, the background-corrected form factor in panel (b) has an apparent low-frequency curvature and a modulation depth of 36% is obtained. If the backgound model parameters t_{bg} and d_{bg} are optimized in the DeerAnalysis software [95], the parameters t_{bg} = 1752 ns and d_{bg} = 0.88 remove the curvature in the form factor (data not shown). For such a small d_{bg}, the background exhibits a peak at $t = 0$ which reduces the apparent modulation depth to 21%. The *real* modulation depth may lie between these two values and may be obtained with a corrected background model, which is currently being developed in the context of Gd-Gd RIDME. In fact, the CIDME experiment with the long pulse duration had $T = 1.1024$ µs. A RIDME experiment with the same T showed a similar background decay than the one observed here in CIDME (data not shown).

However, even if a modulation depth of 36% for the long-pulse CIDME data is assumed, DEER sensitivity remains superior. In particular, CIDME achieved here only 75% of the sensitivity of the DEER experiment. For a distance of 3.4 nm, where a total pulse duration of 128 ns is admissible in DEER, CIDME can therefore not outperform DEER. For shorter distances, however, the pump pulse in DEER needs to be shorter, such that CIDME with longer pulses is likely to be better than DEER. Moreover, the optimum conditions in terms of resonator bandwidth may be different for CIDME than for DEER. In particular, one would expect that the longer pulse lengths in CIDME are advantageous for narrower bandwidths, where the larger quality factor of the resonator results in larger echo signals (see also Section 7.2.3). Furthermore, the longer pulse durations in CIDME are more effective for larger frequency separation between pump and observer, which is for instance important for the study of orientation selection at higher fields when using different spin labels than two Gd-centers.

For pairs of Gd-centers, a large frequency separation between pump and

observer avoids contributions from spin pairs that are not in a weak coupling condition [72, 175]. Interestingly, the long-pulse CIDME data presented here had a narrower distance distribution than the data obtained with the shorter pulses, which can even be recognized by counting the oscillations in the form factor. We have made a similar observation for the data in Fig. 8.3. A narrowing of the distance distribution has also been observed for RIDME [161] as well as for direct excitation of multi-quantum transitions by intense pump pulse in DEER (see Fig. D.14). Since the observed effects for the 3.4 nm distance of Gd-ruler $\mathbf{1_3}$ may be considered as negligibly small, we present data obtained with Gd-ruler $\mathbf{1_1}$, which holds the two Gd-centers at a distance of 2.1 nm.

8.1.5 *Application to short distances*

The superior performance of CIDME for determination of short distances is exemplified using a 50 μM solution of Gd-ruler $\mathbf{1_1}$. DEER experiments with monochromatic pulses at W band and at Q band with this particular compound revealed distance distributions broadened by pseudo-secular contributions [175]. Based on our observations made for Gd-ruler $\mathbf{1_3}$, we would also expect such broadening for a chirp pump pulse with a small frequency offset. Accordingly, consecutive pulses with $t_p = 128$ ns, $\Delta f = 600$ MHz and an offset of 200 MHz were examined. The CIDME results shown in gray in Fig. 8.5 indeed reveal a broad distance distribution. In particular, the time-domain data in panel (a) shows less oscillations than the data obtained with Gd-ruler $\mathbf{1_3}$.
Then, the pumping position was moved further away with consecutive pulses having $t_p = 512$ ns, $\Delta f = 500$ MHz and an offset of 1 GHz. At this larger offset, the results shown in black in Fig. 8.5 display a much narrower distance distribution. Broadening mechanisms due to spin pairs that are not in weak coupling conditions can therefore by suppressed substantially, as has also been suggested in [175]. It is the unique advantage of CIDME that a modulation depth beyond 10% can be achieved at large offsets of 1 GHz. For DEER with chirp pump pulses, one would expect much smaller modulation depths because of the restrictions on pulse duration. By using RIDME, it may be possible to obtain similar results because the flipped B spins are distributed throughout the entire spectrum.

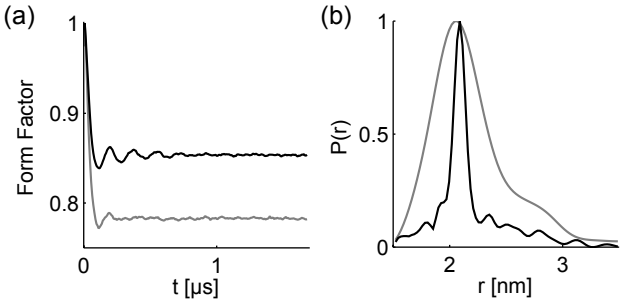

Figure 8.5 – CIDME applied to Gd-ruler $\mathbf{1_1}$ with an inter-spin distance of 2.1 nm. Consecutive pulses with parameters $t_p = 512$ ns, $\Delta f = 500$ MHz and an offset of 1 GHz (black) as well as $t_p = 128$ ns, $\Delta f = 600$ MHz and an offset of 200 MHz (gray) were examined. The observer pulses had durations of 8 ns and 16 ns. Despite the short evolution window, the delay τ_2 needed to be set to 4.5 μs due to a significant increase in a coherent artifact at $t = 0$ at shorter τ_2. (a) Background corrected form factor. (b) Regularized distance distributions obtained with regularization parameters of 0.01 (black) and 10 (gray) based on the L-curve criterion [70].

8.2 MULTI-SPIN CORRELATION

In this section, DEER experiments on systems with more than two coupled spins are presented. In particular, such systems may exhibit significant distortion of DEER data due to mixing products of dipolar frequencies [73, 192, 193]. However, these mixing products are not just artifacts, but do actually contain additional information. It is therefore of interest to separate and extract this information.

The experiments were performed in the context of the Master thesis of Bettina Basel, which has been published in book form [186]. Here, only results that are free of orientation selection are presented. Accordingly, results from a three-spin system with two nitroxide spin labels and one Gd(III) spin label are demonstrated.

The structure of the investigated compound is shown on the top of Fig. 8.6. The helical structure is a polyproline II helix with 18 residues in total and was synthesized and labeled in the group of Prof. Helma Wennemers at ETH Zurich. EPR characterization was performed within the doctoral thesis of Luca Garbuio [194]. Here, the Gd-DOTA spin label was attached at the N terminus, whereas the two nitroxide labels were attached at residues 5 and 11. For EPR experiments, the compound was dissolved to a concentration of 75 μM in a solution of D_2O and glycerol-d_8 (1:1 in volume).

Distance measurements of doubly labeled compounds revealed distance estimates of 2.05 and 3.48 nm for the distances between the Gd center and the nitroxides at residues 5 and 11, respectively [176]. The triangle spanned by the three-spin system can therefore be approximated by means of a triangle with side lengths of 2 and 3.5 nm at an angle γ, as illustrated in the middle of Fig. 8.6. Complementary nitroxide-nitroxide distance measurements on the three-spin system revealed a distance estimate on the order of 2.2 nm [194]. One would therefore expect an angle $\gamma \approx 35°$.

Pump and observation frequencies for the DEER experiment at Q-band frequencies are illustrated in the bottom of Fig. 8.6. In order to excite the entire nitroxide spectrum (red), a constant-rate chirp pulse with Δf = 250 MHz and $t_p = 48$ ns has been used. In order to maximize the adiabaticity of this short pulse, the maximum of the microwave resonator profile (green) was shifted to the pump frequency window. Under these conditions, the observation position in the Gd(III) spectrum (blue) required a frequency separation of 300 MHz with respect to the pump frequency window due to echo reduction effects. The Gd-center could therefore not be observed at the maximum of the spectrum and also not at the maximum of the resonator profile. Note that for this experiment, one would expect better performance for CIDME due to (i) observation at the maximum of the resonator profile thanks to longer pump pulse duration and due to (ii) less pronounced echo reduction effects due to the pump pulse (see Section 8.1).

In the experimental DEER scheme described above, both nitroxide spin labels are inverted. By assuming that the flip angle of the pump pulse is the same for both spin labels, each of the two Gd-nitroxide spin pairs contributes equally by a modulation depth of λ to the DEER form factor. Mathematically, the form factor $F_3(t)$ for this three-spin system reads [73]

$$F_3(t) = (1-\lambda)^2 + (\lambda - \lambda^2) \cdot P(t) + \lambda^2 \cdot T(t) \tag{8.1}$$

where $P(t)$ is the two-spin contribution and $T(t)$ the three-spin contribution. Here, the pair contribution $P(t)$ is due to the inter-spin distances of 2.0 nm and 3.5 nm between the Gd-center and the two nitroxides. Accordingly, the two-spin contribution is expressed as

$$P(t) = \langle \cos(\omega_{kl} t) + \cos(\omega_{km} t) \rangle \tag{8.2}$$

where ω_{kl} and ω_{km} are the orientation-dependent dipolar frequencies related to the 2.0 nm and the 3.5 nm inter-spin distances, respectively. The brackets indicate averaging over all orientations. The spectrum of $P(t)$ is therefore a

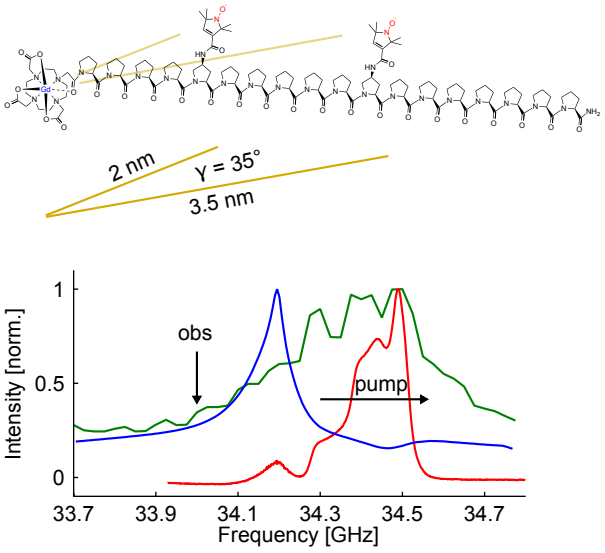

Figure 8.6 – Polyproline II helix as Gd-nitroxide-nitroxide three-spin system. Top: Chemical structure of the helix containing 18 residues and nitroxide spin labels at residues 5 and 11. The Gd-DOTA complex was attached at the N terminus of the helix. Details on the synthesis, spin labeling and Gd-nitroxide distances were reported elsewhere [194, 176]. The relevant distances are indicated in the triangle shown underneath the structure. Note that the predicted angle of $\gamma = 35°$ cannot be represented correctly in the drawing, because the two nitroxide spin labels do not align within the same plane [194]. Bottom: Experimental conditions for the DEER experiment at Q band showing the spectra of Gd(III) (blue) and nitroxide (red) cast to a frequency axis. The resonator profile $\nu_1(f)$ is shown in green and the two black arrows indicate the pump and observation frequencies. The spectra of Gd(III) and nitroxide were separated by means of the repetition time of the experiment and the differences in transition moments [162].

superposition of two Pake patterns.
The expression for the three-spin contribution is

$$T(t) = \langle \cos(\omega_{kl} t) \cdot \cos(\omega_{km} t) \rangle \tag{8.3}$$

Because the three-spin contribution is a product, the shape of $T(t)$ depends on the relative orientation between the two relevant inter-spin vectors. In other words, the three-spin contribution encodes information on the angle γ. For the triangle with side lengths of 2.0 and 3.5 nm, the dependence of the three-spin contribution in frequency domain on the angle γ is illustrated in Fig. 8.7. As is readily seen, the spectral shape has a strong dependence on the relevant angle γ. Note that the features in $T(\nu, \gamma)$ are broadened, because a standard deviation of 0.25 nm in the side lengths of the triangle have been incorporated into the simulation of the three-spin contribution.
The total modulation depth Δ_3 of the form factor $F_3(t)$ depends on the contribution λ of each spin partner via

$$\Delta_3 = 2\lambda - \lambda^2 \tag{8.4}$$

Moreover, the relative contribution of $P(t)$ and $T(t)$ to $F_3(t)$ strongly depends on λ. For small λ, the pair-spin contribution dominates, whereas for larger λ, the three-spin contribution dominates. In the limit $\lambda = 1$, a pure three-spin signal is obtained. The enhanced modulation depth achieved with chirp pump pulses therefore eases the extraction of the three-spin contribution T. Primary experimental data (solid lines) as well as fitted background decays (dashed lines) are shown in Fig. 8.8. The data shown in orange were obtained with the chirp pulse at maximum amplitude, whereas the dark blue and green curves were obtained with the chirp pulse at smaller amplitude settings. The light blue curve was obtained with a monochromatic pump pulse of 17 ns duration applied at the maximum of the nitroxide spectrum.

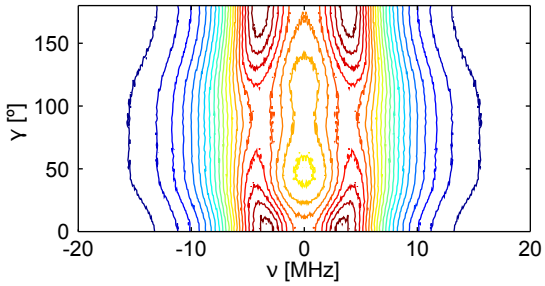

Figure 8.7 – Simulation of the three-spin contribution in frequency domain $T(\nu)$ as a function of the angle γ. A triangle with side lengths of 2 nm and 3.5 nm has been assumed. The simulation furthermore incorporates a standard deviation of 0.25 nm in the side lengths. See [73] for a description of orientation averaging in three-spin systems.

Differences in the form factors at large and at small modulation depths can already be observed in these primary data.
For such a collection of DEER data at variable modulation depth Δ_3, the two-spin and three-spin contributions can be extracted [73]. In particular, Eq. (8.4) allows to determine λ from the experimental Δ_3 [192]. Accordingly, $T(t)$ and $P(t)$ can be extracted within each time step based on the coefficients of a quadratic polynomial in λ fitted to experimental $F_3(t)$ data. The contributions obtained in this way are shown in gray in Fig. 8.9, where the two-spin contribution $P(t)$ is shown in panel (a) and the three-spin contribution $T(t)$ is shown in panel (b). The associated spectra $P(\nu)$ and $T(\nu)$ are shown in panels (c) and (d), respectively. The black curves shown in all panels are simulations of T and P for the expected angle $\gamma = 35°$ (compare Fig. 8.7).
By comparing experimental and simulated three-spin contributions, a rather good agreement with the expected angle γ is observed. By minimization of the root-mean-square deviation between experimental $T(t)$ for $t < 200$ ns and the simulations shown in Fig. 8.7, an even better fit is found for $\gamma = 45°$. At the current stage, however, we would not draw any conclusions about structure based on the rmsd-optimized angle $\gamma = 45°$. In particular, the two relevant inter-spin vectors may have a mutual spatial correlation, which is not encountered for in the simulated triangle. The extraction of an average γ from T, or even a distribution of γ, is also considerably more complicated than the extraction of inter-spin distances from P. In particular, conformational dynamics result in a superposition of Pake patterns for P, whereas T is due to a superposition of patterns, whose shape depends on γ itself (see Fig. 8.7). Moreover, the experimental data may be distorted due to the 48

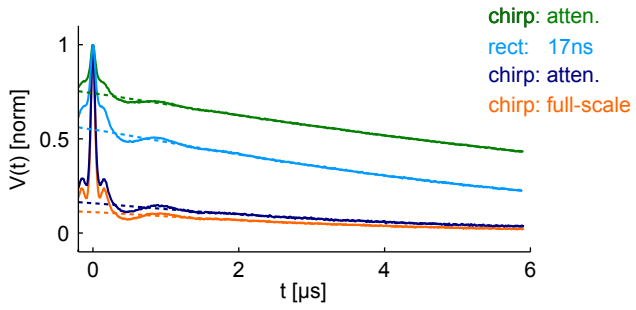

Figure 8.8 – DEER data obtained according to the scheme shown in the bottom of Fig. 8.6. Primary data (solid) are shown with the background decay (dashed). The data shown in orange, dark blue and green were obtained with a chirp pump pulse with $t_p = 48$ ns and $\Delta f = 250$ MHz at different pulse amplitudes. The data shown in light blue was obtained with a 17 ns long monochromatic pulse applied to the maximum of the nitroxide spectrum. The acquisition times were 14, 1.3, 1.3 and 3.7 hours in descending order of the modulation depth (orange to green).

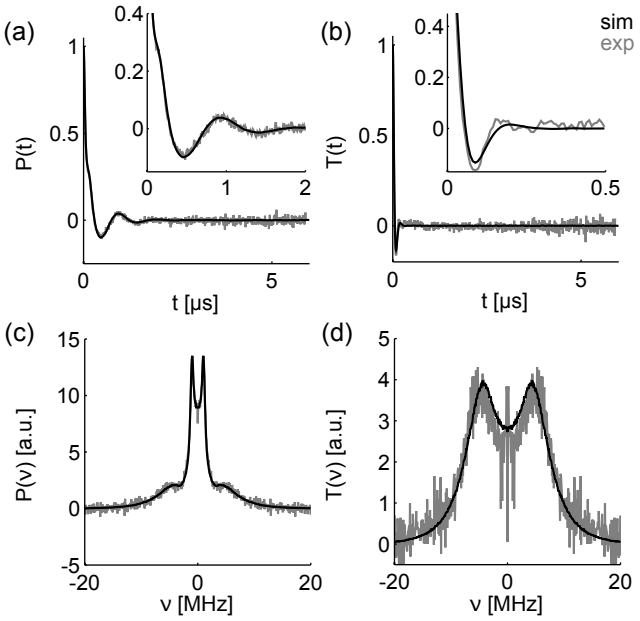

Figure 8.9 – Separation of two-spin and three-spin contribution from the three datasets obtained with chirp pump pulses shown in Fig. 8.8 (gray) as well as simulation based on the expected angle $\gamma = 35°$ (black), using the same parameters as in Fig. 8.7. Time-domain data $P(t)$ and $T(t)$ are shown in panels (a) and (b). Related spectra $P(\nu)$ and $T(\nu)$ are shown in panels (c) and (d).

ns long chirp pulses and residual orientation selection due to non-uniform excitation of the nitroxide spectrum. The short distances encountered with the investigated compound would actually suggest a CIDME experiment.
In summary, the presented experiment approves that the three-spin contribution can be extracted with a moderate experimental overhead at Q-band frequencies and even allow for a certain predictability of $T(t)$. It is worth mentioning that this is primarily due to the constellation of two nitroxides and one Gd(III)-center. In this way, orientation selection is largely suppressed by observation of Gd(III) and pumping of almost the entire nitroxide spectrum. Furthermore, the three-spin contribution $T(t)$ does only depend on one single angle γ. If the three-spin system would consist of three nitroxides, the formulas for $P(t)$ and $T(t)$ become more complicated (see [73]). In fact, experiments on such three-nitroxide model compounds at Q-band frequencies revealed a rather distinct orientation dependence of the three-spin contribution, which severely complicates data analysis [186].
Nevertheless, an extraction of spatial correlation between two relevant inter-spin vectors of the Gd-nitroxide-nitroxide system requires further refinements in the analysis of the three-spin contribution. Besides additional insight into structural composition and dynamics, it should be noted that this approach also has a potential to access longer distances by *bypassing* a long nitroxide-nitroxide distance with a Gd tag at a large angle γ. In particular, the three-spin contribution $T(t)$ of the resulting isosceles triangle will have a faster decay than the two-spin contribution $P(t)$. The time window for the DEER experiment therefore only needs to sustain the shorter Gd-nitroxide distance, which can be up to a factor of two smaller than the bypassed nitroxide-nitroxide distance.

8.3 PULSES OPTIMIZED FOR SELECTIVITY

8.3.1 *Hyperbolic secant pulses*

The hyperbolic secant (HS) pulse is known in NMR spectroscopy since decades [30, 27] and is often preferred when a frequency-selective inversion window is necessary [4]. This pulse is named according to its pulse modulation functions and is sometimes also referred to as sech/tanh pulse. Here, we refer to this type of pulse as HS1 pulse. The modulation functions are given by

$$\nu_1(\tilde{t})^{\text{HS1}} = \nu_{1,\text{max}} \,\text{sech}(\tilde{t}\beta) \tag{8.5}$$

$$f_\text{i}(\tilde{t})^{\text{HS1}} = f_1 + \Delta f \left(\frac{\tanh(\tilde{t}\beta)}{2\tanh(\beta/2)} + \frac{1}{2} \right) \tag{8.6}$$

where the time variable $\tilde{t}$ is a normalized time axis that ranges from -0.5 to 0.5. In analogy to the constant-rate and variable-rate chirps used predominantly throughout this thesis, the relevant pulse parameters are $f_1, f_2, \Delta f, t_\text{p}$ and $\nu_{1,\text{max}}$. Furthermore, there is a specific apodization parameter β for the HS pulse. This parameter scales the (relative) pulse amplitude at the edges to $\text{sech}(\beta/2)$ and has a distinct influence on the selectivity of the pulse. Typical choices are on the order of $\beta = 10$ (see also below in Fig. 8.12a). Note that there are also implementations where $\tilde{t}$ ranges from -1 to 1 and the selectivity parameter β has to be adapted accordingly in these cases.
The selectivity of the HS pulse is a direct consequence of offset-independent adiabaticity [46]: The modulation functions formally establish offset-independent adiabaticity for all excited spins, even for those at the edges of the pulse. In this sense, the HS1 pulse allows for an *adiabatic edge truncation* provided that β is large enough. The adiabaticity factor of the HS1 pulse [195] can be rewritten as

$$Q_\text{crit}^{\text{HS1}} = \frac{4\pi \cdot \nu_{1,\text{max}}^2 \cdot t_\text{p}}{\beta \cdot \Delta f} = \frac{2}{\beta} \cdot Q_\text{crit}^{\text{lin}} \tag{8.7}$$

where $Q_\text{crit}^{\text{lin}}$ is the expression for constant-rate chirps. As compared to a constant-rate chirp, the selective inversion profile of the HS1 pulse ($\beta \approx 10$) therefore degrades the adiabaticity by a factor of 5.
A representative example is given in Fig. 8.10, where a HS1 pulse (orange) is compared to a constant-rate chirp (blue). In order to achieve the same adiabaticity Q_crit at identical peak amplitude $\nu_{1,\text{max}}$, the HS1 pulse is 5 times longer. The amplitude modulation in panel (a) shows the prolonged *adiabatic edge truncation* of the HS1 pulse. In the frequency modulation in panel (b), one recognizes that the sweep-rate is the same for both pulses in the middle of the sweep, where the amplitudes are comparable: A consequence of the pulse's identical adiabaticity factors.
The simulation of $\langle \hat{S}_z \rangle$ for $Q_\text{crit} = 5$ in panel (c) displays the improved selectivity of the HS1 pulse as compared to the constant-rate chirp. A similar result is obtained for $Q_\text{crit} = 2 \cdot \log(2)/\pi$ in panel (d). Notice that a constant-rate chirp with $t_\text{p} = 400$ ns and 1/5 of its power would have the same adiabaticity Q_crit, but an improved selectivity as compared to the shown curve for the chirp (data not shown). In any case, *adiabatic edge truncation* is not possible for a constant-rate chirp, because the apodization of the amplitude modulation function is not counterbalanced by a slower sweep rate (see also [46] for pulses including such a counterbalancing).
Since HS1 pulses for selective inversion ($\beta \approx 10$) have such a pronounced trade-off in adiabaticity, HS pulses of higher orders have been introduced [46],

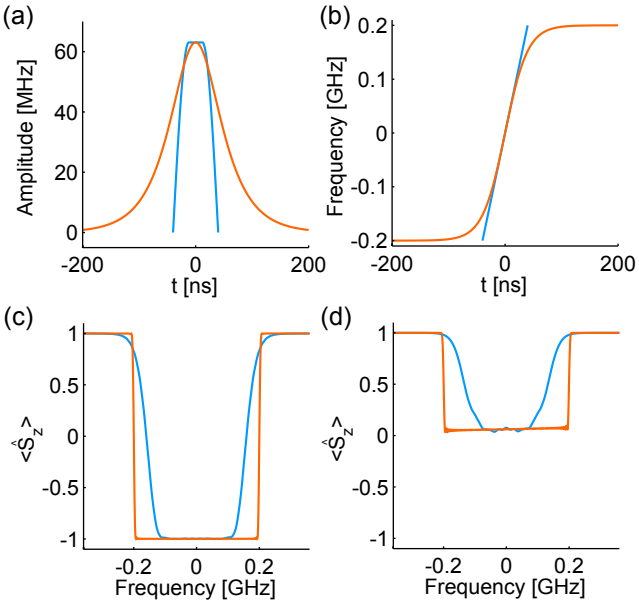

Figure 8.10 – Comparison between HS1 pulse (orange) and constant-rate chirp (blue) with Δf = 400 MHz and identical peak amplitude. The HS1 pulse has t_p = 400 ns and β = 10, such that it has the same adiabaticity Q_{crit} than the constant-rate chirp with t_p = 80 ns and t_{rise} = 28 ns according to Eq. (8.13). (a) Amplitude modulation functions $\nu_1(t)$ for Q_{crit} = 5. (b) Frequency modulation functions $f_i(t)$ (for any Q_{crit}). (c) Simulation of $\langle \hat{S}_z \rangle$ for Q_{crit} = 5. (d) Simulation of $\langle \hat{S}_z \rangle$ for $Q_{crit} = 2 \cdot \log(2)/\pi$, which corresponds to a peak amplitude of $\nu_{1,max}$ = 18.74 MHz.

which are referred to as HSn pulses. The modulation functions for these pulses are

$$\nu_1(\tilde{t})^{\mathrm{HS}n} = \nu_{1,\max} \operatorname{sech}(\tilde{t}^n \beta^p) \tag{8.8}$$

$$f_i(\tilde{t})^{\mathrm{HS}n} = f_1 + \Delta f \int_{-0.5}^{\tilde{t}} \operatorname{sech}^2(\tau^n \beta^p) d\tau \Big/ \int_{-0.5}^{0.5} \operatorname{sech}^2(\tau^n \beta^p) d\tau \tag{8.9}$$

where we have introduced a new exponent p that leaves the pulse amplitude at the edges independent on the order n. Hence

$$p = \frac{\log(\beta \cdot 2^{n-1})}{\log(\beta)} \tag{8.10}$$

For $n = 1$, the solution to the integral in Eq. (8.9) is given above in Eq. (8.6). For $n > 1$, the integral needs to be solved numerically. Accordingly, also the adiabaticity Q_{crit} needs to be computed numerically. Note that there is a variety of implementations with respect to the parameters β, n and $\tilde{t}$ for HS1 and HSn pulses in the literature. Here, we introduced the exponent p due to our choice of $\tilde{t}$. In addition to that, the normalization of the integral in Eq. (8.9) makes the sweep width Δf independent on both n and β.
The influence of n on selectivity is shown in Fig. 8.11. Panels (a) and (b) illustrate the amplitude and frequency modulation functions, respectively, in ascending order n from 1 to 8. The arrows denote the changes along ascending n. In order to have the same adiabaticity Q_{crit} for all orders n, the pulse lengths were chosen as t_p = [400, 188, 143, 124, 114, 108, 103, 100] ns. The parametrization of the pulse's selectivity with the order n becomes apparent in the simulations of $\langle \hat{S}_z \rangle$ for Q_{crit} = 5 and $Q_{crit} = 2 \cdot \log(2)/\pi$ in panels (c) and (d), respectively.
In order to compare the frequency selectivity of different types of pulses, a selectivity-figure κ is introduced:

$$\kappa = \int I \cdot (1 - I)\, df \tag{8.11}$$

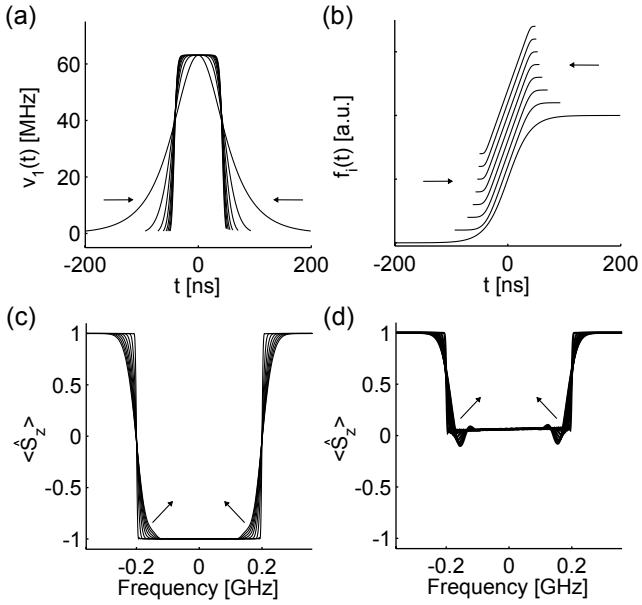

Figure 8.11 – Selectivity parametrization of HSn pulses with Δf = 400 MHz, β = 10, identical peak amplitude and identical adiabaticity Q_{crit}. The illustrated curves correspond to ascending orders n from 1 to 8. The consequences of increasing n are illustrated by means of arrows in all the insets. (a) Amplitude modulation functions $\nu_1(t)$. (b) Frequency modulation functions $fi(t)$, vertically displaced. (c) Simulation of $\langle \hat{S}_z \rangle$ for Q_{crit} = 5. (d) Simulation of $\langle \hat{S}_z \rangle$ for $Q_{\text{crit}} = 2 \cdot \log(2)/\pi$, which corresponds to a peak amplitude of ν_1 = 18.74 MHz.

For the case of a perfectly frequency-selective pulse, the inversion efficiency I is either 0 or 1 with an infinitely steep transition region in-between, and therefore $\kappa = 0$. If the transition region between becomes less steep, the inversion I takes values between 0 and 1, which results in $\kappa > 0$. The selectivity-figure κ should therefore be as small as possible for a frequency selective pulse.
A simulation of the dependence of κ on the apodization parameter β for a set of HSn pulses is shown in Fig. 8.12a. Here, all the pulses had Δf = 500 MHz, t_{p} = 200 ns and Q_{crit} = 5, which has been realized by scaling the pulse amplitude $\nu_{1,\text{max}}$ accordingly. As is readily seen, best selectivity is achieved for a HS1 pulse with β = 10. For higher orders n, selectivity is degraded and the optimum apodization parameter β shifts to smaller values.
Panel (b) of Fig. 8.12 shows the dependence of κ on the pulse length t_{p} for the same set of HSn pulses as well as for constant-rate chirp (dashed blue) and for WURST-N (dashed red) pulses [29]. In this simulation, all pulses had Δf = 500 MHz, Q_{crit} = 5 and an optimum apodization parameter. The optimum apodization was obtained by computation of κ for an adequate set of apodization parameters and selection of the best parameter, as illustrated in panel (a) for HSn pulses. The apodization parameters t_{rise} and N_{WURST} for constant-rate chirps and WURST-N pulses, respectively, showed a pronounced dependence on the pulse length t_{p}. Within the investigated range of 100 ns $< t_{\text{p}} <$ 300 ns, the relevant apodization parameters could be fitted well by the following linear relations

$$t_{\text{rise}}(t_{\text{p}}) = \frac{t_{\text{p}}}{10} + 20 \text{ ns} \tag{8.12}$$

$$N_{\text{WURST}}(t_{\text{p}}) = \frac{t_{\text{p}}}{11} + 0.2 \tag{8.13}$$

$$\beta_{\text{HS1}}(t_{\text{p}}) = \frac{t_{\text{p}}}{270} + 9.2 \tag{8.14}$$

where the pulse length t_{p} has to be provided in nanoseconds.
As is readily recognized in the $\kappa(t_{\text{p}})$ curves in panel (b), frequency-selectivity improves with pulse length t_{p} for all the considered pulse types. Moreover,

the two dashed curves related to pulses with a constant sweep rate of the instantaneous frequency f_i have almost the same selectivity and are competitive with a HS8 pulse for $t_p < 200$ ns. As expected, the HS1 pulse is the best amongst the compared pulses in terms of selectivity.

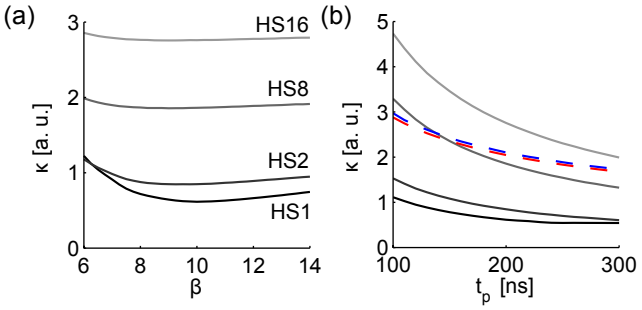

Figure 8.12 – Comparison of selectivity for different kind of pulses with Δf = 500 MHz and Q_{crit} = 5. (a) Dependence of selectivity-figure κ on apodization parameter β for 200 ns long HSn pulses with order as indicated. (b) Dependence of selectivity-figure κ for optimized pulse apodization on pulse length t_p. The solid curves correspond to HSn pulses with order as indicated in panel (a). The dashed blue and red curves correspond to constant-rate chirp and WURST pulses, respectively.

8.3.2 *Bandwidth compensated and asymmetric HS pulses*

The superior frequency selectivity of HS1 pulses thanks to their *adiabatic edge truncation* is interesting for a number of applications in EPR spectroscopy. However, these pulses only fulfill offset-independent adiabaticity in the absence of any bandwidth limitations imposed by the resonator. Moreover, the lineshape of the excited spins may not require frequency selectivity on both sides of the excitation window. One can therefore combine HSn pulses of different orders. Such combined HSn pulses are referred to as HS$\{n_1, n_2\}$ pulses, where n_1 is the order of the first half of the combined pulse and n_2 is the order of the second half. If $n_1 \neq n_2$, we refer to an asymmetric HS pulse. The incorporation of a resonator profile $\nu_1(f)$ into HS pulses is performed in an analogous manner as the compensation of constant-rate chirps in Section 3.4.4. In particular, the frequency modulation $f_i(t)$ of the compensated pulse is obtained via it's inverse $t(f_i)$. The only difference is that the HS pulse to be compensated already has a non-linear time-frequency relation $\tilde{f}_i(t)$ and a specific amplitude modulation $\tilde{\nu}_1(t)$. The formalism to compute $t(f_i)$ given a resonator profile $\nu_1(f)$ and HS$\{n_1, n_2\}$ modulation functions $\tilde{f}_i(t)$ and $\tilde{\nu}_1(t)$ is implemented according to the following formula

$$t(f_i) = \frac{Q_{crit}}{2\pi} \int_{f_1}^{f_i} \left(\nu_1(f)|_{f=\tilde{f}_i} \cdot \tilde{\nu}_1(t)|_{t=t(\tilde{f}_i)} \right)^{-2} d\tilde{f}_i \tag{8.15}$$

Note that in the actual calculation on the computer, $\nu_1(f)|_{f=\tilde{f}_i}$ is the resonator profile $\nu_1(f)$ interpolated along the frequency axis defined by HSn frequency modulation $\tilde{f}_i(t)$. Moreover, $\tilde{\nu}_1(t)|_{t=t(\tilde{f}_i)}$ directly represents the vector that defines the amplitude modulation $\tilde{\nu}_1(t)$. When computing the integral, one should account for the non-constant spacing of the integration variable $d\tilde{f}_i$. In the MATLAB implementation, this is achieved by the call *cumtrapz*$(\tilde{f}_i,\ (...)^{-2})$.
Once the frequency modulation $f_i(t)$ is calculated, the amplitude modulation $\nu_1(t)$ is obtained by interpolation according to the formula

$$\nu_1(t) = \tilde{\nu}_1(t)|_{t=t(f_i)} \tag{8.16}$$

Additionally, the obtained amplitude modulation $\nu_1(t)$ is rescaled using a 10^{th} order polynomial $a_S(\nu_1)$ to compensate for the amplitude compression

of the high-power amplifier within the excitation chain. The calibration of the compression characteristics and its inverse used for the polynomial rescaling has been described in Section 4.2.3.

As a result, the procedure above generates a HS$\{n_1, n_2\}$ pulse with its time axis *warped* for offset-independent adiabaticity in presence of the bandwidth limitation $\nu_1(f)$. To illustrate this effect, an example is provided in Fig. 8.13. At first, we focus on the *warped* time axis that is best seen in the pulse

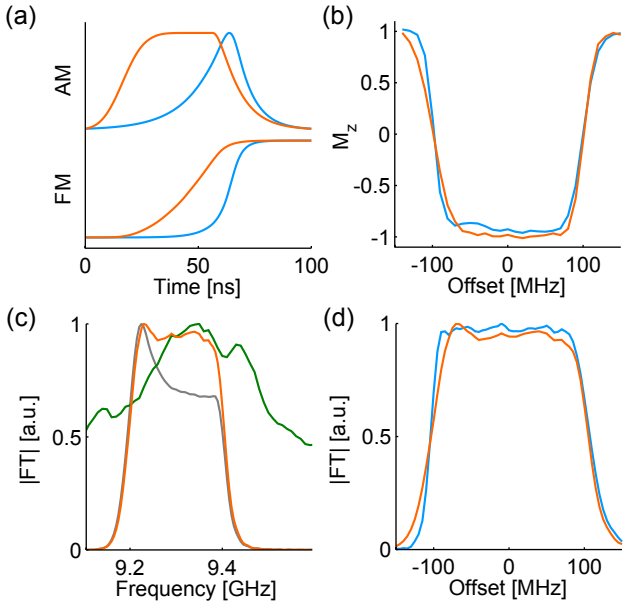

Figure 8.13 – Performance of 100 ns long HS pulses with Δf = 200 MHz and β = 10.4 of order {1,1} (blue) and of order {6,1} (orange). The pre-calculated adiabaticities Q_{crit} were 3.1 and 8.7, respectively. (a) Normalized time-domain modulation functions of pulse amplitude (AM) and frequency (FM). (b) Experimental inversion profile. (c) Compensation of the resonator transfer function (green) by the pulse synthesized by the AWG (gray). The product between the two curves (orange) represents the magnitude FT of the asymmetric HS{6,1} pulse convoluted by the resonator. (d) Comparison between symmetric HS{1,1} pulse (blue) and asymmetric HS{6,1} pulse (orange) convoluted by the resonator. For comparability, both curves were normalized by their maximum value.

modulation functions of the compensated HS{1,1} pulse shown in blue in panel (a). While an ordinary HS1 pulse reaches its maximum amplitude exactly at $t_p/2$, the depicted compensated pulse has its maximum shifted towards the end of the pulse. The reason for this shift is that the pulse spends more time at the lower excitation frequencies, where the coupling $\nu_1(f)$ is smaller than at the higher excitation frequencies (see also discussion of panel (c) below).

Also shown in orange in panel (a) are the modulation functions of a HS{6,1} pulse. The faster rise at the leading pulse edge due to $n_1 = 6$ keeps the pulse amplitude at the maximum for almost half of its duration. The HS{6,1} pulse therefore has a larger power than the HS{1,1} pulse, as is also reflected by the adiabaticities Q_{crit} of 8.7 and 3.1, respectively.

The experimental inversion profiles in panel (b) measured according to the description in Section 4.2.4 reveal two aspects. First, the HS{6,1} pulse achieves a larger peak inversion than the HS{1,1} pulse due to its larger adiabaticity. Second, the HS{1,1} pulse has steep frequency-selective edges on both sides of the excitation window, whereas the HS{6,1} is less steep at the lower frequency edge.

In panel (c), the compensation of the resonator profile (green) is visualized by means of Fourier-transforms. The gray curve is the FT of the HS{6,1} pulse as defined by the modulation functions in panel (a). The orange curve is the FT of the HS{6,1} pulse convoluted by the resonator, which is the

product of the gray and the green curve. The remarkably flat FT of the convoluted pulse is a consequence of offset-independent adiabaticity (see also B.2). Panel (d) compares the FT of the convoluted HS{6,1} and HS{1,1} pulses. The differences in frequency-selectivity observed in the experimental inversion profiles in panel (b) are also readily seen in the FT.

Overall, the ability to adjust the frequency-selectivity of HS{n_1,n_2} pulses and to incorporate experimental bandwidth limitations $\nu_1(f)$ makes this class of pulses advantageous in a number of applications. One application is frequency-selective excitation of few tens of MHz by bandwidth compensated HS1 pulses. For narrower excitation bandwidths, one would expect serious competition from amplitude modulated monochromatic pulses, such as pulses modulated by Gaussian or sinc functions. Another application is frequency-selective inversion by HS$\{n_1, n_2\}$ pulses. Of particular interest are multi-pulse DEER techniques for extended dipolar evolution windows, which require multiple pump pulses [187, 188]. The quality of primary data obtained with these techniques is strongly related to the inversion efficiency and selectivity of the applied pump pulses. In particular, the intended dipolar evolution pathway requires multiple inversions of the pumped spins and an optimum experiment requires a selectivity-figure $\kappa = 0$. In ongoing work on the incorporation of these optimized pulses into multi-pulse DEER, the HS{6,1} pulse depicted in Fig 8.13 showed unprecedented quality of primary data at X band. At Q band, a HS{1,6} pulse was applied and also revealed decent quality, even though experimental inversion quality, and therefore also primary data quality, was degraded when changing from X to Q band (manuscript in preparation).

8.4 2D CORRELATION SPECTROSCOPY

8.4.1 *2D EPR/ESEEM techniques*

This section provides a brief account on 2D EPR/ESEEM techniques, which correlate nuclear frequencies to EPR frequencies. The foundations of this experiment using hard pulses have been described in [196]. In Chapter 4, the correlation between nuclear modulation in time-domain and the nitroxide chirp FT EPR spectrum has been discussed (see for instance Fig. 4.4a). For a 2D EPR/ESEEM spectrum, nuclear frequencies are obtained by a second FT along the indirect dimension of the experiment. For the case of two-pulse ESEEM, the indirect dimension is the incremented inter-pulse delay τ.
As described in Section 2.5.1, two-pulse ESEEM with $S = 1/2$ and $I = 1/2$ results in modulation by the nuclear modulation frequencies ω_α and ω_β as well as by sum and difference combinations ω_+ and ω_-, respectively. In a 2D EPR/ESEEM spectrum, these four nuclear frequencies have a characteristic correlation pattern with the two allowed EPR transitions and the two forbidden electron-nuclear transitions [196]. Accordingly, the 2D correlation pattern simplifies the assignment of all these eight frequencies in the 1D EPR spectrum and in the 1D ESEEM spectrum.
Further simplification of the 2D spectrum is achieved with the three-pulse ESEEM pulse sequence, which results in echo modulation by the fundamental nuclear frequencies ω_α and ω_β exclusively. In this case, the characteristic 2D correlation pattern is the same as if the sum and difference frequencies ω_+ and ω_- are removed from the 2D pattern obtained with two-pulse ESEEM, with the additional benefit of smaller modulation linewidths in three-pulse ESEEM [196]. However, by changing from two-pulse ESEEM to three-pulse ESEEM, there is also a complication related to suppression effects of certain nuclear frequencies. This suppression effect is often referred to as blind-spot behavior and can be compensated by recording several three-pulse ESEEM spectra at different blind-spot positions [18].
The application of chirp pulses to 2D EPR/ESEEM techniques based on two-pulse and three-pulse ESEEM were demonstrated in [64]. Three different single crystals have been investigated: First, γ-irradiated malonic acid served as a well-known reference compound for strongly coupled protons (S = 1/2 and I = 1/2), which has also previously been used to demonstrate 2D EPR/ESEEM spectroscopy with hard pulses [196]. Second, the Cu(II) defect in TiO_2 crystals at natural abundance has been studied, where the electron spin of the Cu(II) ion (S = 1/2) is coupled to the nuclear spin of the copper nucleus (I = 3/2). The spin Hamiltonian parameters of this system have been characterized previously [197]. As a third system, the bispicolinate Cu(II) complex $^{63}Cu(pic)_2$ in a $Zn(pic)_2$ matrix has been investigated, where the electron spin of the Cu(II) ion does not only couple to the copper nucleus (I_1 = 3/2), but also to two ^{14}N ligands (I_2 = 1) and to surrounding protons (I_3 = 1/2) [198].
In order to demonstrate the combined advantages of broad excitation bandwidth with chirp pulses and of enhanced resolution in 2D EPR/ESEEM correlation patterns, results obtained with the $Cu(pic)_2$ complex are illustrated and explained within this thesis. For results obtained with the two other complexes as well as for results based on the three-pulse ESEEM experiment and 3D EPR/ESEEM correlation spectroscopy based on the four-pulse HYSCORE experiment, the reader may refer to the original publication written by T.F. Segawa *et al.* [64]. The author of this dissertation assisted all experiments and data post-processing and also contributed by few technical inputs with respect to spin dynamics simulations and matrix diagonalization. For $Cu(pic)_2$ that is of interest here, anisotropic hyperfine couplings to several nuclei are present. The main intention of the chirp EPR/ESEEM experiments on this compound was to detect modulation frequencies related to the copper nucleus. The experiments have therefore been performed at a crystal orienta-

tion where the secular hyperfine coupling to the copper nucleus was not too large, in other words not directly observable as splitting in the field-swept EPR spectrum due to overlap of hyperfine-split components. The spectrum obtained at this orientation is shown in Fig. 8.14a. In fact, two crystal sites contributed to the spectrum at the chosen crystal orientation. For one of these two sites, a rather large secular hyperfine coupling on the order of 100 G could be deduced from the EPR spectrum. In particular, there was a well resolved quintet at the low field position. The quintet structure resulted from the secular hyperfine interaction between the electron spin and the two magnetically equivalent ^{14}N nuclei. The separation between this resolved quintet and the next potential quintet structure was exactly 100 G. For the other of these two sites, the secular part of the hyperfine coupling was not directly resolved in the EPR spectrum. The contribution from this crystal site was located within 3174 G and 3392 G, where many quintets overlapped in the field sweep.

The width of the entire EPR spectrum at this orientation was on the order of 1.2 GHz, which was beyond the 1 GHz detection window for chirp FT EPR experiments. Two experiments at field positions of 3174 G and 3283 G and with chirp excitation Δf = 900 MHz have therefore been performed to cover the entire spectrum. The FT EPR spectrum obtained at 3283 G with two bandwidth-compensated pulses having durations of 200 ns and 100 ns and a delay between starting pulse flanks of 250 ns is shown in Fig. 8.14b, with magnitude shown in solid red and real part shown in dashed red. The experimental resonator profile is indicated in green and the field sweep converted to a frequency axis in blue. Within experimental uncertainty and imperfections, the attenuation of the FT EPR spectrum due to the resonator can be recognized. There are, however, regions where the FT EPR spectrum was attenuated significantly beyond the resonator profile. The underlying loss mechanisms have not been investigated in detail.

Note also that the field sweep is converted to a frequency axis by assuming that the spectrum is composed by one single isotropic g-factor and by field-independent hyperfine contributions. Differences between the FT EPR line pattern and the line pattern deduced from the field sweep may partially originate from this approximation. Such differences are likely to arise especially in the case considered here, where the EPR spectrum entails distinct features over a large field range. A more precise estimate of the EPR spectrum in frequency domain would require eigenvalues of the Hamiltonian calculated using the g-tensor and A-tensor [18].

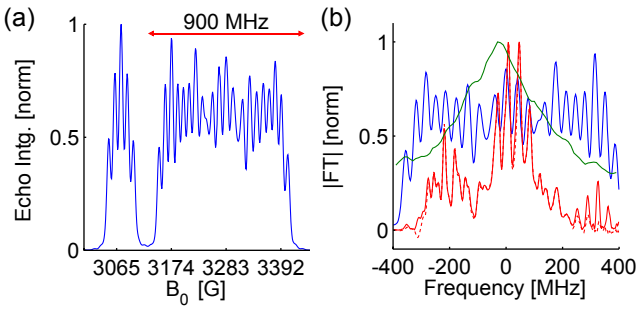

Figure 8.14 – Field-swept EPR spectrum and FT EPR of copper picolinate ^{63}Cu(pic)$_2$ diluted to 1% in a Zn(pic)$_2$ matrix. (a) Field-swept EPR spectrum of relevant crystal orientation obtained at 20 K. The red marker indicates the spectral range covered by a 900 MHz excitation pulse at a field position of 3283 G. (b) Magnitude (solid red) and real part (dashed red) of FT-EPR spectrum obtained with two bandwidth-compensated chirp pulses having durations of 200 ns and 100 ns and a delay between starting pulse flanks of 250 ns. The experimentally obtained resonator profile is shown in green. The field sweep from panel (a) converted to a frequency axis is shown in blue. The same raw experimental data as in the SI of [64] were used for this illustration.

To obtain EPR/ESEEM data, the delay τ between starting pulse flanks was incremented in 1 ns steps from the starting value of 250 ns up to 3249 ns. The magnitude of the 2D FT along the EPR and ESEEM dimension obtained at a field position of 3283 G is shown in Fig. 8.15. The 1D spectrum above the 2D EPR/ESEEM spectrum is the projection of all ESEEM spectra. The 1D spectrum on the right is the magnitude EPR spectrum at the initial delay τ of 250 ns (see also Fig. 8.14b). Contributions from the unmodulated background to the 2D spectrum were removed by subtracting a fifth-order polynomial background fit. The data were acquired at 20 K during 50 minutes, including a [+(+x) -(-x)] phase cycle on the first pulse.

The 2D EPR/ESEEM spectrum contains nuclear frequencies due to two types of nuclei. First, the two low-frequency peaks in the ESEEM projection at 14 MHz and 28 MHz are caused by surrounding protons. On a closer look, the fundamental peak at 14 MHz even reveals the line broadening that one would expect due to protons with distributed hyperfine parameters [18]. Then, there are in total eight further peaks at large frequencies up to almost 200 MHz, which are marked with distinct symbols and colors for negative offset frequencies in the ESEEM projection. These are the frequencies related to the hyperfine coupling to the ^{63}Cu nucleus. With monochromatic pulses, such large nuclear frequencies could not be observed due to limited excitation bandwidth.

The symbols to mark the eight copper frequencies in the ESEEM projection have the following meaning: circles denote fundamental frequencies ω_α and ω_β, the $+$ labels denote sum frequencies ω_+, and the $-$ labels denote difference frequencies ω_-. The colors green and purple are used to distinguish two sets of four modulation frequencies each.

The assignment of these frequencies has been aided by the 2D EPR/ESEEM correlations. As mentioned in the beginning of this section, 2D EPR/ESEEM spectra with $S = 1/2$ and $I = 1/2$ result in a well-defined correlation pattern. In particular, the sum and difference frequencies ω_+ and ω_- correlate with

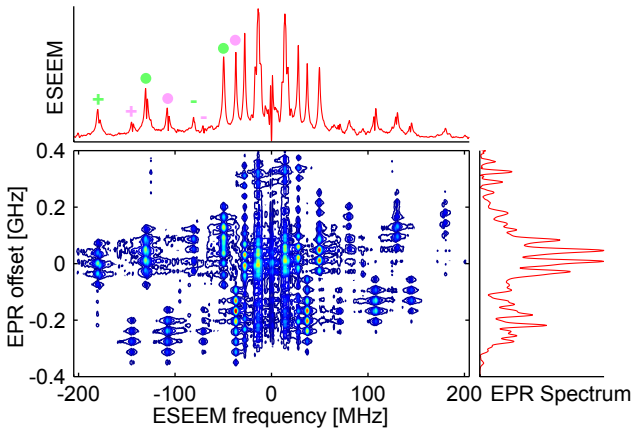

Figure 8.15 – 2D FT EPR/ESEEM spectrum of copper picolinate obtained at a field position of 3283 G. The two-pulse ESEEM experiment was performed with bandwidth-compensated pulses having Δf = 900 MHz and pulse lengths of 200 ns and 100 ns. The delay τ between starting pulse flanks was incremented from 250 ns to 3249 ns in 1 ns steps. Before computing the FT along the indirect dimension, a fifth-order polynomial background fit was subtracted to avoid contributions at the zero ESEEM frequency. The total acquisition time was 50 minutes at a temperature of 20 K. Top: 1D projection of ESEEM frequencies. Four peaks have been marked with filled circles and correspond to two separate pairs of ω_α and ω_β frequencies related to ^{63}Cu. The two pairs are distinguished by their colors in green and purple. The corresponding combination frequencies ω_+ and ω_- are marked by the $+$ and $-$ labels, respectively, with the same color as for the $\omega_\alpha/\omega_\beta$ pairs. Right: Magnitude EPR spectrum at initial delay τ. The same raw experimental data as in [64] were used for this illustration.

one single EPR frequency component [196]. Here, for the case of $I = 3/2$, the two subpatterns in the 2D EPR/ESEEM spectrum resemble this characteristic correlation pattern. At the bottom left of the 2D spectrum, for instance, an isolated EPR quintet at $-|\omega_+|$ around -150 MHz is identified (marked by the purple $+$ in ESEEM projection). At $+|\omega_+|$ on the right half of the 2D plot, another quintet is seen at a higher EPR offset on the order of -0.15 GHz. The EPR offset centered within this two quintets represents the EPR resonance frequency at the center of the allowed and forbidden EPR doublets (of quintets). In an analogous manner, two EPR quintets can be identified for ω_- around ± 75 MHz marked by the purple $-$ in ESEEM projection) for positive and negative ESEEM frequencies. Also these two quintets are centered with respect to the above mentioned EPR resonance frequency. Congruent observations can be made when considering the combination frequencies colored green in the ESEEM projection. This set of nuclear frequencies correlates to a different part of the EPR spectrum around zero frequency offsets. For the four fundamental frequencies ω_α and ω_β marked by filled circles, isolated quintets can not be identified due to correlation to more than one EPR frequency component.

Note that the larger of the fundamental ^{63}Cu frequencies contains an additional splitting on the order of 2 MHz of unknown origin. Such a splitting is also observed for all the ^{63}Cu combination frequencies and one would assume that the combination frequencies entail this splitting due to the splitting present in the fundamental frequency. Moreover, experiments performed at a lower magnetic field position of 3174 G revealed a third set of nuclear frequencies with modulations up to 300 MHz (see [64]). One would therefore assume that the three sets of nuclear frequencies correspond to the three single-quantum transitions of the $I = 3/2$ spin of the copper nucleus. For the second site with the larger secular hyperfine splitting and the well-resolved quintet in the EPR spectrum (see Fig. 8.14a), no fast modulation frequencies could be observed (see also [64]).

Overall, the experimental observation of fast modulation frequencies related to the nucleus of a transition metal ion, as demonstrated here for Cu(II), is a novelty. In combination with the improved resolution in the 2D EPR/ESEEM spectra, this methodology may help to refine structural models. The applicability of this technique to powder samples as well as peculiarities in the spin dynamics and practice with quadrupole splittings await further investigations. Within the context of this thesis, a key aspect of this new type of experiment is that it can be realized at all. Out of all other 2D correlation experiments performed on the home-built AWG spectrometer up to the time of writing, the 2D spectrum shown in Fig. 8.15 remains the one with the widest spread in pronounced correlation peaks in both the direct EPR dimension as well as in the indirect dimension of the experiment.

8.4.2 *Q-band FT EPR*

In this section, the chirp FT EPR approach presented in Chapter 4 at X band is extended to Q band. These experiments became feasible thanks to the Q-band operation mode of the home-built AWG spectrometer described in Section 7.1. In order to test the technique, the same 1 mM solution of TEMPOL as used in the X-band experiments has been used (see Section 4.2.6). Note that at X band, the experiments relied on a commercial microwave resonator from Bruker. At Q band, a home-built loop-gap resonator was employed, which has been designed and constructed by René Tschaggelar and Oliver Oberhänsli, respectively. With this Q-band resonator, the performance in terms of excitation power and bandwidth was the same at X band and at Q band. In fact, the shortest π pulse was 5.5 ns and the bandwidth due to the resonator was on the order of 250 MHz for X band as well as for Q band. The results from a chirp echo optimized according to the procedure described in Section B.3 are shown in Fig. 8.16. Panel (a) shows the digital modulation functions of the FP90 and FP180 pulses for echo generation. The curvature in the frequency modulation $f_i(t)$ accounts for the resonator profile obtained at a digital driving amplitude in close vicinity to the optimized FP90 pulse amplitude. In analogy to the results obtained at X band, the FP90 pulse had length t_p = 128 ns and sweep width Δf = 500 MHz.
Fig. 8.16b shows real (solid) and imaginary (dashed) components of the echo transients obtained with the chirp pulses (black) and a Hahn echo generated with optimized excitation pulse durations of 2.75 ns and 5.5 ns (gray). Due to the broader bandwidth of the chirp pulses, a shorter echo transient was attained with chirp pulses than with monochromatic pulses.
Computation of the FT results in the spectra shown in Fig. 8.16c, where real and and imaginary components have the same coloring as in panel (b). The black arrows highlight the most significant differences between the two FT spectra. First, the up-arrow for negative frequency offset denotes the improved spectral width of the chirp echo as compared to the Hahn echo.

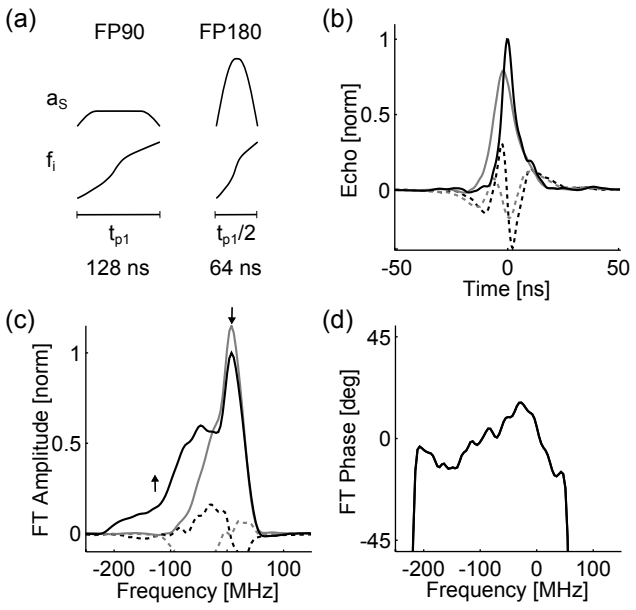

Figure 8.16 – Chirp echo of nitroxide at Q band. (a) Digital modulation functions $a_S(t)$ and $f_i(t)$ for the FP90 and FP180 pulse. (b,c) Real part (solid lines) and imaginary part (dashed lines) of chirp echo (black) and Hahn echo (gray) in time domain (b) and frequency domain (c). The arrows in (c) indicate the performance of the chirp echo relative to the Hahn echo (up-arrow: better performance, down-arrow: worse performance). The center frequency $(f_1 + f_2)/2$ of the chirp pulses was at -50 MHz with respect to abscissa in this figure. (d) Frequency domain phase of chirp echo (black)

Second, the down-arrow at the peak of the spectrum points at an additional loss mechanism attributed to the chirp echo. Based on our previous results at X band, it is presumed that this signal loss is also at Q band due to enhanced instantaneous diffusion for the broadband chirp echo. At lower spin concentrations, one would not expect such an effect (see Section B.4).
The phase of the FT spectrum obtained with the chirp pulse is shown in Fig. 8.16d and has a deviation on the order of $\pm 15°$ from the zero-line.
For a comparison between the FT spectrum and the echo-detected field-swept spectrum, nuclear modulations were removed by averaging FT spectra over different pulse delays τ (see also Section 4.3.2). The nuclear modulations are illustrated in Fig. 8.17a by showing the influence of the pulse delay τ on the FT spectrum. Fig. 8.17b compares the modulation-averaged FT spectrum (solid black) to the field-swept spectrum cast along a frequency axis (gray). The ratio between the two spectra is indicated by the dashed black curve. Within experimental uncertainty, there is a good agreement between this ratio and the resonator profile $\nu_1(f)$ obtained at full-scale amplitude (green). In analogy to the result obtained at X band, this approves that the bandwidth limitation imposed by the resonator is largely compensated by the excitation pulses.
Fig. 8.17c also shows the 2D EPR/ESEEM correlation spectrum obtained from a dataset extending to $2\tau = 4.68$ μs. As can be seen in the ESEEM projection on the top, the main contribution is at ± 106 MHz. Note that this fast modulation corresponds to twice the proton frequency. At X band, both the fundamental and the double proton frequency were observed at larger modulation amplitudes (see for instance Fig. B.6). The smaller modulation

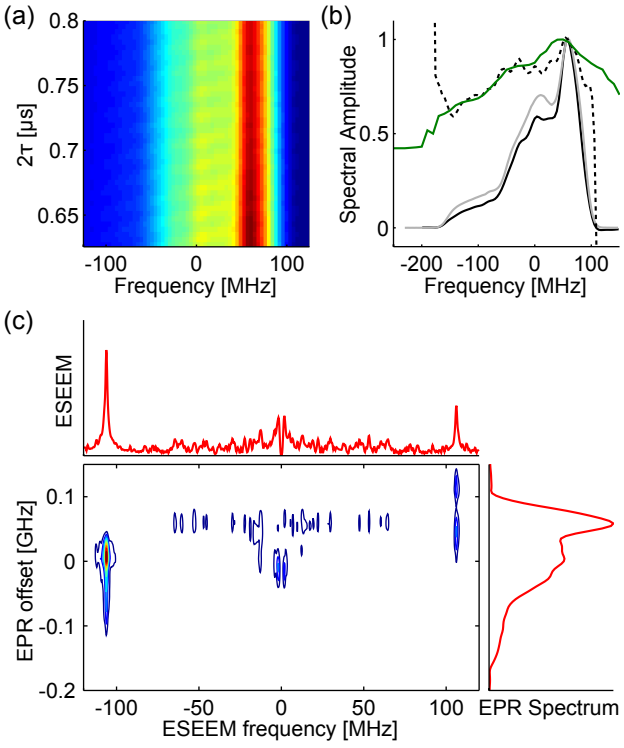

Figure 8.17 – Nuclear modulations and comparison with field-swept spectrum. (a) Chirp echo in frequency domain measured for different evolution times 2τ, where τ is the delay between the starting flanks of the two chirp pulses. (b) Chirp echo in frequency domain averaged over several nuclear modulation periods (solid black) and conventional field-swept echo-detected spectrum converted to a frequency scale (light gray). The ratio between the two spectra (dashed black) shows the perturbation of the chirp echo spectrum, which appears to be dominated by the resonator that is indicated by $\nu_1(f)$ obtained at full-scale (green). (c) 2D EPR/ESEEM correlation spectrum of a dataset extending up to delays $2\tau = 4.68$ μs, starting from $2\tau = 0.7$ μs with an increment in τ of 2 ns.

amplitude at Q band is due to the larger nuclear Zeeman splitting. The absence of the fundamental proton frequency at Q band may be related to broadening mechanisms. In a three-pulse ESEEM experiment, evolution of nuclear (single-quantum) coherence results in narrower line widths in three-pulse ESEEM spectra as compared to two-pulse ESEEM spectra [18]. Accordingly, a weak signature of the fundamental proton frequency could be observed in an EPR-correlated three-pulse ESEEM experiment at Q band (data not shown).

As a further test of Q-band FT EPR, the EPR-correlated inversion recovery experiment was implemented. The results obtained previously at X band are illustrated in Fig. 8.18a, where the upper plot shows the EPR spectrum and the lower plot the apparent T_1 time. Cross-talk across the frequency-dependent T_1 times due to formally forbidden electron-nuclear transitions has been minimized by properly adjusting the inter-pulse delay τ of the chirp echo pulses (see Section 4.3.4).

At Q band, the same timings were used for the inversion recovery experiment as at X band (see Section 4.2.5). The result is shown in Fig. 8.18b, again with the EPR spectrum in the upper plot and the apparent T_1 times in the lower plot. Since the nuclear modulations at Q band were much less pronounced than at X band, no special considerations on the above mentioned cross-talk were made.

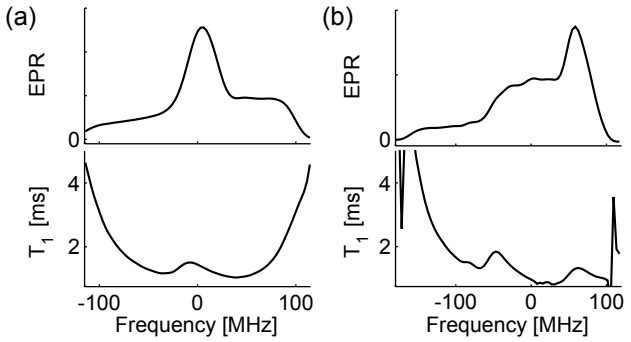

Figure 8.18 – EPR-correlated inversion recovery of nitroxide at X band (a) and at Q band (b). The upper plot in each panel is the FT EPR spectrum and the lower plot is the apparent T_1 time, which corresponds here to the $1/e$ decay time extracted from the recovery dynamics. See Section 4.2.5 for a detailed description on the timings of the pulse sequence and the processing of the data. The X-band data originate from the dataset shown previously in Fig. 4.6.

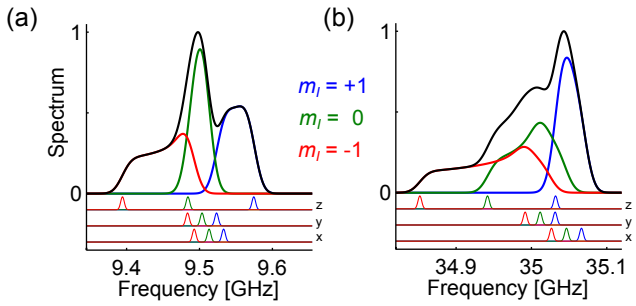

Figure 8.19 – Simulation of nitroxide spectra in frequency domain using the software EasySpin [184, 185] at X band (a) and at Q band (b). The sum of all transitions is shown in black, whereas the transitions separated by means of the nitrogen nuclear spin projection m_I are shown in red ($m_I = -1$), green ($m_I = 0$), and blue ($m_I = +1$). The smaller curves underneath the spectra denote the lines that correspond to the principal directions x, y, and z. For the simulations, the principal values of the g tensor were [2.008 2.006 2.002] and the principal values of the collinear A tensor were [20 20 90] MHz. Convolution broadening by 20 MHz and by 5 MHz was used for the powder average and for the three principal directions, respectively.

The origin of the anisotropy in T_1 times has been studied previously at X band [105]. In particular, stochastic vibrations couple more effectively to orientations where the p-type orbital along the z axis in the nitroxide PAS is perpendicular to the applied magnetic field. Consequently, these transverse orientations have a shorter T_1 time than the parallel orientations.
In order to ease the identification of the relevant orientations, representative nitroxide spectra are shown in Fig. 8.19. The lower three rows show the resonances along the three principal orientations x, y, and z, while the upper part shows the powder spectrum (black). The colors are used to distinguish contributions from different projections of the nitrogen nuclear spin projection m_I (see legend). In this way, the spectral positions of the relevant z orientations with respect to the powder spectrum can be located. A comparison between these positions and the local maxima in T_1 reveals that the expected T_1 anisotropy is obtained both at X and at Q band. In particular, there is a *local maximum* in T_1 related to each of the three m_I transitions oriented along z. The notion of a *local maximum* is not well defined at those positions where uniquely orientations along z contribute to the spectrum, since the T_1 curves diverge.
In summary, the results presented in this section approve Q-band FT EPR capabilities for the home-built AWG spectrometer. In the subsequent section, this new capability is applied to systems that exhibit dipolar coupling between a pair of spins.

8.4.3 *Dipolar couplings*

8.4.3.1 *Selective and non-selective excitation*

The differences between partial and complete excitation of a spin system are very distinct when considering coupled spin systems. In particular, a spin echo with soft selective pulses refocuses all weak couplings of the type $\hat{S}_z\hat{I}_z$ between the excited and the non-excited spins. A spin echo with hard non-selective pulses on the contrary does not refocus weak couplings of this kind [18]. The related echo modulation phenomena in case of electron-electron couplings have been investigated in the late sixties [199]. For these modulations to be significant, however, a large fraction of the spectrum needs to be excited and electron-nuclear modulations compete with the electron-electron modulations.

Because often a smaller fraction of the spectrum is excited in EPR, echo experiments are better described in terms of soft selective excitation. A prominent example for a spin echo due to soft excitation pulses is the four-pulse DEER experiment [65]. If relaxation is neglected, the observation pulses refocus all weak dipolar couplings in the absence of the pump pulse. Accordingly, there is no coherent contribution due to the dipolar coupling to the spin echo in this case. Controlled evolution under the dipolar coupling in DEER is achieved by defocusing the dipolar interaction with the pump pulse.

The boundaries of assuming soft selective pulses for four-pulse DEER experiments have been analyzed recently [178]. In particular, there are numerous unwanted residual dipolar evolution pathways because both the pump and the observation pulses are not ideally selective for a spin pair with overlapping spectra, as is for instance the case for nitroxide pairs. One such pathway is due to the echo modulation phenomena related to dipolar electron-electron spin couplings mentioned above for non-selective pulses. Note that this particular pathway sets an upper boundary on the excitation bandwidth of the observation pulses for four-pulse DEER in such spin systems:

With an increasing fraction of the spectrum being observed, the fraction of spin partners that lie within the observation window, and therefore experience non-selective excitation, increases. As a consequence, the *modulation depth* of this unwanted dipolar evolution pathway scales with the excitation bandwidth of the observation pulses.

Based on the above considerations on selective and non-selective excitation in systems with dipolar electron-electron couplings, pronounced echo modulations are expected if the entire spectrum is excited with chirp pulses. Importantly, the spin dynamics during a chirp pulse are not the same as during a hard non-selective excitation pulse. The interference effects related to a pair of nitroxides during a FP90 pulse at Q band have been investigated using spin dynamics simulations (see Fig. 6d in [35]). These simulations revealed that interference effects are negligible for distances above 5 nm for a constant-rate FP90 pulse with t_p = 200 ns and Δf = 500 MHz. Moreover, coherence loss to double quantum coherence due to interference effects was still quite small for a distance of 4.0 nm. For distances below 2.0 nm, coherence loss was beyond 10 % and therefore significant.

In the experiment, bandwidth-compensated pulses with a variable sweep rate are used and the pulse lengths are often shorter than 200 ns. For the 128 ns FP90 pulse used in Section 8.4.2, for instance, the relevant 250 MHz frequency window of the nitroxide spectrum is passed within 50 ns. This is twice as fast as for the 200 ns FP90 pulse examined in [35], where the relevant window is passed within 100 ns. However, the sweep rate of the compensated FP90 pulse has a considerable variation throughout the spectrum. If the slowest sweep rate throughout the nitroxide spectrum is considered, a 250 MHz frequency window is passed with a constant sweep rate within 110 ns, which is close to the 100 ns passage time for the constant-rate pulse simulated in [35]. The simulation parameters in [35] are therefore adequate to approximate the experimental conditions achieved with the home-built

AWG spectrometer.
As a model system for the experiments, a nitroxide-ruler holding two nitroxide spin labels at a well-defined distance about 4.0 nm was used. The synthesis and EPR characterization of this ruler have been reported elsewhere [200, 157]. The structure of the ruler will be shown further below in Fig. 8.23d, where the geometry of the ruler will be relevant for interpreting experimental results. For all EPR experiments, the compound has been dissolved to a concentration of 50 μM in a deuterated ortho-terphenyl solvent, which provides very long phase memory times at the measurement temperature of 50 K.
The two-pulse echo decay obtained with this model compound is shown below in Fig. 8.20a. The data shown in black were obtained using a chirp echo with Δf = 500 MHz and t_p = 128 ns for the FP90 pulse. The data shown in gray were obtained with monochromatic pulses with pulse durations of 2.75 ns and 5.5 ns. The integrated echo transients correspond to the contribution to the spin echo from the maximum of the nitroxide spectrum. As is readily seen, the chirp echo features stronger modulations than the Hahn echo. In order to approve that the observed modulations are due to dipolar couplings, a four-pulse DEER experiment using a HS{1,6} pump pulse with $t_p = 100$ ns and $\Delta f = 100$ MHz is shown in Fig. 8.20b (see caption for further details).
The inability to refocus the dipolar coupling with non-selective pulses could therefore be reproduced experimentally with chirp pulses. Due to the dead-time and inability to isolate exclusively the dipolar interaction from other interactions, this type of experiment is not well suited for distance measurements. In fact, the dephasing of the chirp echo due to the dipolar coupling may be an obstacle if other interactions than the dipolar interaction are to be studied by FT EPR techniques. EPR-correlated hyperfine techniques are for instance not admissible in biradical systems.

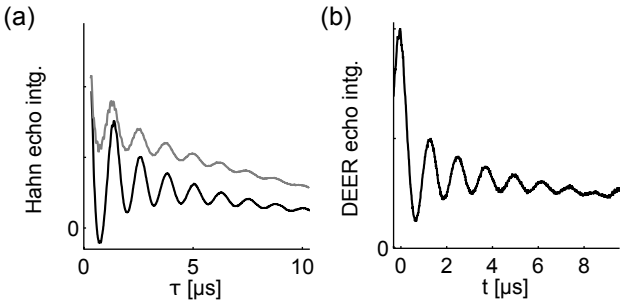

Figure 8.20 – Dipolar modulation in two-pulse echo decay. (a) Two-pulse echo decay obtained with chirp pulses (black) and monochromatic pulses (gray). The adjustable pulse parameters for all the pulses corresponded to those used in Section 8.4.2 (see also description in text). (b) DEER experiment using a HS{1,6} pump pulse with $t_p = 100$ ns and $\Delta f = 100$ MHz. The observation frequency was 100 MHz below the maximum of the nitroxide spectrum. The pump frequency window was centered at the maximum of the nitroxide spectrum, which corresponds to a frequency separation of 50 MHz between pump and observation frequencies. The observer pulses had durations of 12 ns.

8.4.3.2 *2D SIFTER*

In order to separate dipolar interactions with FT EPR techniques, a way to refocus the dipolar coupling with non-selective pulses is required. There are two methods in the context of dead-time free pulsed EPR distance measurements. The first method relies on double-quantum coherence and is implemented by means of the six-pulse double-quantum coherence (DQC) EPR pulse sequence [201]. In brief, this pulse sequence refocuses the dipolar coupling by (i) transferring (anti-phase) single-quantum coherence to double-quantum coherence, (ii) refocusing the double-quantum coherence, and (iii) evolution back to an observable spin echo. The inability to refocus the dipolar

coupling with non-selective pulses is therefore circumvented by transferring the relevant dynamics under the dipolar coupling to double-quantum coherence. In a more rigorous treatment, one finds that the relevant dynamics under the coupling are anti-phase coherences (see also [202]). Thanks to the refocusing of the coupling, the net evolution under the dipolar coupling can be controlled by adjusting delays before and after the DQC refocusing block.
The second method relies on a solid echo and is implemented by means of the four-pulse SIFTER pulse sequence, where SIFTER stands for single-frequency technique for refocusing (dipolar couplings) [203]. This pulse sequence relies on the fact that the relevant dynamics under the coupling - the anti-phase coherences - are refocused with a solid echo sequence $(\pi/2)_x - \tau - (\pi/2)_y - \tau -$ echo. In an analogous way as in the six-pulse DQC sequence, the net evolution under the dipolar coupling is controlled by adjusting the delays before and after the *refocusing event*, which is in the example here the $(\pi/2)_y$ pulse. Because the solid echo does not refocus the resonance offset, additional π pulses need to be incorporated before and after the $(\pi/2)_y$ pulse. This yields the four-pulse SIFTER sequence $(\pi/2)_x - \tau_1 - (\pi)_x - \tau_1 - (\pi/2)_y - \tau_2 - (\pi)_x - \tau_2 -$ echo, which is illustrated in the top row of Fig. 8.21. The dipolar evolution time t depends on the delays via $t = 2(\tau_1 - \tau_2)$.
Both the DQC and the SIFTER experiment perform non-ideal due to the limited excitation bandwidth of monochromatic hard pulses. Recently, it has been demonstrated that the SIFTER experiment can be improved by using frequency-swept pulses with enhanced excitation bandwidth [147]. In particular, a large dipolar modulation depth on the order of 95% has been achieved for X-band SIFTER, which confirms a broad excitation bandwidth. At Q band, limitations in power and bandwidth constrained the dipolar modulation depth to 10%. In order to perform the SIFTER experiment with chirp pulses, the authors used pulse length ratios 2 : 1 : 2 : 1 for the four pulses ①, ②, ③ and ④, respectively. This pulse sequence allowed for 1D SIFTER experiments, which implies that the echo transients were either integrated or sampled by one single point.
In order to demonstrate a 2D experiment that correlates the dipolar coupling to the FT EPR spectrum, we have therefore chosen to further elaborate on the results obtained previously with the 1D SIFTER experiment in [147]. In particular, different pulse length ratios are needed to obtain FT EPR spectra. With pulse length ratios 2 : 1 : 2 : 1, neither the dipolar coupling nor the resonance offset is refocused properly. In order to obtain all possible pulse length ratios that refocus the relevant interactions, one could use the mathematical expression for multi-pulse chirp refocusing reported in [35]. Here, we follow the less general but more instructive approach based on pictorial representations.
In the bottom of Fig. 8.21, two such representations are shown. The time-frequency profiles of the four pulses are indicated by the black segments and were chosen to represent constant-rate pulses. The relative pulse durations are indicated by the numbers next to the pulses. These therefore represent chirp SIFTER with 4 : 3 : 2 : 1 and 2 : 2 : 2 : 1 schemes. Both of these schemes refocus the resonance offset. In order to realize this, the reader may directly follow the relevant refocused primary echo sequence due to the pulses ①, ② and ④:
The pulses ① and ② result in a frequency-dispersed echo at the position of pulse ③. Both the 4 : 3 and the 2 : 2 ratios of these first two pulses result in the same frequency dispersion of the echo at ③. In particular, this frequency dispersion is the same as a single $\pi/2$ chirp of duration 2 would cause, which coincides with the time-frequency profile of pulse ③. Importantly, this establishes refocusing of the resonance offset at the time where pulse ③ acts, which is the main purpose of pulse ② in the SIFTER pulse sequence. The dispersed echo at ③ is refocused according to a 2 : 1 scheme by pulse ④. The resulting refocused primary echo is therefore free of frequency-dispersion,

such that the EPR spectrum can be obtained by computation of the FT (see [124] for further details on frequency-dispersed echoes).
The situation is different when considering the dipolar coupling. Here, only the solid echo sequence of the pulses ① and ③ needs to be considered. The orange and blue vertical rulers denote the periods of dipolar phase acquisition. The position where the dipolar coupling refocuses is indicated by the green time-frequency profile at the position of the echo. As these profiles indicate, only the 4 : 2 ratio between pulses ① and ③ removes the frequency dispersion, while the corresponding ratio of 2 : 2 leaves the refocusing position of the dipolar evolution frequency-dispersed[1].
If we rely on our usual implementation for nitroxides, where the shortest pulse in the sequence has a duration of 64 ns, the 4 : 3 : 2 : 1 sequence results in a FP90 pulse of 256 ns duration at ①, whereas the 2 : 2 : 2 : 1 sequence results in a 128 ns FP90 pulse at ①. Both schemes for 2D SIFTER therefore have specific limitations when applied to short distances: The increased duration of the first pulse in the 4 : 3 : 2 : 1 scheme is prone to coherence loss due to interference during the chirp pulse [35]. The frequency-dispersion in the dipolar evolution of the 2 : 2 : 2 : 1 scheme leads to an equivalent effect as is encountered for four-pulse DEER with a chirp pump pulse.
For ease of implementation, we chose the 2 : 2 : 2 : 1 scheme for 2D SIFTER. The frequency dispersion by 128 ns in this scheme was not considered to be problematic, since a 4 nm distance can be reliably measured with 128 ns long pump pulses in four-pulse DEER. Thanks to the deuterated buffer of the nitroxide-spacer, a long dipolar evolution time of 19.7 μs could be acquired. By integration of the echo transients during post-processing, the 1D SIFTER time trace shown in Fig. 8.22 is obtained, with real and imaginary components in black and gray, respectively. As is readily seen, dipolar modulations extend over several oscillation periods due to the stiffness of the model compound.
It is important to point out that SIFTER entails unwanted dipolar evolution pathways due to imperfections of the inversion pulses [203, 147]. These imperfections lead to refocusing of the dipolar evolution at ② or ④ and result

[1] Further analysis by product operator formalism revealed that the pictorial analysis of the dipolar evolution as presented here is not complete. In particular, each of the four pulses introduces additional effects: The two $\pi/2$ pulses cause asymmetry with respect to the order in which a coupled spin pair is excited, whereas the two π pulses refocus part of the dipolar evolution.

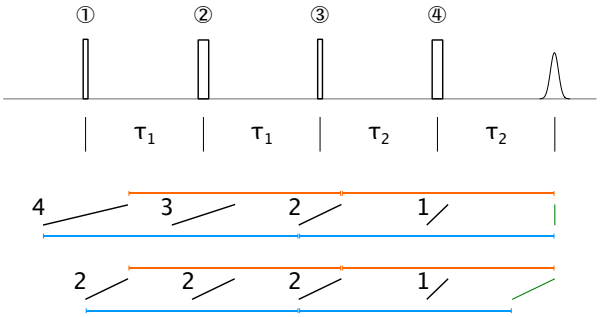

Figure 8.21 – Four-pulse SIFTER and realizations with chirp pulses that are compatible with FT EPR. Top: Pulse sequence for monochromatic hard pulses, where the length of each pulse is illustrated according to the flip angle of either $\frac{\pi}{2}$ or π. The Gaussian profile at the end denotes the position of the detected echo. Bottom: Two graphical representations of chirp SIFTER with pulse length ratios 4 : 3 : 2 : 1 and 2 : 2 : 2 : 1, as indicated by the numbers next to the time-frequency profiles of the pulses (black). The two time periods of dipolar evolution are indicated by the horizontal rulers above (orange) and below (blue) the pulse sequence. In the 4 : 3 : 2 : 1 realization, the dipolar coupling is refocused at one particular time instant, which coincides with the echo refocusing position (vertical green line). In the 2 : 2 : 2 : 1 realization, the refocusing position of the dipolar coupling has a frequency dispersion, which is illustrated by the tilted green line.

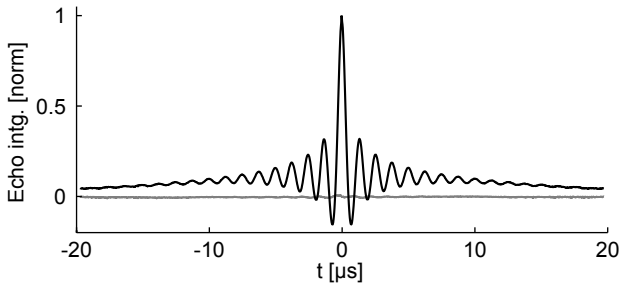

Figure 8.22 – One-dimensional SIFTER data by integration of the echo transient. Here, the echo integral corresponded to the spin packets at the maximum of the nitroxide spectrum. For the 2 : 2 : 2 : 1 pulse sequence, bandwidth-compensated pulses with durations of 128 ns and 64 ns and Δf = 500 MHz were implemented. The phases of the pulses ②, ③ and ④ were varied according to the 16-step phase cycle reported in [203]. The pulse delays τ_1 and τ_2 were incremented with a step size of 12 ns, which resulted in a time increment in t of 24 ns. In total, the time t was stepped from -19.704 μs to 19.704 μs using 1643 points. The echo position $2(\tau_1 + \tau_2)$ was varied to average residual modulations, starting from 40 μs using an increment of 392 ns for 12 datasets. The acquisition of one dataset required 2.3 hours.

in residual modulations with zero-time at the beginning and the end of the SIFTER trace. These modulations depend on either τ_1 or τ_2, in such a way that the oscillation frequency is half the oscillation frequency of the intended SIFTER oscillation. To separate these residual modulations, we recorded SIFTER data at 12 different echo positions $2(\tau_1 + \tau_2)$ (see caption for details). In this way, the phase of the SIFTER oscillation remained unchanged, whereas the phase of the residual modulations was varied over a full oscillation period. Accordingly, averaging the 12 datasets effectively canceled those residual modulations, as can be recognized by the absence of such modulations in the data shown in Fig. 8.22 and further below in 2D EPR-correlated SIFTER data. Moreover, variation of the residual modulations allowed to quantify their modulation depth. In particular, the residual modulation at the beginning of the trace due to imperfections in ④ had a peak-to-peak modulation amplitude of 3.5%. The residual modulation at the end of the trace due to imperfections in ② had a peak-to-peak modulation amplitude of 6%. The larger modulation amplitude due to ② can be related to the smaller adiabaticity factor of pulse ② as compared to pulse ④ (2.06 vs 2.63).

Besides the suppression of these weak residual modulations by averaging, there may still be room for reducing the modulation amplitude in the first place. In particular, the pulses ② and ④ refocus the resonance offset. Due to the double-refocusing, these pulses implement an ABSTRUSE scheme and largely compensate Bloch-Siegert phase shifts [60, 35]. In presence of spatial inhomogeneities in ν_1, refocusing with two frequency-swept π pulses allows for larger adiabaticity than refocusing with a single frequency-swept π pulse. In fact, the 64 ns FP180 pulse in the 2 : 2 : 2 : 1 SIFTER scheme had 77% larger field amplitude than the optimized 64 ns FP180 pulse in the 2 : 1 chirp echo in Section 8.4.3.1.

However, the amplitudes of pulses ② and ④ have been set up individually, by first optimizing ② and then optimizing ④. Based on our previous experience with refocused chirp echoes [35], such a two-step optimization procedure may not result in optimum pulse amplitudes. One needs to either repeat the two-step procedure several times, or one needs to optimize the amplitudes of ② and ④ concurrently while maintaining equal adiabaticity factors. The concurrent optimization procedure is recommended for setting up future experiments. This also allows to deliberately use too large adiabaticities, therefore trading echo intensity for smaller residual modulations. With the pulse parameters in the experiment, the largest possible adiabaticity for the

64 ns FP180 pulse would have been 3.65. Note that the modulation averaging procedure implemented here also trades echo intensity against smaller residual modulations, because the prolongation of the pulse sequence results in a loss of echo intensity.

For 2D EPR-correlated SIFTER data, the echo transients were processed by two-dimensional Fourier-transform. Upon the first FT along the EPR dimension, a Gaussian background decay has been fitted to EPR-correlated SIFTER traces. Due to an artificial contribution of quartz in the EPR spectrum (see below), subtraction of this Gausssian background decay yielded the best results. Before computing the second FT along the SIFTER dimension, the remaining constant offset was subtracted. Due to the long dipolar evolution window, it was also possible to use a Chebychev window to apodize EPR-correlated SIFTER traces without significant broadening of dipolar spectra. With a shorter dipolar evolution window, such an apodization may no longer be admissible and a different approach for symmetrizing the EPR-correlated SIFTER traces would be required.

The magnitude of the 2D correlation spectrum obtained according to the above description is shown in Fig. 8.23a. The FT EPR spectrum on the right hand side corresponds to the real part of the FT at $t = 0$ and approves refocusing of the resonance offset. However, around an EPR offset of -80 MHz, an unusual peak in the FT EPR spectrum is observed. This peak is related to quartz from the sample tube and was presumably higher than usual due to quartz splinters above the sample from a breakage at the entrance of the sample tube. This quartz artifact caused the peak around zero dipolar frequency observed at the corresponding position in the 2D correlation pattern and also influenced the amplitude of the main dipolar ridge around ± 0.8 MHz. In addition, background correction resulted in a discontinuity in dipolar spectra around the zero frequency.

Other than these artifacts, the 2D correlation spectrum encodes the frequency splitting between dipolar doublets throughout the entire EPR spectrum. The SIFTER projection above the correlation spectrum resembles a Pake pattern. The dependence of the dipolar coupling on EPR frequency is due to orientational effects, as illustrated in the following. In particular, normalized SIFTER data at three distinct EPR frequencies labeled *i*, *ii* and *iii* are illustrated in Figs. 8.23b and c in time domain and in frequency domain, respectively. The positions within the EPR spectrum are indicated by the horizontal markers in the correlation spectrum in panel (a). Positions *i* and *iii* correspond to canonical orientations along the x and z axis in the nitroxide PAS, respectively. At position *ii* a multitude of spin orientations contribute to the EPR spectrum (see also Fig. 8.19b).

In order to relate the orientations of the nitroxide to the spin-spin orientations, the structure of the nitroxide-ruler is shown in Fig. 8.23d. The two vectors labeled *i* and *iii* denote the orientations of the static magnetic field with respect to the ruler. Because the N-O bond is collinear with the inter-spin vector, the canonical orientation along x in the nitroxide PAS corresponds to a parallel alignment between the magnetic field and the inter-spin vector. The dipolar interaction for such a configuration results in a splitting by twice the fundamental splitting ω_{dd}, which corresponds to the parallel singularity at the shoulders of the Pake pattern. The canonical orientation along z in the nitroxide PAS corresponds to a orthogonal alignment between the magnetic field and the inter-spin vector. In this configuration, the dipolar interaction results in a splitting by the fundamental frequency ω_{dd}, which corresponds to the transverse singularity at the horns of the Pake pattern.

The Pake singularities predicted from the structure of the ruler are reproduced in the SIFTER slices in panels (b) and (c). In fact, the double frequency at the parallel singularity at position *i* and the fundamental frequency at the transverse singularity at position *iii* are readily identified. At position *ii*, the contribution of several orientations results in a dipolar spectrum resembling a Pake pattern. The pronounced asymmetry in the dipolar spectrum observed

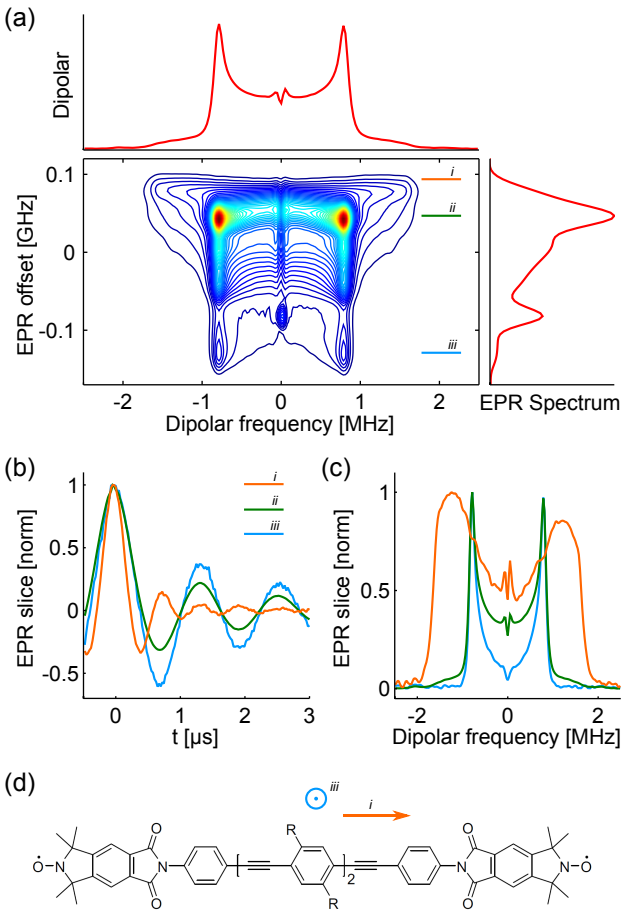

Figure 8.23 – 2D EPR-correlated SIFTER. (a) Magnitude 2D FT of SIFTER echoes with background correction as described in the text. The dipolar spectrum above the correlation spectrum is the projection of the illustrated 2D spectrum. The EPR spectrum on the right is the real part of the FT for $t = 0$. Relevant EPR positions are indicated by the horizontal markers labeled *i*, *ii* and *iii*. (b, c) Normalized SIFTER traces at relevant EPR positions in time domain (b) and in frequency domain (c). (d) Structure of the investigated nitroxide-ruler (see also [200, 157]). The vectors in blue and orange indicate the orientations of the magnetic field at the EPR positions *i* and *iii*. Note that there is no way to differentiate between positive and negative direction in the high-temperature approximation.

at postion *i* is probably due to the steep ascent in the EPR lineshape. In fact, pronounced asymmetries have also been observed at the fundamental dipolar frequency in regions of steep ascent around the main peak of the EPR spectrum.

Based on these considerations, we therefore conclude that it is in principle possible to use the 2D SIFTER technique to study the relative orientation between spin labels. At present, such studies are performed using the four-pulse DEER experiment at W-band frequencies recorded for a set of pump and observation positions [204]. Multiple DEER experiments are therefore required, which results in a longer acquisition time than for 2D SIFTER.

However, it is important to point out the differences between DEER and 2D SIFTER with respect to orientation selection. In DEER, the observation frequency selects the relevant position in the EPR spectrum. In the 2D SIFTER correlation spectrum, this corresponds to the EPR frequency offset. In presence of orientation selection, however, the dipolar pattern obtained with DEER and 2D SIFTER may be entirely different. The reason is that the pump position in DEER selects the orientation of the coupled spin partner, whereas 2D SIFTER reveals the dipolar spectrum due to all coupled spin partners. With pump and observation positions at canonical orientations in the nitroxide PAS, DEER therefore probes specific geometrical correlations between

the orientations of the coupled spins. 2D SIFTER on the contrary reveals geometrical correlations between the orientation of one spin and the inter-spin vector, without information on the orientation of the coupled spin (see below: pseudo-secular contributions in principle encode this information). Accordingly, there are four angles that determine the correlation pattern in 2D SIFTER data, namely the two angles required to describe the orientation of the inter-spin vector related to each of the two spins. On the contrary, DEER data with orientation selection encodes five angles [71], so that the fewer parameters in 2D SIFTER may simplify the extraction of orientational information from experimental data.

Since the orientation between the inter-spin vector and the spin-label are identical for both spin labels of the nitroxide-ruler investigated here, both spin labels contribute in the same way to the 2D correlation spectrum. In a simulation study of six-pulse DQC with hard pulses [205], 2D correlation spectra of spin pairs with different relative orientation to the inter-spin vector have been calculated. For these cases, the 2D correlation spectrum is a superposition of two spectra (see for instance Fig. 8c in [205]). Note that to date, 2D correlation spectra by six-pulse DQC with hard pulses have been demonstrated at 17.25 GHz microwave frequency by combining two datasets covering one half of the EPR spectrum each [138].

An additional relevant difference between DEER and 2D SIFTER is the role of pseudo-secular contributions to the dipolar interaction. While spin pairs that are not in weak coupling conditions can be suppressed by the frequency separation between pump and observer in DEER, this is not possible in SIFTER [203]. As suggested in [205], the pseudo-secular contribution in 2D correlation spectra provides additional information on the frequency separation between coupled spin pairs. Provided that these contributions can be resolved experimentally, information on the orientation of the coupled spin partner could in principle be extracted from 2D SIFTER spectra.

For improved resolution of the g-tensor, 2D SIFTER at W-band frequencies would be advantageous. The feasibility of FT EPR with chirps at W-band remains to be investigated and a W-band setup with 2 W excitation power is currently under construction.

9

CONCLUSIONS

In brief, the results of this thesis affirm that excitation bandwidth in EPR can be enhanced by roughly one order of magnitude using frequency-swept microwave pulses. The sensitivity enhancement achieved by these pulses can be classified into two groups:
(1) Sensitivity enhancement by inversion of unobserved spins over extended bandwidths, which includes the DEER and population transfer experiments. These experiments are of pump-probe type and a distinct advantage is that the probe part of the pulse sequence can be realized with existing spectrometers, while the extension of the pump part of the pulse sequence to frequency-swept pulses requires only moderate technical modifications of an existing spectrometer.
(2) Sensitivity enhancement by increasing the fraction of spins that directly constitute the echo signal, which results in FT EPR spectra of larger bandwidths, but also in more efficient excitation over a certain bandwidth by means of frequency-selective pulses. While these approaches are promising for establishing new types of multi-dimensional experiments, the technical requirements on the spectrometer are more elaborate than for the pump-probe type of experiments, especially for FT EPR spectra and correlation experiments in the ultra-wideband regime.
A key to the achieved excitation bandwidths is the compensation of bandwidth limitations imposed by the resonator. Also in this respect, it is important to differentiate between the two classes of experiments. For pump-probe type of experiments, the compensation procedure establishes a targeted adiabaticity factor within a broad frequency band at minimum expense in pulse duration. In this way, the pumped spins contribute equally to the intended transfer of population or coherence, which eases optimization and interpretation of the experiment. In favorable cases, it is sufficient to approximate the characteristics of the resonator by a simple parametrization. Combined with the experience of the experimenter on the details of the utilized resonator, this eases a rather fast extraction of the relevant resonator parameters.
The situation is different for FT EPR approaches, since the degree of bandwidth compensation has a direct influence on the quality of obtained spectra. Especially the coherence excitation pulses have a critical dependence on the field strength inside the microwave resonator. Moreover, even refocusing pulses that are often claimed to be adiabatic perform non-optimal in presence of spatial inhomogeneities in the driving field. Since the presented FT EPR experiments are bound to spectrometers providing coherent AWG excitation pulses and versatile pulse sequence programming, a fast characterization of the resonator often allows for highly accurate compensation. Spatial inhomogeneity, on the contrary, can not be compensated by adaptation of the frequency-swept pulse. If the resultant signal losses are significant and can not be compensated with multiple refocusing pulses, different classes of pulses may need to be taken into consideration, such as optimal control pulses or adiabatic plane rotations.
Given the alleviated technical requirements for the pump-probe type of experiments, one would expect that these approaches are more readily adopted in different laboratories in a short term perspective than the FT EPR approaches. Nevertheless, there are currently a lot of efforts to implement AWGs into EPR spectrometers for coherent pulses, both by vendors and by individual

research groups. Besides the sensitivity enhancements presented within this thesis and by others, these ambitions are also motivated by potential reductions in maintenance and cost of EPR spectrometers. In this way, pulsed EPR becomes accessible to more laboratories.

Within the actual context of solid state EPR for structural insight into spin-labeled biomacromolecules, the sensitivity enhancement of pump-probe type distance measurements is especially important. The optimized Gd-Gd distance experiments, for instance, remain unprecedented for determining long distances at the time of writing. The presented methodology and optimization protocols when pumping transition metal ions can also be translated to further optimize nitroxide-nitroxide distance measurements or more complicated spin topologies, such as multiple spin labels.

FT EPR approaches have the potential to become an important technique in several aspects. For systems with diluted electron spins, sensitivity of known pulse sequences can be enhanced by incorporation of frequency-swept pulses, as exemplified for relaxation and ESEEM studies. In particular, ESEEM techniques are important in revealing structural information on coordination complexes. The broad spectrum due the spin bearing transition metal ion is a well suited candidate for frequency-swept excitation pulses. Besides enhancing the intensity of the relevant spin echo, correlation to the EPR spectrum by the additional dimension of the experiment as well as potential contributions from directly coordinated nuclei may entail further insight.

For systems with coupled electron spins, dipolar coupling may result in unwanted signal loss when incorporating frequency-swept pulses into pulse sequences designed for selective pulses. In this case, refocusing techniques such as the solid echo or multi-quantum filtering need to be incorporated, as exemplified for the solid echo. The correlation of dipolar spectra to the EPR spectrum reveals additional information on geometry. Even if the problem of extracting relative orientations is likely to remain a very difficult problem also with FT EPR techniques, the dispersion of Pake singularities within the correlation pattern may provide information on conformational flexibility. Other than dipolar couplings, it should be noted that solid echoes and multi-quantum techniques may also be adopted to spins $S > 1/2$, as long as a significant part of the high-spin multiplet spectrum can be covered by the frequency-swept pulses.

Overall, one can therefore expect that frequency-swept pulses, and shaped pulses in general, will become an important tool in pulsed EPR spectroscopy with applications to problems of relevance in structural biology and chemistry.

A

SUPPORTING INFORMATION TO CHAPTER 3

A.1 PHASE / GROUP DELAY RETRIEVAL FROM MAGNITUDE RESPONSE

This section describes the detailed procedure to reconstruct phase and group delay from the experimental magnitude response $\nu_1(f)$. The basis of the phase retrieval is that the experimental $\nu_1(f)$ is the magnitude of a causal (and stable) transfer function $H(f)$. As a consequence of causality, the transfer function $H(f)$ exhibits the following two relations [206, 207]:
The real and imaginary parts of $H(f)$ are connected by the Hilbert transform, which is known as the Kramers-Kronig relation. The connection between magnitude and phase of $H(f)$ is given by the Bode relations. In this case, the logarithm of the magnitude and the phase are Hilbert transformation pairs, provided that $H(f)$ obeys the minimum phase criterion, which is related to the location of the zeros of $H(f)$. For a given magnitude response, phase retrieval by the Bode relation therefore results in the phase response of minimum phase delay. The corresponding impulse response $h(t)$ then follows the excitation as instantaneously as causality allows for.
Any transfer function that does not obey the minimum phase criterion can be factorized into a minimum phase and an all-pass system. A potential all-pass factor present in $H(f)$, which affects the phase characteristic exclusively, is therefore not retrieved by this procedure. On one hand, this leads to the exclusion of uniform pulse delays in the excitation chain, $\tau_g(0)$, which is advantageous, because the spins are not susceptible to such delays (see the discussion of $\hat{\tau}_g$ in Section 3.2.2). On the other hand, there are other all-pass factors than time delays [208], which could introduce group delay variations not resolved by the retrieval procedure (see also [209]). At this point, we have no means for disproving such contributions and can thus only assume that the excitation chain is minimum phase. As shown in Section 3.4.3, this assumption is good enough to obtain enhanced adiabaticity by group delay compensation.
Furthermore, group delay variations prior to the power amplifier are not retrieved due to amplitude compression. But as a consequence of the wide bandwidths of the components prior to the power amplifier, those variations are presumably small. In other words, total group delay variation is dominated by the TWT amplifier itself and the resonator, and except for potential all-pass contributions, the behavior of these two components as parts of the excitation chain, when driven by sinusoidal functions of constant full-scale amplitude (see Section 3.4.1), is included with our approach.
Recalling Section 3.4.1, the experimental $\nu_1(f)$ is not complete, because it can only be measured for a set of frequencies between 9 and 10 GHz with the actual measurement setup limited by the observer frequency range of the Elexsys E580 or E680 spectrometer. Accordingly, an extrapolation of measurement data is required in order to perform the discrete Hilbert transformation. For this purpose, we used the ideal model H_{id} of an RLC series circuit from Eq. (3.5) to construct $\hat{\nu}_1(f)$, which is defined at all frequencies. The construction of $\hat{\nu}_1(f)$ is by exponentially approaching $|H_{id}(f)|$ starting from the boundaries of $\nu_1(f)$ with a decay constant of 100 MHz / ln(2). Fig. 3.5a depicts both the resulting $\hat{\nu}_1(f)$ (black) and $|H_{id}(f)|$ (gray) in the frequency range of interest. The model parameters of $H_{id}(f)$ are the ideal resonator

center frequency $\hat{f}_0$ and its ideal quality factor $\hat{Q}_L$. We found that the group delay variation in the frequency range of interest is very insensitive to the choice of $\hat{f}_0$ and $\hat{Q}_L$, such that $\hat{f}_0$ = 9.35 GHz and $\hat{Q}_L = 37$ were chosen solely for an appropriate overlap at the boundaries of $\nu_1(f)$.
One implication of extending $\nu_1(f)$ by $|H_{id}(f)|$ is that $H_{id}(f)$ itself is not a minimum phase realization because of one zero at $f = 0$ and one zero when $f \to \infty$. The zero at the origin must be canceled, which was done by substitution with its adjacent non-zero element in $\hat{\nu}_1(f)$. However, the asymptotic zero at infinity cannot be canceled. Recalling that each zero on the frequency axis shifts the response with respect to discrete time excitation by half a sample [208], the minimum phase realization of $\hat{\nu}_1(f)$ responds half a sample faster than $H_{id}(f)$. Consequently, the phase $\hat{\beta}(f)$ retrieved from the logarithm of $\hat{\nu}_1(f)$ has a positive slope, as seen in Fig. 3.5b by the phase offset between $\angle H_{id}(f)$ (dashed gray) and the phase retrieved from $|H_{id}(f)|$ (gray). In fact, the actual group delay due to the zero at infinity depends on the Nyquist frequency chosen to construct $\hat{\nu}_1(f)$ and the value of half a sample was reached asymptotically for very fast THz Nyquist frequencies. Since the contribution by a delay of half sample to the total group delay is rather small in the frequency range of interest, we have always used a Nyquist frequency of 54 GHz and 2^{14} points to construct $\hat{\nu}_1(f)$. The phase $\hat{\beta}(f)$ retrieved in this way is shown in Fig. 3.5b (black).
The retrieved phase $\hat{\beta}(f)$ and corresponding magnitude $\hat{\nu}_1(f)$ define a minimum phase transfer function $\hat{H}(f)$. The corresponding impulse response $\hat{h}(t)$ can be obtained by the inverse Fourier transform. For the actual Nyquist frequency of 54 GHz and 2^{14} points, $\hat{h}(t)$ has a length of roughly 152 ns with time origin in the center upon cyclic permutation. A zoom at the origin of the real part of $\hat{h}(t)$ is shown in Fig. A.1 and reveals a causal response. The imaginary part of $\hat{h}(t)$ vanishes, because $\hat{\nu}_1(f)$ is symmetrical with respect to the frequency origin. The potential use of such an approach for optimal control pulses, where an impulse response can be included in the optimization process [15, 85], requires further investigation.

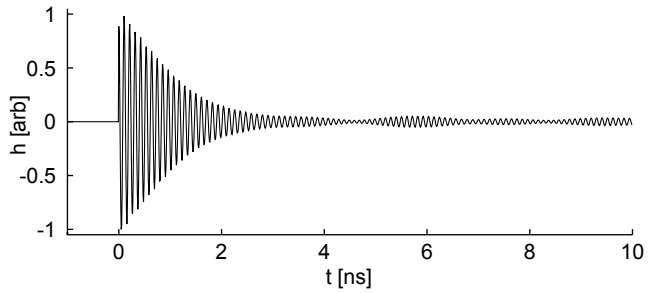

Figure A.1 – Causal and real-valued impulse response $\hat{h}(t)$ by inverse Fourier transformation of $\hat{H}(f)$ shown from $t = -1$ ns to $t = 10$ ns.

A.2 PULSED ELDOR DETECTED MAGNETIZATION TRANSFER

We used pulsed ELDOR techniques to detect magnetization transfer of inverted spins to distant spins [108]. In the actual experiment, the central line of TEMPOL at 50 K is inverted by a monochromatic rectangular 32 ns pulse. The inversion pulse originated from the AWG and its frequency was set to the center frequency f_0 of the resonator. Using a (16-32 ns) Hahn echo detection scheme that includes a [+(+x) -(-x)] phase cycle, the transfer and recovery of longitudinal magnetization upon the inversion pulse was observed at distinct parts of the spectrum by using different observation frequencies. The observation frequency was stepped automatically using ProDel[1] in 10 MHz steps from 9.183 GHz to 9.423 GHz. At each observation frequency, recovery

[1] Optimized code for precise frequency stepping available upon request

traces were measured up to a recovery delay of 15.35 ms, starting at 400 ns with an increment of 5 μs, in 53 minutes total measurement time each by using a repetition rate of 58 Hz. Each trace was normalized to the equilibrium magnetization obtained from the last 30 data points. Amplitude and phase of the observation pulses were initially set up at the center frequency f_0 of the resonator. Due to the automated frequency stepping, echo signals recorded at offset from f_0 had reduced amplitude and a shift in the phase. The associated phase shift was corrected in a postprocessing step based on the phase obtained from the last 30 data points.
The results are shown in Fig. A.2. Fig. A.2a shows several time slices of recovery traces at different observation frequencies. Each time slice has a color coding resembling the recovery delay: the red curve has the shortest delay and the blue curve has the longest delay. For visualization purposes, the actual time spacing between each time slice is logarithmic. In addition, each recovery trace was renormalized to the intensity of the field-swept nitroxide spectrum at the corresponding observation frequency. The figure therefore reveals how the nitroxide spectrum recovers upon inversion of the central line. As expected from previous work [108, 210], magnetization transfer is weak and cannot be observed in Fig. A.2a. On a closer look to recovery traces however, a signature of magnetization transfer can be found. As an example, the trace at a frequency of 9.393 GHz is shown in Fig. A.2b up to a delay of 10 ms. At the very beginning of the trace, there is a small offset due to excitation by the rectangular inversion pulse. Up to a delay of 1 ms, transfer of inverted spins from the central line leads to a slight reduction in magnetization. At longer delays, relaxation is predominant.

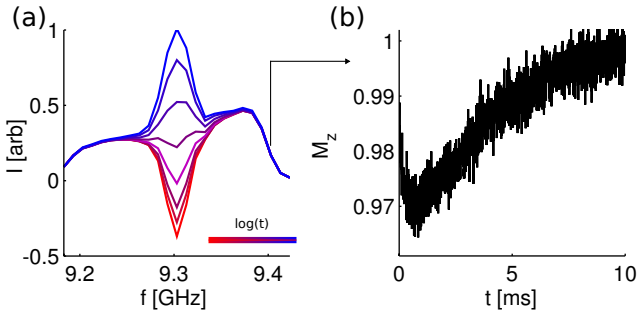

Figure A.2 – Magnetization transfer detected by pulsed ELDOR. (a) Time slices of recovery traces at different frequencies and renormalized to the field-swept nitroxide spectrum. Logarithmic spacing between time slices indicated by the color coding from red to blue. (b) Recovery trace at 9.393 GHz showing signature of magnetization transfer.

A.3 OPTIMIZATION OF MODULATION DEPTH

In order to achieve higher modulation depths than those shown in Fig. 3.8, we applied group delay compensation and also changed experimental conditions by using an Elexsys E580 spectrometer (spectrometer II) instead of the E680 we used so far (spectrometer I). With the same fully overcoupled resonator and the same sample tube inserted, $\nu_1(f)$ on the two spectrometers was as illustrated in Fig. A.3a and A.3b (gray). The apparent differences in $\nu_1(f)$ between spectrometer I and spectrometer II highlight the aforementioned influence of the excitation chain as a whole (Section 3.4.1). These differences arise most likely due to combined effects of component-specific variations in the high power branch following the TWT amplifier. These include the characteristic of the TWT amplifier as well as specific reflections. Note that on no account, the observed differences in $\nu_1(f)$ can be generalized to the type of the spectrometer (E680 or E580). In fact, we would expect different magnitude and phase characteristics, $\nu_1(f)$ and $\beta(f)$, for the same type of spectrometer, depending on differences between spectrometer components.

In other words, $\nu_1(f)$ and $\beta(f)$ are very sensitive to the quality of components, transmission lines and connections. On top of this, $\nu_1(f)$ and $\beta(f)$ may vary somewhat between experiments on the *same* spectrometer, due to variations of the resonator/sample systems. Such variations are expected in the position and orientation of the sample in the resonator or in the position of the coupling antenna, even though in this work a locking nut was used to define the latter position. Not surprisingly, $\nu_1(f)$ on spectrometer I varies somewhat when the same sample tube is reinserted, presumably in a slightly different orientation and position (see Fig. A.3a and Fig. 3.8a). As can be seen in Fig. A.3a and A.3b from the retrieved $\nu_\beta(f)$ (black), the smoother shape of $\nu_1(f)$ on spectrometer II results in less pronounced group delay variations than on spectrometer I.

Measurements of $M_z(\Delta f)$ using $\hat{\tau}_g$ compensated (solid black) or uncompensated (solid gray) pulses are shown in Fig. A.3c. On spectrometer I, the observation frequency was 9.333 GHz, which is the center frequency of the corresponding $\nu_1(f)$. On spectrometer II, the observation frequency was 9.303 GHz. The central line of the nitroxide associated with the copper-nitroxide complex was set to be in resonance at the corresponding observation frequency. All other parameters of this measurement are described in Sections 3.4.2 and 3.3.4. The chirp pulse had therefore a length of 128 ns and Δf was centered with respect to the corresponding observation frequency. While the measurements in spectrometer I revealed a slight improvement in $M_z(f)$ when using $\hat{\tau}_g$ compensated instead of uncompensated pulses, no significant changes were seen on spectrometer II.

To compare modulation depths, we used a 64 ns UWB pulse with Δf = 800 MHz. This particular sweep width was chosen because it turned out to be the optimum on spectrometer II. On spectrometer I, exactly the same pulse frequencies as in Section 3.4.6 were used. On spectrometer II, all frequencies were 10 MHz lower and the magnetic field was set accordingly. The resulting DEER form factors are shown in Fig. A.3d. On spectrometer I, where each DEER trace was recorded for 3 hours, $\hat{\tau}_g$ compensation (black, 21.4% modulation depth) resulted in a 3% higher modulation depth compared to the uncompensated chirp (gray, 20.8% modulation depth). On spectrometer II, where each DEER trace was recorded for 16 hours for further data analysis, the improvement by $\hat{\tau}_g$ compensation is 1.5% (from 23.8% to 24.1%). This smaller improvement observed on spectrometer II is in agreement with the smaller overall $\nu_\beta(f)$ found on spectrometer II as compared to spectrometer I. Nevertheless, the $\hat{\tau}_g$ compensation described in Section 3.4.3 was sufficient also in this case to slightly improve the net inversion.

As a result, the maximum modulation depth that we achieved for a 64 ns pulse is 24%. By using the monochromatic rectangular 8 ns pulse measured on spectrometer II under the same conditions as a reference (see Fig. A.3d, actual length was 7.5 ns), the enhancement in modulation depth is 3.14 and the enhancement in total detection sensitivity is 2.47 due to echo reduction. If we consider the highest modulation depth of 8% that we ever achieved with a monochromatic rectangular 8 ns pulse, a threefold enhancement in modulation depth results. In fact, this 8 ns reference (data not shown) was acquired on spectrometer I at the conditions given in Fig. A.3a with a pulse length of exactly 8 ns.

For the discussion of remaining distance distortions in the main text, the form factors measured on spectrometer II for the $\hat{\tau}_g$ compensated UWB pulse and the corresponding monochromatic rectangular 8 ns pulse from Fig. A.3d are reproduced in Fig. 3.9a.

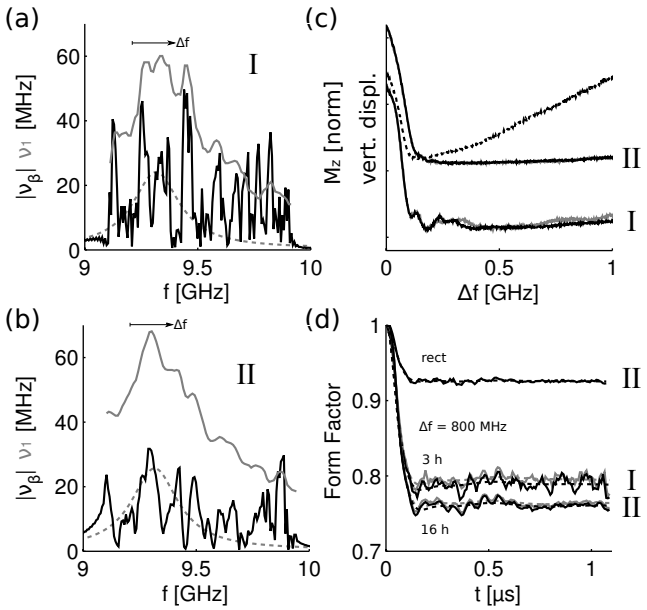

Figure A.3 – DEER modulation depth enhancement on two different spectrometers, using the same resonator. (a) Experimental conditions in the Elexsys E680 (I): $|\nu_\beta|$ of $\hat{H}(f)$ (black) and $H_{\mathrm{id}}(f)$ (dashed gray) with a chirp rate of (640 MHz / 32 ns). $\nu_1(f)$ (gray) is indicated for reference. Note the differences to $\nu_1(f)$ in Fig. 3.8a of the same sample tube, but a different insertion. (b) Experimental conditions in the Elexsys E580 (II): $|\nu_\beta|$ of $\hat{H}(f)$ (black) and $H_{\mathrm{id}}(f)$ (dashed gray) with a chirp rate of (640 MHz / 32 ns). $\nu_1(f)$ (gray) is indicated for reference. Note the apparent differences to $\nu_1(f)$ in I in Figs. 3.8a or A.3a, where the same resonator and the same sample tube was used. (c) Effect of $\hat{\tau}_g$ compensation: $M_z(\Delta f)$ for a 128 ns pulse at the respective f_0 (compare to Section 3.4.3) when using $\hat{\tau}_g$ compensated (solid black) instead of uncompensated pulses (solid gray). Upper curves measured in II (gray underneath black), lower curves in I. The vertical displacement between the upper and lower curves is 0.5. Also shown for II is $M_z(\Delta f)$ with 6 dB attenuation after the TWT (dashed black), which yielded the 6 dB figure of 86% at Δf = 525 MHz that was mentioned in Section 3.4.2. (d) Experimental (solid) and fitted (dashed) DEER form factor obtained for a monochromatic rectangular 8 ns pump pulse on spectrometer II (black, upper curve) and for a 64 ns UWB pump pulse (Δf = 800 MHz) with (black) and without (gray) $\hat{\tau}_g$ compensation on spectrometers I and II as indicated. Data acquisition on II was longer for further distance analysis (see Fig. 3.9).

B

SUPPORTING INFORMATION TO CHAPTER 4

B.1 AWG SPECTROMETER

In this section, some more details are given on the home-built X-band spectrometer described in the main text. A schematic of the spectrometer is depicted in Fig B.1. The associated component listing is given in Table B.1.

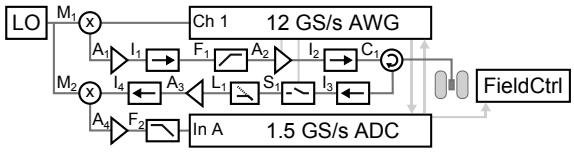

Figure B.1 – Spectrometer layout showing main signal path (dark gray) and control triggers (light gray). Component listing in Table B.1

The main signal path initiates at the output of the AWG, where pulse sequences are generated at intermediate frequencies (IF) around 1.3 GHz with full-scale amplitude of roughly 3 dBm. This IF is fed to the mixer for upconversion to X-band with an 8 GHz local oscillator (LO). One single mixer is used, which results in sidebands around 9.3 GHz and around 6.7 GHz. Before directing this signal to the high-power amplifier, a high-pass filter removes the lower sideband. Note that the upconversion results in spurious signals, such as LO feed-through and higher order mixing products of the LO and the IF. In the present work, the maximum bandwidth of the signals was roughly 700 MHz around 9.3 GHz. In this regime, spurious signals fall outside the bandwidth, where these could perturb the spin system. We know from experience with the upconversion setup shown in Fig B.1 that this is no longer the case if signal bandwidths exceed 1 GHz. In such cases, it is required to reduce the amplitude of the IF generated by the AWG by some 10 dB, which will in turn enhance LO feed-through.
In the receiver, microwave signals are amplified by a low noise amplifier, which is protected from excitation pulses by an active switch and an auxiliary passive limiter. Upon downconversion, the signals at an IF around 1.3 GHz are amplified and acquired by the digitizer. Due to the 1.5 GS/s sampling rate of the digitizer, the digitized echoes appear in the Nyquist window from 0 to 750 MHz, an acquisition concept often referred to as *subsampling*. The analog bandwidth of the digitizer allows for subsampling of signals in the second Nyquist window from 750 MHz to 1.5 GHz and from the third Nyquist window from 1.5 GHz to 2.25 GHz. The chirp echo spectra presented in the main text had its spectral content in the second Nyquist window exclusively. For the UWB chirp echo of copper, we needed to use a different LO frequency of 8.125 GHz to center the resonator with respect to the second Nyquist window.
A key requirement for coherent averaging of echoes on this spectrometer is that all clocks are synchronized to one single reference. The corresponding devices are found under the label CLK in Table B.1. In experiments where the position of the echo changes as a function of time, identical phase for all acquired echoes can be achieved by programming the increment of the echo position at the time resolution of the digitizer.
As mentioned in the main text, the entire N-dimensional pulse sequence is

Label	Device
AWG	Agilent M8190A with options 002, 12G, AMP, SEQ, FSW, 02G
ADC	SP Devices ADQ412-3G USB
FieldCtrl	Bruker E32
M_1, M_2	MITEQ M0812 or DM0412LW2
I_1, I_3, I_4	Meuro CIS080120F
I_2, C_1	RYT Ind. 300190
F_1	Minicircuits VHF-8400
F_2	Minicircuits SLP-2400
A_1	Minicircuits ZX60-01412L
A_2	Applied Systems Engineering TWT 117X
A_3	Meuro MLB0812G3013
A_4	Minicircuits ZX60-V62
S_1	Meuro SPST00518N6
L_1	Meuro MLT080120T15
LO	Nexyn NXPLOS-0800-03615 (8 GHz) Agilent E8257D (8.125 GHz)
CLK	Nexyn NXPLOS-1200-03593 (12 GHz AWG Clk) Nexyn NXOS-PLXO-100-03593 (10 MHz $\rightarrow$ 100 MHz) Agilent E8257D 10 MHz RefClk (Master for ADC and all derived clocks)

Table B.1 – Component listing for Figure B.1 and instrument clocking scheme (CLK)

preloaded to the AWG before starting an experiment. The control scheme during each point of the experiment is implemented as follows: (i) A hardware trigger issued by the digitizer initiates the generation of the pulse sequence that corresponds to the actual data point. (ii) The AWG repeats this pulse sequence as specified by the number of accumulations per point. The pulse sequence of the AWG includes fast triggers for blanking and protection as well as for the digitizer. (iii) A background process on the control computer recognizes that the digitizer averaged all accumulations and gathers the data. Upon success, the digitizer sends the hardware trigger to advance the AWG to the next data point. If the experiment requires a step in the magnetic field for the next data point, the digitizer releases another hardware trigger for the field controller.

Note that during an experiment, this scheme requires software interaction with the digitizer exclusively. In the standard setup, where the digitizer acquires signals over a length of 2.7 μs (4096 sampling points), these software interactions lead to an idle time of 6 to 7 ms after the last accumulation of each data point. For the experiments with nitroxide, this was below the repetition time of the experiment and therefore did not lead to any prolongation of the experiment. For the experiments with copper, the prolongation due to the idle time was below one percent. With respect to faster relaxing compounds, we expect a significant further reduction in this idle time by programming the experiment control into the user-programmable logic inside the digitizer.

Another point mentioned in the text is the limited sensitivity of the spectrometer in Fig. B.1. The main reason for this is a restriction on the overall gain of amplifiers in the receiver. If we would enhance this gain further, the residual leakage of excitation pulses into the receiver would saturate the digitizer. This problem will be addressed by a secondary receiver protection switch. In general, we expect the architecture of the receiver upon optimization of detection sensitivity to differ from the one shown in Fig. B.1.

B.2 LIMITATIONS OF PULSE COMPENSATION APPROACH

As pointed out in the main text and previously [74], there is a limitation on the shape of the transfer function $\nu_1(f)$ to be compensated. The origin of this limitation is the chirp-specific approximation

$$\nu_1(t) \approx \nu_1(f)\Big|_{f=f_i(t)}$$

which means that the time domain pulse amplitude is given by the frequency domain transfer function evaluated at the instantaneous frequency f_i of the chirp (see [74]). Only for a pulse at a fixed frequency and of infinite duration, i.e. a stationary signal, the above statement is mathematically exact. Because this approximation considerably alleviates the relation between time and frequency domain, it is of interest to see where this can still be used in practice.

The goal of the compensation is to achieve an offset independent adiabaticity Q_{ref}. For a variable-rate chirp with instantaneous sweep rate $\delta f/\delta t$, this relates to the frequency domain as

$$Q_{\text{ref}} = 2\pi\ \nu_1^2(t)\ \delta t/\delta f \approx 2\pi\ \delta E/\delta f$$

where δE is the spectral energy $\nu_1^2(f)\delta t$. [1]

As a consequence, a simplification of pulse dynamics is appropriate in those situations, where the energy density of the compensated pulse seen by the spins is constant. Since the flatness of the energy density of the pulse seen by the spins is related to the FT of the digital pulse multiplied by the transfer function $\nu_1(f)$, a self-consistency check can be performed.

Four examples of this consistency check are summarized in Fig. B.2. The experimental transfer functions $\nu_1(f)$ (green curves) define the compensation target. The numerically obtained variable-rate chirps (light gray curves) assume simplified pulse dynamics. The square root energy densities seen by the spins (black curves) illustrate the actual performance of the compensation.

Panels (a) and (b) depict AP pulses from previous work [74]. The almost flat pulse profile at the spins suggests that both AP pulses achieve a compensation of $\nu_1(f)$. In inset (b), the flatness is somewhat better than in inset (a) due to less pronounced narrowband features in $\nu_1(f)$. As a consequence of the distinct features in $\nu_1(f)$ in inset (a), there is a significant perturbation of the phase of the pulse. In previous work [74], we have shown that this can be accounted for by simplification of the actual phase perturbation. As stated in the main text, we currently do not see a need to consider any phase perturbations if the spectrometer provides sufficient bandwidth and a sufficiently smooth transfer function $\nu_1(f)$. However, we expect that at faster sweep rates than those used in the present work, phase perturbations may again become significant.

Panel (c) depicts an AP pulse on a previous realization of our home-built spectrometer, which had standing waves in the excitation arm. At this time, the components I_2 and C_1 were WR90 waveguide components, which required adapters for connection by coaxial cables to A_2, S_1 and the resonator. The isolator I_3 was not mounted. Upon optimization of the excitation arm, we added I_3 and changed to coaxial components for I_2, C_1 and I_3. Note that the change to coaxial components was mainly due to the utilized coax to waveguide adapters, which here lead to unfavorable loading conditions for the power amplifier [211].

Due to the standing waves at this earlier stage of the coherent spectrometer development, the flatness in inset (c) is considerably worse than in insets (a) and (b). The variable-rate AP pulse is therefore not able to compensate all

[1] In [46], the authors have arrived at a related result that connects the adiabaticity to the power spectral density of the pulse.

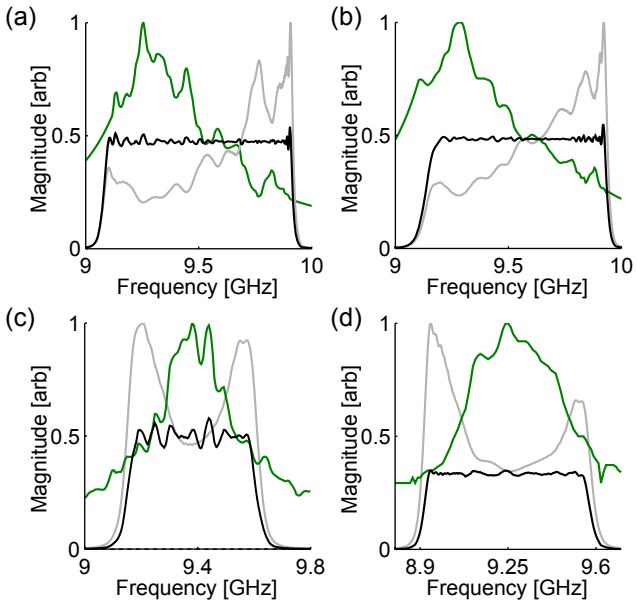

Figure B.2 – Pulse compensation under various experimental conditions $\nu_1(f)$ (green). The Fourier transform of the digital pulses with variable-rate chirp are shown in light gray. The pulses seen by the spins are shown in black. (a) Experimental conditions from [74] with shortest π pulse of 9 ns. Chirp parameters: t_p = 998 ns, Δf = 858 MHz and Q_{ref} = 4.17. (b) Experimental conditions from [74] with shortest π pulse of 7.7 ns. Chirp parameters: t_p = 580 ns, Δf = 850 MHz and Q_{ref} = 4.16. (c) Experimental conditions from an earlier stage of the spectrometer employed in this work with shortest π pulse of 5 ns. Chirp parameters: t_p = 128 ns, Δf = 500 MHz and Q_{ref} = 5.24. (d) Experimental conditions for experiments on copper in this work with shortest π pulse of 5.5 ns. Chirp parameters: t_p = 200 ns, Δf = 700 MHz and Q_{ref} = 0.54 in order to generate the FP90 pulse for the chirp echo. Note that the sharp dip in $\nu_1(f)$ around 9.62 GHz is due to crossing from the 2nd to the 3rd Nyquist window, where the subsampled echo has zero frequency. Phase cycling or proper adjustment of the relative excitation phase may be used to suppress this specific artifact. Because chirp echoes were always *tuned* such as to avoid any Nyquist window crossings, this artefact is irrelevant for the present work.

features of $\nu_1(f)$. With the optimized excitation arm, such problems were not observed, as seen in inset (d) or in the main text. The variable-rate chirp in inset (d) actually is the FP90 pulse from the UWB chirp echo of copper in the main text. The experimental performance of this pulse is illustrated in Fig. B.4c.

In the following, experimental data from the home-built spectrometer that had standing waves and limited compensation performance are presented. The results obtained with Δf = 500 MHz chirps are summarized in Fig. B.3: Panel (a) shows the residual longitudinal magnetization upon constant-rate AP pulses. The gray curve corresponds to a 128 ns pulse and is therefore comparable to the gray curve in Fig. 4.2b from the main text. Despite comparable peak power of the pulse, the 128 ns pulse does not achieve a flat inversion. The black curve is a pulse of twice the length, which results in improved inversion efficiency. Panel (b) shows residual longitudinal magnetization upon $\pi/2$ pulses realized with a variable-rate chirp (black), a constant-rate chirp (gray) and a 2.5 ns long hard pulse (dashed gray). Notably, the residual features upon the variable-rate chirp are quite comparable to the FT of the pulse seen by the spins (black in Fig. B.2c). As in the main text, the excitation bandwidth of the uncompensated pulses is reduced due to the resonator.

Fig. B.3c shows the nuclear modulation averaged chirp echo spectrum of nitroxide (solid black) together with the conventional field-swept echo-detected spectrum (light gray). The ratio between the two spectra (dashed black) shows significant attenuation below $\nu_1(f)$ (green). In fact, one of the two oscillatory fringe patterns in $\nu_1(f)$ appears enhanced in the ratio between the spectra,

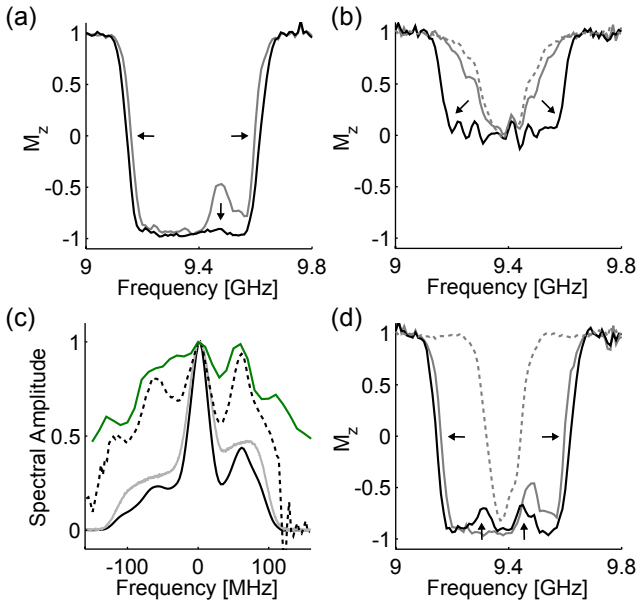

Figure B.3 – Limitations of pulse compensation with 128 ns long 500 MHz chirps under non-favorable experimental conditions for $\nu_1(f)$ (see Fig. B.2c). (a) Longitudinal magnetization upon constant-rate AP pulse with t_p = 128 ns (gray) and t_p = 256 ns (black). (b) Longitudinal magnetization upon $\pi/2$ pulse realized with variable-rate chirp (black), constant-rate chirp (solid gray) and hard pulse (dashed gray, 2.5 ns). The variable-rate chirp compensates for $\nu_1(f)$ at full-scale amplitude (green in Fig. B.2c). The prominent features that are not compensated almost directly translate into M_z, because there is a linear dependence between M_z and small perturbations in ν_1 of a FP90 chirp (see Fig. 4.1 in main text). (c) Chirp echo in frequency domain averaged over one nuclear modulation period (solid black) and conventional field-swept echo-detected spectrum converted to a frequency axis (light gray). The ratio between the two spectra (dashed black) shows the perturbation of the chirp echo spectrum, which appears influenced by the resonator that is indicated by $\nu_1(f)$ obtained at full-scale (green). (d) Longitudinal magnetization upon adiabatic pulse realized with variable-rate chirp (black), constant-rate chirp (solid gray) and hard pulse (dashed gray, 5 ns). The variable-rate chirp compensates for $\nu_1(f)$ at full-scale amplitude (green in Fig. B.2c). While the variable-rate chirp shows the expected broadening of the inversion profile (left and right arrows), the inversion band drops in the vicinity of the features that are not compensated by the pulse (see the black curve in Fig. B.2c and down arrows)

which suggests that a single standing wave each arises both in the detection and excitation arm. The only place where this could happen is in-between the resonator and the circulator.
Fig. B.3d shows residual longitudinal magnetization upon π pulses realized with a variable-rate chirp (black), a constant-rate chirp (gray) and a 5 ns long hard pulse (dashed gray). Interestingly, the variable-rate AP pulse does not strictly outperform the constant-rate AP pulse. In fact, the inversion efficiency is reduced in those areas where the pulse compensation is not successful.

B.3 CHIRP ECHO SETUP

This section details the procedure to set up the pulse amplitudes for a chirp echo with variable-rate pulses. At the onset of an experiment, one needs to choose a suitable sweep width Δf and the frequency positioning of the chirp with respect to the resonator and spectrum. For sensitivity reasons, it is usually a good idea to center everything at the resonator, whose transfer function can be determined rather fast by recording $\nu_1(f)$ at full-scale amplitude. The remaining three parameters, i.e. the pulse length and the amplitude of each of the pulses, are found as follows:
First, the pulse lengths needs to be set. For the chirp echo, the pulse length is

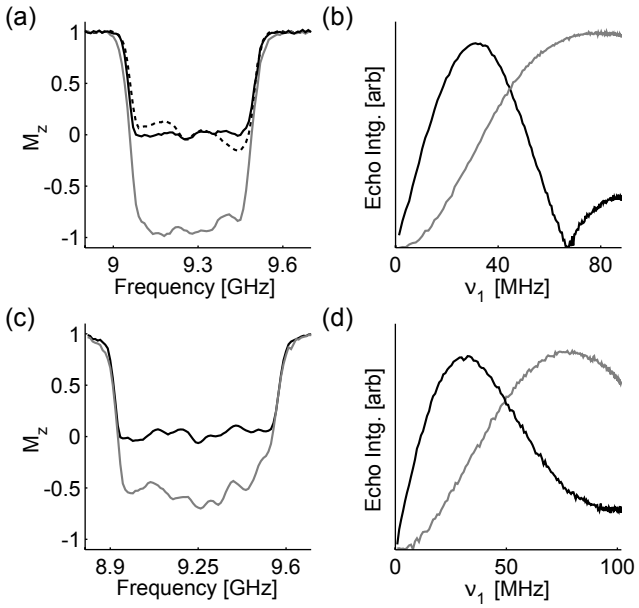

Figure B.4 – Residual longitudinal magnetization and pulse amplitudes used for the chirp echoes. (a) Longitudinal magnetization upon FP90 (solid black) and FP180 (gray) pulses, which both compensate for $\nu_1(f)$ that was acquired with a digital pulse amplitude close to the one of the FP90 pulse. The initial choice of the pulse amplitude for $\nu_1(f)$ was based on the pulse amplitude required for a FP90 pulse that compensates for $\nu_1(f)$ measured at full-scale amplitude. Such a FP90 pulse will show a larger perturbation of the intended flip angle, as seen by the dashed black curve. (b) Calibration of the pulse amplitude for the nitroxide chirp echo with the 128 ns FP90 pulse (black, ν_1^{opt} = 31 MHz) and the 64 ns FP180 pulse (gray, ν_1^{opt} = 80 MHz). The resulting amplitude ratio was 2.6. (c) Longitudinal magnetization upon FP90 (solid black) and FP180 (gray) UWB pulses, which both compensate for $\nu_1(f)$ that was acquired with a digital pulse amplitude close to the one of the FP90 pulse. (d) Calibration of the pulse amplitude for the UWB chirp echo with the 200 ns FP90 pulse (black, ν_1^{opt} = 32.5 MHz) and the 100 ns FP180 pulse (gray, ν_1^{opt} = 77.5 MHz). The resulting amplitude ratio was 2.4.

limited by the FP180 pulse, which requires an adiabaticity factor of roughly 2.5 during a short time. A good initial choice can therefore be obtained with a variable-rate pulse that achieves a higher adiabaticity factor at full-scale amplitude. Note that the pulse adiabaticity is calculated in the computation of the variable-rate chirp.

Second, the amplitude of the FP90 pulse needs to be calibrated. This is achieved by recording the echo amplitude for a parametrically swept pulse amplitude a_S. The FP180 pulse is left at full-scale during this step. Typical results are shown by the black curves in Fig. B.4b and d. Note that in the abscissa, the field strength ν_1 is shown, which is obtained from the digital amplitude a_S by the polynomial $\nu_1(a_S)$. Unless one wants to know the adiabaticity of the FP90 pulse at the reduced digital amplitude, there is no need to relate the digital amplitude to ν_1.

Third, the amplitude of the FP180 pulse is set up, which is performed in the same manner as for the FP90 pulse. Typical results are shown by the gray curves in Fig. B.4b and d. If no maximum can be found, the pulses are probably too short and one needs to start over with longer pulses.

Upon these three steps, the variable-rate chirps compensate for $\nu_1(f)$ at full-scale. Since the pulses have a reduced digital amplitude, the actual transfer function $\nu_1(f)$ experienced by the pulse may be different. To account for this difference, we record $\nu_1(f)$ at the digital pulse amplitude of the FP90 pulse and re-optimize the pulse amplitudes. During re-optimization, the pulse amplitudes do not change much, but the experimental excitation profile of the pulse may change. An example is given in Fig. B.4a. The dashed black curve is an FP90 pulse that compensates for $\nu_1(f)$ at full-scale, whereas the

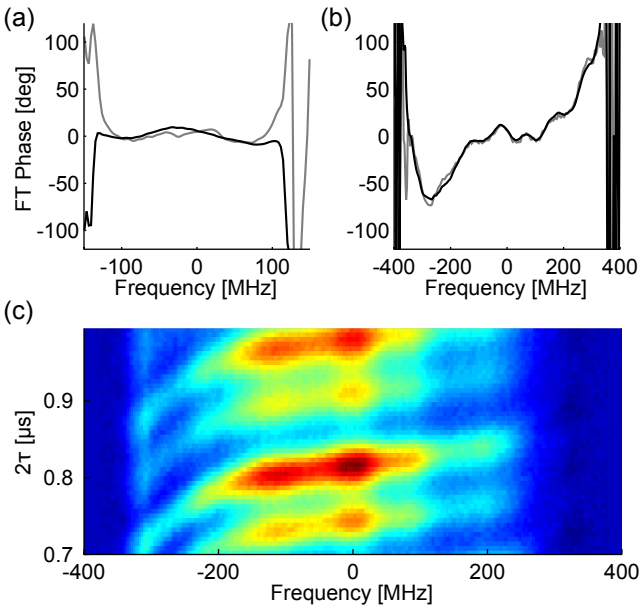

Figure B.5 – Spectral phases upon nuclear modulation averaging. (a) Modulation averaged phase (black) and phase at a specific pulse delay (gray) of nitroxide. Throughout a nuclear modulation period, the spectral phase showed variations above 10°. (b) Modulation averaged phase (black) and phase at a specific pulse delay (gray) of copper. Throughout a nuclear modulation period, phase variations were on the order of a few degrees. (c) Echo spectra of copper measured for different evolution times 2τ, where τ is the evolution time between the two pulses for those spins that are excited at the lower frequency edge of the pulse. In other words: τ is the delay between leading pulse flanks of the FP90 and FP180 pulse.

solid black curve is an FP90 pulse that compensates for $\nu_1(f)$ obtained at the actual digital amplitude of the pulse. As readily seen, the latter achieves a more uniform excitation.
We expect that one does not require the transfer function $\nu_1(f)$ exactly at the digital amplitude of the pulse. One could thus directly start an experiment with recording $\nu_1(f)$ at a reduced digital amplitude that is chosen based on experience.

B.4 INSTANTANEOUS DIFFUSION AT HIGH CONCENTRATIONS

As mentioned in the main text, we also measured the echo decay for a 100 μM nitroxide sample. The normalized echo integrals of these experiments are shown in Fig B.6a. The decay characteristic obtained with chirp pulses (black) is comparable to the one obtained with hard rectangular pulses (gray). For the 1 mM sample shown in Fig. B.6b on the contrary, a significantly faster decay is observed with chirp pulses. Note the alignment between the nuclear modulations of the chirp echo and the Hahn echo, which is due to the time shift $\Delta\tau$ in the pulse sequence timing explained in Section 4.2.5.

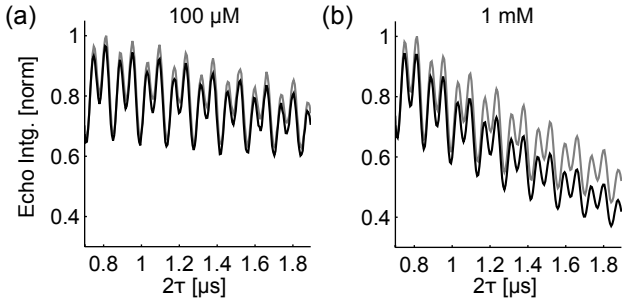

Figure B.6 – Nitroxide echo decay and modulation at spin concentrations of 100 μM (a) and 1 mM (b) using either a conventional Hahn echo (gray) or a chirp echo (black). τ is the evolution time of the central nitroxide line between the two pulses.

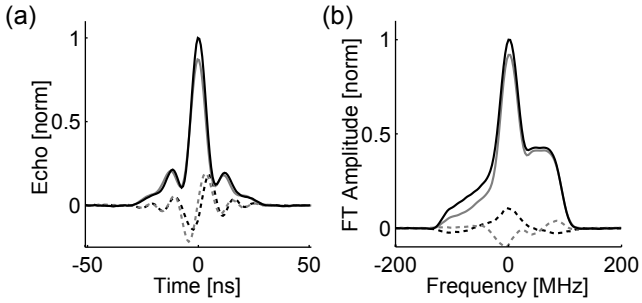

Figure B.7 – Chirp echo of nitroxide using constant-rate chirps. (a,b) Real part (solid lines) and imaginary part (dashed lines) of chirp echo with variable-rate chirps (black, as in main text) and constant-rate chirps (gray) in time domain (a) and frequency domain (b). The pulse amplitudes of constant-rate FP pulses were optimized in the same way as the variable-rate FP pulses.

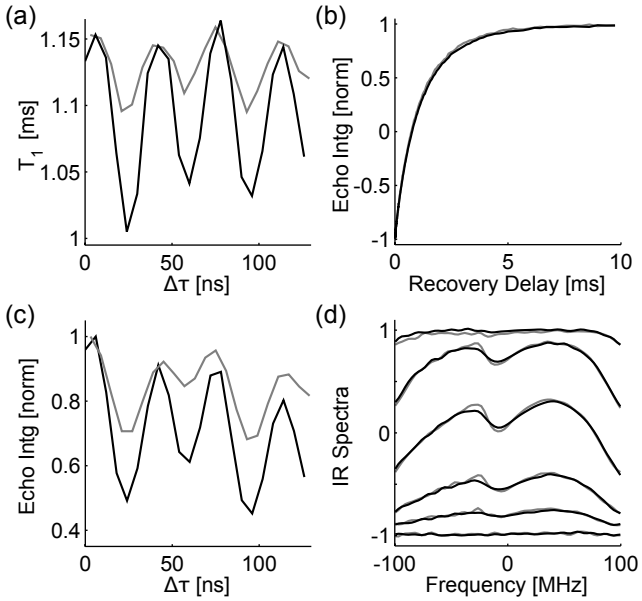

Figure B.8 – Nuclear modulation and T_1 times. (a) T_1 times at a frequency offset of -26 MHz observed with chirp (black) or Hahn echoes (gray) for different inter-pulse delay offsets $\Delta\tau$. The chirp data corresponds to a vertical cut through Fig. 4.7 in the main text. The Hahn echo data was acquired separately. (b) Magnetization decay for Hahn echo data from inset a) with longest (black) and shortest (gray) relaxation time. The T_1 times differ by 4%, which is barely observable in the primary data. (c) Nuclear modulation at a frequency offset of -26 MHz observed with chirp (black) or Hahn echoes (gray) for different inter-pulse delay offsets $\Delta\tau$. (d) Normalized chirp echo spectra for recovery delays of [0.001, 0.1, 0.3, 1, 3, 10] ms using a $\Delta\tau$ time of 0 ns (black) and 24 ns (gray).

C

SUPPORTING INFORMATION TO CHAPTER 5

C.1 AWG EXTENSION

This section describes the connectivity of the AWG to the Bruker Elexsys spectrometer. The formation of monochromatic rectangular microwave pulses in the Elexsys spectrometer is done at X band. In Q-band operation, these pulses are frequency translated using a mixer and a synthesizer. In particular, the carrier frequency of the pulses formed at X band remains fixed at f_{bridge} = 9.6453 GHz, whereas the synthesizer frequency is adjusted to create the desired Q-band frequency. Consequently, the UWB channel was designed to provide shaped X-band pulses at frequencies around f_{bridge} and was connected to the Elexsys spectrometer via a coupler that is otherwise used to inject microwave pulses at a different carrier frequency, the so called *ELDOR* channel. A schematic of this UWB channel is shown in Fig. C.1.

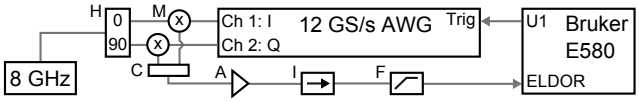

Figure C.1 – Schematic of incoherent UWB channel realized by AWG upconversion. H: 90° hybrid, M: Mixer (MITEQ, DM0412LW2), C: Combiner, A: Amplifier (MEURO, MBM0812G2423), I: Isolator, F: Filter (Minicircuits VHF-8400). See text for details.

For the UWB channel, pulse formation was initiated at the AWG upon trigger reception from the Elexsys spectrometer. The pulses synthesized by the AWG satisfied the relation 8 GHz + $f_{\text{AWG}} \in [f_{\text{bridge}} - \Delta f_{\text{bridge}}/2, f_{\text{bridge}} + \Delta f_{\text{bridge}}/2]$, where Δf_{bridge} = 2.5 GHz is the operational bandwidth of the bridge, and had a full scale amplitude of -10 dBm. The frequency translation to X band was by an IQ mixer assembled out of two mixers, a combiner and a 90° hybrid. The microwave carrier for the mixer was 8 GHz (NEXYN, NXPLOS) and an amplifier after the IQ mixer provided the amplitude necessary for insertion into the ELDOR channel. Since there was no fixed phase relation between the microwave pulses from this UWB channel and the microwave carrier of the Elexsys bridge, the UWB channel was incoherent. One can therefore assume that any coherence excited by a shaped pulse from the UWB channel was averaged out in repeated acquisitions.

The primary purpose of this IQ mixer for upconversion is to distinguish between the upper and the lower sideband around the mixer carrier at 8 GHz. In this way, it is possible to generate a microwave pulse in one sideband, with only a residual amount of power directed into the other sideband. This is a crucial capability if the frequencies of the UWB pulse occupy both sidebands. For the experiments presented in this work, this capability turned out to be redundant, because a bandwidth of 2.5 GHz around f_{bridge} for UWB pulses was sufficient. A high pass filter with a cutoff frequency at 8.4 GHz was thus added after the amplifier.

The complications related to pulse distortions mentioned at the end of Section 5.3.2 in the main text are discussed in the next section.

C.2 PULSE DISTORTIONS

As mentioned in the main text, *pulse distortions* were one of the limitations for population transfer. This section explains these issues to the hardware-oriented reader. With pulse distortions, we refer to the following situation: Suppose we want to apply a microwave pulse at frequency f_{mw}. Before reaching the spins, this pulse needs to pass the high-power traveling-wave-tube (TWT) amplifier, which is often operated close to saturation. Due to this saturation, the amplified microwave pulse can no longer be described by a perfect cosine function. Typically, there is clipping of the waveform above some amplitude level. In the frequency domain, this leads to higher (odd) harmonics of the input frequency, which is often referred to as harmonic distortion [212]. Consequently, we do not just inject one pulse at a frequency of f_{mw} down to the probehead, but concurrently also some other *spurious pulses* at higher (odd) harmonics. Indeed, these higher harmonics do neither couple well to the spins (resonator bandwidth) nor do they affect the spins in any significant sense (large resonance offset).
The situation is more subtle if a pulse carrying two frequencies $f_{\mathrm{mw},1}$ and $f_{\mathrm{mw},2}$ passes the power amplifier. In this case, the amplified pulse contains a number of (odd) mixing products of $f_{\mathrm{mw},1}$ and $f_{\mathrm{mw},2}$. Prominent output frequencies are the third-order products $2 \cdot f_{\mathrm{mw},1} - f_{\mathrm{mw},2}$ and $2 \cdot f_{\mathrm{mw},2} - f_{\mathrm{mw},1}$. This process is often referred to as intermodulation distortion [212]. As shown in the following example, these combination frequencies can couple well to the spins and lead to resonant excitation.
As explained in the previous section, the observation frequency at Q band translates to a frequency of $f_{\mathrm{bridge}} = 9.6453$ GHz at X band. Since in our experiments the observation frequency was tuned to the maximum of the Gd(III) spectrum as well as the maximum coupling by the resonator, this X-band frequency of $f_{\mathrm{bridge}} = 9.6453$ GHz couples extraordinarily well to the spins. Frequencies below or above f_{bridge} are coupled worse due to the bandwidth of the resonator. If intermodulation (at Q band) was to cause a spurious tone at the (X-band equivalent) frequency f_{bridge}, the effect may turn out rather significant. Assuming that shaped pulses at X band originate from an AWG frequency translated by $f_{\mathrm{LO}} = 8$ GHz using one single mixer, the frequency output by the AWG leads to a pair of frequencies at X band centered around 8 GHz, i.e. $f_{\mathrm{LO}} \pm f_{\mathrm{AWG}}$. Accordingly, a relevant case is when the AWG outputs a frequency of $f_{\mathrm{AWG}} = 0.55$ GHz, hence $f_{\mathrm{mw},1} = 8.55$ GHz, $f_{\mathrm{mw},2} = 7.45$ GHz and $2 \cdot f_{\mathrm{mw},1} - f_{\mathrm{mw},2} \approx f_{\mathrm{bridge}}$. Frequency translation to Q band then results in unwanted excitation at the observation frequency. Note that physically, the frequencies $f_{\mathrm{mw},1}$ and $f_{\mathrm{mw},2}$ are first translated to Q band and only after passing the saturated Q-band amplifier, the spurious frequency appears.
To demonstrate the above case, Fig. C.2a shows the polarization enhancement as a function of the start frequency of the population transfer chirp. The orange curves show up-chirps, with (solid) or without (light) compensation of the resonator bandwidth, whereas the blue curves show down-chirps. In fact, this is exactly the same type of experiment as shown in Fig. 5.5c, however, obtained with an earlier implementation of the AWG upconverter, which did not use any high-pass filtering or IQ-mixing [74]. Focusing on the orange curves, a rather severe kink is observed at a frequency offset around -1.09 GHz (I). It is at exactly this frequency, where the start frequency of the chirp was at $f_{\mathrm{AWG}} = 0.55$ GHz, thus causing excitation of the observed spins. Below this frequency offset, the spurious chirp pulse due to intermodulation thus passed the observed spins and led to a reduction in polarization by tipping the magnetization. Below this point, another rather pronounced step is observed for an offset around -1.31 GHz (II). Here the start frequency of the chirp was at $f_{\mathrm{AWG}} = 0.33$ GHz, which resulted in a fifth-order product at f_{bridge} ($3 \cdot 8.33$ GHz$-2 \cdot 7.67$ GHz). In summary for the up-chirps, intermodulation distortion leads to spurios chirp pulses at

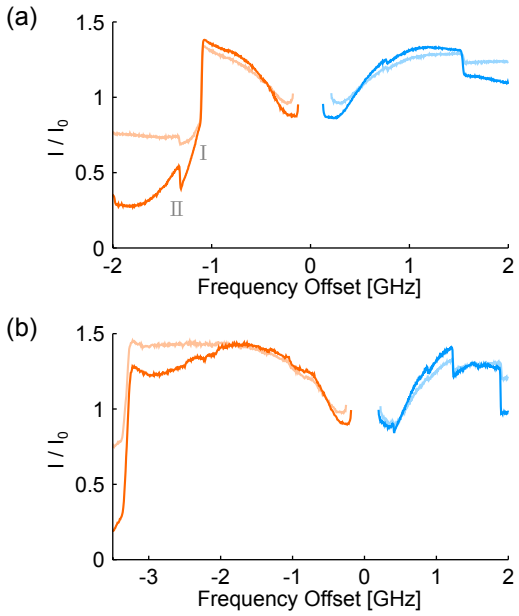

Figure C.2 – Unwanted excitation of central line due to spurious frequencies. Both panels show the polarization enhancement as a function of f_1, the start frequency of the chirp, at fixed end frequencies f_2 for up-chirps (orange) and down-chirps (blue) with $t_p = 2\ \mu$s (compare Fig. 5.4c in main text). The curves with light colors were obtained with constant-rate chirps. (a) Setup with a single mixer for upconversion, without a high-pass filter after the mixer. (b) Setup with IQ mixer for upconversion, without a high-pass filter after the mixer.

higher frequencies, which eventually tilt the spins to be polarized. The steps observed for the down-chirps have a related, but different origin, and will be addressed further below.

In order to avoid such spurious chirp pulses, microwave pulses injected into the TWT need to have one single instantaneous frequency. For the example above, this can be achieved by canceling the image frequency $f_{LO} - f_{AWG}$ by using an IQ mixer or a filter. Here, we give an example with the IQ mixer described in the previous section, but without any filtering. The corresponding polarization enhancements as a function of the start frequency of the chirps are shown in Fig. C.2b. For the up-chirp, one readily sees that the steps around -1.09 GHz and -1.31 GHz were no longer observed. A pronounced step can be seen at -3.3 GHz, which corresponds to $f_{AWG} = -1.6453$ GHz. This step is thus due to imperfections of the IQ mixer, which result in improper cancellation. The IQ mixer was actually calibrated for best cancellation at $f_{AWG} = 0.55$ GHz and it is not surprising, that imbalance in the IQ mixer would require a different calibration at a 2 GHz frequency offset. The calibration procedure at $f_{AWG} = 0.55$ GHz is outlined in Fig. C.3 and was performed by minimizing the impact of the intermodulation tone onto the observed spins (see caption for description).

For the steps in polarization enhancement observed with down-chirps, a related effect took place. With frequencies above the observed spins, the intermodulation process described for the up-chirps does not apply here. However, the upconversion mixer itself may create spurious chirp pulses by higher-order mixing products: While a single mixer primarily outputs first order products at $f_{LO} \pm f_{AWG}$, mixing products of higher order may also occur. Using a spectrum analyzer and test tones from the AWG at strategical frequencies, the steps observed for the down-chirps in Fig. C.2b have been assigned to such mixing products. The solution to minimize such products is rather straightforward: Reduction of the drive level of the AWG at the mixer, which resulted in the -10 dBm full scale amplitude used in the main text. A lower drive level results in lower power microwave pulses, which requires a different power leveling after the mixer. Furthermore, the relative strength of carrier leakage at f_{LO} increases towards smaller drive levels.

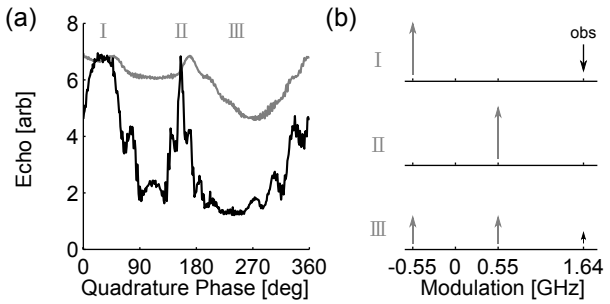

Figure C.3 – Cancellation of intermodulation distortion by properly phasing the IQ mixer obtained with (gray) and without (black) high-pass filter. (a) Hahn echo signal as a function of the relative phase at the quadrature output of the AWG. The pulse from the AWG had a length of 100 ns and a constant frequency of $(f_{\text{bridge}} - 8)/3$. The echo signal shows two maxima, I and II. At I, one single frequency in the lower sideband was generated. At II, one single frequency in the upper sideband was generated. For these two cases, the power amplifier sees one single tone at its input. The label III represents an intermediate situation, where the IQ pairs were not in phase quadrature. The power amplifier therefore sees two tones at its input and directs some power into the observation frequency - a process called intermodulation distortion. The corresponding frequency constellations are shown in panel (b). The frequency axis denotes the output frequency of the IQ pair output by the AWG. In this view, the observation frequency f_{bridge} is at 1.6453 GHz.

Since present experiments did not require the bandwidth provided by the IQ mixer, a high-pass filter was installed, as described in the previous section. As a side effect, this filter also reduced the carrier leakage. The filter in principle renders the IQ mixer redundant in terms of excitation bandwidth. However, we could still observe an effect of the phase on the IQ mixer at $f_{\text{AWG}} = 0.55$ GHz (see gray in Fig. C.3a). The rejection of the image at 7.45 GHz by the high-pass filter was therefore not sufficient with respect to third order intermodulation. For upconversion setups using a single mixer combined with a filter instead of the IQ mixer, this needs to be taken in consideration. The upconversion arm described in [113] is such a single mixer setup with a filter. There, however, the operational bandwidth was from 8.75 GHz to 9.5 GHz, thus not including the critical 8.55 GHz frequency (see also Appendix B).
At the current stage, the spurious intermodulation chirps are reduced to a negligible level. However, if sample heating would not inhibit the use of longer pulses with larger bandwidths, such problems might again become important. A general aspect of these spurious chirps is that their impact is only significant at the center of the resonator. Off the center, the adiabaticity of these spurious chirps is reduced by a fair amount. Furthermore, a spurious chirp at the center of the resonator implies that the intended chirp pulse couples weakly to the spins, as it is off the center (for single mode resonators). Since we use pulses which compensate for the coupling to the spins, the chirp pulse slows down its sweep rate towards the weaker coupling off the center [74]. As a consequence, the spurious chirp has a slowed down sweep rate when passing the center of the resonator, which compensates for its low power and results in an enhanced adiabaticity. This is actually the reason, why all of the steps in Fig. C.2 are larger for the compensated pulses than for the non-compensated pulses.
We may add that for the excitation power of the spectrometer at bandwidths around 300 MHz, representative values for π pulses on $S = 1/2$ spins are on the order of 12 to 14 ns, which corresponds to π pulses on the central line of Gd(III) in the range of 3 to 3.5 ns. The longer pulse lengths on the CT on the order of 4.5 ns related to the experiments in the main text were due to a temporary replacement power amplifier. In fact, this temporary replacement showed an unexpected spurious response that reduced the efficiency for down-chirps. To circumvent this specific response, the drive level on the

amplifier was reduced by reducing the AWG drive level from −4 dBm to −10 dBm, thus prolonging the pulse length (see the corresponding reduction factor of 75% at the end of Section 5.3.2 in the main text). It was presumed that the larger input bandwidth of the replacement amplifier caused these extra spurious frequencies to appear, but a Q-band filter to test this assumption was not available.

As a reference, the spurious response with a drive level of −4 dBm is shown in Fig. C.4. These data were taken with the UWB channel shown in Fig. C.1, however, with the proper power amplifier allowing for operation at a −4 dBm drive level from the AWG. In order to ease the identification of spurious tones, an ELDOR hole-burning type experiment was performed. The effect of a monochromatic high-turning angle (HTA) pulse with frequency varied over a range of 4 GHz was probed by Hahn echo observation at the center of the resonator/Gd(III) spectrum. Curve (a) was obtained with a 100 ns long HTA pulse. Before the pulse overlapped at the center, the echo intensity was enhanced by a few percent due to population transfer from its immediate neighbor transitions. In addition, there were two distinct peaks at offsets beyond 1.5 GHz, which correspond to spurious tones exciting the observed spins. The most pronounced one at an offset of 1.766 GHz was actually also observed as a small step when setting up the population transfer.

For curve (b), the pulse length was increased to 1 μs. Population transfer could no longer be observed, but additional spurious tones of smaller amplitude appeared. At a frequency offset of −0.822 GHz, the second harmonic of the AWG output excited the observed spins. Inspection of the X-band pulses from the UWB channel with a spectrum analyzer revealed that this second harmonic distortion led to a spurious signal at f_{bridge} with a level 44 dB below the full-scale level. When setting up the population transfer experiment, this second harmonic spurious did not lead to an observable step. A 1 μs monochromatic pulse concentrates way more power at a given frequency than an UWB chirp pulse with twice the pulse length.

Curve (c) was obtained with a miscalibrated quadrature phase. As was already observed for a 100 ns pulse (see gray in Fig. C.3), there was third-order intermodulation despite the high-pass filter for image rejection. In curve (d),

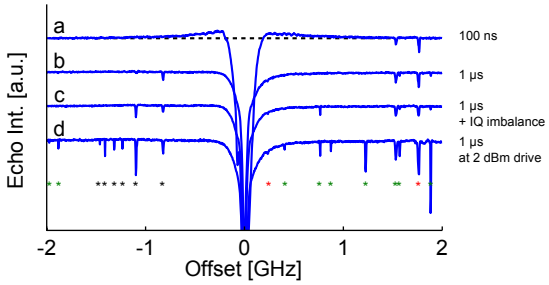

Figure C.4 – Spurious response probed by hole burning experiment using a monochromatic high-turning angle (HTA) pulse over an offset range of 4 GHz. All curves were normalized to an intensity of 1 and vertically displaced by 0.15. The 100 ns HTA pulses were sinusoidally smoothened during 10 ns, the 1 μs were smoothened during 250 ns. All HTA pulses were at maximum power. (a) 100 ns HTA pulse showing two higher order spurs as well as population transfer, exclusively from neighbor transitions. (b) 1 μs long HTA pulse showing a spur at an offset of $-1.6453/2$, thus a second harmonic of the frequency f_{AWG} ouput by the AWG. (c) 1 μs long HTA pulse with quadrature phase offset by 30°, which shows additional spurs. At an offset of $-1.6453 \cdot 2/3$ for instance, a third order intermodulation spur is detected. (d) 1 μs long HTA pulse at 2 dBm drive level, which uncovers a number of spurious frequencies. The ones marked with a black star do formally only depend on the AWG output frequency f_{AWG}. The ones with a green star are mixing products between f_{AWG} and the translation frequency f_{LO} = 8 GHz. The two spurs with a red star were not assigned, since these depended on other frequencies.

the entire spurious response was stimulated by doubling the drive amplitude at the AWG to 2 dBm. All the lines marked with a black star are formally harmonics of the AWG output frequency f_{AWG}. From the even harmonics, only the second and fourth harmonics could be detected, whereas for the odd harmonics, the highest one was the ninth harmonic. The lines marked with a green star are mixing products, which formally depend on f_{AWG} and the translation frequency f_{LO} = 8 GHz.
All the frequencies marked in green or black give rise to a tone at f_{bridge} = 9.6453 GHz, which was verified experimentally by inspection of the X-band pulses from the UWB channel with a spectrum analyzer. However, there are two frequencies marked with a red star. These cannot be assigned as mixing products of f_{AWG} and f_{LO}, and these were also not detected with a spectrum analyzer at X-band. In particular, the rather pronounced peak at 1.766 GHz does depend on the frequency translation from X to Q band inside the Bruker spectrometer: A change in the Q-band observation frequency moved the position of this peak. Such a behavior was not observed for the other tones labeled in green and black. Since this spurious frequency at 1.766 GHz emerged as a small step in setting up the down-chirp for population transfer, this frequency could become important for down-chirps of longer duration with optimized start frequencies beyond this 1.766 GHz frequency offset.

C.3 SAMPLE HEATING

Due to the long chirp pulses, sample heating effects were observed. The most direct approach to such effects is observation of the intensity of the Hahn echo upon pre-polarization pulses, as shown in Fig. C.5a. The orange and blue curves show the polarization enhancement as a function of time for the up-chirp and down-chirp optimized in Section 5.4.1 in the main text. The solid green curve was obtained by sequentially combining the two pulses, whereas the dashed green curve was obtained with two optimized pulses with half the pulse length (1 μs).
Before each of these measurements, the sample was in thermal equilibrium. Once the pre-polarization pulses were switched on at time $t = 0$, one would expect the pre-polarized signal to remain constant at all times. The actual data, however, showed decaying polarization. When comparing the up-chirp to the down-chirp, the decay upon the up-chirp was more pronounced. This pronounced decay shape also appeared for the sequentially combined pulses. Consequently, the up-chirp induced this unexpected behavior.
For an estimate of the sample heating, we measured the echo intensity at various temperatures (Fig. C.5b) and observed a decay of roughly 9% per K. The local heating due to the up-chirp was thus on the order of 1 K. With the shorter 1 μs pulses combined together, heating effects were less pronounced. Nevertheless, the net enhancement with the shorter pulses remained smaller than for the combined 2 μs pulses. Notably, we could observe back-action from this local heating to the temperature reading of the regulation system (Oxford CF935). This effect has been suppressed by using sufficient under-pressure above 200 mbar to the cryostat.
This sample heating is one reason for not increasing the pulse length in order to obtain larger signal enhancements. At least with our experimental setup, the pulse length was restricted by technical limitations and not by relaxation characteristics of the sample. Since only the up-chirp at negative frequency offsets led to significant heating, a heating mechanism specific to the utilized resonator is presumed. In fact, the resonator employs oversized sample tubes for a larger filling factor [213, 150], which may in turn increase possible heating by the electric field.
Because the unstable baseline due to the heating is undesirable in almost all measurements, approaches towards a more stable baseline have been tested. Sufficient stabilization for distance measurements reported in Section 5.4.3 in the main text was achieved by means of (i) *pre-heating* the sample with pulses prior to acquisition and (ii) adaptation of the time for each scan (increase in shots per point). Further information is found in Fig. C.6 below. In all

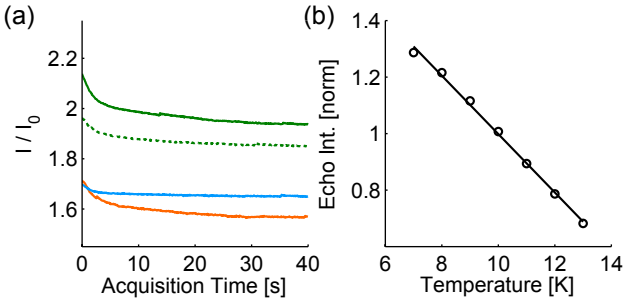

Figure C.5 – Sample heating due to pre-polarization chirps. (a) Time dependence of the intensity of the pre-polarized central line for 2 μs long up-chirp (orange), down-chirp (blue) and sequential combination of both (solid green). All chirps with optimized positioning as depicted in Fig 5.4c in the main text. The dashed green line was obtained with two sequentially combined 1 μs chirps ($f_1 = -1.14$ GHz to $f_2 = -0.124$ GHz and $f_1 = 1.062$ GHz to $f_2 = 0.142$ GHz). (b) Experimental equilibrium polarization versus temperature (black circles) and linear fit with a descent of 9% per K. Note that the repetition time was kept constant, such that the values at lower temperatures were reduced by saturation.

other experiments in the main text, such as the pulse calibration experiments described in Section 5.4.1 or the field-sweeps in Section 5.4.2, no particular stabilization of the baseline was implemented.
Considering the polarization enhancements at $t = 0$, each of the 2 μs long pulses led to roughly 70% stronger signals. The simulation in Section 5.2.2 in the main text actually showed an enhancement of 78%. Despite a number of approximations involved in this particular powder simulation (see Section 5.3.4 and Fig. C.13a), the described procedure seems to be an appropriate starting point for further refinements. For the sequential combination of these two pulses at $t = 0$, one may expect twice the experimental enhancement of 70%. However, the experimental enhancement was 114%. Understanding the origin of this reduced experimental enhancement with combined pulses requires further investigation. A partial contribution to this reduction was an apparently longer equilibration time with the combined pulses (see Fig. C.7 below). At present, the most important aspect is the significant increase of experimental enhancements with the combined pulses.

C.3.1 *Heating transients*

In this section, the heating transients due to the up-chirp are shown in more detail. The black curve in Fig. C.6a corresponds to the green curve in Fig. C.5, but acquired for a longer time. As can be seen, it took almost 1 minute to fully equilibrate to the new conditions brought by the chirp pulse. The way around this long equilibration time was by pre-heating the sample, which we performed for 34 seconds, as indicated by the arrow. The resulting transient (gray) was much shorter. The pre-heating was readily implemented as a loop with a predefined number of repetitions of the pulse sequence, but without any actual acquisition command. Upon the termination of this loop, the main acquisition loop started, which led to a reprogramming time-out on the order of 1 second. It is presumed that it is thermalization during this delay, which caused the remaining transient observed with pre-heating. We would expect this transient to become even shorter and less pronounced for faster reprogramming times. We observed this kind of delays also after each completed average in the main acquisition loop, however, not during the loop, since phase cycling can be performed without any reprogramming delays.
With the shorter transient upon pre-heating, the number of shots per point was adjusted to concentrate this transient only in the first few points of a 1D experiment. Indeed, the four-pulse DEER sequence is an especially generous case, since the first few points are anyhow not used in the data analysis. Fig. C.6b thus shows the baseline of the pre-polarized DEER experiment in the absence of the pump pulse using 200 (blue), 400 (magenta) or 600 (black) shots per point. For the black curve, the transient has decayed sufficiently before the DEER signal started at t = 0. The baseline fluctuations starting from t = 0 were on the order of 0.5%. The inset on the right hand side furthermore shows the three curves as a function of acquisition time. In the overlay, all curves reveal a residual slow decay after the initial steep descent. It is presumed that this decay resulted from too short pre-heating time. In the actual pre-polarized DEER experiment, however, the second average of the scan is effectively pre-heated for a longer time period due to the previous scan. Accordingly, one would expect this slower transient to vanish in averaged data. Nevertheless, pre-heating of the very first scan turned out to be always advantageous, since the transient of the first scan was otherwise too extended. At reduced concentrations and extended dipolar evolution times, heating transients may become comparable to the noise level, so that pre-heating can be largely neglected when using a sufficient number of shots per point.

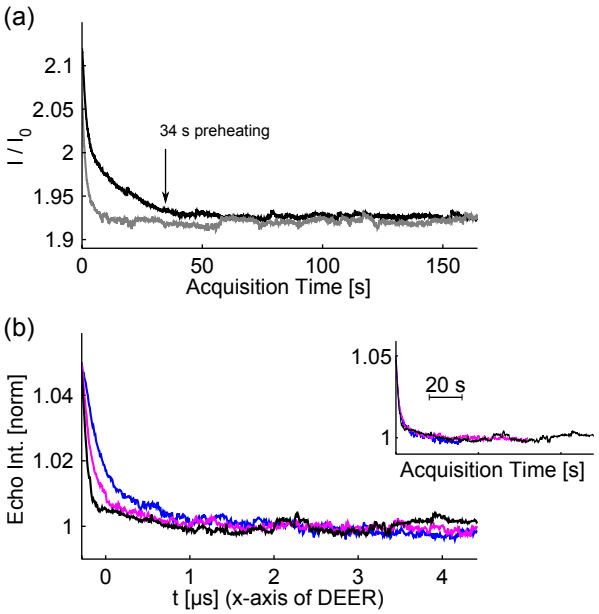

Figure C.6 – Pre-heating to reduce transients at the beginning of experiments. (a) Time dependence of the pre-polarized central line intensity (double-sided pre-polarization) for extended acquisition time, as compared to the Fig C.5. The black curve was obtained without pre-heating. The gray curve was obtained with pre-heating for 34 seconds, as indicated by the black arrow. The transient with the long time-constant could be reduced with the pre-heating. A faster transient at the beginning remained. This originated from thermalization during the reprogramming-timeout in between scans, which is on the order of 1 s. (b) Shortening of the remaining fast transient with pre-heating by changing the shots per point: 200 shots (blue), 400 shots (magenta), 600 shots (black). The x-axis is indicated as the time axis that would result for a DEER experiment. The inset shows the same data as a function of acquisition time. Some residual slow transient can be identified, because the three curves show a similar trend.

C.4 RELAXATION EFFECTS

C.4.1 *Saturation effects for double-sided transfer*

As discussed above at the end of Section C.3, the combined enhancement with two chirp pulses was not the sum of the enhancements achieved with one single chirp. The two single pulses led to an enhancement of 70%, whereas the combined enhancement was 114%. It was found that the combined enhancement had a different dependence on the repetition time of the experiment.
Fig. C.7a shows intensities of the pre-polarized central line for various repetition times. Pre-polarization was either by up-chirps (orange), down-chirps (blue), or the sequential combination (green open circles). Influences of heating were minimized by measuring these intensities shortly after starting the experiment. Ten shots at the beginning were skipped to avoid apparent contributions from saturation at fast repetition times. The expected intensities obtained by summing the enhancements from the up-chirp and the down-chirp are indicated by the green triangles. As is seen in this representation, the shot repetition time had a weaker influence on the data obtained with a single chirp pulse than on the data obtained with the combined pulses.
Fig. C.7b shows the loss factor, which is the experimental intensity with the combined chirps (green circles in panel a) divided by the expected intensity (green triangles in panel a). This factor increases for longer repetition times to a maximum of roughly 93%. The different behavior of the double-sided enhancement suggests different equilibration dynamics. For further investigation, simulations of the multi-level dynamics are required.

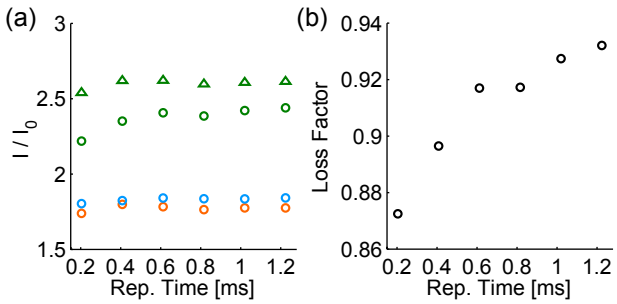

Figure C.7 – Dependence of the intensity of the pre-polarized central line on the repetition time of the experiment. The up-chirp had optimized frequencies $f_1 = -1.46$ GHz and $f_2 = -0.18$ GHz. The down-chirp had $f_1 = 1.5$ GHz and $f_2 = 0.154$ GHz. (a) Experimental intensity upon up-chirp (orange), down-chirp (blue), and sequential combination (green open circles). The intensities were extracted just after turning on the pre-polarization pulses to minimize heating contributions. For each data point, the equilibrium intensity I_0 for normalization was obtained using the corresponding repetition time. The green triangles represent the intensity one would expect from summing the experimental up-chirp and down-chirp enhancements. (b) Loss factor obtained by dividing the experimental combined intensity (green circles in a) by the expected intensities (green triangles in a).

C.4.2 *Loss of enhancement with prolonged evolution times*

In this section, echo-detected field-sweep spectra of Gd-ruler $\mathbf{1_3}$ were recorded with inter-pulse delay between observation pulses prolonged to 7 μs. This inter-pulse delay mimics the long evolution times of coherence on Gd(III) transitions that is typical for DEER experiments. The equilibrium spectrum obtained in this way is illustrated by the solid black curve in Fig. C.8a. As compared to the spectrum recorded under ordinary conditions (dashed black), the shoulders of the spectrum were largely attenuated by transverse

relaxation. With pre-polarization from both sides, the spectrum indicated by the green curve was obtained. The range, over which the pre-polarized signal is stronger than the peak equilibrium signal, was here reduced from 16 mT to 9 mT. The normalized intensities I/I_0 for this case are shown in Fig. C.8b. The solid curves show the data for up-chirp (orange), down-chirp (blue) and the combination (green), whereas the dashed green curve shows the data for the combination under ordinary conditions from Fig. 5.5b in the main text. Interestingly, the polarization enhancement with the prolonged pulse delay already dropped to 0 beyond ± 50 mT. The transitions beyond these points could thus no longer be observed with this scheme. In general, the solid green curve appears vertically offset from the dashed green curve, which indicates that some transitions did no longer contribute to the observed signal. Only at the central line, whose FWHM is indicated by the dashed black lines, the vertical offset is negligible, because the relative contribution of satellite transitions is rather small there. Outside the central line, this vertical offset was on the order of 15% of the dashed green curve.
The reduction to zero enhancement at ± 50 mT actually indicates that only inversion of the CT results in detectable polarization enhancement. Beyond ± 50 mT, the CT does no longer contribute and population is only transferred within satellite transitions (see main text). For the data obtained with 7 μs inter-pulse delay, it is thus reasonable to assume that out of all satellites, exclusively the $\pm 3/2 \leftrightarrow \pm 1/2$ transitions contributed to the observed signal.

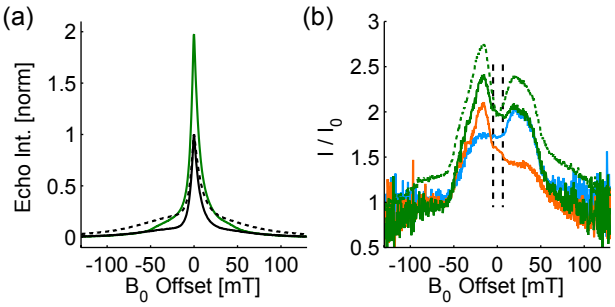

Figure C.8 – Pre-polarized field-swept spectra with inter-pulse delay prolonged to 7 μs. (a) Field-sweep obtained with sequentially combined chirps (green) and without pre-polarization (solid black). The dashed black curve represents the equilibrium reference from Fig 5.5a in the main text. (b) Field dependence of polarization obtained with up-chirp (orange), down-chirp (blue) and sequential combination of both (solid green). The dashed green curve represents the corresponding curve from Fig 5.5b in the main text. The dashed black vertical lines indicate the FWHM of the central line.

C.5 PRE-POLARIZED DISTANCE MEASUREMENTS

In the following, supplementary DEER data are presented. First of all, all the data from Fig. 5.7 in the main text are shown in Fig. C.9, where the data without pre-polarization are shown in red and the data with pre-polarization are shown in black. In addition, the reference experiment obtained with a 9 ns long monochromatic rectangular pump pulse at a frequency offset of -0.3 GHz is shown in blue, which is an experimental scheme according to [143]. This experiment resulted in a 25% larger echo signal, but only 4% modulation depth. This led to the enhancement factor of 1.8 by using an optimized chirp pump pulse instead of a monochromatic pump pulse. Combining this enhancement with the signal enhancement by pre-polarization, a net enhancement factor of 3.33 was obtained. The distance distributions obtained with the chirp pump pulse and with the monochromatic pump pulse showed reasonable agreement.
Besides this monochromatic pump pulse, pre-polarized DEER data from two

other experiments are presented. In Fig. C.10, essentially the same experiment on Gd-ruler $\mathbf{1_3}$ as the one in the main text is shown. These data confirm again that distance distributions overlay quite well, independent on whether pre-polarization was used or not. The only problem with these data is the lower polarization enhancement of 68%, which was due to erroneous programming of the chirp start frequencies after the optimization. The modulation depth was roughly 10%.
Another dataset is presented in Fig. C.11. Here, Gd-ruler $\mathbf{2_2}$ with a distance of roughly 3.0 nm between the two Gd(III) ions was used (see Section 5.3.1.1 and [142]). Pre-polarization resulted in an enhancement of 86% and the modulation depth was 7%. As can be recognized by comparing the heating transient in the on the top right with equivalent insets in Fig. C.10 and C.11, the transient was somewhat longer due to acquisition with only 200 shots per point. The resulting distance distributions showed reasonable agreement.

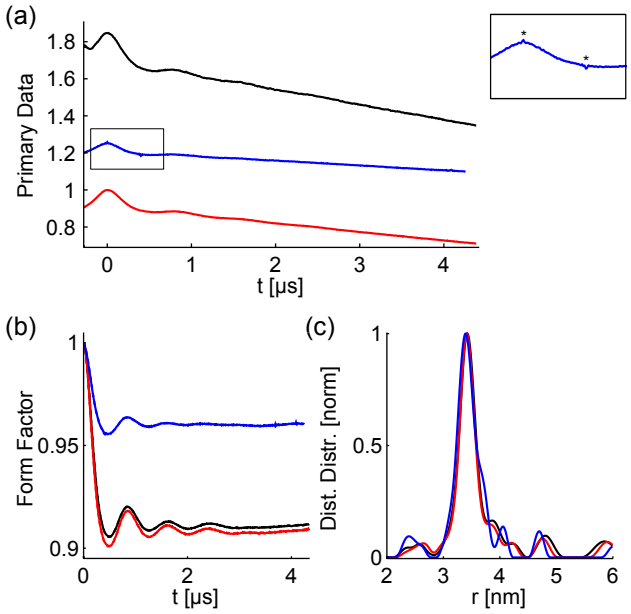

Figure C.9 – Pre-polarized DEER experiments on Gd-ruler $\mathbf{1_3}$ using a 192 ns long chirp pump pulse (compare Fig. 5.7 in main text) and reference experiment with a rectangular 9 ns pump pulse at −0.3 GHz. (a) Primary data obtained with pre-polarization to 1.85 (black), without pre-polarization (red) and with rectangular pulse (blue). Ordinate normalized to echo signal of red curve. The echo signal with the rectangular pump is 1.25. The inset shows a zoom on the rectangular pump data and reveals two artificial spikes marked with *. These originate from coherence excited by the pump and refocused by the observer pulses, thus an effect of spectral overlap between pump and observer. (b) Form factors with (black) and without (red) pre-polarization showing modulation depths on the order of 9% and form factor for rectangular pulse (blue) with modulation depth of 4%. The two spikes visible at the end of the blue curve are of the same origin as those highlighted in the inset above. (c) Regularized distance distributions with (black) and without (red) pre-polarization and rectangular pulse (blue).

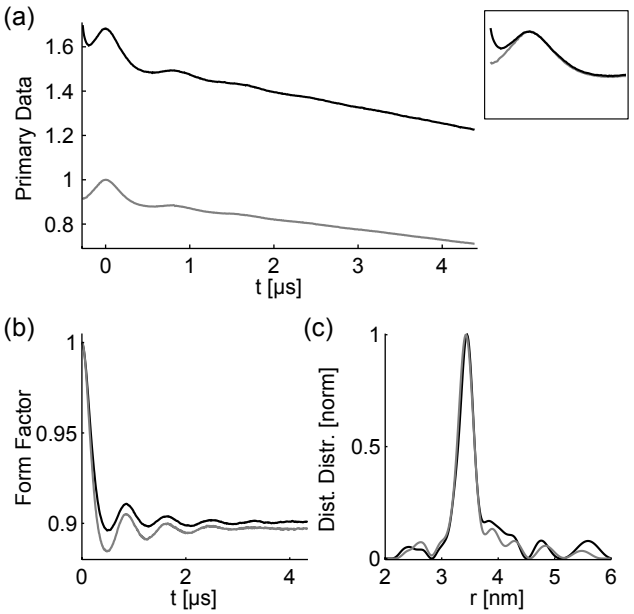

Figure C.10 – Pre-polarized DEER experiments on Gd-ruler $\mathbf{1_3}$ with a Gd-Gd distance of about 3.4 nm using a 192 ns long chirp pump pulse ($f_1 = -0.875$ GHz to $f_2 = -0.3$ GHz, adiabaticity on CT of 2.24). The 2 μs pre-polarization pulses had ranges $f_1 = -1.396$ GHz to $f_2 = -0.092$ GHz and $f_1 = 1.286$ GHz to $f_2 = 0.150$ GHz. (a) Primary data obtained with pre-polarization to 1.68 (black) and without pre-polarization (gray). The inset on the right-hand side shows the initial part of the two curves on top of each other. The pre-polarization was only 1.68 due to erroneous programming of chirp start frequencies f_1. The correct optima would be $f_1 = -1.228$ GHz and $f_1 = 1.07$ GHz. (b) Form factors with (black) and without (gray) pre-polarization showing modulation depths of 10%. (c) Regularized distance distributions with (black) and without (gray) pre-polarization.

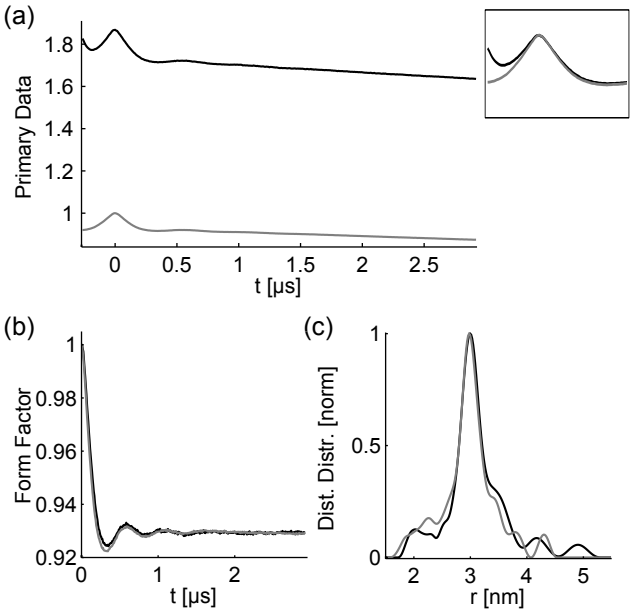

Figure C.11 – Pre-polarized DEER experiments on Gd-ruler $\mathbf{2_2}$ with a Gd-Gd distance of about 3.0 nm using a 64 ns long constant-rate chirp pump pulse ($f_1 = -0.75$ GHz to $f_2 = -0.3$ GHz). The 2 μs pre-polarization pulses had ranges $f_1 = -1.273$ GHz to $f_2 = -0.121$ GHz and $f_1 = 1.349$ GHz to $f_2 = 0.133$ GHz. (a) Primary data obtained with pre-polarization to 1.86 (black) and without pre-polarization (gray). The inset on the right-hand side shows the initial part of the two curves on top of each other. (b) Form factors with (black) and without (gray) pre-polarization showing modulation depths of 7%. (c) Regularized distance distributions with (black) and without (gray) pre-polarization.

C.6 SUPPLEMENTARY SIMULATIONS

In this final section, supplementary simulations are presented. At first, Fig. C.12 shows the simulation subset in Fig. 5.2a of the main text. In Fig. C.12a, a zoom on the satellite transitions is shown. The grid for computing the spectrum consisted of 90 points for all involved parameters, such that smoother histograms were obtained. Fig. C.12b shows the sum of all single-quantum transitions on this fine parameter grid. The red curve was calculated with perturbation theory, whereas the blue curve (underneath the red curve) was obtained by diagonalization of the laboratory frame Hamiltonian. For the given parameter grid, the two methods resulted in almost indistinguishable results. Needless to add, the diagonalization in the laboratory frame on this grid required more computation time. Moreover, our simulation approach does not support non-diagonal Hamiltonians with spectrum beyond the Nyquist range of 6 GHz due to the time stepping in the rotating frame. The perturbation approach was thus essential. Fig. C.12c shows the same view as in panel a, but with the coarser grid used in the actual spin dynamics simulations.
Fig. C.13a relates the powder simulations with a Gaussian distribution of D values (μ_D = 1.2 GHz and σ_D = 0.24 GHz) (black) to the echo-detected spectrum of Gd-PyMTA of Gd-ruler $\mathbf{1_3}$ (blue). Note that at present, simulated spectra assume the high-temperature limit and that all transitions are observed with the same efficiency. For the experimental data, however, the echo-detection introduces additional transition-specific weightings and the high-temperature limit is not strictly valid. Neglecting ZFS contributions, the equilibrium polarizations for an $S = 7/2$ system at 10 K and 35 GHz are

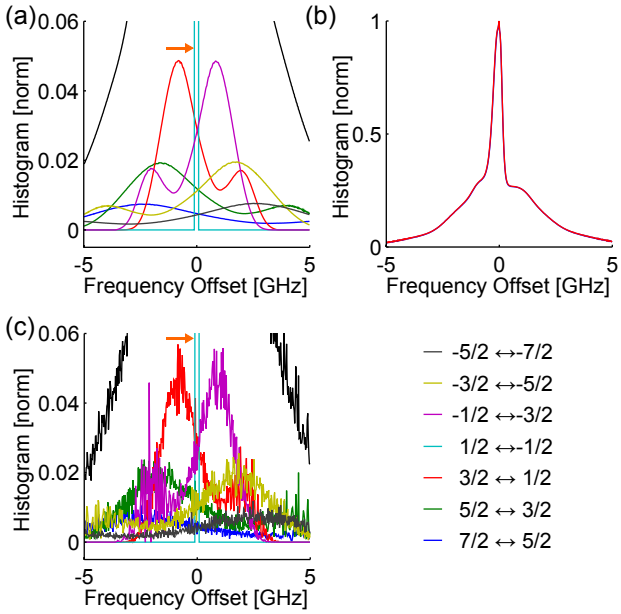

Figure C.12 – Supplementary Gd(III) spectra from powder simulations. See Section 5.3.4 in the main text for simulation method. (a) Histogram of single-quantum transition frequencies of $\hat{\mathcal{H}}_{\mathrm{ZFS}}$ (black) obtained with perturbation theory for frequency offsets of $\pm$ 5 GHz with 24 MHz step size. A zoom on the satellite transitions of the simulation subset is shown, according to the color legend on the bottom right. The grid for averaging over D, E, θ and ϕ consisted of 90 points in each dimension, thus much finer than in the main text (1000x more configurations). The spectrum calculation required 2.2 minutes. The orange arrow indicates the frequency range of the chirp pulse from -1.348 GHz to -0.124 GHz. (b) The ZFS spectrum of all single-quantum using the fine grid of (a) obtained with perturbation theory (red) as well spectrum calculated with eigenvalues of the full Hamiltonian and transformation of $\hat{S}_x$ into the eigenframe for transition moments (blue, underneath red). (c) Same data as in (a), but for the grid used in the spin dynamics simulation in the main text.

already non-equal: The central transition carries only 60% of the polarization of the lowest transition, the highest transition even only 37%. Inclusion of such effects into the simulation may help to refine parameter grids for better fits between experiment and simulation. For the present purpose, however, the simulations served to confirm the experimental trends with respect to different Gd(III) complexes.

Fig. C.13b shows the same black circles as Fig. 5.2b in the main text, which correspond to polarization upon the chirp for the various D values. The gray open circles were obtained with a chirp having inverted sweep direction, thus only polarizing the CT via one immediate neighbor transition. Due to the exclusion of polarization from satellites further out, the achieved polarizations were all lower than for the up-chirp simulated in the main text. This simulation was performed to support the conclusions drawn in Section 5.4.1.1. The underlying dynamics of polarization averaged over all involved D values is shown in panel c.

The last figure, Fig. C.14, shows the evolution of polarization during the up-chirp in Fig. 5.2 of the main text for a set of the individual D values, as indicated in each plot.

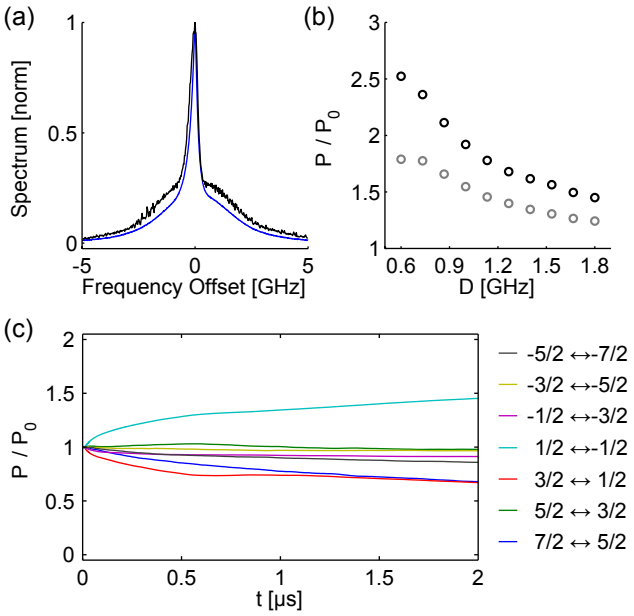

Figure C.13 – Powder simulation of chirp with inverted direction. (a) Histogram of powder simulations with μ_D = 1.2 GHz and σ_D = 0.24 GHz (black) compared to experimental echo-detected field-swept spectrum of Gd-ruler $\mathbf{1_3}$ connected to a frequency axis. Note that the simulated spectrum assumes only Zeeman and ZFS contributions in the high-temperature limit. (b) Simulated polarization of the powder- and E-averaged subset of the CT upon the chirp pulse at various D values. The black dots are the ones from the main text. The gray dots were simulated with the same parameters, just that the direction of the chirp was inverted. In this way, the CT can only be polarized via one of its neighbor transitions. (c) Simulated evolution of powder- and ZFS-averaged polarization under the chirp with inverted direction for the simulation subset. Color legend on the right-hand side. For the CT, the polarization upon the pulse is 1.48, which corresponds to the weighted average of polarizations in panel (b). This polarization is lower than the one simulated in the main text by 0.3. As a consequence for the simulation in the main text, 38% of the population transferred to the CT origins from transitions beyond the immediate neighbors.

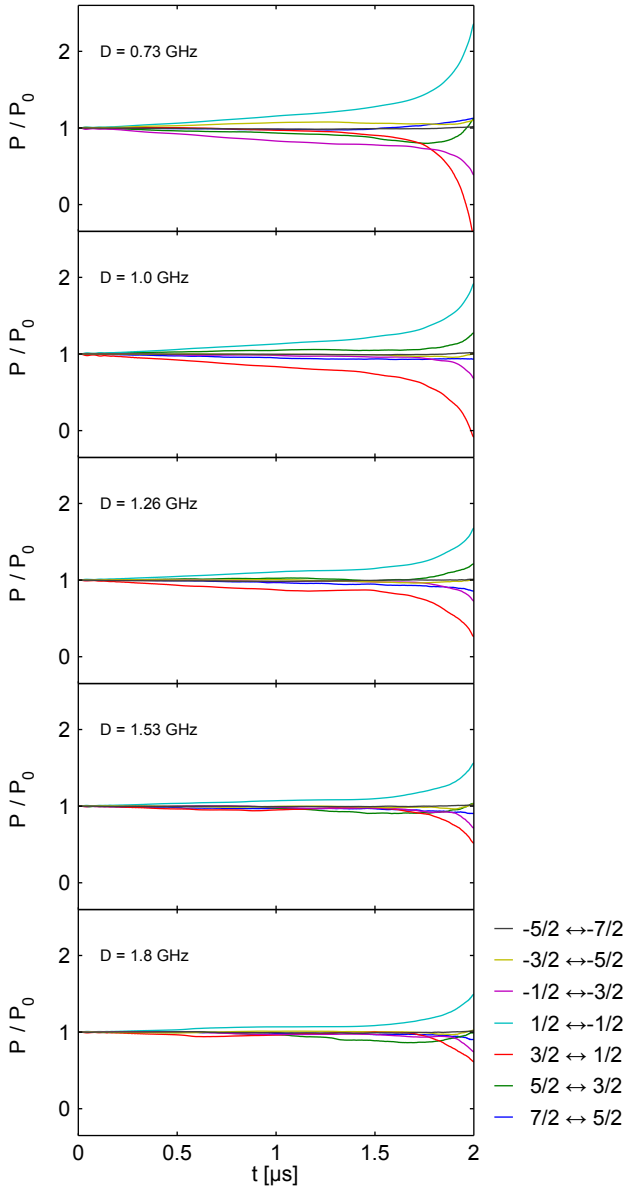

Figure C.14 – Evolution of polarizations averaged over orientation and E distribution within simulation subset (see main text) for 5 different D values, as indicated on each figure. Color legend on bottom right

D

SUPPORTING INFORMATION TO CHAPTER 6

D.1 TWO-POINT PARAMETERS

D.1.1 *Comparison of λ_{2P} and λ*

The essence of the fast in-situ sensitivity optimization described in Section 6.3.2 of the main text is the extraction of the modulation depth from two data points of the primary DEER signal $V(t)$. The resulting parameter $\lambda_{2P} = 1 - V(t_r)/V_0$ does not quantitatively relate to the actual modulation depth λ. But it is clear that if λ increases, also λ_{2P} increases, which allows for sensitivity optimization based on $\eta_{2P} = V_0 \cdot \lambda_{2P} = V_0 - V(t_r)$.
Since we recorded DEER data for 42 different pulse parameters in Section 6.3.1 of the main text, we here compare the actual modulation depth to λ_{2P}. The pulse parameters for each of the 42 experiments are summarized in Table D.1. Primary data obtained with t_p = 128 ns and a frequency offset $f_2 = -300$ MHz are shown in Fig. D.1a. By setting the delay τ_2 to 6 μs, a long dipolar time evolution window was used and each trace was recorded for 44 minutes (32 scans). Acquisition of all the data was automated by means of a *two-dimensional* DEER experiment, where the second dimension was used to address the different parameter constellations.
The correlation between the actual modulation depth λ and the adiabaticity Q_{CT} discussed in the main text is shown in Fig. D.1c. As in Figs. 6.2d and e, the two data points with Δf = 250 MHz are marked in gray. Below in Figs D.1d and e are the comparisons with two-point parameters. Panel (d) shows λ_{2P} versus λ for $t_r = 1\mu$s (orange) and $t_r = 4\mu$s (blue). In both cases, λ_{2P} correlates well with λ. Panel (e) approves that this also holds for the sensitivity η_{2P}. Note that in the actual experiment, there may be a slight variation in the t = 0 time of the dipolar evolution that translates into η_{2P}. Such a variation in t = 0 occurs if the offset between the pulse sequence time t' and the dipolar evolution time t varies with the pulse parameters (see also Section 6.2.2.1 in the main text). Moreover, it remains to be tested how well this procedure works in heterogeneous systems, where the optimal parameters may be distributed.

t_p [ns]	Δf [GHz]	f_2 [GHz]
32	0.25, 0.5, 0.75, 1.0, 1.25	−0.3
64	0.25, 0.5, 0.75, 1.0, 1.25	−0.3, −0.4
128	0.5, 0.75, 1.0, 1.25	−0.3, −0.4
256	0.5, 0.75, 1.0, 1.25, 1.5, 1.75	−0.3, −0.4
400	0.5, 0.75, 1.0, 1.25, 1.5, 1.75	−0.3, −0.4

Table D.1 – Pulse parameters for the 42 experiments obtained with Gd-ruler **1**$_3$. Each of the listed sweep widths Δf are combined with the end frequencies f_2, which are indicated relative to the observation frequency. The Δf values printed in gray are only combined with the end frequency $f_2 = -0.3$ GHz.

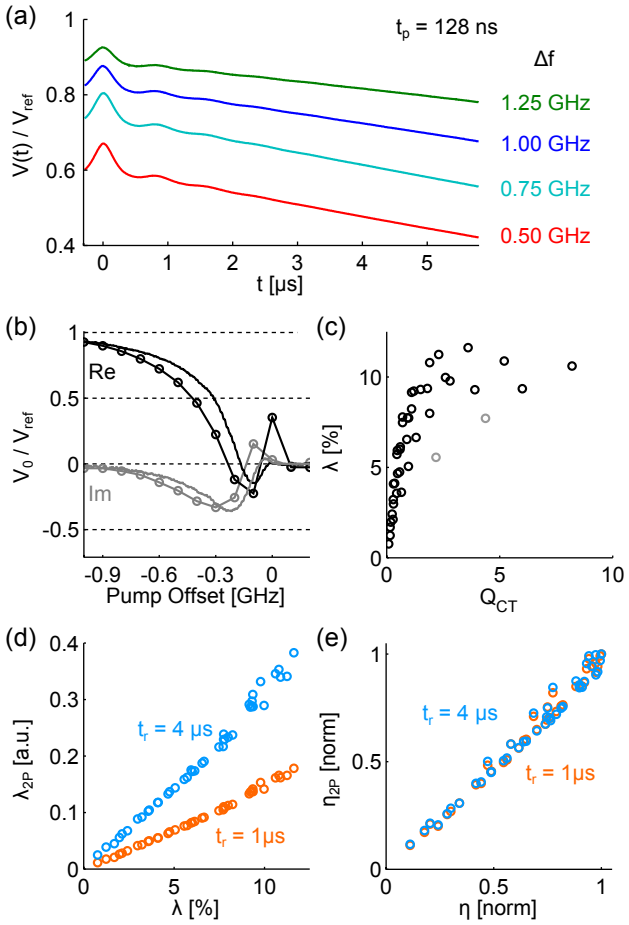

Figure D.1 – Calibration of two-point parameters using the 42 experiments obtained with Gd-ruler $\mathbf{1_3}$. (a) Primary DEER data for t_p = 128 ns, f_2 = −300 MHz, and sweep width Δf as indicated next to each curve. 32 scans each. (b) Echo intensity as a function of pump offset f_2 for a 128 ns long chirp with Δf = 750 MHz. Solid curves are experimental data as shown in Fig. 6.2b. Dashed curves are corresponding simulations. (c) Correlation between modulation depth λ and adiabaticity Q_{CT}. Circles in gray correspond to chirp pulses with Δf = 250 MHz (see also Table D.1). (d) Correlation between modulation depth λ and two-point modulation depth λ_{2P} using t_r = 1 μs (orange) or t_r = 4 μs (blue). (e) Correlation between normalized sensitivities η and η_{2P}.

D.1.2 *Examples*

D.1.2.1 *Gd-ruler* $\mathbf{1_3}$

In the following, examples of the sensitivity optimization are provided. The data for Gd-ruler $\mathbf{1_3}$ is shown in Fig. D.2. The top panel shows η_{2P} as a function of the sweep width Δf and the offset frequency f_2 for one single 128 ns chirp pulse. The bottom panel shows the data for two consecutive 64 ns chirp pulses. The green circles denote the parameters that were used in Fig 6.9. Both panels have the same color scale, such that the sensitivity advantage of consecutive pulses is directly visible. Moreover, one can see that the optima for one single pulse and consecutive pulses lie in different regions. The single pulse requires large sweep widths at small offset frequencies. At very large sweep widths Δf, even *overlapping* pulses with $f_2 > 0$ are favored. The optimum for the consecutive pulses is found for smaller Δf and comparably larger offsets $|f_2|$, where the adiabaticity is larger and the echo reduction by the second pulse becomes negligible (see main text). Note that the acquisition of such a two-dimensional η_{2P} map requires only 2 minutes, one minute for each point, and the selection of parameters Δf and f_2 from such a map is rather straight forward.

The data shown in Fig. D.2 may raise a question with regard to *overlapping*

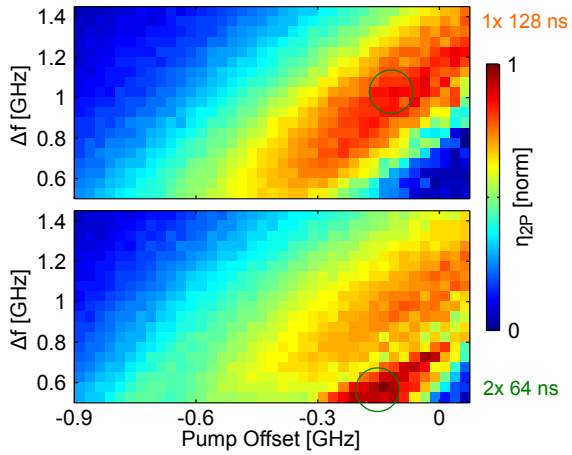

Figure D.2 – Optimization of η_{2P} using $t_r = 4\ \mu s$ and $\tau_2 = 5\ \mu s$ with Gd-ruler $\mathbf{1_3}$. Data in upper panel obtained with one single pulse having t_p = 128 ns. Data in lower panel obtained with two consecutive pulses, each having t_p = 64 ns. Both figures have the same color scale.

pulses with $f_2 > 0$. To understand these cases, one needs to consider the frequency dependence introduced by the resonator and the compensation thereof, which is illustrated in Fig. D.3. Panel (a) shows an idealized resonator profile (green) with parameters that are typical for our experimental setup. Also shown is the FT of a pulse that compensates for this resonator profile (gray) and the FT of this pulse *as seen by the spins* (black). The flat plateau of the black curve indicates an offset independent adiabaticity factor (see Section B.2). A magnified view of the FT seen by the spins is provided in panel (b), where both the compensated pulse (solid) as well as an uncompensated pulse (dashed) is illustrated. Note that here, the pulses seen by the spins were computed by convolution in time domain with the resonator impulse response. For a technical reason, this procedure includes low pass filtering and explains the residual curvature in the plateau of the compensated pulse. The orange vertical markers in panel (b) denote the start and end frequencies f_1 and f_2, respectively. As is readily seen, the flat plateau of the compensated pulse is asymmetric with respect to these two markers. In particular, there is a large gap below the end frequency f_2. The sweep width Δf is therefore not directly related to the excitation bandwidth. The reason for the pronounced asymmetry is the acceleration of the frequency sweep towards the center frequency of the resonator, where the coupling to the spins increases. In this sense, the frequencies passed at the end of the pulse are passed almost suddenly and therefore provide only a weak excitation. As a consequence, the pulse edges at the end of the pulse become *smeared out*. A related complication

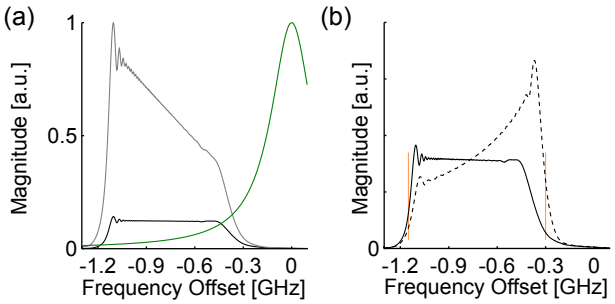

Figure D.3 – Pulse compensation for a 192 ns long 850 MHz chirp with offset $f_2 = -300$ MHz. (a) Magnitude FT of the pulse synthesized by the AWG (gray), magnitude FT of the pulse predicted at the level of the spins (black), and magnitude response $\nu_1(f)$ of an idealized resonator with Q_L = 110 and f_0 = 34.3 GHz (green). (b) Magnitude FT of the pulse predicted at the level of the spins for compensated pulse (solid black) and uncompensated pulse (dashed black).

is residual coherence excitation of the observed A spins by the pump pulse (see main text). The opposite effect is observed for the pulse edge at the beginning of the pulse. Here, the resonator results in a slower passage for the compensated pulse. In comparison to the uncompensated pulse, the compensated pulse has a more compressed edge on this side.
Another aspect related to the data shown in Fig. D.2 is the alignment of the regions of optimum sensitivity. The main reason is directly evident from Fig. D.4, where the adiabaticity factor Q_{CT} is illustrated. As one can observe, the regions of constant adiabaticity Q_{CT} do more or less determine the orientations of regions of optimum sensitivity. Clearly, the actual performance also depends on the spectral overlap between the effective excitation band and the pumped B spins, which is not included in the adiabaticity factor Q_{CT} (see also Section 6.3.1 of the main text).

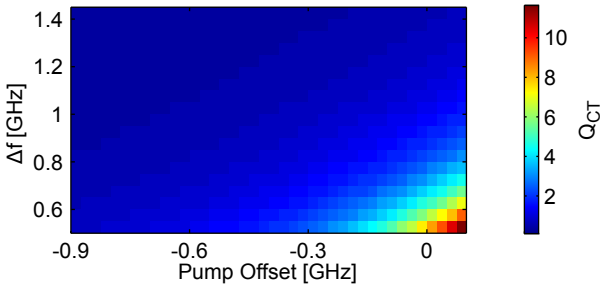

Figure D.4 – Adiabaticity factor Q_{CT} for parameter range sampled in η_{2P} optimization for a chirp pulse with $t_p = 64$ ns and resonator parameters as in Fig. D.3 ($Q_L = 110$ and $f_0 = 34.3$ GHz).

D.1.2.2 *Gd-rulers with larger distances*

Sensitivity optimization for larger distances is essentially the same procedure as the one described for Gd-ruler $\mathbf{1_3}$. The procedure does not require much more time, provided that one acquires η_{2P} maps for a reasonable choice of the delay τ_2. For Gd-ruler $\mathbf{1_7}$, $\mathbf{1_9}$, and $\mathbf{1_{11}}$, we used $\tau_2 = 7$ μs and $t_r = 5$ μs. The maps are shown in Fig. D.5. Note that the increased noise level in these data is not only due to prolongation of τ_2 from 5 μs to 7 μs, but also due to the lower concentrations used for the long-distance measurements. For Gd-ruler $\mathbf{1_7}$, the characteristic is similar to the map for Gd-ruler $\mathbf{1_3}$ shown above (see also below). The η_{2P} maps for Gd-ruler $\mathbf{1_9}$ and $\mathbf{1_{11}}$ have an almost identical characteristic, which differs from the characteristic seen for Gd-ruler $\mathbf{1_3}$ and $\mathbf{1_7}$. For Gd-ruler $\mathbf{1_9}$, we have also recorded a η_{2P} map for one single pump pulse with a duration of 384 ns (data not shown). By comparison, we found that the consecutive pulses achieve a better sensitivity and require pulses of higher adiabaticity.
The differences in η_{2P} maps between Gd-ruler $\mathbf{1_9}/\mathbf{1_{11}}$ and Gd-ruler $\mathbf{1_3}/\mathbf{1_7}$ are most likely related to instrumentation. In particular, η_{2P} maps of Gd-ruler $\mathbf{1_3}$ and $\mathbf{1_7}$ exhibit a rather abrupt boundary at the regions of highest sensitivity (see straight line drawn on top of Gd-ruler $\mathbf{1_7}$ data). The origin of this boundary is seen in Fig. D.6a, where the gray curve shows $V_0(f_2)$ at $\Delta f = 500$ MHz for Gd-ruler $\mathbf{1_7}$. The pronounced step around $f_2 = -600$ MHz defines the abrupt boundary in η_{2P}. Here, this step can be explained by spurious excitation by third order intermodulation (see [137]). During another measurement session with the same sample tube of Gd-ruler $\mathbf{1_7}$, there was no spurious excitation (see black curve in Fig. D.6a). For Gd-ruler $\mathbf{1_3}$, whose η_{2P} map is shown above in Fig. D.2, it is also a step in V_0 which defines the abrupt boundary in η_{2P} (data not shown). In this case, the step is presumably also due to spurious excitation, but we did not investigate the actual origin of the spurious tone.
The aforementioned boundaries in η_{2P} maps of Gd-ruler $\mathbf{1_3}$ and $\mathbf{1_7}$ may have

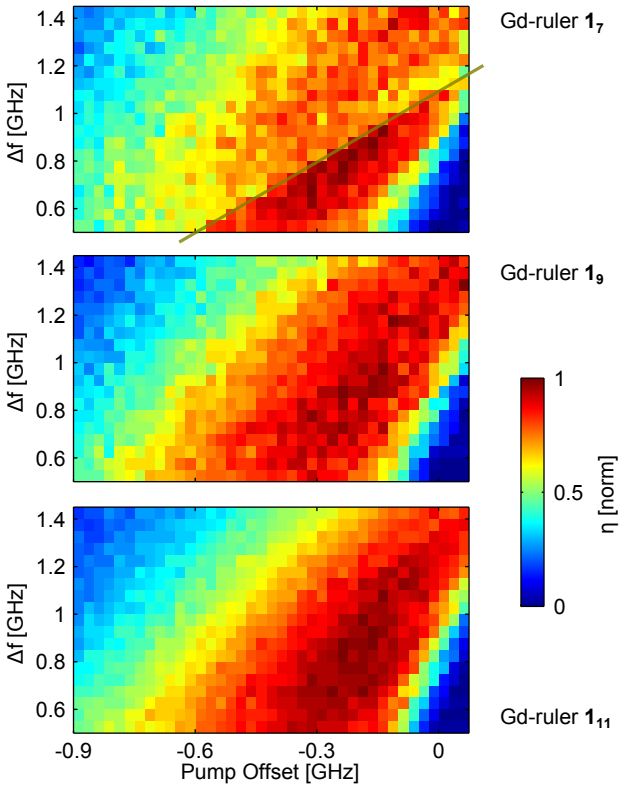

Figure D.5 – η_{2P} maps acquired with $t_r = 5$ μs and $\tau_2 = 7$ μs with Gd-ruler $\mathbf{1_7}$, $\mathbf{1_9}$, and $\mathbf{1_{11}}$. All data obtained with two consecutive pulses, each having t_p = 192 ns. There is no relation between the colors amongst the three figures.

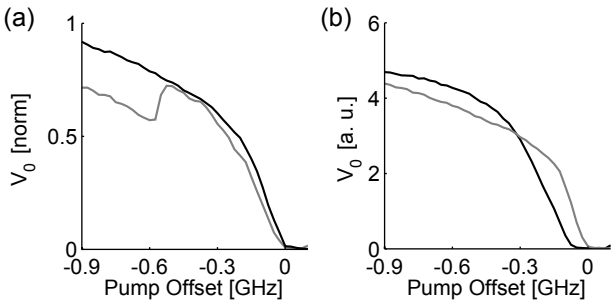

Figure D.6 – Dependence of echo intensity V_0 on pump offset f_2 for chirp pulses with Δf = 500 MHz. (a) Two different datasets obtained with consecutive pulses, each 192 ns long, with Gd-ruler $\mathbf{1_7}$. The gray curve belongs to the data shown in Fig. D.5. The black curve was obtained using exactly the same sample tube re-inserted into the microwave resonator during another measurement session. The curves are normalized by the echo intensity obtained with Δf = 1.45 GHz and $f_3 = -900$ MHz. (b) Single pulse (black) and consecutive pulse (gray) data obtained with Gd-ruler $\mathbf{1_{11}}$, each 192 ns long. The consecutive pulse data belong to the data shown in Fig. D.5. Normalized data V_0/V_{ref} for Δf = 850 MHz is shown in Fig. 6.7.

influenced the pulse parameters chosen for the experiments. For reference, Table D.2 lists the pulse parameters for the long-distance measurements with consecutive pulses of 192 ns duration each. The frequency positioning parameters Δf and f_2 are all comparable. The adiabaticity factor Q_{CT} is larger for Gd-ruler $\mathbf{1_7}$ compared to Gd-rulers $\mathbf{1_9}$ and $\mathbf{1_{11}}$. This may explain the apparent modulation depths below 10% seen for Gd-ruler $\mathbf{1_9}$ and $\mathbf{1_1 1}$. Note however that in the present work at Q-band frequencies, pulse compensation relies on model fits to experimental $\nu_1(f)$ data. Due to the fitting, adiabaticity factors are not as quantitative as in our work at X-band frequencies [35].

Gd-ruler	Δf [MHz]	f_2 [MHz]	Q_{CT}
$\mathbf{1_7}$	700	−225	3.5 (2.9)
$\mathbf{1_9}$	700	−250	2.3 (2.7)
$\mathbf{1_{11}}$	800	−250	2.0

Table D.2 – Pulse parameters for the long-distance experiments. For reference, the adiabaticity parameters Q_{CT} given in brackets for Gd-ruler $\mathbf{1_7}$ and $\mathbf{1_9}$ were computed with the resonator parameters of Gd-ruler $\mathbf{1_{11}}$.

D.1.2.3 *Compensation of echo reduction with consecutive pulses*

In the main text, Fig. 6.7a shows evidence for compensation of echo reduction mechanisms by consecutive pulses at small offset frequencies $|f_2| < 120$ MHz. The data obtained with Gd-ruler $\mathbf{1_{11}}$ using $\Delta f = 850$ MHz pulses is complemented with data obtained using $\Delta f = 500$ MHz pulses in Fig. D.6b. For this narrower sweep range, the compensation is clearly visible: The echo intensity with consecutive pump pulses (gray) exceeds the echo intensity with one single pump pulse (black) for $|f_2| < 300$ MHz.
For a more complete picture, Fig D.7 shows the difference between V_0 obtained with a single pump pulse and consecutive pump pulses. In regions where the difference is negative, consecutive pump pulses result in a larger echo than one single pump pulse. The compensation mechanism by the second pulse is therefore more effective for small sweep ranges Δf. A possible explanation for this effect is inhomogeneity in ν_1, which is explained below in Section D.8.2 of this appendix.

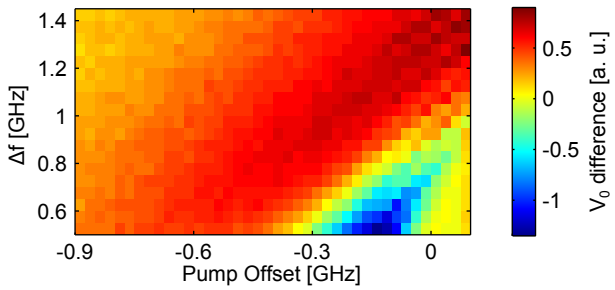

Figure D.7 – Difference between V_0 obtained with a single 192 ns long chirp pulse and two consecutive pulses of 192 ns duration each. A negative difference implies that the echo signal with the consecutive pulses is larger than with the single pulse.

D.2 DIPOLAR HARMONICS

As mentioned in the main text, chirp pulses may excite multi-quantum transitions which lead to higher harmonics of the dipolar frequency. With our current experimental setup, such harmonics are excited by applying the pump pulse at the center of the resonator, where the field strength ν_1 is large. The related DEER data presented in the main text in Fig. 6.4 are shown in blue in Fig. D.8. In addition, the data shown in orange were obtained with twice the pulse length ($t_p = 128$ ns). As can be seen in both time-domain data in panel (a) and distance-domain data in panel (b), the longer pulse results in a narrower distance distribution and a slightly longer oscillation period. The data shown in green were obtained with a 192 ns long chirp with $\Delta f = 800$ MHz and reproduce the data of the 128 ns long pulse.
The pulses related to Fig. D.8 are constant-rate chirps and therefore not compensating for the resonator profile. For completeness, we also examined compensated pulses for multi-quantum excitation. The results for a 64 ns long chirp pulse with $\Delta f = 600$ MHz and $f_2 = -300$ MHz at three different pulse amplitudes are shown in Fig. D.9. As distance domain data in panel b show,

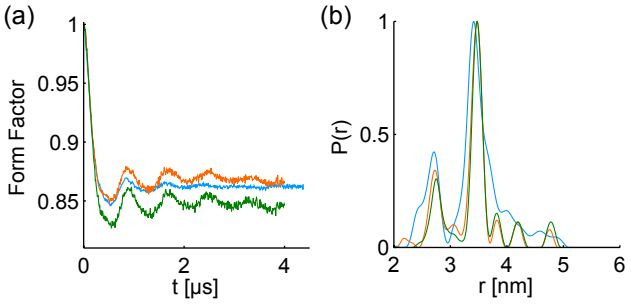

Figure D.8 – Dipolar harmonics excited with constant-rate chirps with $f_2 = -300$ MHz applied at the center frequency of the resonator using the following pulse parameters. Blue: $t_p = 64$ ns, $\Delta f = 600$ MHz. Orange: $t_p = 128$ ns, $\Delta f = 600$ MHz. Green: $t_p = 192$ ns, $\Delta f = 800$ MHz. The normalized echo intensities V_0/V_{ref} were 0.11, 0.07 and 0.05, respectively. 50 scans each.

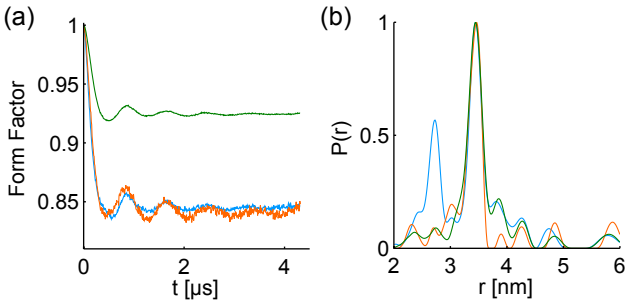

Figure D.9 – Dipolar harmonics excited with compensated chirps applied at the center frequency of the resonator. The parameters for all pulses were $t_p = 64$ ns, $f_2 = -300$ MHz and $\Delta f = 600$ MHz. Variation of the flip angle was achieved by changing the pulse amplitude. Blue: Full scale amplitude resulting in shortest π pulse on the CT of 3 ns. Orange: Amplitude resulting in shortest π pulse on the CT of 17 ns. Green: Amplitude resulting in shortest π pulse on the CT of 48 ns. The normalized echo intensities V_0/V_{ref} were 0.16, 0.09 and 0.87, respectively. The increase in amplitude from 0.09 to 0.16 when going from a reduced amplitude to the full-scale amplitude is not fully understood. It is presumed that the multi-quantum excitation of the full-scale pulse has also an influence on V_0/V_{ref}. 30 scans each.

the pulse with the strongest amplitude (blue) excited $\Delta m_s = 2$ transitions. Altogether, the data give insight into the mechanism of multi-quantum excitation. In principle, there a two possibilities to excite a $\Delta m_S = 2$ dipolar harmonic: First, the pulse may directly excite the formally forbidden multi-quantum transition. Second, the pulse may excite two neighbor transitions one after another, thereby inducing a net change of $\Delta m_S = 2$.

Since we were able to excite dipolar harmonics with sweep widths Δf as low as 400 MHz (data not shown), efficient spectral coverage of two neighboring satellite transitions is rather unlikely. Therefore, we anticipate that the chirp pulse directly excites multi-quantum transitions. Using fictitious spin 1/2 operators, an adiabaticity factor specific to the multi-quantum transition can be defined [214, 49, 153]. In analogy to the adiabaticity factor of a single-quantum transition, the adiabaticity factor of a double-quantum transition is influenced by pulse parameters, such as pulse length t_p and sweep width Δf (see Fig. D.8), or pulse amplitude ν_1 (see Fig. D.9). However, there is a specific dependence of the adiabaticity factor for $\Delta m_S = 2$ transitions on the ratio between ν_1 and the ZFS splitting. As a consequence, we expect excitation of dipolar harmonics to be more prominent for smaller ZFS parameters.

Under our current experimental conditions, the sensitivity of the data with dipolar harmonics is degraded due to observation off the central frequency of the resonator and due to echo intensities V_0/V_{ref} reduced to small values by the pump pulse. Such experiments are therefore not envisaged for distance measurements. However, excitation of dipolar harmonics is important in

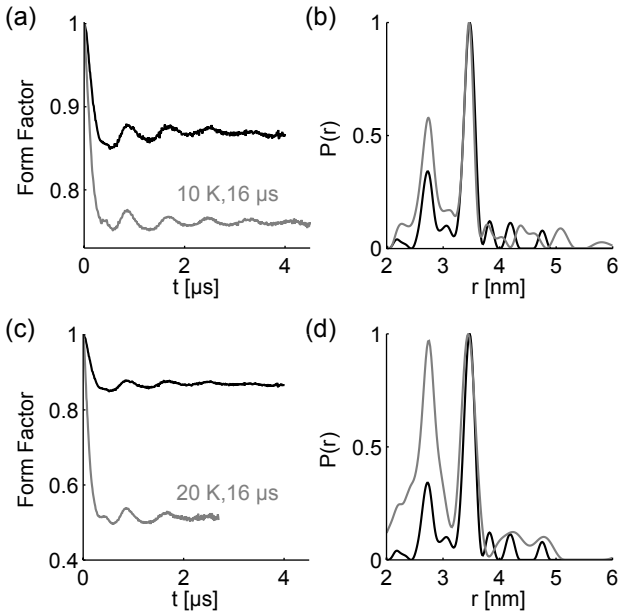

Figure D.10 – Comparison between DEER (black) at 10 K and RIDME (gray) at 10 K (a,b) and 20 K (c,d) using a mixing time of 16 μs (see [161]).

RIDME experiments [161]. The investigation of dipolar harmonics with chirp pulses on model systems may provide additional insight with respect to distance determination. Fig. D.10 shows a preliminary comparison between RIDME data (gray) obtained with Gd-ruler $\mathbf{1_3}$ at W band (see [161]) and the data obtained with the 192 ns long chirp pulse (black, green in Fig. D.8).

D.3 MODULATION DEPTH WITH CONSECUTIVE CHIRP PULSES

Fig. 6.8 of the main text shows the modulation depth obtained with a single chirp on each side as well as with the two consecutive pulses. The related primary DEER signal $V(t)/V_{\text{ref}}$ is shown in Fig. D.11a. As is readily seen, the echo signal with consecutive pulses (green) is not reduced further below the echo signal with the down-chirp (blue). Similar observations were made with 64 ns long chirp pulses. The primary DEER signal $V(t)/V_{\text{ref}}$ is shown in panel b, the form factor in panel c, and the distance distributions in panel d. In this case, the modulation depth with the consecutive pulse is almost the sum of modulation depth obtained with the individual pulses. The loss is only 0.6%, whereas the loss for the 128 ns reported in the main text is 2%. It is presumed that this is due to the net pulse length of the consecutive pulse: The longer consecutive pulse with 256 ns combined duration leads to more pronounced interference than with one single 128 ns pulse. In fact, a direct comparison between background-corrected dipolar spectra obtained with the consecutive pulses do show pronounced attenuation of the shoulders of the Pake pattern for the longer 256 ns pulse (data not shown). Note that in general, one would expect that a single chirp pulse and consecutive pulses lead to comparable interference if the net pulse length is the same. In both cases, coherence is continously transferred throughout almost the entire pulse duration.

D.4 LOSS OF MODULATION DEPTH FOR LONG EVOLUTION WINDOWS

Longer dipolar evolution windows reduce the modulation depth, as shown in Fig. 6.10 of the main text and previously in [168]. In order to clarify that the reduction in λ is not related to apparent differences in the background decay, the primary DEER signal $V(t)/V_0$ is shown in Fig. D.12a.
Possible intermolecular relaxation mechanisms were tested by recording data with Gd-ruler $\mathbf{1_7}$ at various concentrations from 25 μM up to 1 mM. The

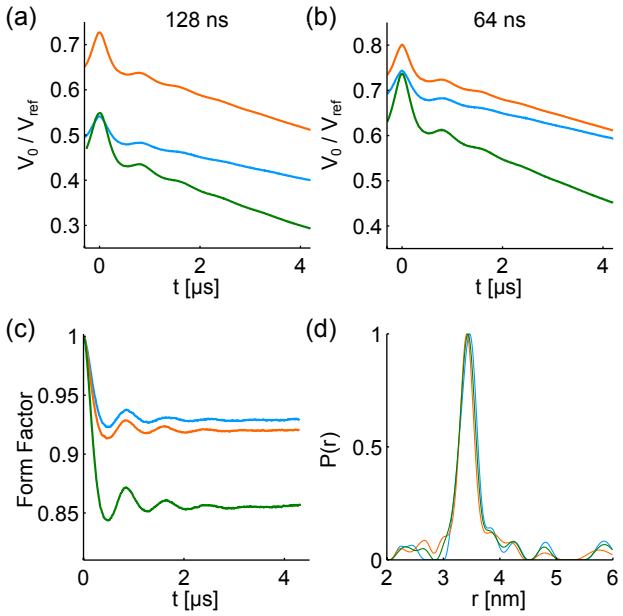

Figure D.11 – Modulation depth enhancement with consecutive pump pulses. Orange curves obtained with one up-chirp, blue curves with one down-chirp, and green curves with two consecutive chirps. (a) Primary data related to the 128 ns pulses shown in Fig 6.8 of the main text. The normalized echo intensities V_0/V_{ref} are 0.72 (orange), 0.54 (blue) and 0.54 (green). (b) Primary data obtained with 64 ns pulses with $|f_2|$ = 300 MHz and Δf = 430 MHz. The normalized echo intensities V_0/V_{ref} are 0.8 (orange), 0.75 (blue) and 0.73 (green). (c,d) Form factor and regularized distance distributions of data in panel b. Modulation depths are 7.9% (orange), 7.0% (blue) and 14.3% (green), which corresponds to a loss of 0.6%. All data acquired with 20 scans each and all 64 ns and 128 ns pulses have Q_{CT} on the order of 1.9.

resulting $\lambda_{2\text{P}}$ and V_0/V_{ref} are shown in Figs. D.12b and c, respectively. Within experimental uncertainty, neither of the data show an apparent dependence on concentration. Furthermore, the relative change in V_0/V_{ref} with τ_2 is small compared to the change observed in $\lambda_{2\text{P}}$. Note that V_0/V_{ref} does not only incorporate the echo reduction due to the pump pulse, but also the ability to refocus the dipolar coupling: The pump pulse at $t = 0$ dephases the observer spins via the dipolar coupling, which is refocused with the last π pulse. With V_0/V_{ref} being almost independent on τ_2, there is no indication of a τ_2-dependent mechanism which influences dipolar refocusing. Examples of two such mechanisms are mentioned in the main text (relaxation and residual excitation of pump spins by the observation pulses).
The loss of dipolar modulation depth was also confirmed with Gd-ruler $\mathbf{1_9}$. Also in this case, $\lambda_{2\text{P}}$ decays with τ_2 (Fig. D.12d) while V_0/V_{ref} does not change much (Fig. D.12e).

D.5 SENSITIVITY ENHANCEMENT BY POPULATION TRANSFER

All distance measurements with long τ_2 above 15 μs were pre-polarized to increase the echo signal. The parameters for all pulses are found in Table D.3. Note that the extraordinary high adiabaticity Q_{CT} for the up-chirp applied for Gd-ruler $\mathbf{1_7}$ (first row in the table) is explained by the comparably narrow sweep width Δf = 865 MHz. The sweep width could not be extended above 1 GHz due to pronounced sample heating caused by another resonant mode of the microwave resonator. For the other up-chirps listed in the table, ordinary values of Δf on the order of 1.2 GHz were feasible. Note that for all pre-polarized DEER signals, the transient at the beginning of the time trace can be identified (see Fig. 6.11a of the main text). The transient was made shorter

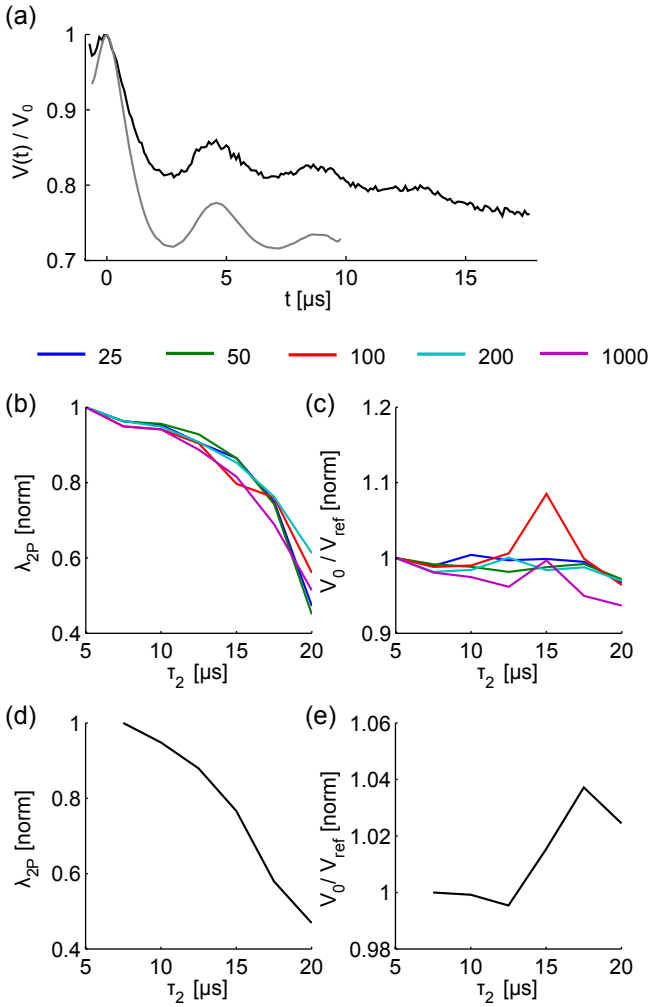

Figure D.12 – Dependence of modulation depth and echo intensity on τ_2. (a) Primary data $V(t)/V_0$ for the data shown in the main text in Fig. 6.10 acquired using 25 and 258 scans for the short and long τ_2 setting, respectively. (b,c) Normalized λ_{2P} and normalized echo intensity V_0/V_{ref} as a function of τ_2 for Gd-ruler $\mathbf{1_7}$ at various concentrations (see color legend above, concentrations specified in μM). (d,e) Normalized λ_{2P} and normalized echo intensity V_0/V_{ref} as a function of τ_2 for Gd-ruler $\mathbf{1_9}$.

than in our previous work [137] by setting the number of shots per point to 1000×2 instead of 300×2.

Experimental data is shown in Fig D.13. Panel a shows the decay of the primary two-pulse echo obtained with 12 ns pulses as a function of the inter-pulse delay. The $1/e$ decay is at $\tau = 4.4$ μs, which implies a phase memory time $T_m = 8.8$ μs. The inter-pulse delay, where the echo decays to 10% of its initial amplitude, is at 8.74 μs, and therefore comparable with W-band data for a different solvent mixture [175]. Panel b shows the echo transient related to V_{ref} at $\tau_2 = 20$ μs of Gd-ruler $\mathbf{1_9}$ with (green) and without (black) pre-polarization. As can be seen, the pre-polarized echo is almost twice the

Gd-ruler	Δf [GHz]	f_2 [GHz]	Q_{CT}
$\mathbf{1_7}$	0.865	−0.125	29.0
$\mathbf{1_7}$	1.4	0.125	8.5
$\mathbf{1_9}$	1.2	−0.156	8.3
$\mathbf{1_9}$	1.392	0.125	6.3
$\mathbf{1_{11}}$	1.208	−0.112	10.4
$\mathbf{1_{11}}$	1.358	0.142	7.6

Table D.3 – Pulse parameters for 2 μs long pre-polarization of long-distance experiments. Negative frequencies f_2 indicate up-chirps, positive f_2 down-chirps.

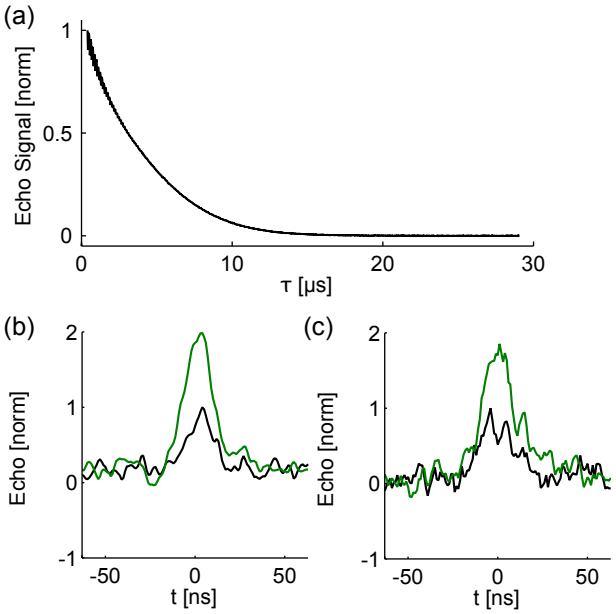

Figure D.13 – Sensitivity enhancement by population transfer. (a) Decay of primary echo as a function of the inter pulse delay τ for Gd-ruler $\mathbf{1_7}$. A pulse length of 12 ns for excitation and refocusing pulses was used. (b) Normalized echo transient at τ_2 = 20 μs with (green) and without (black) pre-polarization for Gd-ruler $\mathbf{1_9}$. 1000 averages at 30 dB gain of the video amplifier. (c) Normalized echo transient at τ_2 = 20 μs with (green) and without (black) pre-polarization for Gd-ruler $\mathbf{1_{11}}$. 1000 averages at maximum gain of the video amplifier (69 dB). An offset correction by a normalized amplitude of 0.3 was applied to raw data.

equilibrium echo. Panel c shows an equivalent result for Gd-ruler $\mathbf{1_{11}}$. The higher apparent noise level in panel c, as compared to panel b, is most likely due to non-optimum receiver settings: The data in panel c was acquired at the full *video gain* of 69 dB and had a normalized offset of 0.3, which is not shown in the figure. Such a large gain leads to clipping of noise due to the vertical resolution of the digitizer. With the vertical offset, the clipping level depends on the sign of the added noise, such that signal averaging is less effective in this case. On the employed spectrometer, acquisition of such small signals is more efficient with a receiver gain on the order of 30 dB which avoids clipping of noise. Note that noise clipping is very easy to check by looking at the transient signal with one average.

D.6 SUPPLEMENTARY DISTANCE DISTRIBUTIONS

D.6.1 *Gd-ruler* $\mathbf{1_3}$

In this section, representative distance distributions obtained with different pump pulses are compared (see Fig. D.14). These are a chirp exciting dipolar hamonics (orange), a consecutive chirp at the sensitivity optimum (blue), and a monochromatic rectangular pulse (green). See caption for pulse parameters and relation to data presented elsewhere in the text.
Most noticeable in the distance domain data is the second dipolar harmonic, which results in an additional distance peak for the orange curve. Furthermore, there are slight deviations within the main distance peak around 3.4 nm. Whether such deviations are of any concern for distance determination depends on the required precision. In either case, we observed the depicted trend in a number of experiments with Gd-ruler $\mathbf{1_3}$. Namely that rectangular pulses result in shortest distances, chirp pulses at the sensitivity optimum in intermediate distances, and chirp pulses exciting dipolar harmonics in longest distances. Note that we are here referring to small shifts in distance peaks. For instance, the shift between the distance peak of the dipolar har-

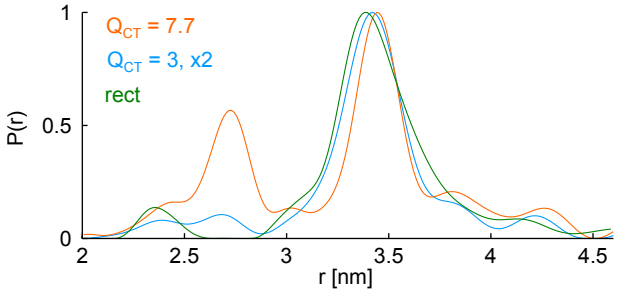

Figure D.14 – Comparison of typical distance distributions obtained with Gd-ruler $\mathbf{1_3}$. The orange curve excites dipolar harmonics by a 64 ns pulse and corresponds to the data shown in blue in Fig. D.9b. The blue curve is obtained with consecutive chirps of 64 ns duration each and corresponds to the data shown in the main text in Fig. 6.9. The green curve is obtained with a monochromatic rectangular pump pulse of 8 ns duration shaped by a sine function with a frequency 300 MHz below the observation frequency (see also Fig. D.18). Adiabaticities Q_{CT} are indicated in the legend.

monic data and the distance peak of the rectangular pulse data is only 0.06 nm. Apart from these shifts, one unique feature of the data with dipolar harmonics is the narrowing of the distance distribution, as already mentioned above in Fig. D.8.

D.6.2 *Gd-ruler* $\mathbf{1_5}$

The form factor and resulting distance distributions obtained with Gd-ruler $\mathbf{1_5}$ with a 4.7 nm distance are shown in Fig. D.15a and b, respectively. Gray curves were obtained with one single chirp pulse of 192 ns duration and offset frequency $f_2 = -300$ MHz, whereas black curves were obtained with consecutive pulses with 192 ns length each. Here, the parameters of the pulses (see caption) were not optimized with η_{2P}.
In the time domain data, the dipolar evolution is measured up to 14 μs and shows distinct oscillations. With the long time window for this 4.7 nm distance, the distance distributions (regularized with regularization parameter 1) shown in panel b are of high significance. Interestingly, these distributions do not show the asymmetry with a tail towards short distances observed in previous studies using ortho-terphenyl as a matrix [156, 157]. In particular, there are tails towards both short and long distances in the present case, which are reproduced in both data sets. We tentatively attribute the absence of a pronounced asymmetry to the longer persistence length at the glass transition temperature of the D_2O/glycerol solvent. While the persistence length in ortho-terphenyl was found to be 16.7 nm [157], a persistence length of 25.05 nm is predicted for the solvent used in this work (see below in Section D.6.4).

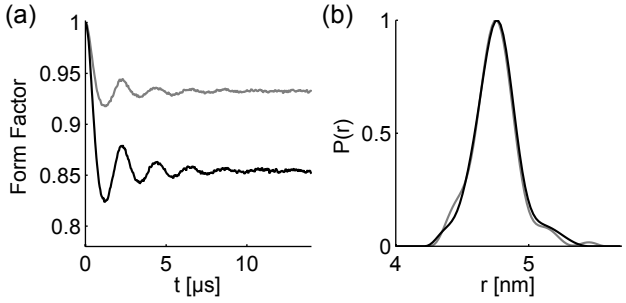

Figure D.15 – DEER results of Gd-ruler $\mathbf{1_5}$ obtained with one single chirp pulse (gray) and consecutive pulses (black) using the parameters t_p = 192 ns, Δf = 850 MHz and $|f_2|$ = 300 MHz (gray). 43 scans each.

D.6.3 *Gd-rulers* $\mathbf{1_9}$ *and* $\mathbf{1_{11}}$

Separation between the intermolecular background and pairwise distance information is a delicate task, especially in the case of limited time windows. For Gd-ruler $\mathbf{1_9}$, the background was fitted starting at a time t_{bg} = 5.4 μs with a stretched exponential decay that corresponds to a background dimension d_{bg} = 3.9. For Gd-ruler $\mathbf{1_{11}}$, the parameters were t_{bg} = 7.5 μs and d_{bg} = 4.5. The rationale for these parameters was a DEER measurement with a 20 μs time window of Gd-ruler $\mathbf{1_5}$, which resulted in d_{bg} = 4.1 and d_{bg} = 4.5 when fitting the background with t_{bg} = 5.0 μs and t_{bg} = 7.5 μs, respectively (data not shown).
In the following, we investigate on how robust the choice of background parameters is with respect to the mean distances reported in the main text. Note that these mean distances were obtained by evaluating the relevant distance peak in a predefined distance window. Most critical are the data of Gd-ruler $\mathbf{1_{11}}$ with the longest distance. For this purpose, we used the validation tool of DeerAnalysis for broad variation of t_{bg} and d_{bg} on a 7×7 grid from 5 μs to 8 μs and from 3.5 to 5, respectively. The result for Gd-ruler $\mathbf{1_{11}}$ is shown in Fig. D.16a. The black curve is the result with the lowest

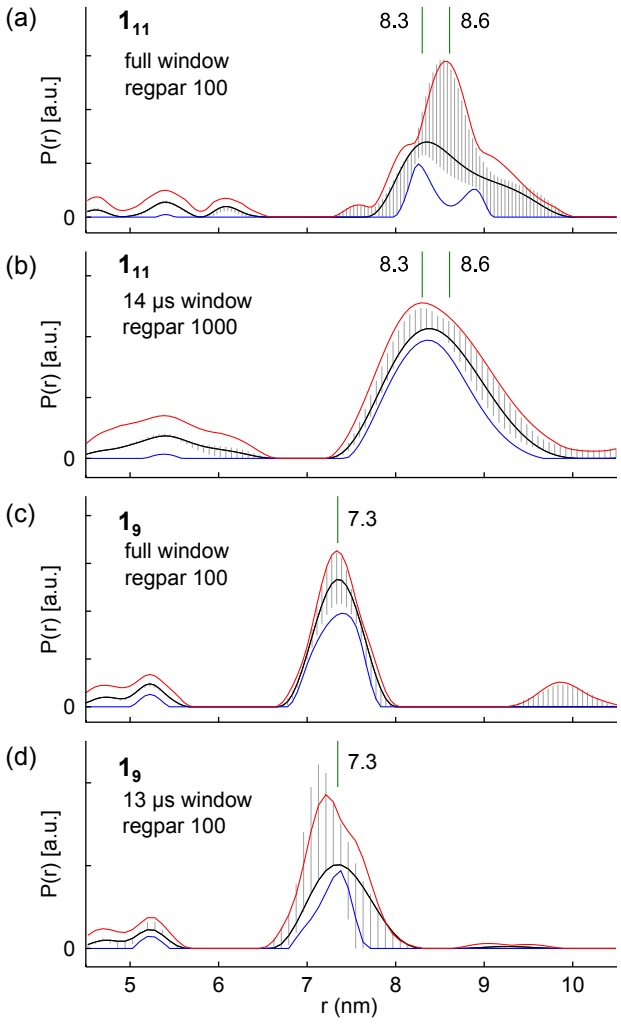

Figure D.16 – Dependence of distance distribution on background parameters t_{bg} and d_{bg} using a 7×7 grid from 5 μs to 8 μs and from 3.5 to 5, respectively. Black: best fit to experimental data in time domain. Gray vertical: variation of distance distributions. Red and blue: outer limits. (a) Gd-ruler $\mathbf{1_{11}}$ with a regularization parameter of 100 (b) Gd-ruler $\mathbf{1_{11}}$ deliberately cut off at 14 μs with a regularization parameter of 1000. (c) Gd-ruler $\mathbf{1_9}$ with a regularization parameter of 100. (d) Gd-ruler $\mathbf{1_9}$ deliberately cut off at 13 μs with a regularization parameter of 100.

deviation to the experimental time domain DEER data and coincides with our parameter choice of t_{bg} = 7.5 μs and d_{bg} = 4.5. The gray vertical lines denote the variation of all distance distributions computed with the 7 × 7 parameter combinations, with limits denoted by the blue and red line.

Around 8.6 nm, there is a pronounced peak in probability amplitude due to distance distributions which define a narrower distance peak than the distribution shown in black. The narrowest distribution with a full width at half maximum (FWHM) on the order of 0.5 nm corresponds to parameters t_{bg} = 5 μs and d_{bg} = 3.5. While these parameters yield a well-defined distance peak with a mean distance of 8.5 nm, the deviation to time domain data increased remarkably. With a regularization parameter of 1000, we achieved a similar result. In particular, the smallest deviation to experimental data was also obtained for t_{bg} = 7.5 μs and d_{bg} = 4.5 and also resulted in a distance peak with mean distance of 8.6 nm (see further below in Fig. D.17c).

In a recent study at W-band [175], an experimental distance of 8.3 nm was reported for Gd-ruler $\mathbf{1_{11}}$. Since the data reported in that study had a shorter time window, we performed the same validation for our data cut off at 14 μs. For these truncated data, a regularization parameter of 1000 was chosen. As the result in Fig. D.16b shows, our data reproduce the peak distance of 8.3 nm reported in [175] with high likelihood throughout all 7 × 7 parameter combinations. The difference between our data and the data in [175] thus may be related to the length of the time window.

We performed the same procedure with Gd-ruler $\mathbf{1_9}$ using the full time window (panel c), as well as a window cut off at 13 μs (panel d). Using the full window, there are only small changes in the position and width of the distance distribution. In the case of Gd-ruler $\mathbf{1_9}$, the reported mean distance of 7.3 nm is therefore significant. With a shorter time window, the variation in distance distributions is enhanced.

Given the differences in peak distance and width of the distribution for Gd-ruler $\mathbf{1_{11}}$ between our study and the previous study [175], we include results from another preparation of Gd-ruler $\mathbf{1_{11}}$ at a larger concentration to the discussion. Due to reduced control of the concentration during this particular preparation, the actual concentration is not well known. The data shown in the main text are reprinted in blue in Figs. D.17 a-c, where panel (c) shows the distance peak with a regularization parameter of 1000 instead of 100, which results in the same mean distance of 8.6 nm (see above). Also shown in panel (c) are two vertical blue lines that denote the positions of 8.3 nm and 8.6 nm. The data of the sample with larger concentration is shown in black. Due to reduced data quality of this data set, the time domain data were conditioned with a second-order Butterworth low pass filter with cutoff frequency at 3 MHz. The distance distributions reveal a slightly shorter distance for the sample with higher concentration. In particular, a mean distance of 8.5 nm is obtained. With respect to the width of the distance distribution, it is evident from Fig. D.17b that there is not much of a difference between the two datasets. Using the best fit to the background decay, we have therefore observed two times a FWHM on the order of 1.2 nm, which is twice as wide as in [175]. Notice that the dipolar evolution window of 22 μs in our measurements is just at the border, where the width of the distance distribution is significant [179]. Moreover, the choice of the background is critical for Gd-ruler $\mathbf{1_{11}}$, as seen in Fig. D.16a. Under these conditions, it is difficult to obtain the width precisely.

Variation of the background parameters (panel d) leads to a similar pattern than in Fig. D.16a, however shifted to shorter distances. This is clearly visible by the narrow distributions, which result in a distance peak close to 8.3 nm. At a shorter time window of 14 μs (panel e), narrow distributions exhibit a distance peak below 8.3 nm. The narrowest distribution with a full width at half maximum (FWHM) on the order of 0.85 nm corresponds to parameters t_{bg} = 5 μs and d_{bg} = 3.5 and has its maximum located slightly below 8.2 nm.

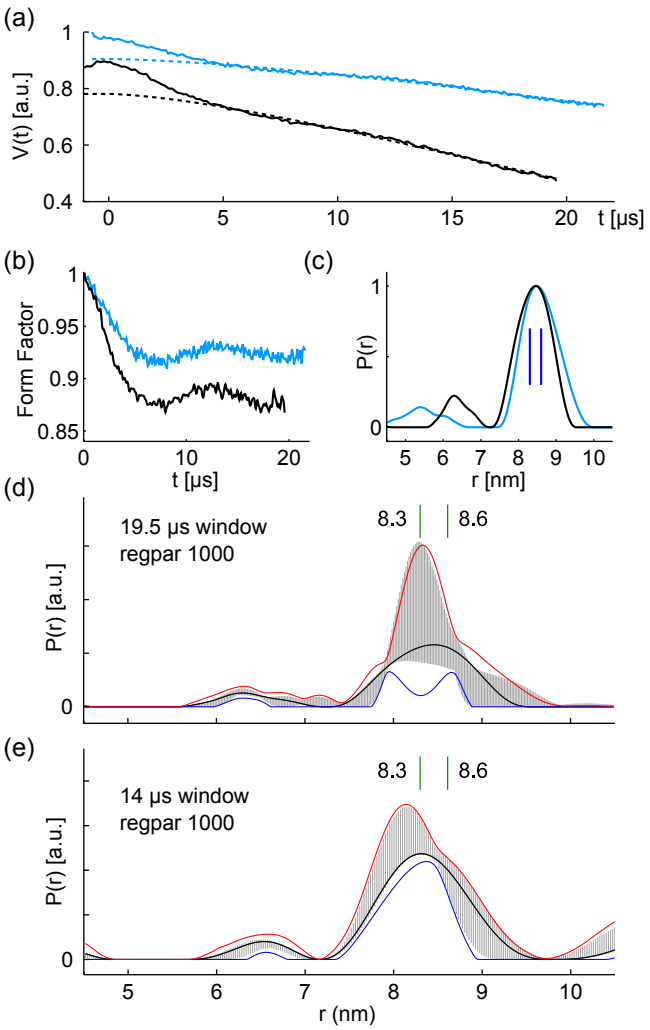

Figure D.17 – Comparison of Gd-ruler $\mathbf{1_{11}}$ data from main text (blue) with supplementary data at higher concentration (black). (a) Primary DEER signal $V(t)$ with vertical displacement. (b) Form factor. (c) Regularized distance distributions with regularization parameter of 1000 in both cases. (d,e) Influence of background parametrization (see Fig. D.16) on distance distribution for the DEER data at full length (d), as well as for data deliberately cut off at 14 μs (e).

Note that for this higher concentrated sample, there is a smaller chance to reproduce the 8.3 nm distance peak reported in [175].

D.6.4 *Persistence length calculations*

In analogy to [175], the distance expectations are based on the formula

$$R = \sqrt{2 \cdot l_{ps}(T_g) \cdot l_{ct} - 2 \cdot l_{ps}(T_g)^2 \cdot (1 - e^{-l_{ct}/l_{ps}(T_g)})} \tag{D.1}$$

$$l_{ps}(T_g) = l_{ps}(246\ \mathrm{K})\ \frac{246\ \mathrm{K}}{T_g} \tag{D.2}$$

where $l_{ps}(246\ \mathrm{K}) = 16.7$ nm [157]. Note that Eq. (D.2) assumes that the bending modulus of the compound is not influenced by temperature, the choice of the spin label, and the interaction of the side chains with the solvent. With the Gd-rulers diluted in a 1:1 mixture of D_2O and glycerol-d_8, a glass transition temperature of T_g = 164 K is assumed based on the value reported for a 1:1 mixture of H_2O and glycerol [215]. Note that there probably is a residual difference between protonated and deuterated solvents [216]. As a result, a persistence length of $l_{ps}(164\ \mathrm{K})$ = 25.05 nm is obtained. Altogether,

the expected distances are 6.0 nm, 7.2 nm, and 8.5 nm and illustrated together with the distance distributions in the main text in Fig. 6.11c. Within the approximations of the distance prediction and experimental uncertainty, the agreement between experimental data and expected distances is sufficient. Note that in a recent study [175], the expected distances were slightly different due to a different mixture of D_2O and glycerol-d_8.

D.7 GD DEER WITH MONOCHROMATIC PULSES

D.7.1 *Single pump pulse*

This section presents results obtained with monochromatic pump pulses. In particular, the importance of observation of the central peak of the spectrum is underlined. This scheme was already proposed in [143] and verified experimentally at W-band in [175]. Fig. D.18 shows experimental results for Gd-ruler $\mathbf{1_3}$. The utilized experimental schemes are illustrated in panel a. Scheme I and II represent those cases, where the central peak is pumped and observed with a spacing of 160 MHz, whereas scheme III involves a pump pulse 300 MHz away from the center. The primary DEER signals are shown in panel b and reveal that the echo signal increases in ascending order when going from scheme I to scheme III. Panel c shows that the situation is reverse for the modulation depth, which increases in ascending order when going from scheme III to scheme I. Distance domain data in panel d are in sufficient agreement.
If only the modulation depth is considered, one would promote scheme I as the best of the three cases, since it has twice the modulation depth. The distinct nuclear modulations observed with scheme I are an indication of

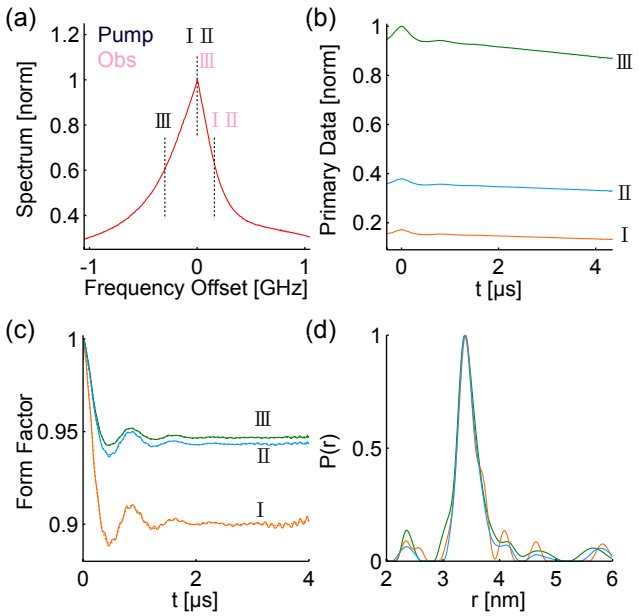

Figure D.18 – Different DEER schemes with monochromatic pulses. (a) Illustration of the applied schemes using the echo-detected field-sweep cast in frequency scale (red). Scheme I and II have a spacing of 160 MHz between pump and observation frequencies. Scheme III has a spacing of 300 MHz. Observation pulses were all 12 ns. Pump pulses were 3 ns (Scheme I), 14 ns with sinusoidal edge smoothing during 2 ns (Scheme II), and 8 ns with sinusoidal smoothing during 4 ns, thus an entirely sine shaped pulse (Scheme III). (b) DEER signals $V(t)$ obtained with the three different schemes according to the indicated labeling and coloring. The same coloring is used in (c) and (d), where form factors and distance distributions are illustrated. All data were acquired with 33 scans and the primary data obtained with schemes I and II were divided by two due to a gain setting 6 dB above the setting used for Scheme III.

overlapping pulses, which is to no surprise with a 3 ns short pump pulse. Note that the modulation depth achieved here is comparable to the modulation depth reported in [79] using an 8 ns pump pulse. The deviations in pump pulse durations are due to differences in ZFS. The experiments in [79] employed Gd-DOTA spin labels, whose central line shows less broadening than for Gd-PyMTA employed in our DEER experiments. In any case, scheme I performs the worst in terms of DEER sensitivity η. Even scheme II outperforms scheme I, since the doubling of the modulation depth with scheme I is entirely compensated by the difference in echo intensity. Highest sensitivity is obtained with scheme III, which has the smallest modulation depth among the three schemes.

D.7.2 *Consecutive pump pulses*

In order to enhance the sensitivity with rectangular pulses, monochromatic rectangular pulses may also be applied consecutively spanning different frequency windows, as demonstrated in the main text using chirp pulses. We noted a hypothesis about such a scheme in [167]. Moreover, a related approach has been demonstrated in [83], where a single multi-frequency pulse was used. Also with consecutive monochromatic pulses, one might be confronted with the choice of pulse parameters, such that a fast optimization of η_{2P} is appropriate.
We chose to sweep the offset frequency between the pump and the observation pulses as well as the pulse length of the pump pulse. The pulse amplitude was set to the maximum and one could in principle vary also the pulse amplitude. The resulting η_{2P} maps are shown in Fig. D.19, for one single pump pulse (top) as well as for two consecutive pump pulses (bottom). Note that the curved features seen in both figures are due to the dependence of V_0/V_{ref} on the pulse parameters, while the modulation depth λ_{2P} is a rather smooth function (data not shown). Moreover, the characteristic obtained with one single pulse is also observed with consecutive pulses, but imposed with additional *wiggles*. An important precaution related to this η_{2P} experiment is the variation of the pulse length t_p, which changes the zero-time of the DEER signal. If t_p is to be varied over a larger range, this may require extra consideration.
Based on η_{2P}, we chose a pump pulse with 4.5 ns length and an offset frequency of -250 MHz. Fig. D.20 shows the DEER results for one single pulse

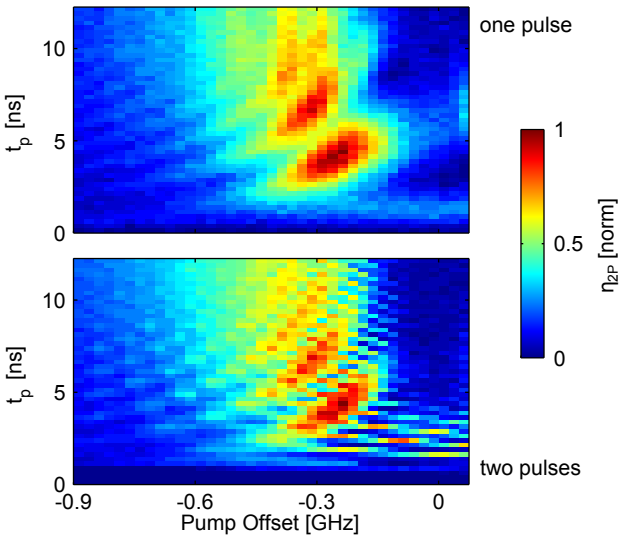

Figure D.19 – Optimization of monochromatic pulses with η_{2P} by variation of the spacing between pump and observation frequencies and pulse length. Top: One single pulse. Bottom: Consecutive pulses. There is no relation between the colors amongst the two figures.

(gray) and consecutive pulses (black). The form factor in panel (a) shows modulation depths of 7% and 12%, respectively, and distance distributions in panel (b) are of sufficient agreement. The echo intensities V_0/V_{ref} are 0.76 and 0.7, respectively. In comparison to the consecutive chirp pulse data in the main text, the consecutive monochromatic pulses achieve 0.83 times the sensitivity of the consecutive chirp pulses. Furthermore, the sensitivity obtained with one single chirp pulse is comparable to the sensitivity reported here for consecutive rectangular pulses.

In terms of sensitivity, consecutive monochromatic pulses are therefore quite competitive, at least with our experimental setup. However, data quality is influenced by pulse overlap. Artifacts towards the end of the form factor as well as at $t = \tau_1$ are readily observed as spikes in the single pulse data. It appears that with two pulses these effects can be partially compensated. Nevertheless, significant nuclear modulation remains also for consecutive pulses, which requires nuclear modulation averaging.

To illustrate the pulse overlap, we simulated the inversion profile of a 4.5 ns long monochromatic pulse subject to the an idealized resonator with quality factor of 110 at 34.25 GHz and shortest π pulse of 3.3 ns, as deduced from experimental data. For simplicity, a spin of $S = 1/2$ is considered. As the resulting inversion profile in Fig. D.21 shows, the pump pulse results in considerable excitation around the center frequency. The asymmetry in the profile originates from the resonator.

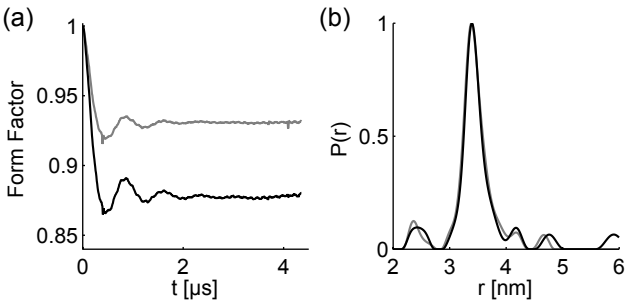

Figure D.20 – DEER results for monochromatic pump pulses, either one single pulse (gray) or consecutive pulses (black) with pulse lengths of 4.5 ns and an offset of −250 MHz. (a) Form factor. (b) Regularized distance distributions. 30 scans each.

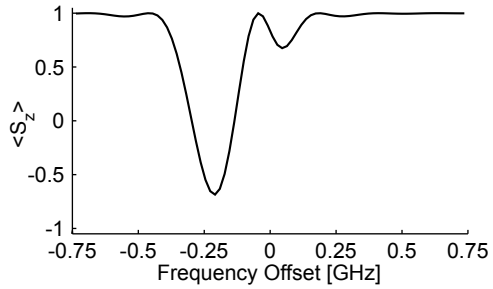

Figure D.21 – Inversion profile of a 4.5 ns monochromatic pulse for a spin $S = 1/2$ and a resonator parametrized by a quality factor of 110 at 34.25 GHz and shortest π pulse of 3.3 ns. The frequency of the pulse is at an offset of −250 MHz.

D.8 SUPPLEMENTARY SIMULATIONS

D.8.1 *Simulation method*

This section gives further insight into the spin dynamics simulations performed in this work. In all simulations, a single effective spin $S = 7/2$ with Zeeman and zero-field splitting (ZFS) is considered. Powder averages include averaging over orientations as well as over ZFS parameters D and E. The Hamiltonian for this system is derived using analytical formulas for third order perturbation [151, 152]. The grids for averaging over orientation and ZFS parameters are exactly the same as those described in our previous work on population transfer [137], therefore having $10 \times 15 \times 20 \times 20$ dimensions for D, E, θ, and ϕ, respectively. Note that in this work, we considered the entire set of Hamiltonians for simulation, which results in 60000 parameters to simulate one echo. For the ZFS parameters of the Gd-PyMTA spin labels, we used μ_D = 1.2 GHz and σ_D = 0.24 GHz. For Gd-DOTA spin labels, we used μ_D = 0.6 GHz and σ_D = 0.12 GHz.
Propagation of the spin density in Hilbert space is performed with the software package SPIDYAN (SPIn DYnamics ANalysis)[1], where a sampling rate of 24 GS/s was used for discretization of time. The simulated pulse sequence is illustrated in Fig. D.22. In the top graph, the pulse amplitude ν_1 is illustrated. The three short *sticks* represent the $\pi/2$ and π pulses, which all have a duration of 12 ns. The timing parameters of the sequence are τ_1 = 400 ns and τ_2 = 4 μs. The 192 ns long pump pulse starts at t' = 40 ns. The curvature in the amplitude is due to the resonator, which enhances the field amplitude towards the center frequency of the resonator. The idealized resonator used in the simulation is parameterized by a quality factor of 110 at 34.3 GHz with shortest π pulse of 3.1 ns on the CT. In the bottom graph, the corresponding frequency modulation function is shown. The frequency modulation of the pump pulse is a non-linear function of time in order to compensate for the resonator profile [74].

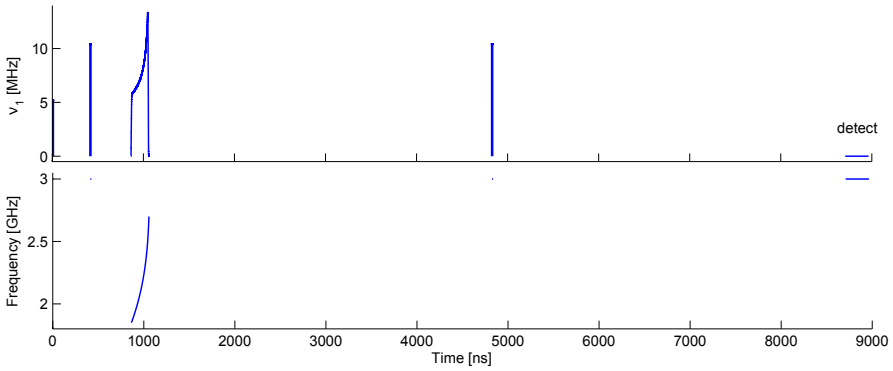

Figure D.22 – Simulated pulse sequence for 192 ns long 850 MHz chirp with −300 MHz offset from the observer spins.

Propagation at the sampling rate of 24 GS/s is only performed during the pulses using precomputed matrix propagators, whereas the gaps in-between pulses are propagated in one single step. During detection, which is indicated at the very end of the illustrated sequence, the density matrix is again computed for each time step and detection operators are applied. Unless explicitly indicated otherwise, we use the $\hat{S}_+$ operator on the CT for detection. Satellite transitions were therefore excluded in the detection process[2]. With a rotating frame Zeeman frequency of 3 GHz, the detected echo signals were

[1] See http://www.epr.ethz.ch/software/index
[2] $\hat{S}_+$ of the CT's neighbor transitions were also calculated. The echo contributions on these satellites did not depend significantly on parameters of the pump pulse. The reason for this is the narrow spectral extent of orientations which show contributions of satellite transitions to the spin echo at the central line of the spectrum.

downconverted and filtered. Magnitude and phase were extracted by integration of the echo for 12 ns around the refocusing position. As a reference value V_{ref} for magnitude and phase, the echo was simulated with a pump pulse of close to zero amplitude.
Downconverted and filtered echo signals obtained in this way are shown in Fig. D.23. Panel (a) shows echoes averaged over ten D values, which describe a Gaussian distribution parametrized by μ_D = 1.2 GHz and σ_D = 0.24 GHz (see Section C.6 for discretization of E values and orientation). The vertically offset echo traces correspond to different frequency offsets f_2 between pump and observation pulses. The step size is 100 MHz and a few values of f_2 are indicated. The green bar on the top and the bottom of the graph indicates the 12 ns long integration window that results in the data shown in Figs. 6.5a and c of the main text. On a DELL precision T1700 computer using MATLAB R2014b, the simulation of one such echo takes on the order of 2.8 hours.
Panels b and c show data extracted from the same simulation, but without averaging over D values. In this way, the dependence of echo parameters on the splitting parameter D can be accessed. In the data for the two different D values, the reduced grid size explains the larger *noise* contributions. Note that phase cycling on the short 12 ns refocusing pulses may be used to improve data quality on these smaller grid sizes at minimum computational effort. In this work, the phase cycling capability of SPIDYAN was not used. The EPR spectrum related to D = 1 GHz is shown in the main text in Fig. 6.5d.
Echo intensities extracted for a large range of D values from 0.15 GHz to 2.5 GHz are shown in Fig. 6.6 of the main text. The relative echo intensity V_0/V_{ref} is shown below in Fig. D.24 and complements the discussion in the main text. The effects observed in absolute echo intensities for small $D < 0.4$

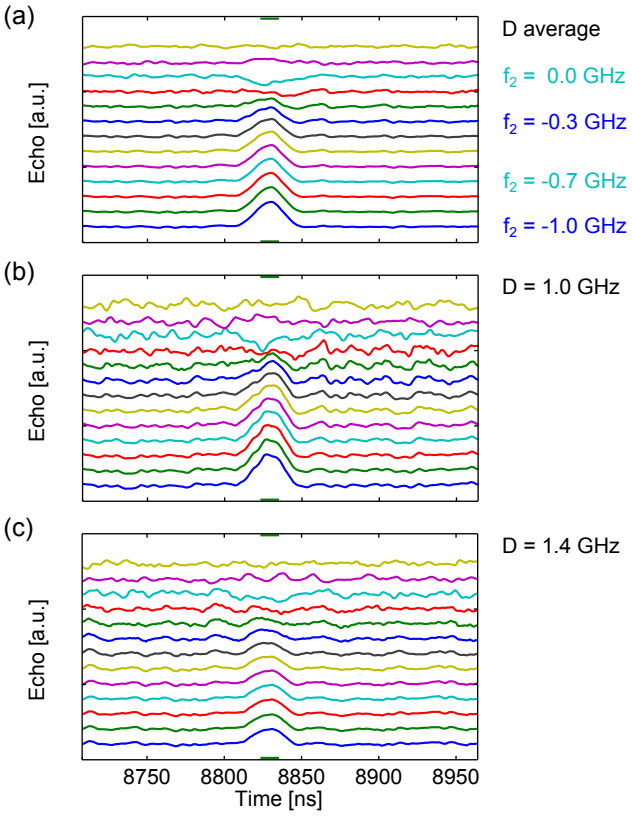

Figure D.23 – Simulated echoes for average over D values with μ_D = 1.2 GHz and σ_D = 0.24 GHz (a) and two selected D values (b,c). The numerous traces in each graph represent different offset frequencies f_2 between pump and observation frequencies. In panel (a) some of these frequencies are labeled. The step size of f_2 is 100 MHz. The echo integration window is indicated by the green bars on the top and bottom of each graph. The integrated echo intensities of this simulation are shown in Figs. 6.5a and c of the main text.

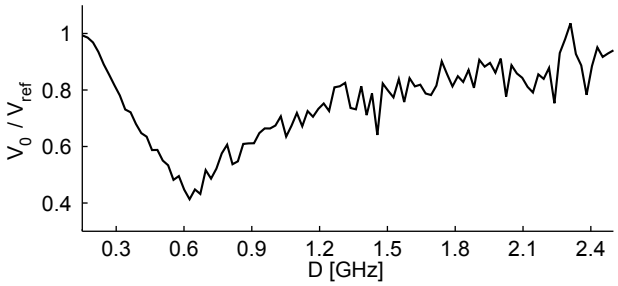

Figure D.24 – Normalized echo intensity V_0/V_{ref} related to Fig. 6.6 of the main text.

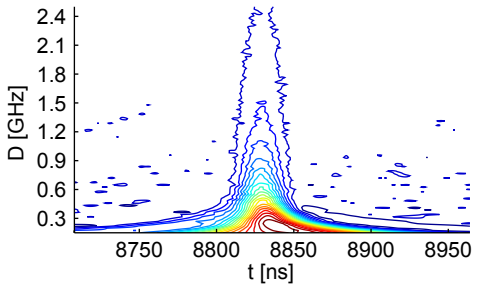

Figure D.25 – Refocused echo transient as a function of D value, where each D value represents a powder spectrum averaged over orientation and E values (see Fig. 6.5d of the main text).

GHz are illustrated in Fig. D.25 by means of echo transients in the absence of the pump pulse. The increase of the echo intensity with D can readily be seen. On a close look, a delay in the echo refocusing time can be identified for small D values. Furthermore, the contour lines level off at the smallest D values. We ascribe these observations to changes in transition moments in the regime where the field strength ν_1 becomes comparable to the splitting parameter D. Transition-selective excitation is no longer predominant in this regime.

D.8.2 *Compensation mechanisms of echo reduction with consecutive pulses*

Two potential effects which explain the behavior of the echo intensity V_0/V_{ref} with consecutive pulses are underlined with spin dynamics simulations. The first effect is the generation of triple-quantum coherence and the second effect is echo dephasing by spatial inhomogeneity in ν_1.
For the former effect, we simulated the pulse sequence with the second pump pulse added and extracted the generated triple-quantum coherence by taking the absolute value of the $\hat{S}^+$ operator of the $3/2 \leftrightarrow -3/2$ transition. The result is shown in black in Fig. D.26a and also shown is reference data obtained with only one single pump pulse (gray). Clearly, the second pulse leads to increased triple-quantum coherence generation. When looking at the difference between the two curves shown in panel (b), the characteristic does qualitatively agree to the (inverted) V_0/V_{ref} curve for one single pump pulse shown above in Fig. D.24. This indicates that triple-quantum coherence is generated by subsequent inversion of the CT's neighbor transitions. As discussed in the main text, this effect can explain why the echo intensity does not decrease when adding a second pump pulse. However, triple-quantum coherence generation cannot result in an increase in echo intensity when adding a second pump pulse.
In order to study the effect related to spatial inhomogeneities in ν_1, the dynamical Bloch-Siegert phase induced by the pump pulse needs to be taken into consideration. Fig. D.27a shows experimental (solid) and simulated

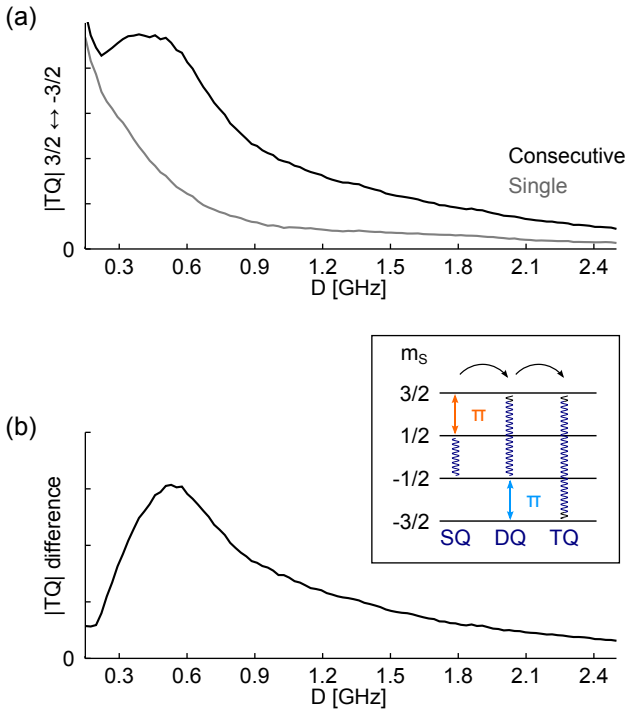

Figure D.26 – Triple-quantum (TQ) generation with consecutive chirp pulses. (a) Absolute value of triple-quantum coherence with one and two chirps having t_p = 192 ns, Δf = 850 MHz and $|f_2|$ = 300 MHz. (b) Difference between the two curves in panel (a) (consecutive minus single pulse data). Inset: Illustration of the triple-quantum coherence generation process showing only the relevant m_S energy levels. The first pulse (orange) here perfectly inverts the upper neighbor transition and therefore transfers single-quantum (SQ) coherence on the CT to double-quantum (DQ) coherence. The second pulse (blue) perfectly inverts the lower neighbor transition and transfers DQ to TQ coherence.

(solid with dots) phases for Gd-PyMTA (black) and Gd-DOTA (gray) as a function of the pump offset frequency f_2. Note that in the main text, the corresponding real and imaginary components as well as the magnitudes are illustrated in Fig. 6.5. For reasonably large offsets $|f_2|$, the simulations reproduce the trends observed in the experiments. Interestingly, the Bloch-Siegert phase appears to depend on the ZFS splitting, because Gd-PyMTA experiences a larger shift than Gd-DOTA. We have not further investigated this effect. Probably it is related to the spectral width of the observed spin packet. Note that the kink at an offset frequency f_2 close to 0 in the simulations of Gd-PyMTA and Gd-DOTA are due to problems related to phase unwrapping in data processing (removal of phase discontinuities).

One aspect worth considering is whether there is any spectral dephasing of the echo due to the Bloch-Siegert shift. For this purpose, we repeated the simulation for Gd-PyMTA in absence of any connectivity between the energy levels. This was implemented by considering only a spin of $S = 1/2$ with Zeeman frequencies distributed according to the CT resonance frequencies of the Hamiltonian calculated for the $S = 7/2$ system including the ZFS splitting. In Fig. D.27b, the resulting magnitude of V_0/V_{ref} is shown. As is readily seen, there is almost no *spectral dephasing* of the echo in the case of a spatially homogeneous field ν_1 (see [177] for examples of spectral dephasing due to Bloch-Siegert shifts)). In such a case, compensation of the dynamical phase shift by application of consecutive chirp pulses cannot result in larger echo intensity, as experimentally observed above in Fig. D.7.

In a related study of distance measurements between a Gd(III) center and a nitroxide with a monochromatic pump pulse [170], such spectral dephasing was found to be important. In that study, however, the observation and pump positions were both located on the satellite shoulders of the Gd(III) spectrum (due to pumping of the nitroxide). In such a situation, effects related to the

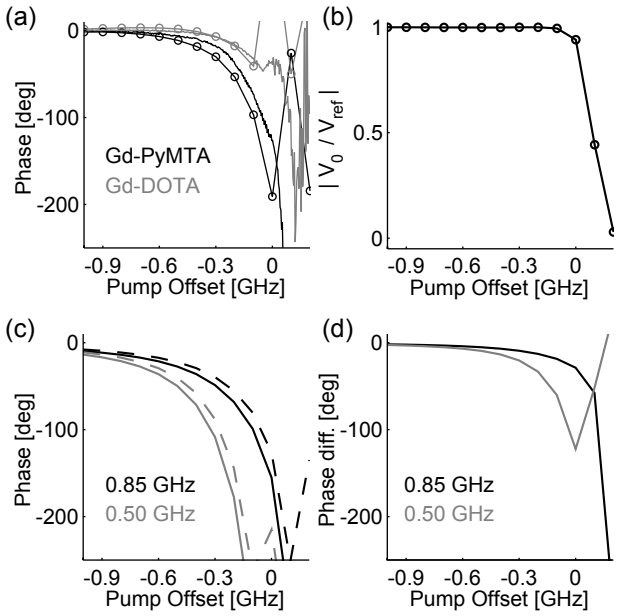

Figure D.27 – Bloch-Siegert phase shift and spatial inhomogeneity in ν_1. (a) Phase of echo signal V_0/V_{ref} as a function of the pump offset frequency f_2 for Gd-PyMTA (black) and Gd-DOTA (gray). Simulated data points are indicated by circles. Magnitudes and real/imaginary components are shown in Fig. 6.5 of the main text. (b) Simulation of echo magnitude $|V_0/V_{\text{ref}}|$ as a function of the pump offset frequency f_2 by considering exclusively the CT of the Gd(III) high spin with pulse parameters Δf = 850 MHz and $t_{\text{p}} = 192$ ns. (c) Simulated echo phase as a function of f_2 for a pump pulse with Δf = 500 MHz (gray) and Δf = 850 MHz (black). Solid curves represent data with shortest π pulse of 3.1 ns. Dashed curves correspond to a 10% lower amplitude in ν_1, thus a shortest π pulse of 3.5 ns. (d) Phase difference between the data in panel (c) for Δf = 500 MHz (gray) and Δf = 850 MHz (black). The difference is obtained by subtraction of the data with the lowered ν_1 from the data with the stronger ν_1. The simulations for the $S = 1/2$ case (b,c,d) were computed using a sampling rate of 12 GS/s for time discretization.

level connectivity of the Gd(III) high-spin state are not important, because the neighbor transitions of the observed satellites are spread far away from the pump frequency. Nevertheless, the results in that study indicate that the absence of spectral dephasing of the echo with a chirp pump pulse may be specific to frequency-swept excitation or to our experimental parameters.

The situation is different if one considers a spatial distribution of field strengths ν_1, which results in a spatial distribution of dynamical phases induced by the chirp pulse [35, 60]. We considered this aspect by simulating the phase shift for two different field amplitudes ν_1, again for $S = 1/2$ in order to exclude effects originating from the level connectivity. Resulting echo phases simulated for chirp pulses with Δf = 500 MHz (gray) and with Δf = 850 MHz (black) are shown in Fig. D.27c. Solid lines have the typical field strength ν_1 used throughout this work, whereas dashed lines have the field strength reduced by 10%.

The Bloch-Siegert phase shift due to the Δf = 500 MHz pulse is larger than the shift due to the Δf = 850 MHz pulse, which is explained by the larger adiabaticity with Δf = 500 MHz. Moreover, the phase shift depends on the field strength ν_1, as seen by the smaller phase shift of the dashed lines compared to the solid lines. We did not investigate in detail the scaling of the dynamical phase shift with the field strength. Based on our previous work [35], we would expect an almost linear dependence between the echo phase and the adiabaticity of the pulse, and therefore a square dependence on ν_1.

In order to illustrate the concept of echo dephasing by inhomogeneities in ν_1, the phase difference between the solid and dashed lines in panel (c) are

shown in panel (d). Here, one observes that a larger phase difference is accumulated with $\Delta f = 500$ MHz than with $\Delta f = 850$ MHz. Note that the sudden jumps observed in some of the phases shown in panels (c) and (d) are due to problems with phase unwrapping (removal of phase discontinuities). Neglecting these discontinuities, we find that the echo phase for a chirp pulse with $\Delta f = 500$ MHz is more sensitive to spatial inhomogeneities than a pulse with $\Delta f = 850$ MHz. At an offset of $f_2 = -100$ MHz for instance, our simulation reveals a spatial variation in the echo phase by 60° for a spatial variation of 10% in ν_1 with $\Delta f = 500$ MHz. At the same frequency offset, the $\Delta f = 850$ MHz pulse introduces a spatial variation on the order of 19°. The actual effect on the echo intensity depends on the spatial distribution in ν_1. The interested reader finds further considerations in the SI of our previous work [35].

Spatial inhomogeneities in ν_1 could therefore explain why consecutive pulses compensate for echo reduction effects at small Δf, which is observed experimentally (see Fig. D.7 as well as Figs. D.6 and 6.7a). From this point of view, the second consecutive pump pulse reverts the spatial phase distribution induced by the first pulse. Experimentally, we can only access the spatially averaged echo phase, which is indeed almost left unchanged when applying consecutive chirp pulses (see Fig. 6.7b). The actual spatial field distribution inside our resonator is not known. Therefore, we can not verify whether or not this compensation mechanism is responsible for the experimental observations.

In summary, inhomogeneity in ν_1 is the only effect accessible by our set of simulations that explains the increase in echo signal when adding a second consecutive pump pulse. Since our simulation only considers an isolated $S = 7/2$ spin system, it may well be possible that there are other compensation mechanisms. In particular, coupling to other spins is expected to alter the spin dynamics for offset frequencies $|f_2|$ which are on the order of the coupling strength. Under this assumption, it is only at small offset frequencies $|f_2| < 100$ MHz, where such additional effects could take place.

E

DATA REFERENCE

In order to find out where the data origins, the following table gives information about all the figures that illustrate experimental and simulated data. Figures *drawn by hand* for illustration purposes or to describe chemical structures or electronic circuits are not listed here. Some paths are abbreviated by the name tags summarized below

tag	path
AWGSPEC	./MATLAB/HACK/MEX/ADQ412/testing/test_impl
Gd-DEER1	./20130516_GdQ/20140723_measwithniwi_andbeyond
Gd-DEER2	./20130516_GdQ
HSn	./teaching/2015_FS_Andreas/andreas_windowsdata/simulations

Table E.1 – Name tags for abbreviating long file paths

item	*path*	*description*
Fig 2.2	./20140320_spidyansims/20151222_passage_eigenvalues	passage_eig.m for panels b and d
Fig 2.2c	./20120509_chirp_simulations/inv_rec_tempol_3	Figure 11 from hid_traces.m, run with either $\nu_1 = 62.5$ MHz and by this value reduced by $\sqrt{2}$ for half the adiabaticity
Fig 2.3	./20140320_spidyansims/20151222_passage_eigenvalues	passage_eig.m for panels a and b
Fig 2.3c	*AWGSPEC*/20141120_sensup/20150202_Herasil_1st	vis_chirp_inversion_thintthick.m
Fig 2.4	./20140320_spidyansims/20151222_passage_eigenvalues	Mz_inv.m for panels a and b, Mz_inv_hardop5.m for panel c, Mz_coh.m for panel d
Fig 2.5	./20140320_spidyansims/ adiabaticity_Q_sims	robustenss.m
Fig 3.1	./20120509_chirp_simulations/inv_rec_tempol_3	Figures 1, 6, 10 and 11 from hid_traces.m
Fig 3.3	./20120509_chirp_simulations/inv_rec_tempol_3	Figure 54 from vis_model.m for panel a, Figure 1 from nonlinearity.m for panel b
Fig 3.4	./20120509_chirp_simulations/inv_rec_tempol_3	alph_prim.m for panel a, sca_prim.m for panels b and c, offs_prim.m for panel d
Fig 3.5	./20120509_chirp_simulations/inv_rec_tempol_3	kk_lorentianoverlay for panels a-c, alph_sim_pub.m for panel d, sca_sim.m for panel e, offs_sim.m for panel f
Fig 3.6	./20120509_chirp_simulations/inv_rec_tempol_3	Figures 10, 12, 13, 11 from adaptation_figs.m for panels a-d, respectively
Fig 3.7a	./20120509_chirp_simulations/inv_rec_tempol_2	Figure 7 from ir_eval.m, see path of panel b for relevant svg source file
Fig 3.7b	./20120509_chirp_simulations/inv_rec_tempol_3	Figure 8 from ir_eval_2D_fit.m, also pub_relsignorm.svg for panel b

Fig 3.8	./20120509_chirp_simulations/cu2_deer_3	vis_model_cu_3.m for panel a, Figures 81-83 from deer_2Dfin_set_best.m for panels b-d, mod_enhancement.m for panel e
Fig 3.9	./20120509_chirp_simulations/cu2_deer_6	Figure 20, 21 and 23 from compare_expcond_pub.m
Fig 4.1	*AWGSPEC*/20130729_chirptest/20131126_tempol	Figure 5 of second cell of vis_chirpcals.m
Fig 4.2	*AWGSPEC*/20130729_chirptest/20131126_tempol	vis_fstepnut_p1_scalist_pub.m for panel a, vis_adaptation.m for panel c, vis_fdom1_bwc_unc_AP_FP.m and vis_fdom2_cecho_opts.m to obtain panels b and d
Fig 4.3	*AWGSPEC*/20130729_chirptest/20131126_tempol	vis_adaptation.m for panel a, vis_cecho_PUB.m for panels b-d
Fig 4.4	*AWGSPEC*/20130729_chirptest/20131126_tempol	Figure 34 and 12 from vis_cecho_t2_pub.m
Fig 4.5	*AWGSPEC*/20130729_chirptest/20131206_copper	Figures 13 and 14 from vis_cecho_pub.m for panels a, b and d, vis_fieldsweep.m for inset in a, vis_cecho_t2.m for panel c
Fig 4.6	*AWGSPEC*/20130729_chirptest/20140224_1mtempol_equivalence	Figure 22 from vis_cecho_ir_fit_pub_up.m and vis_updown_comparison.m
Fig 4.7	*AWGSPEC*/20130729_chirptest/20140305_1mtempol_equivalence	vis_cecho_ir_nucmod.m
Fig 5.1	20140320_spidyansims/perturbdozer_sims	Gd_bulldozer_single_pub.m
Fig 5.2	20140320_spidyansims/perturbdozer_sims	Figure 9, 10 and 20 from vis_Gd_bulldozer_powder_pub.m
Fig 5.4	*Gd-DEER1*/20140804_3p5nm_pDEER	vis_model_gdgd_pub.m for panel a, Figure 1 and 2 from vis_poltrans_pub.m for panels b and c
Fig 5.5	*Gd-DEER1*/20140804_3p5nm_pDEER	Figure 3 and 4 from second cell of vis_poltrans_pub.m
Fig 5.6	*Gd-DEER1*/20140807_bulldozer_variousZFS/	vis_poltrans.m in subfolders ./dota/ and ./dtpa/
Fig 5.7	*Gd-DEER1*/20140804_3p5nm_pDEER	Figure 18-20 from vis_pdeer_pub.m
Fig 6.2b	*Gd-DEER1*/20140326_3p5nm_strongpump_and_compensation	vis_echored_centobs_pub.m
Fig 6.2	*Gd-DEER1*/20140326_3p5nm_strongpump_and_compensation/deer_rlc_centobs	Figure 53, 7, 5 and 6 from pub_fig_adiaby.m for panels a, c-e
Fig 6.3	*Gd-DEER1*/20150123_3p5nm sample_2pointagain/34GHz_exp	vis_singlepulse_2point.m
Fig 6.4	*Gd-DEER1*/20140305_3p5nm_sample	pub_fig_centpump.m
Fig 6.5	20140320_spidyansims/perturbdozer_sims	Figure 14, 15, 17 (first occurrence), 23 from vis_deerechoredv2_allsimsunified.m for panels a-d
Fig 6.6	20140320_spidyansims/perturbdozer_sims	Figure 12 from vis_deerechoredv2_pub_range_24GHz.m

Fig 6.7	20140320_spidyansims/ perturbdozer_sims	Figure 17 (second occurrence), 19 (second occurrence) from vis_deerechoredv2_allsimsunified.m
Fig 6.8	*Gd-DEER1*/ 20140528_3p5nm_doubledeer	pub_deer_set128.m
Fig 6.9	*Gd-DEER1*/20150123_3p5nm sample_2pointagain/34GHz_exp	vis_singlevspatch_2point.m
Fig 6.10a	*Gd-DEER1*/ 20150114_GDMQ6nm	pub_fig_modloss_6nm.m
Fig 6.10b	*Gd-DEER1*/ 20150121_GDMQ6nm_2Ptau2	vis_2P_mod_relaxation.m
Fig 6.11	*Gd-DEER1*/ 20150121_GDMQ8p5nm_smp2	vis_6nmandlonger_pub.m
Fig 7.4	*AWGSPEC*/20141120_sensup/ 20151130_Herasil_SNRstdX2	vis_fstepnut_p1_pub.m for panel a, vis_echocmp_pub.m for panels b - d
Fig 7.5	*AWGSPEC*/20141120_sensup/ 20151201_Herasil_SNRstdQ3	vis_fstepnut_p1.m for panel a, vis_echocmp_pub.m for panels b - d
Fig 7.6	*AWGSPEC*/20141120_sensup/ 20151021_Herasil_SNRstdX	vis_fstepnut_all.m
Fig 7.7	./20121102_hwcals/ 20151008_resonatorscaling	nitroxide_opt_X_diss.m and nitroxide_opt_Q_diss.m
Fig 7.8	./20121102_hwcals/ 20151008_resonatorscaling	refecho_12ns_respars.m for panel a and compensation.m for panel b
Fig 8.1	*Gd-DEER1*/ 20151104_CIDME_3p4nm	vis_CIDME_scheme.m for generation of panels b and c
Fig 8.2	*Gd-DEER1*/ 20151104_CIDME_3p4nm	vis_echored_pub.m for generation of panel a
Fig 8.3	*Gd-DEER1*/ 20151104_CIDME_3p4nm	pub_cidme_centpump.m for generation of panels a and b
Fig 8.4	*Gd-DEER1*/ 20151104_CIDME_3p4nm	pub_cidme_vs_deer.m for generation of panels a and b
Fig 8.5	*Gd-DEER1*/ 20151106_CIDME_2p1nm	pub_cidme_short.m for generation of panels a and b
Fig 8.6	*Gd-DEER2*/20140422_GdNo_ triradical_Qband	vis_exp_1.m for plot of spectra and resonator
Fig 8.7	*Gd-DEER2*/20140422_GdNo_ triradical_Qband	sim_GdNo_3spin.m, figure(106)
Fig 8.8	*Gd-DEER2*/20140422_GdNo_ triradical_Qband	DEER_set_new_pub.m, figure(1)
Fig 8.9	*Gd-DEER2*/20140422_GdNo_ triradical_Qband	plot_and_sim_T_and_P_pub.m for generation of all panels
Fig 8.10	*HSn*/	ando_HS1vslin.m for simulation and figure generation of all four panels
Fig 8.11	*HSn*/	ando_HSnvslin.m for simulation and figure generation of all four panels
Fig 8.12	*HSn*/	ando_vis_multipletesting_summary.m for figure generation of all panels. Polynomials for optimum β, t_{rise} and N_{WURST} are computed in vis_multipletesting_HS1.m, vis_multipletesting_rise.m and vis_multipletesting_WURST.m (variables beta_pol, tr_pol and N_pol)
Fig 8.13	*AWGSPEC*/20141120_sensup/ 20150511_MSA236_biradical	vis_fdom2_HS1_swp_pub.m produces all four panels
Fig 8.14	*AWGSPEC*/20140523_takCuPic/ 20140825_70dg_9p5GHz_20K	vis_fieldsweep_talk for panel a, vis_cecho_t2_chirp_diss for panel b

Fig 8.15	*AWGSPEC*/20140523_takCuPic/20140825_70dg_9p5GHz_20K	vis_cecho_t2_chirp_diss for the 2D EPR/ESEEM spectrum
Fig 8.16	*AWGSPEC*/20141120_sensup/20150911_Qtest	vis_cecho_PUB.m produces panels b - d
Fig 8.17	*AWGSPEC*/20141120_sensup/20150911_Qtest	vis_cecho_t2_pub.m produces panels a - b, vis_cecho_t2_chirp_talk.m for panel c
Fig 8.18a	*AWGSPEC*/20130729_chirptest/20140224_1mtempol_equivalence	vis_cecho_ir_fit_pub_up.m, figures 55 and 155
Fig 8.18b	*AWGSPEC*/20141120_sensup/20150911_Qtest	vis_cecho_ir_fit_pub.m, figures 55 and 155
Fig 8.19	./20121102_hwcals/20151008_resonatorscaling	nitroxide_freq_X_diss.m and nitroxide_freq_Q_diss.m
Fig 8.20	*AWGSPEC*/20141120_sensup/20150917_QDEER5_MSA236	vis_cecho_swps_modcomp.m for panel a and vis_deer_boxcar.m for panel b
Fig 8.22	*AWGSPEC*/20141120_sensup/20150917_QDEER5_MSA236	vis_sift_ft_quick_nucavg.m
Fig 8.23	*AWGSPEC*/20141120_sensup/20150917_QDEER5_MSA236	vis_sift_ft_quick_nucavg.m
Fig A.1	./20120509_chirp_simulations/inv_rec_tempol_3	Figure 79 from kk_lorentianoverlay_impresp.m
Fig A.2	./20121102_hwcals/20121115_nutationday241/relax	Figure 4 and 5 from vis_relax.m
Fig A.3	./20120509_chirp_simulations/cu2_deer_6	kk_lorentianoverlay.m for panel a, compare_adiab.m for panel c, Figure 9 from compare_expcond_pub.m for panel d
Fig A.3b	./20120509_chirp_simulations/cu2_deer_5	kk_lorentianoverlay.m
Fig B.2a	./20120509_chirp_simulations/inv_rec_tempol_3	adaptation_figs.m
Fig B.2b	./20121102_hwcals/20121101_f241_nutationday	vis_adaptation_pub.m
Fig B.2c	*AWGSPEC*/20130729_chirptest/20130806_cavity1tempol	vis_adaptation.m
Fig B.2d	*AWGSPEC*/20130729_chirptest/20131206_copper	vis_adaptation_pub.m
Fig B.3	*AWGSPEC*/20130729_chirptest/20130806_cavity1tempol	vis_fdom7_linup_grd.m for panel a, vis_cecho_t2.m for panel c, vis_fdom6_optpulses.m for panel b and d and vis_fdom3_uncmp_vs_comp for chirp data of panel d
Fig B.4a,b	*AWGSPEC*/20130729_chirptest/20131126_tempol	vis_fdom2_cecho_opts.m and vis_cecho_swps_pub.m
Fig B.4c,d	*AWGSPEC*/20130729_chirptest/20131206_copper	vis_fdom1_bwc_unc_AP_FP.m and vis_cecho_swps_pub.m
Fig B.5a	*AWGSPEC*/20130729_chirptest/20131126_tempol	Figure 35 from vis_cecho_t2.m
Fig B.5	*AWGSPEC*/20130729_chirptest/20131206_copper	Figure 12 and 35 from vis_cecho_t2.m for panels b and c, respectively
Fig B.6a	*AWGSPEC*/20130729_chirptest/20131220_100utempol	Figure 13 from vis_cecho_t2_pub_short.m
Fig B.6b	*AWGSPEC*/20130729_chirptest/20131126_tempol	Figure 13 from vis_cecho_t2_pub_short.m

Fig B.7	*AWGSPEC*/20130729_chirptest/20131126_tempol	vis_cecho_PUB.m
Fig B.8	*AWGSPEC*/20130729_chirptest/20140311_1mtempol_rectnucmodt1	Figures 10-12 from vis_cecho_ir_nucmod_rect.m for panels a-c
Fig B.8d	*AWGSPEC*/20130729_chirptest/20140305_1mtempol_equivalence	Figure 2 from vis_cecho_ir_nucmod.m
Fig C.2a	*Gd-DEER1*/20130710_qbandawg/prototype6/recovered_sample	vis_poltrans.m
Fig C.2b	*Gd-DEER1*/20130710_qbandawg/prototype6/0715/IQpoltrns	vis_poltrans.m
Fig C.3	*Gd-DEER1*/20140508_3p5nm_pDEER	vis_iqopt.m
Fig C.4	*Gd-DEER1*/20141110_ bulldozer_wrapup	vis_holeburn.m
Fig C.5a	*Gd-DEER1*/20140804_3p5nm_pDEER	vis_heating.m
Fig C.5b	*Gd-DEER1*/20140509_3p5nm_pDEER	temperature_pub.m
Fig C.6	*Gd-DEER1*/20140804_3p5nm_pDEER	vis_heating.m
Fig C.7	*Gd-DEER1*/20141110_ bulldozer_wrapup	vis_srtpol.m
Fig C.8	*Gd-DEER1*/20140804_3p5nm_pDEER	Figure 3 and 4 from third cell of vis_poltrans_pub.m
Fig C.9	*Gd-DEER1*/20140804_3p5nm_pDEER	Figure 18-20 from vis_pdeer_pub.m
Fig C.10	*Gd-DEER1*/20140509_3p5nm_pDEER	Figure 8-10 from vis_pdeer_pub.m
Fig C.11	*Gd-DEER1*/ 20130826_qbandawg/MQ_poltrns_1	Figure 8-10 from vis_pdeer_pub.m
Fig C.12	20140320_spidyansims/ perturbdozer_sims	Figure 9 from vis_Gd_bulldozer_powder_pub.m for panels c (4th cell) and a (8th cell, running Gd_spec_perturb.m before hand with the appropriate parameters), Figure 21 from Gd_spec_eigvals_transprob_longcomp.m for panel b (load 20140625_gd_spec_eigvals_trans_longcomp.mat before)
Fig C.13	20140320_spidyansims/ perturbdozer_sims	Figure 11 from vis_Gd_bulldozer_powder_pub.m for panel a, Figure 10 and 20 from vis_Gd_bulldozer_powder_ud_pub.m for panels b and c, where panel b requires also the up-chirp data from vis_Gd_bulldozer_powder_pub.m
Fig C.14	20140320_spidyansims/ perturbdozer_sims	Figure 21 from vis_Gd_bulldozer_powder_pub.m
Fig D.1	*Gd-DEER1*/ 20140326_3p5nm_strongpump_and_ compensation/deer_rlc_centobs	Figure 10, 41, 11 and 12 from pub_fig_adiaby.m for panels a, c-e
Fig D.1b	20140320_spidyansims/ perturbdozer_sims	Figure 117 from vis_deerechoredv2_pub_24GHz_256_750.m

Fig D.2	*Gd-DEER1*/20150123_3p5nm sample_2pointagain/34GHz_exp	vis_ered_2D_3p5nm_34G_adiacontour.m with the appropriate source files
Fig D.3	20140320_spidyansims/ perturbdozer_sims	Figure 30 and 31 from vis_deerechoredv2_pub_range_24GHz.m
Fig D.4	*Gd-DEER1*/20150123_3p5nm sample_2pointagain/34GHz_exp	vis_ered_2D_3p5nm_34G_adiacontour.m
Fig D.5	*Gd-DEER1*/ 20150114_GDMQ6nm	vis_ered_2D_6nm.m
Fig D.5	*Gd-DEER1*/ 20150205_GdMQ7p3nm_downconc	vis_ered_2D_7p3.m
Fig D.5	*Gd-DEER1*/ 20150121_GDMQ8p5nm_smp2	vis_ered_2D_8p5.m
Fig D.6a	*Gd-DEER1*/ 20150121_GDMQ6nm_2Ptau2	Figure 11 from vis_ered_2D_cmp_6nmsmps.m
Fig D.6b	*Gd-DEER1*/ 20150121_GDMQ8p5nm_smp2	Figure 9 from vis_ered_2D_cmp_8p5nm.m
Fig D.7	*Gd-DEER1*/ 20150121_GDMQ8p5nm_smp2	Figure 4 from vis_ered_2D_cmp_8p5nm.m
Fig D.8	*Gd-DEER1*/ 20140305_3p5nm_sample	pub_fig_centpump_SI.m
Fig D.9	*Gd-DEER1*/ 20150112_3p5nm_rescentpump	vis_deer_set_64nsrlc.m
Fig D.10	*Gd-DEER1*/ 20140305_3p5nm_sample	pub_fig_RIDMEcmp_10K.m and pub_fig_RIDMEcmp_20K.m
Fig D.11	*Gd-DEER1*/ 20140528_3p5nm_doubledeer	pub_deer_set128.m and pub_deer_set64.m
Fig D.12a	*Gd-DEER1*/ 20150114_GDMQ6nm	pub_fig_modloss_6nm.m
Fig D.12b,c	*Gd-DEER1*/ 20150122_GDMQ6nm_concser	vis_2P_comparison.m
Fig D.12d,e	*Gd-DEER1*/ 20150120_GDMQ7p3nm_2	vis_2P_mod_relaxation.m
Fig D.13a	*Gd-DEER1*/ 20150313_GdMQ6nm_Tmod	vis_T2.m
Fig D.13b	*Gd-DEER1*/ 20150205_GdMQ7p3nm_downconc	vis_deerecho.m
Fig D.13c	*Gd-DEER1*/ 20141217_GDMQ8p5nm_2	vis_deerecho.m
Fig D.14	*Gd-DEER1*/20150123_3p5nm sample_2pointagain/ 20150130_rect2P_try	vis_somedeerdistrs.m
Fig D.15	*Gd-DEER1*/ 20141219_GDMQ4p7nm	vis_4p7nm_longtaumeas.m
Fig D.16	*Gd-DEER1*/ 20150121_GDMQ8p5nm_smp2	vis_validation.m
Fig D.17	*Gd-DEER1*/ 20150121_GDMQ8p5nm_smp2	vis_8p5nmcmp_pub.m for panels a-c, vis_validation_other8p5nmsample.m for panels d-e
Fig D.18	*Gd-DEER1*/ 20140305_3p5nm _sample/Weekend_20140308	talk_best_mod_cmp.m
Fig D.19	*Gd-DEER1*/20150123_3p5nm sample_2pointagain/ 20150130_rect2P_try	vis_ered_2D_rect.m
Fig D.20a	*Gd-DEER1*/ 20140326_3p5nm _strongpump_and_ compensation/deer_rlc_centobs	Figure 51 from pub_fig_adiaby.m

Fig D.20	*Gd-DEER1*/20150123_3p5nm sample_2pointagain/ 20150130_rect2P_try	vis_deerrect_dta.m
Fig D.21	./20140320_spidyansims/ adiabaticity_Q_sims	Sz_profile_rect.m
Fig D.22	20140320_spidyansims/ perturbdozer_sims	Figure 1 and 2 from vis_deerechoredv2_pub_range_24GHz.m
Fig D.23	20140320_spidyansims/ perturbdozer_sims	Figure 66 (three times) from vis_deerechoredv2_pub_range_24GHz.m
Fig D.24	20140320_spidyansims/ perturbdozer_sims	Figure 112 (first occurrence) from vis_deerechoredv2_pub_range_24GHz.m
Fig D.25	20140320_spidyansims/ perturbdozer_sims	Figure 78 from vis_deerechoredv2_pub_range_24GHz.m
Fig D.26	20140320_spidyansims/ perturbdozer_sims	Figure 120 and 121 from vis_deerechoredv2_pub_range_24GHz.m
Fig D.27	20140320_spidyansims/ perturbdozer_sims	Figure 19 (first occurrence), 201, 202, 203 from vis_deerechoredv2_allsimsunified.m for panels a-d

F

BIBLIOGRAPHY

[1] J. R. Klauder, A. C. Price, S. Darlington, and W. J. Albersheim. The theory and design of chirp radars. *Bell Syst. Tech. J.*, 39:745–808, 1960.

[2] Gordon G. Brown, Brian C. Dian, Kevin O. Douglass, Scott M. Geyer, Steven T. Shipman, and Brooks H. Pate. A broadband Fourier transform microwave spectrometer based on chirped pulse excitation. *Rev. Sci. Instrum.*, 79:053103, 2008.

[3] G. Barratt Park and Robert W. Field. Edge effects in chirped-pulse Fourier transform microwave spectra. *J. Mol. Spectrosc.*, 312:54 – 57, 2015.

[4] Michael Garwood and Lance DelaBarre. The return of the frequency sweep: Designing adiabatic pulses for contemporary NMR. *J. Magn. Reson.*, 153:155 – 177, 2001.

[5] Niels Chr. Nielsen, Cindie Kehlet, Steffen J. Glaser, and Navin Khaneja. *Encyclopedia of Magnetic Resonance*, chapter Optimal Control Methods in NMR Spectroscopy. Wiley, 2010.

[6] Thomas Wacker. *FID-detektiertes spektrales Lochbrennen in der Elektronen-Spin-Resonanz*. PhD thesis, Diss. Naturwiss. ETH Zürich, Nr. 9913. Ref.: A. Schweiger; Korref.: RR Ernst, 1992.

[7] Richard H Crepeau, Antonue Dulic, Jeff Gorcester, Timothy R Saarinen, and Jack H Freed. Composite pulses in time-domain ESR. *J. Magn. Reson.*, 84:184 – 190, 1989.

[8] Thomas Prisner and Klaus-Peter Dinse. ESR with stochastic excitation. *J. Magn. Reson.*, 84:296 – 308, 1989.

[9] N. Devasahayam, R. Murugesan, K. Matsumoto, J.B. Mitchell, J.A. Cook, S. Subramanian, and M.C. Krishna. Tailored sinc pulses for uniform excitation and artifact-free radio frequency time-domain EPR imaging. *J. Magn. Reson.*, 168:110 – 117, 2004.

[10] Jonathan Stuart Hodges. *Engineering coherent control of quantum information in spin systems*. PhD thesis, Massachusetts Institute of Technology, 2007.

[11] J. S. Hodges, J. C. Yang, C. Ramanathan, and D. G. Cory. Universal control of nuclear spins via anisotropic hyperfine interactions. *Phys. Rev. A*, 78:010303, Jul 2008.

[12] G. D. Fuchs, V. V. Dobrovitski, D. M. Toyli, F. J. Heremans, and D. D. Awschalom. Gigahertz dynamics of a strongly driven single quantum spin. *Science*, 326:1520–1522, 2009.

[13] K. Wago, D. Botkin, C. S. Yannoni, and D. Rugar. Force-detected electron-spin resonance: Adiabatic inversion, nutation, and spin echo. *Phys. Rev. B*, 57:1108–1114, 1998.

[14] Daniel Rugar, R Budakian, HJ Mamin, and BW Chui. Single spin detection by magnetic resonance force microscopy. *Nature*, 430:329–332, 2004.

[15] Philipp E. Spindler, Yun Zhang, Burkhard Endeward, Naum Gershernzon, Thomas E. Skinner, Steffen J. Glaser, and Thomas F. Prisner. Shaped optimal control pulses for increased excitation bandwidth in EPR. *J. Magn. Reson.*, 218:49 – 58, 2012.

[16] A. Abragam. *Principles of Nuclear Magnetism*. Oxford University Press, USA, 1983.

[17] Malcolm H Levitt. *Spin dynamics: Basics of nuclear magnetic resonance*. John Wiley & Sons, 2001.

[18] A. Schweiger and G. Jeschke. *Principles of Pulse Electron Paramagnetic Resonance*. Oxford University Press, USA, 2001.

[19] Michael Deschamps, Gwendal Kervern, Dominique Massiot, Guido Pintacuda, Lyndon Emsley, and Philip J. Grandinetti. Superadiabaticity in magnetic resonance. *J. Chem. Phys.*, 129:204110, 2008.

[20] Stephan Pribitzer, Andrin Doll, and Gunnar Jeschke. SPIDYAN, a MATLAB library for simulating pulse EPR experiments with arbitrary waveform excitation. *J. Magn. Reson.*, 263:45 – 54, 2016.

[21] F. Bloch. Nuclear induction. *Phys. Rev.*, 70:460–474, 1946.

[22] R. K. Wangsness and F. Bloch. The dynamical theory of nuclear induction. *Phys. Rev.*, 89:728–739, 1953.

[23] Alfred G Redfield. On the theory of relaxation processes. *IBM J. Res. Dev.*, 1:19–31, 1957.

[24] M Goldman. Introduction to some basic aspects of NMR. Technical report, CEA Centre d'Etudes de Saclay, 91-Gif-sur-Yvette (France). Dept. de Recherche sur l'Etat Condense, les Atomes et les Molecules, 1992.

[25] Malcolm H. Levitt. *Encyclopedia of Magnetic Resonance*, chapter Composite Pulses. John Wiley & Sons, Ltd, 2007.

[26] A.J. Shaka. Composite pulses for ultra-broadband spin inversion. *Chem. Phys. Lett.*, 120:201 – 205, 1985.

[27] J. Baum, R. Tycko, and A. Pines. Broadband and adiabatic inversion of a two-level system by phase-modulated pulses. *Phys. Rev. A*, 32:3435–3447, 1985.

[28] J. M. Böhlen and G. Bodenhausen. Experimental aspects of chirp NMR spectroscopy. *J. Magn. Reson.*, 102:293 – 301, 1993.

[29] E. Kupĉe and R. Freeman. Adiabatic pulses for wideband inversion and broadband decoupling. *J. Magn. Reson.*, 115:273 – 276, 1995.

[30] M.S Silver, R.I Joseph, and D.I Hoult. Highly selective $\pi/2$ and π pulse generation. *J. Magn. Reson.*, 59:347 – 351, 1984.

[31] F. Bloch, W. W. Hansen, and M. Packard. The nuclear induction experiment. *Phys. Rev.*, 70:474–485, 1946.

[32] Sandra S. Eaton and Gareth R. Eaton. Chapter one - rapid-scan EPR of nitroxide spin labels and semiquinones. In Peter Z. Qin and Kurt Warncke, editors, *Electron Paramagnetic Resonance Investigations of Biological Systems by Using Spin Labels, Spin Probes, and Intrinsic Metal Ions, Part A*, volume 563 of *Methods in Enzymology*, pages 3 – 21. Academic Press, 2015.

[33] M. V. Berry. Quantum phase corrections from adiabatic iteration. *Proc. R. Soc. London A: Math., Phys. Eng. Sci.*, 414:31–46, 1987.

[34] Daniel Rosenfeld and Yuval Zur. Is the sech/tanh adiabatic pulse really adiabatic? *J. Magn. Reson.*, 132:102 – 108, 1998.

[35] Gunnar Jeschke, Stephan Pribitzer, and Andrin Doll. Coherence transfer by passage pulses in electron paramagnetic resonance spectroscopy. *J. Phys. Chem. B*, 119:13570–13582, 2015.

[36] Lev D Landau. Zur Theorie der Energieübertragung. II. *Physics of the Soviet Union*, 2:28, 1932.

[37] Clarence Zener. Non-adiabatic crossing of energy levels. *Proc. R. Soc. London A: Math., Phys. Eng. Sci.*, 137:696–702, 1932.

[38] ECG Stueckelberg. Theory of inelastic collisions between atoms (theory of inelastic collisions between atoms, using two simultaneous differential equations). *Helv. Phys. Acta, (Basel)*, 5:369–422, 1932.

[39] Ettore Majorana. Atomi orientati in campo magnetico variabile. *Il Nuovo Cimento*, 9:43–50, 1932.

[40] Francesco Di Giacomo and Evgenii E Nikitin. The Majorana formula and the Landau-Zener-Stückelberg treatment of the avoided crossing problem. *Physics-Uspekhi*, (5):515, 2005.

[41] J. W. Zwanziger, S. P. Rucker, and G. C. Chingas. Measuring the geometric component of the transition probability in a two-level system. *Phys. Rev. A*, 43:3232–3240, 1991.

[42] Josef W. Zwanziger, Ulrike Werner-Zwanziger, and Frank Gaitan. Non-adiabatic rapid passage. *Chem. Phys. Lett.*, 375:429 – 434, 2003.

[43] Kent R. Thurber and Robert Tycko. Theory for cross effect dynamic nuclear polarization under magic-angle spinning in solid state nuclear magnetic resonance: The importance of level crossings. *J. Chem. Phys.*, 137:084508, 2012.

[44] Mathieu Munsch, Gunter Wüst, Andreas V Kuhlmann, Fei Xue, Arne Ludwig, Dirk Reuter, Andreas D Wieck, Martino Poggio, and Richard J Warburton. Manipulation of the nuclear spin ensemble in a quantum dot with chirped magnetic resonance pulses. *Nature nanotech.*, 9:671–675, 2014.

[45] Eriks Kupĉe and Ray Freeman. Optimized adiabatic pulses for wideband spin inversion. *J. Magn. Reson. A*, 118:299 – 303, 1996.

[46] Alberto Tannús and Michael Garwood. Improved performance of frequency-swept pulses using offset-independent adiabaticity. *J. Magn. Reson. A*, 120:133 – 137, 1996.

[47] Michael Garwood and Yong Ke. Symmetric pulses to induce arbitrary flip angles with compensation for RF inhomogeneity and resonance offsets. *J. Magn. Reson.*, 94:511 – 525, 1991.

[48] J. A. Ferretti and R. R. Ernst. Interference effects in NMR correlation spectroscopy of coupled spin systems. *J. Chem. Phys.*, 65:4283–4293, 1976.

[49] J. Haase, M.S. Conradi, C.P. Grey, and A.J. Vega. Population transfers for NMR of quadrupolar spins in solids. *J. Magn. Reson. A*, 109:90 – 97, 1994.

[50] Kyryl Kobzar, Thomas E. Skinner, Navin Khaneja, Steffen J. Glaser, and Burkhard Luy. Exploring the limits of broadband excitation and inversion pulses. *J. Magn. Reson.*, 170:236 – 243, 2004.

[51] Kyryl Kobzar, Thomas E. Skinner, Navin Khaneja, Steffen J. Glaser, and Burkhard Luy. Exploring the limits of broadband excitation and inversion: II. Rf-power optimized pulses. *J. Magn. Reson.*, 194:58 – 66, 2008.

[52] Mari A Smith, Haitao Hu, and A.J Shaka. Improved broadband inversion performance for NMR in liquids. *J. Magn. Reson.*, 151:269 – 283, 2001.

[53] Douglas Brown. Constant amplitude broadband refocusing pulses from numerical optimization. *Magn. Reson. Chem.*, 49:705–709, 2011.

[54] Thomas E. Skinner, Kyryl Kobzar, Burkhard Luy, M. Robin Bendall, Wolfgang Bermel, Navin Khaneja, and Steffen J. Glaser. Optimal control design of constant amplitude phase-modulated pulses: Application to calibration-free broadband excitation. *J. Magn. Reson.*, 179:241 – 249, 2006.

[55] Naum I. Gershenzon, Thomas E. Skinner, Bernhard Brutscher, Navin Khaneja, Manoj Nimbalkar, Burkhard Luy, and Steffen J. Glaser. Linear phase slope in pulse design: Application to coherence transfer. *J. Magn. Reson.*, 192:235 – 243, 2008.

[56] Dietmar Kunz. Frequency-modulated radiofrequency pulses in spin-echo and stimulated-echo experiments. *Magn. Reson. Med.*, 4:129–136, 1987.

[57] J. M. Böhlen, Martial Rey, and Geoffrey Bodenhausen. Refocusing with chirped pulses for broadband excitation without phase dispersion. *J. Magn. Reson.*, 84:191 – 197, 1989.

[58] Michael Braun and Steffen J. Glaser. Cooperative pulses. *J. Magn. Reson.*, 207:114 – 123, 2010.

[59] Lyndon Emsley and Geoffrey Bodenhausen. Phase shifts induced by transient Bloch-Siegert effects in NMR. *Chem. Phys. Lett.*, 168:297 – 303, 1990.

[60] Kristin E. Cano, Mari A. Smith, and A.J. Shaka. Adjustable, broadband, selective excitation with uniform phase. *J. Magn. Reson.*, 155:131 – 139, 2002.

[61] S.N. Shevchenko, S. Ashhab, and Franco Nori. Landau-Zener-Stückelberg interferometry. *Phys. Rep.*, 492:1 – 30, 2010.

[62] Yosuke Kayanuma. Phase coherence and nonadiabatic transition at a level crossing in a periodically driven two-level system. *Phys. Rev. B*, 47:9940–9943, 1993.

[63] VF Yudanov, KM Salikhov, GM Zhidomirov, and Yu D Tsvetkov. Effect of the magnetic nuclei of a matrix to the form of decay in spin-echo signal in free radicals. *J. Strukt. Khim*, 10:732–734, 1969.

[64] Takuya F. Segawa, Andrin Doll, Stephan Pribitzer, and Gunnar Jeschke. Copper ESEEM and HYSCORE through ultra-wideband chirp EPR spectroscopy. *J. Chem. Phys.*, 143:044201, 2015.

[65] M Pannier, S Veit, A Godt, G Jeschke, and H.W Spiess. Dead-time free measurement of dipole-dipole interactions between electron spins. *J. Magn. Reson.*, 142:331 – 340, 2000.

[66] Gunnar Jeschke and Yevhen Polyhach. Distance measurements on spin-labelled biomacromolecules by pulsed electron paramagnetic resonance. *Phys. Chem. Chem. Phys.*, 9:1895–1910, 2007.

[67] Daniel R. Kattnig, Jörg Reichenwallner, and Dariush Hinderberger. Modeling excluded volume effects for the faithful description of the background signal in double electron-electron resonance. *J. Phys. Chem. B*, 117:16542–16557, 2013.

[68] Gunnar Jeschke. DEER distance measurements on proteins. *Annu. Rev. Phys. Chem.*, 63:419–446, 2012.

[69] G Jeschke, G Panek, A Godt, A Bender, and H Paulsen. Data analysis procedures for pulse ELDOR measurements of broad distance distributions. *Appl. Magn. Reson.*, 26:223–244, 2004.

[70] Yun-Wei Chiang, Peter P. Borbat, and Jack H. Freed. The determination of pair distance distributions by pulsed ESR using tikhonov regularization. *J. Magn. Reson.*, 172:279 – 295, 2005.

[71] Russell G. Larsen and David J. Singel. Double electron–electron resonance spin–echo modulation: Spectroscopic measurement of electron spin pair separations in orientationally disordered solids. *J. Chem. Phys.*, 98:5134–5146, 1993.

[72] A. Potapov, Y. Song, T.J. Meade, D. Goldfarb, A.V. Astashkin, and A. Raitsimring. Distance measurements in model bis-Gd(III) complexes with flexible bridge. Emulation of biological molecules having flexible structure with Gd(III) labels attached. *J. Magn. Reson.*, 205:38 – 49, 2010.

[73] Gunnar Jeschke, Muhammad Sajid, Miriam Schulte, and Adelheid Godt. Three-spin correlations in double electron-electron resonance. *Phys. Chem. Chem. Phys.*, 11:6580–6591, 2009.

[74] Andrin Doll, Stephan Pribitzer, René Tschaggelar, and Gunnar Jeschke. Adiabatic and fast passage ultra-wideband inversion in pulsed EPR. *J. Magn. Reson.*, 230:27 – 39, 2013.

[75] Gunther H. Rist and James S. Hyde. Ligand ENDOR of metal complexes in powders. *J. Chem. Phys.*, 52:4633–4643, 1970.

[76] Arthur E. Stillman and Robert N. Schwartz. Study of dynamical processes in liquids by electron spin echo spectroscopy. *J. Phys. Chem.*, 85:3031–3040, 1981.

[77] Paul A. S. Cruickshank, David R. Bolton, Duncan A. Robertson, Robert I. Hunter, Richard J. Wylde, and Graham M. Smith. A kilowatt pulsed 94 GHz electron paramagnetic resonance spectrometer with high concentration sensitivity, high instantaneous bandwidth, and low dead time. *Rev. Sci. Instrum.*, 80:103102, 2009.

[78] Igor Tkach, Giuseppe Sicoli, Claudia Höbartner, and Marina Bennati. A dual-mode microwave resonator for double electron-electron spin resonance spectroscopy at W-band microwave frequencies. *J. Magn. Reson.*, 209:341 – 346, 2011.

[79] A. Raitsimring, A. Astashkin, J. Enemark, A. Blank, Y. Twig, Y. Song, and T. Meade. Dielectric resonator for Ka-band pulsed EPR measurements at cryogenic temperatures: Probehead construction and applications. *Appl. Magn. Reson.*, 42:441–452, 2012.

[80] S. Takahashi, L.-C. Brunel, D. T. Edwards, J. van Tol, G. Ramian, S. Han, and M. S. Sherwin. Pulsed electron paramagnetic resonance spectroscopy powered by a free-electron laser. *Nature*, 489:409 – 413, 2012.

[81] Sushil K. Misra, Harvey A. Buckmaster, Edward Reijerse, Sankaran Subramanian, and Murali C. Krishna. Spectrometers. In Sushil K. Misra, editor, *Multifrequency Electron Paramagnetic Resonance*, pages 115–228. Wiley, 2011.

[82] James S. Hyde, Robert A. Strangeway, Theodore G. Camenisch, Jason W. Sidabras, Richard R. Mett, George A. Rinard, Richard W. Quine, Sandra S. Eaton, and Gareth R. Eaton. Multifrequency EPR: Experimental considerations. In Sushil K. Misra, editor, *Multifrequency Electron Paramagnetic Resonance*, pages 229–294. Wiley, 2011.

[83] Yuki Asada, Risa Mutoh, Masahiro Ishiura, and Hiroyuki Mino. Nonselective excitation of pulsed ELDOR using multi-frequency microwaves. *J. Magn. Reson.*, 213:200 – 205, 2011.

[84] Yingjie Zhang, Colm A. Ryan, Raymond Laflamme, and Jonathan Baugh. Coherent control of two nuclear spins using the anisotropic hyperfine interaction. *Phys. Rev. Lett.*, 107:170503, Oct 2011.

[85] Troy W. Borneman and David G. Cory. Bandwidth-limited control and ringdown suppression in high-Q resonators. *J. Magn. Reson.*, 225:120 – 129, 2012.

[86] Mark Tseitlin, Richard W. Quine, George A. Rinard, Sandra S. Eaton, and Gareth R. Eaton. Digital EPR with an arbitrary waveform generator and direct detection at the carrier frequency. *J. Magn. Reson.*, 213:119 – 125, 2011.

[87] Mark Tseitlin, Richard W. Quine, Sandra S. Eaton, and Gareth R. Eaton. Use of polyphase continuous excitation based on the Frank sequence in EPR. *J. Magn. Reson.*, 211:221 – 227, 2011.

[88] M. Joshi. Ultra wide bandwidth. In *Education Technology and Computer (ICETC), 2010 2nd International Conference*, volume 5, june 2010.

[89] Malcolm H. Levitt. The signs of frequencies and phases in NMR. *J. Magn. Reson.*, 126:164 – 182, 1997.

[90] M. Mehring and J. S. Waugh. Phase transients in pulsed NMR spectrometers. *Rev. Sci. Instrum.*, 43:649–653, 1972.

[91] Thomas M Barbara, Joel F Martin, and Jon G Wurl. Phase transients in NMR probe circuits. *J. Magn. Reson.*, 93:497 – 508, 1991.

[92] A.A.M. Saleh. Frequency-independent and frequency-dependent nonlinear models of TWT amplifiers. *IEEE Trans. Commun.*, 29:1715 –1720, 1981.

[93] Y. Tabuchi, M. Negoro, K. Takeda, and M. Kitagawa. Total compensation of pulse transients inside a resonator. *J. Magn. Reson.*, 204:327 – 332, 2010.

[94] Evelyn Narr, Adelheid Godt, and Gunnar Jeschke. Selective measurements of a nitroxide-nitroxide separation of 5 nm and a nitroxide-copper separation of 2.5 nm in a terpyridine-based copper(II) complex by pulse EPR spectroscopy. *Angew. Chem. Int. Ed. Engl.*, 114:4063–4066, 2002.

[95] G. Jeschke, V. Chechik, P. Ionita, A. Godt, H. Zimmermann, J. Banham, C. Timmel, D. Hilger, and H. Jung. DeerAnalysis2006 - a comprehensive software package for analyzing pulsed ELDOR data. *Appl. Magn. Reson.*, 30:473–498, 2006.

[96] L.O. Chua and C.-Y. Ng. Frequency domain analysis of nonlinear systems: General theory. *IEEE J. Electron. Circuits Systems*, 3:165 –185, july 1979.

[97] A. Gelb and W.E. Vander Velde. *Multiple-input describing functions and nonlinear system design*. McGraw-Hill electronic sciences series. McGraw-Hill, 1968.

[98] J. R. Klauder and P. W. Anderson. Spectral diffusion decay in spin resonance experiments. *Phys. Rev.*, 125:912–932, 1962.

[99] Jack H. Freed. Theory of saturation and double resonance in electron spin resonance spectra. VI. saturation recovery. *J. Phys. Chem.*, 78:1155–1167, 1974.

[100] James S. Hyde. Saturation recovery methodology. In Larry Kevan and Robert N. Schwartz, editors, *Time Domain Electron Spin Resonance*, pages 1–30. Wiley, 1979.

[101] Sandra S. Eaton and Gareth R. Eaton. Saturation recovery EPR. In Sandra R. Eaton, Gareth R. Eaton, and Lawrence J. Berliner, editors, *Biomedical EPR, Part B: Methodology, Instrumentation, and Dynamics*, volume 24/B of *Biological Magnetic Resonance*, pages 3–18. Springer US, 2005.

[102] Arthur Schweiger. Pulsed electron spin resonance spectroscopy: Basic principles, techniques, and examples of applications. *Angew. Chem. Int. Ed. Engl.*, 30:265–292, 1991.

[103] Igor V. Koptyug, Stefan H. Bossmann, and Nicholas J. Turro. Inversion-recovery of nitroxide spin labels in solution and microheterogeneous environments. *J. Am. Chem. Soc.*, 118:1435–1445, 1996.

[104] H. Jäger, A. Koch, V. Maus, H.W. Spiess, and G. Jeschke. Relaxation-based distance measurements between a nitroxide and a lanthanide spin label. *J. Magn. Reson.*, 194:254 – 263, 2008.

[105] J.L. Du, G.R. Eaton, and S.S. Eaton. Temperature, orientation, and solvent dependence of electron spin-lattice relaxation rates for nitroxyl radicals in glassy solvents and doped solids. *J. Magn. Reson. A*, 115:213 – 221, 1995.

[106] J.W. Saalmueller, H.W. Long, G.G. Maresch, and H.W. Spiess. Two-dimensional field-step ELDOR. A method for characterizing the motion of spin probes and spin labels in glassy solids. *J. Magn. Reson. A*, 117:193 – 208, 1995.

[107] Hideo Sato, Steven E. Bottle, James P. Blinco, Aaron S. Micallef, Gareth R. Eaton, and Sandra S. Eaton. Electron spin-lattice relaxation of nitroxyl radicals in temperature ranges that span glassy solutions to low-viscosity liquids. *J. Magn. Reson.*, 191:66 – 77, 2008.

[108] S.A Dzuba, A.G Maryasov, K.M Salikhov, and Yu.D Tsvetkov. Super-slow rotations of nitroxide radicals studied by pulse EPR spectroscopy. *J. Magn. Reson.*, 58:95 – 117, 1984.

[109] A.D. Milov, A.B. Ponomarev, and Yu.D. Tsvetkov. Electron-electron double resonance in electron spin echo: Model biradical systems and the sensitized photolysis of decalin. *Chem. Phys. Lett.*, 110:67 – 72, 1984.

[110] Irene M. C. van Amsterdam, Marcellus Ubbink, Gerard W. Canters, and Martina Huber. Measurement of a Cu-Cu distance of 26 Å by a pulsed EPR method. *Angew. Chem. Int. Ed. Engl.*, 42:62–64, 2003.

[111] Bela E. Bode, Jörn Plackmeyer, Thomas F. Prisner, and Olav Schiemann. PELDOR measurements on a nitroxide-labeled Cu(II) porphyrin: Orientation selection, spin-density distribution, and conformational flexibility. *J. Phys. Chem. A*, 112:5064–5073, 2008.

[112] Christopher W. M. Kay, Hassane El Mkami, Richard Cammack, and Robert W. Evans. Pulsed ELDOR determination of the intramolecular distance between the metal binding sites in dicupric human serum transferrin and lactoferrin. *J. Am. Chem. Soc.*, 129:4868–4869, 2007.

[113] Andrin Doll and Gunnar Jeschke. Fourier-transform electron spin resonance with bandwidth-compensated chirp pulses. *J. Magn. Reson.*, 246:18 – 26, 2014.

[114] Jeff Gorcester and Jack H. Freed. Two-dimensional Fourier transform ESR correlation spectroscopy. *J. Chem. Phys.*, 88:4678–4693, 1988.

[115] Petr P. Borbat, Richard H. Crepeau, and Jack H. Freed. Multifrequency two-dimensional Fourier transform ESR: An X/Ku-band spectrometer. *J. Magn. Reson.*, 127:155 – 167, 1997.

[116] Baldev R. Patyal, Richard H. Crepeau, Dan Gamliel, and Jack H. Freed. Two-dimensional Fourier transform ESR in the slow-motional and rigid limits: SECSY-ESR. *Chem. Phys. Lett.*, 175:445 – 452, 1990.

[117] Jack H. Freed. New technologies in electron spin resonance. *Annu. Rev. Phys. Chem.*, 51:655–689, 2000.

[118] Sushil K. Misra and Jack H. Freed. Molecular motions. In Sushil K. Misra, editor, *Multifrequency Electron Paramagnetic Resonance*, pages 497–544. Wiley, 2011.

[119] Philipp E. Spindler, Steffen J. Glaser, Thomas E. Skinner, and Thomas F. Prisner. Broadband inversion PELDOR spectroscopy with partially adiabatic shaped pulses. *Angew. Chem. Int. Ed.*, 52:3425–3429, 2013.

[120] I Niemeyer, J H Shim, J Zhang, D Suter, T Taniguchi, T Teraji, H Abe, S Onoda, T Yamamoto, T Ohshima, J Isoya, and F Jelezko. Broadband excitation by chirped pulses: Application to single electron spins in diamond. *New J. Phys.*, 15:033027, 2013.

[121] Hua Wu, Erik M. Gauger, Richard E. George, Mikko Möttönen, Helge Riemann, Nikolai V. Abrosimov, Peter Becker, Hans-Joachim Pohl, Kohei M. Itoh, Mike L. W. Thewalt, and John J. L. Morton. Geometric phase gates with adiabatic control in electron spin resonance. *Phys. Rev. A*, 87:032326, 2013.

[122] Thomas Kaufmann, Timothy J. Keller, John M. Franck, Ryan P. Barnes, Steffen J. Glaser, John M. Martinis, and Songi Han. DAC-board based X-band EPR spectrometer with arbitrary waveform control. *J. Magn. Reson.*, 235:95 – 108, 2013.

[123] Florian Dolde, Ville Bergholm, Ya Wang, Ingmar Jakobi, Boris Naydenov, Sébastian Pezzagna, Jan Meijer, Fedor Jelezko, Philipp Neumann, Thomas Schülte-Herbrurg, Jacob Biamonte, and Jörg Wrachtrup. High-fidelity spin entanglement using optimal control. *Nat. Comm.*, 5:3371, 2014.

[124] Rangeet Bhattacharyya and Lucio Frydman. Quadrupolar nuclear magnetic resonance spectroscopy in solids using frequency-swept echoing pulses. *J. Chem. Phys.*, 127:194503, 2007.

[125] Luke A. O'Dell. The WURST kind of pulses in solid-state NMR. *Solid State Nucl. Magn.*, 55-56:28 – 41, 2013.

[126] J. M. Böhlen, I. Burghardt, M. Rey, and G. Bodenhausen. Frequency-modulated chirp pulses for broadband inversion recovery in magnetic resonance. *J. Magn. Reson.*, 90:183 – 191, 1990.

[127] Ronald N. Bracewell. *The Fourier transform and its applications*. McGraw-Hill, 2000.

[128] Geoffrey Bodenhausen, Ray Freeman, and David L Turner. Suppression of artifacts in two-dimensional J spectroscopy. *J. Magn. Reson.*, 27:511 – 514, 1977.

[129] Yoav Shrot and Lucio Frydman. Spatially encoded NMR and the acquisition of 2D magnetic resonance images within a single scan. *J. Magn. Reson.*, 172:179 – 190, 2005.

[130] Kristin E. Cano, Mari A. Smith, and A.J. Shaka. Adjustable, broadband, selective excitation with uniform phase. *J. Magn. Reson.*, 155:131 – 139, 2002.

[131] Kyryl Kobzar, Sebastian Ehni, Thomas E. Skinner, Steffen J. Glaser, and Burkhard Luy. Exploring the limits of broadband 90° and 180° universal rotation pulses. *J. Magn. Reson.*, 225:142 – 160, 2012.

[132] D. I. Hoult and R. E. Richards. The signal-to-noise ratio of the nuclear magnetic resonance experiment. *J. Magn. Reson.*, 24:71–85, 1976.

[133] V.L. Ermakov, J. M. Böhlen, and G. Bodenhausen. Improved schemes for refocusing with frequency-modulated chirp pulses. *J. Magn. Reson. A*, 103:226 – 229, 1993.

[134] Dan Gamliel and Jack H Freed. Theory of two-dimensional ESR with nuclear modulation. *J. Magn. Reson.*, 89:60 – 93, 1990.

[135] Th. Wacker and A. Schweiger. Fourier transform EPR-detected NMR. *Chem. Phys. Lett.*, 186:27 – 34, 1991.

[136] A. M. Raitsimring, K. M. Salikhov, B. A. Umanskii, and Yu. D. Tsvetkov. Instantaneous diffusion in the electron spin echo of paramagnetic centers stabilized in a solid host. *Sov. Phys Solid State*, 16:492, 1974.

[137] Andrin Doll, Mian Qi, Stephan Pribitzer, Nino Wili, Maxim Yulikov, Adelheid Godt, and Gunnar Jeschke. Sensitivity enhancement by population transfer in Gd(III) spin labels. *Phys. Chem. Chem. Phys.*, 17:7334–7344, 2015.

[138] Peter P. Borbat and Jack H. Freed. Pulse dipolar electron spin resonance: Distance measurements. In Christiane R. Timmel and Jeffrey R. Harmer, editors, *Structure and Bonding*, volume 152, pages 1–82. Springer Berlin Heidelberg, 2013.

[139] Arnold M. Raitsimring, Chidambaram Gunanathan, Alexey Potapov, Irena Efremenko, Jan M. L. Martin, David Milstein, and Daniella Goldfarb. Gd3+ complexes as potential spin labels for high field pulsed EPR distance measurements. *J. Am. Chem. Soc.*, 129:14138–14139, 2007.

[140] Daniella Goldfarb. Gd3+ spin labeling for distance measurements by pulse EPR spectroscopy. *Phys. Chem. Chem. Phys.*, 16:9685–9699, 2014.

[141] Andrea Martorana, Giuliano Bellapadrona, Akiva Feintuch, Enza Di Gregorio, Silvio Aime, and Daniella Goldfarb. Probing protein conformation in cells by EPR distance measurements using Gd3+ spin labeling. *J. Am. Chem. Soc.*, 136:13458–13465, 2014.

[142] Mian Qi, Andreas Groß, Gunnar Jeschke, Adelheid Godt, and Malte Drescher. Gd(III)-PyMTA label is suitable for in-cell EPR. *J. Am. Chem. Soc.*, 136:15366–15378, 2014.

[143] A. Raitsimring, A.V. Astashkin, J.H. Enemark, I. Kaminker, D. Goldfarb, E.D. Walter, Y. Song, and T.J. Meade. Optimization of pulsed-DEER measurements for Gd-based labels: Choice of operational frequencies, pulse durations and positions, and temperature. *Appl. Magn. Reson.*, 44:649–670, 2013.

[144] R. V. Pound. Nuclear electric quadrupole interactions in crystals. *Phys. Rev.*, 79:685–702, 1950.

[145] Jürgen Haase and Mark S. Conradi. Sensitivity enhancement for NMR of the central transition of quadrupolar nuclei. *Chem. Phys. Lett.*, 209:287 – 291, 1993.

[146] Renée Siegel, Thomas T. Nakashima, and Roderick E. Wasylishen. Sensitivity enhancement of NMR spectra of half-integer quadrupolar nuclei in the solid state via population transfer. *Concept Magn. Reson. A*, 26:47–61, 2005.

[147] Philipp Schöps, Philipp E. Spindler, Andriy Marko, and Thomas F. Prisner. Broadband spin echoes and broadband SIFTER in EPR. *J. Magn. Reson.*, 250:55 – 62, 2015.

[148] A.A. Dubinskii, Yu.A. Grishin, A.N. Savitsky, and K. Möbius. Submicrosecond field-jump device for pulsed high-field eldor. *Appl. Magn. Reson.*, 22(3):369–386, 2002.

[149] Ilia Kaminker, Alexey Potapov, Akiva Feintuch, Shimon Vega, and Daniella Goldfarb. Population transfer for signal enhancement in pulsed EPR experiments on half integer high spin systems. *Phys. Chem. Chem. Phys.*, 11:6799–6806, 2009.

[150] Yevhen Polyhach, Enrica Bordignon, René Tschaggelar, Sandhya Gandra, Adelheid Godt, and Gunnar Jeschke. High sensitivity and versatility of the DEER experiment on nitroxide radical pairs at Q-band frequencies. *Phys. Chem. Chem. Phys.*, 14:10762–10773, 2012.

[151] E. Meirovitch and R. Poupko. Line shape studies of the electron spin resonance spectra of manganese protein complexes. *J. Phys. Chem.*, 82:1920–1925, 1978.

[152] George H. Reed and George D. Markham. EPR of Mn(II) complexes with enzymes and other proteins. In Lawrence J. Berliner and Jacques Reuben, editors, *Biological Magnetic Resonance*, pages 73–142. Springer US, 1984.

[153] E. Van Veenendaal, B. H. Meier, and A. P. M. Kentgens. Frequency stepped adiabatic passage excitation of half-integer quadrupolar spin systems. *Mol. Phys.*, 93:195–213, 1998.

[154] Raj K Gupta, James A Ferretti, and Edwin D Becker. Rapid scan Fourier transform NMR spectroscopy. *J. Magn. Reson.*, 13:275 – 290, 1974.

[155] A.M. Raitsimring, A.V. Astashkin, O.G. Poluektov, and P. Caravan. High-field pulsed EPR and ENDOR of Gd3+ complexes in glassy solutions. *Appl. Magn. Reson.*, 28:281–295, 2005.

[156] Adelheid Godt, Miriam Schulte, Herbert Zimmermann, and Gunnar Jeschke. How flexible are poly(para-phenyleneethynylene)s? *Angew. Chem. Int. Ed.*, 45:7560–7564, 2006.

[157] Gunnar Jeschke, Muhammad Sajid, Miriam Schulte, Navid Ramezanian, Aleksei Volkov, Herbert Zimmermann, and Adelheid Godt. Flexibility of shape-persistent molecular building blocks composed of p-phenylene and ethynylene units. *J. Am. Chem. Soc.*, 132:10107–10117, 2010.

[158] Luca Garbuio, Enrica Bordignon, Evan K. Brooks, Wayne L. Hubbell, Gunnar Jeschke, and Maxim Yulikov. Orthogonal spin labeling and Gd(III)-nitroxide distance measurements on bacteriophage T4-lysozyme. *J. Phys. Chem. B*, 117(11):3145–3153, 2013.

[159] Petra Lüders, Heidrun Jäger, Marcus A. Hemminga, Gunnar Jeschke, and Maxim Yulikov. Distance measurements on orthogonally spin-labeled membrane spanning walp23 polypeptides. *J. Phys. Chem. B*, 117(7):2061–2068, 2013.

[160] Maxim Yulikov, Petra Lüders, Muhammad Farooq Warsi, Victor Chechik, and Gunnar Jeschke. Distance measurements in Au nanoparticles functionalized with nitroxide radicals and Gd3+-DTPA chelate complexes. *Phys. Chem. Chem. Phys.*, 14:10732–10746, 2012.

[161] Sahand Razzaghi, Mian Qi, Anna I. Nalepa, Adelheid Godt, Gunnar Jeschke, Anton Savitsky, and Maxim Yulikov. RIDME spectroscopy with Gd(III) centers. *J. Phys. Chem. Lett.*, 5:3970–3975, 2014.

[162] Petra Lüders, Gunnar Jeschke, and Maxim Yulikov. Double electron-electron resonance measured between Gd3+ ions and nitroxide radicals. *J. Phys. Chem. Lett.*, 2(6):604–609, 2011.

[163] Maxim Yulikov. Spectroscopically orthogonal spin labels and distance measurements in biomolecules. In *Electron Paramagnetic Resonance*, volume 24, pages 1–31. The Royal Society of Chemistry, 2015.

[164] Andrin Doll, Mian Qi, Nino Wili, Stephan Pribitzer, Adelheid Godt, and Gunnar Jeschke. Gd(III)-Gd(III) distance measurements with chirp pump pulses. *J. Magn. Reson.*, 259:153 – 162, 2015.

[165] Devin T. Edwards, Zhidong Ma, Thomas J. Meade, Daniella Goldfarb, Songi Han, and Mark S. Sherwin. Extending the distance range accessed with continuous wave EPR with Gd3+ spin probes at high magnetic fields. *Phys. Chem. Chem. Phys.*, 15:11313–11326, 2013.

[166] Alexey Potapov, Hiromasa Yagi, Thomas Huber, Slobodan Jergic, Nicholas E. Dixon, Gottfried Otting, and Daniella Goldfarb. Nanometer-scale distance measurements in proteins using Gd3+ spin labeling. *J. Am. Chem. Soc.*, 132:9040–9048, 2010.

[167] Y. Song, T.J. Meade, A.V. Astashkin, E.L. Klein, J.H. Enemark, and A. Raitsimring. Pulsed dipolar spectroscopy distance measurements in biomacromolecules labeled with Gd(III) markers. *J. Magn. Reson.*, 210:59 – 68, 2011.

[168] Michal Gordon-Grossman, Ilia Kaminker, Yana Gofman, Yechiel Shai, and Daniella Goldfarb. W-band pulse EPR distance measurements in peptides using Gd3+-dipicolinic acid derivatives as spin labels. *Phys. Chem. Chem. Phys.*, 13:10771–10780, 2011.

[169] Hiromasa Yagi, Debamalya Banerjee, Bim Graham, Thomas Huber, Daniella Goldfarb, and Gottfried Otting. Gadolinium tagging for high-precision measurements of 6 nm distances in protein assemblies by EPR. *J. Am. Chem. Soc.*, 133:10418–10421, 2011.

[170] Ilia Kaminker, Hiromasa Yagi, Thomas Huber, Akiva Feintuch, Gottfried Otting, and Daniella Goldfarb. Spectroscopic selection of distance measurements in a protein dimer with mixed nitroxide and Gd3+ spin labels. *Phys. Chem. Chem. Phys.*, 14:4355–4358, 2012.

[171] Erez Matalon, Thomas Huber, Gregor Hagelueken, Bim Graham, Veronica Frydman, Akiva Feintuch, Gottfried Otting, and Daniella Goldfarb. Gadolinium(III) spin labels for high-sensitivity distance measurements in transmembrane helices. *Angew. Chem. Int. Ed.*, 52:11831–11834, 2013.

[172] Ilia Kaminker, Igor Tkach, Nurit Manukovsky, Thomas Huber, Hiromasa Yagi, Gottfried Otting, Marina Bennati, and Daniella Goldfarb. W-band orientation selective DEER measurements on a Gd3+/nitroxide mixed-labeled protein dimer with a dual mode cavity. *J. Magn. Reson.*, 227:66 – 71, 2013.

[173] Benesh Joseph, Vladimir M. Korkhov, Maxim Yulikov, Gunnar Jeschke, and Enrica Bordignon. Conformational cycle of the vitamin B12 ABC importer in liposomes detected by double electron-electron resonance (DEER). *J. Biol. Chem.*, 289:3176–3185, 2014.

[174] Devin T. Edwards, Thomas Huber, Sunyia Hussain, Katherine M. Stone, Maia Kinnebrew, Ilia Kaminker, Erez Matalon, Mark S. Sherwin, Daniella Goldfarb, and Songi Han. Determining the oligomeric structure of proteorhodopsin by Gd3+-based pulsed dipolar spectroscopy of multiple distances. *Structure*, 22:1677 – 1686, 2014.

[175] Arina Dalaloyan, Mian Qi, Sharon Ruthstein, Shimon Vega, Adelheid Godt, Akiva Feintuch, and Daniella Goldfarb. Gd(III)-Gd(III) EPR distance measurements - the range of accessible distances and the impact of the zero field splitting. *Phys. Chem. Chem. Phys.*, 17:18464, 2015.

[176] Luca Garbuio, Bartosz Lewandowski, Patrick Wilhelm, Ludmila Ziegler, Maxim Yulikov, Helma Wennemers, and Gunnar Jeschke. Shape persistence of polyproline II helical oligoprolines. *Chem. Eur. J.*, 21:10747–10753, 2015.

[177] Michael K. Bowman and Alexander G. Maryasov. Dynamic phase shifts in nanoscale distance measurements by double electron electron resonance (DEER). *J. Magn. Reson.*, 185:270 – 282, 2007.

[178] K.M. Salikhov and I.T. Khairuzhdinov. Four-pulse ELDOR theory of the spin 1/2 label pairs extended to overlapping EPR spectra and to overlapping pump and observer excitation bands. *Appl. Magn. Reson.*, 46:67–83, 2015.

[179] Gunnar Jeschke. Interpretation of dipolar EPR data in terms of protein structure. In Christiane R. Timmel and Jeffrey R. Harmer, editors, *Structural Information from Spin-Labels and Intrinsic Paramagnetic Centres in the Biosciences*, volume 152 of *Structure and Bonding*, pages 83–120. Springer Berlin Heidelberg, 2013.

[180] Gareth R. Eaton, Sandra S. Eaton, Richard W. Quine, Deborah Mitchell, Velavan Kathirvelu, and Ralph T. Weber. A signal-to-noise standard for pulsed EPR. *J. Magn. Reson.*, 205:109 – 113, 2010.

[181] G.A. Rinard, R.W. Quine, S.S. Eaton, G.R. Eaton, and W. Froncisz. Relative benefits of overcoupled resonators vs inherently low-Q resonators for pulsed magnetic resonance. *J. Magn. Reson. A*, 108:71 – 81, 1994.

[182] Aharon Blank and Haim Levanon. Filling factor in a pulsed electron paramagnetic resonance experiment. *Spectrochim. Acta A*, 58:1329 – 1335, 2002.

[183] Aharon Blank. General experimental aspects of EPR microscopy. In Sushil K. Misra, editor, *Multifrequency Electron Paramagnetic Resonance*, pages 795–823. Wiley, 2011.

[184] Stefan Stoll and Arthur Schweiger. Easyspin, a comprehensive software package for spectral simulation and analysis in EPR. *J. Magn. Reson.*, 178:42 – 55, 2006.

[185] Joscha Nehrkorn, Joshua Telser, Karsten Holldack, Stefan Stoll, and Alexander Schnegg. Simulating frequency-domain electron paramagnetic resonance: Bridging the gap between experiment and magnetic parameters for high-spin transition-metal ion complexes. *J. Phys. Chem. B*, 119:13816–13824, 2015.

[186] Bettina Basel. Dipolar correlation spectroscopy: Higher-order correlation terms in three-spin double electron-electron resonance (deer). *BestMasters*, 2015.

[187] Peter P. Borbat, Elka R. Georgieva, and Jack H. Freed. Improved sensitivity for long-distance measurements in biomolecules: Five-pulse double electron-electron resonance. *J. Phys. Chem. Lett.*, 4:170–175, 2013.

[188] Philipp E. Spindler, Izabela Waclawska, Burkhard Endeward, Jörn Plackmeyer, Christine Ziegler, and Thomas F. Prisner. Carr-purcell pulsed electron double resonance with shaped inversion pulses. *J. Phys. Chem. Lett.*, 6:4331–4335, 2015.

[189] Sergey Milikisyants, Francesco Scarpelli, Michelina G. Finiguerra, Marcellus Ubbink, and Martina Huber. A pulsed EPR method to determine distances between paramagnetic centers with strong spectral anisotropy and radicals: The dead-time free RIDME sequence. *J. Magn. Reson.*, 201:48 – 56, 2009.

[190] L.V. Kulik, S.A. Dzuba, I.A. Grigoryev, and Yu.D. Tsvetkov. Electron dipole-dipole interaction in ESEEM of nitroxide biradicals. *Chem. Phys. Lett.*, 343:315 – 324, 2001.

[191] Andrei V. Astashkin. Chapter ten - mapping the structure of metalloproteins with RIDME. In Peter Z. Qin and Kurt Warncke, editors, *Electron Paramagnetic Resonance Investigations of Biological Systems by Using Spin Labels, Spin Probes, and Intrinsic Metal Ions, Part A*, volume 563 of *Methods in Enzymology*, pages 251 – 284. Academic Press, 2015.

[192] Tona von Hagens, Yevhen Polyhach, Muhammad Sajid, Adelheid Godt, and Gunnar Jeschke. Suppression of ghost distances in multiple-spin double electron-electron resonance. *Phys. Chem. Chem. Phys.*, 15:5854–5866, 2013.

[193] Angeliki Giannoulis, Richard Ward, Emma Branigan, James H. Naismith, and Bela E. Bode. PELDOR in rotationally symmetric homo-oligomers. *Mol. Phys.*, 111:2845–2854, 2013.

[194] Luca Garbuio. Extending Gd(III)-nitroxide DEER methodology from model systems to biological applications. *Diss. ETH Nr. 22278*, 2014.

[195] Eriks Kupĉe and Ray Freeman. Stretched adiabatic pulses for broadband spin inversion. *J. Magn. Reson.*, 117:246 – 256, 1995.

[196] Sanghyuk Lee, Baldev R. Patyal, and Jack H. Freed. A two-dimensional Fourier transform electron-spin resonance (ESR) study of nuclear modulation and spin relaxation in irradiated malonic acid. *J. Chem. Phys.*, 98:3665–3689, 1993.

[197] A. T. Brant, Shan Yang, N. C. Giles, M. Zafar Iqbal, A. Manivannan, and L. E. Halliburton. Oxygen vacancies adjacent to Cu2+ ions in TiO_2 (rutile) crystals. *J. Appl. Phys.*, 109, 2011.

[198] J. Ammeter, G. Rist, and Hs. H. Günthard. Influence of the host lattice upon EPR coupling parameters and d-d transitions of planar copper (II) complexes. *J. Chem. Phys.*, 57:3852–3866, 1972.

[199] V.F. Yudanov, K.M. Salikhov, G.M. Zhidormirov, and Yu.D. Tsvetkov. Modulation effects in the electron spin echo of biradical systems. *Theor. Exp. Chem.*, 5:451–455, 1972.

[200] Muhammad Sajid, Gunnar Jeschke, Michael Wiebcke, and Adelheid Godt. Conformationally unambiguous spin labeling for distance measurements. *Chem. Eur. J.*, 15:12960–12962, 2009.

[201] Petr P. Borbat and Jack H. Freed. Multiple-quantum ESR and distance measurements. *Chem. Phys. Lett.*, 313:145 – 154, 1999.

[202] Petr. P. Borbat and Jack. H. Freed. Double-quantum ESR and distance measurements. In Lawrence J. Berliner, Gareth R. Eaton, and Sandra S. Eaton, editors, *Distance Measurements in Biological Systems by EPR*, volume 19 of *Biological Magnetic Resonance*, pages 383–459. 2002.

[203] G. Jeschke, M. Pannier, A. Godt, and H.W. Spiess. Dipolar spectroscopy and spin alignment in electron paramagnetic resonance. *Chem. Phys. Lett.*, 331:243 – 252, 2000.

[204] Ye. Polyhach, A. Godt, C. Bauer, and G. Jeschke. Spin pair geometry revealed by high-field DEER in the presence of conformational distributions. *J. Magn. Reson.*, 185:118 – 129, 2007.

[205] S.K. Misra, P.P. Borbat, and J.H. Freed. Calculation of double-quantum-coherence two-dimensional spectra: Distance measurements and orientational correlations. *Appl. Magn. Reson.*, 36:237–258, 2009.

[206] H.W. Bode. *Network Analysis and Feedback Amplifier Design*. Bell Telephone Laboratories series. D. Van Nostrand Company Inc., 1945.

[207] John Bechhoefer. Kramers–Kronig, Bode, and the meaning of zero. *Am. J. Phys.*, 79:1053–1059, 2011.

[208] A.V. Oppenheim and R.W. Schafer. *Discrete-time signal processing*. Prentice-Hall signal processing series. Prentice Hall, 1989.

[209] P. Perry and T.J. Brazil. Hilbert-transform-derived relative group delay. *IEEE Trans. Microw. Theory Techn.*, 45:1214 –1225, aug 1997.

[210] G.G. Maresch, M. Weber, A.A. Dubinskii, and H.W. Spiess. 2D-ELDOR detection of magnetization transfer of nitroxides in disordered solid polymers. *Chem. Phys. Lett.*, 193:134 – 140, 1992.

[211] Larry Marks. Personal communication with Larry Marks from Applied Systems Engineering, the manufacturer of the high-power amplifier. Note that loading conditions of a high-power amplifier include higher harmonics. The problem was recognized by means of long ringing ($>$ 100 ns) upon a pulse, which was also observed without the resonator connected (direct connection between I_2 and S_1 in spectrometer schematic.

[212] D.M. Pozar. *Microwave Engineering*. Wiley, 4 edition, 2011. pp 513-514.

[213] René Tschaggelar, Besnik Kasumaj, Maria Grazia Santangelo, Jörg Forrer, Patrik Leger, Henry Dube, François Diederich, Jeffrey Harmer, Rolf Schuhmann, Inés García-Rubio, and Gunnar Jeschke. Cryogenic 35 GHz pulse ENDOR probehead accommodating large sample sizes: Performance and applications. *J. Magn. Reson.*, 200:81 – 87, 2009.

[214] Shimon Vega. Fictitious spin 1/2 operator formalism for multiple quantum NMR. *J. Chem. Phys.*, 68:5518–5527, 1978.

[215] Debamalya Banerjee and S.V. Bhat. Vitrification, relaxation and free volume in glycerol-water binary liquid mixture: Spin probe ESR studies. *J. Non-Crys. Sol.*, 355:2433 – 2438, 2009.

[216] Catalin Gainaru, Alexander L. Agapov, Violeta Fuentes-Landete, Katrin Amann-Winkel, Helge Nelson, Karsten W. Köster, Alexander I. Kolesnikov, Vladimir N. Novikov, Ranko Richert, Roland Böhmer, Thomas Loerting, and Alexei P. Sokolov. Anomalously large isotope effect in the glass transition of water. *PNAS*, 111:17402–17407, 2014.

G

ACKNOWLEDGEMENTS

First, I am very thankful to Prof. Gunnar Jeschke for supervision of my PhD project. He gave me the very generous opportunity of a PhD project tailored to my skills as electrical engineer and my interest in physics. He was always open for discussing problems and new ideas and established a very fruitful working atmosphere, both from a scientific and an administrative point of view.

I am also obliged to Prof. Matthias Ernst for being the co-examiner of my thesis.

Moreover, I need to thank a number of other people with whom I directly worked together during my project. Spin dynamics simulations were always very important for understanding and interpreting the experiments, such that I am grateful for all interactions with Stephan Pribitzer, who is the core developer of SPin DYnamics Analysis (SPIDYAN).

Furthermore, I thank Dr. Takuya Segawa for his fruitful work on chirp ESEEM techniques and DNP as well as for discussions in general. It was highly rewarding for me to witness how instrumentation and methodology developed within this thesis and also from my master thesis could be continued in his work.

During my project, I also got to explore a number of interesting sub-projects by supervision of semester and master theses. Here, I am grateful to the work of several eager students. In particular, multi-spin correlations were explored within the master thesis of Bettina Basel. Systematic optimization of the pump pulse in Gd-Gd distance measurements started with the semester project of Nino Wili. The bandwidth-compensated and asymmetric HS pulses were implemented within the semester project of Andreas Dounas. These pulses found direct application in multi-pulse DEER experiments that were examined in the master thesis of Janne Soetbeer under the supervision of Dr. Yevhen Polyhach.

For mechanical support, I am indebted to Oliver Oberhänsli. He always contributed fruitfully to solving mechanical problems with his expertise and knowledge in mechanics. For electronics support and design of microwave resonators, I am thankful to René Tschaggelar. The home-built Q-band resonators turned out to pair well with the requirements for chirp pulses.

I am also thankful to Dr. Maxim Yulikov, Dr. Enrica Bordignon and Dr. Yevhen Polyhach, who were always open to share their expertise and knowledge. For initial training on pulse EPR spectrometers, I thank Dr. Sahand Razzaghi for his helpful advises.

In addition, I am indebted to everyone who provided me with stock solutions of model compounds. I am most grateful for the model compounds for distance measurements synthesized in the group of Prof. Adelheid Godt at the Bielefeld University. The Gd-rulers synthesized by Mian Qi were the key to the optimization of the Gd-distance measurements and the new CIDME experiment. For the synthesis of the terpyridine-based copper-nitroxide complex used in the first chirp DEER experiments, I am thankful to Dr. Evelyn Wessel (née Narr). The rigid nitroxide-nitroxide spacer synthesized by Dr. Muhammad Sajid was very important for the 2D SIFTER experiment.

Furthermore, I am thankful for the polyproline helix labeled as a Gd-

nitroxide-nitroxide system from the group of Prof. Helma Wennemers from ETH Zurich, which was studied by means of EPR within the PhD project of Dr. Luca Garbuio. Stock solutions of Gd-DOTA and Gd-DTPA complexes prepared by Dr. Luca Garbuio were also important for studying the influence of ZFS parameters on coherence and population transfer experimentally.

An extraordinary appreciation goes to all present and former group-members for the time spent together. In particular, I want to mention my office-mates Simon Böhm, Dr. Vidmantas Kalendra, Dr. Benesh Joseph, Christoph Gmeiner, and Katharina Keller.

For friendship, variety and support in general, I want to thank all my friends and my family. Most importantly, I want to express my gratitude to Celia for her love and support at all times.

curriculum vitæ

Mister Andrin Doll

Birth	October 1st 1984 in Bülach, Switzerland
Address	Albisriederstrasse 15, CH-8003 Zürich andrin@posteo.de

Education

Jan 2012 - Jun 2016	PhD study at ETH Zürich in the laboratory of physical chemistry supervised by Prof. Dr. G. Jeschke. Topic: Frequency-swept microwave pulses for **electron paramagnetic resonance** (EPR)
Sep 2008 - Feb 2011	MSc in electrical engineering with focus on *Micro- and Optoelectronics* at ETH Zürich Project 1: Groupvelocity in **photonic crystals** by interferometry Project 2: Periodic boundary conditions in **3D finite-element simulations** Master thesis: **Dynamic nuclear polarization** (DNP) in membrane proteins
Oct 2004 - Sep 2007	BSc in electrical engineering at ETH Zürich with focus on *Communication*
Aug 1998 - Sep 2004	Higher education entrance certificate at the *Kantonsschule Zürcher Unterland* in Bülach with focus on old languages

Professional Activities

Jan 2012 - Jun 2016	Tutorial assistance during PhD: Informatics I, Labcourse on LabVIEW, Metrology, Physical Chemistry 3: Molecular Quantum Mechanics, Physical Chemistry 4: Magnetic Resonance
Aug 2011 - Dec 2011	**R&D** internship at Zurich Instruments: Technical documents and blogs, LabVIEW programming, hardware prototyping for impedance measurements
Oct 2009 - May 2010	Internship at EMPA Dübendorf (Swiss federal laboratories for materials science and technology): Phase sensitive **scanning near-field optical microscopy** of photonic crystal waveguides
Jun 2009 - Aug 2009	Supporting work at the institute for electronics (ETH), Prof. H. Jäckel: drawing of photonic crystal waveguide designs for e-beam lithography and subsequent measurements

Military substitute service (Alternative civilian service)

Mar 2008 - Sep 2008	Civil service in a social pedagogic community in Croatia. Agriculture, handcrafting and social works
Oct 2007 - Feb 2008	Civil service at the PMOD/WRC (world radiation center) in Davos, Switzerland: Data evaluation **software in C** of the in-house unit PREMOS (solar radiometer) on the French CNES satellite PICARD

Publications by June 1, 2016

May 2016	*T.F. Segawa, M. Doppelbauer, L. Garbuio, A. Doll, Y.O. Polyhach, G. Jeschke*, Water accessibility in a membrane-inserting peptide comparing Overhauser DNP and pulse EPR methods, J. Chem. Phys. 144, 194201

Jan 2016 *S. Pribitzer, A. Doll, G. Jeschke*, SPIDYAN, a MATLAB library for simulating pulse EPR experiments with arbitrary waveform excitation, J. Magn. Reson. 263, 45-54

Aug 2015 *A. Doll, M. Qi, N. Wili, S. Pribitzer, A. Godt, G. Jeschke*, Gd(III)-Gd(III) distance measurements with chirp pump pulses, J. Magn. Reson. 259, 153-162

Jul 2015 *T.F. Segawa, A. Doll, S. Pribitzer, G. Jeschke*, Copper ESEEM and HYSCORE through ultra-wideband chirp EPR spectroscopy, J. Chem. Phys. 143, 044201

May 2015 *G. Jeschke, S. Pribitzer, A. Doll*, Coherence transfer by passage pulses in electron paramagnetic resonance spectroscopy, J. Phys. Chem. B 119, 13570-13582

Feb 2015 *A. Doll, M. Qi, S. Pribitzer, N. Wili, M. Yulikov, A. Godt, G. Jeschke*, Sensitivity enhancement by population transfer in Gd(III) spin labels, Phys. Chem. Chem. Phys. 17, 7334-7344

Jun 2014 *A. Doll and G. Jeschke*, Fourier-transform electron spin resonance with bandwidth-compensated chirp pulses, J. Magn. Reson 246, 18-26

Jan 2013 *A. Doll, S. Pribitzer, R. Tschaggelar, G. Jeschke*, Adiabatic and fast passage ultra-wideband inversion in pulsed EPR, J. Magn. Reson 230, 27-39

Jun 2012 *A. Doll, E. Bordignon, B. Joseph, R. Tschaggelar, G. Jeschke*, Liquid state DNP for water accessibility measurements on spin-labeled membrane proteins at physiological temperatures, J. Magn. Reson 222, 34-43 (**cover article**)

Oral Conference Contributions and Awards

Dec 2015 Early Postdoc.Mobility fellowship from the SNSF for a stay at Claude Fermon's group at the CEA Saclay, starting from July 2016

Jul 2015 Contributed talk at the rocky mountain conference on magnetic resonance, Snowbird, Utah, USA, Title: Considerations on frequency-swept excitation pulses

Mar 2015 JEOL **student lecturer award** at the royal society of chemistry (RSC) EPR meeting, Southampton, England. Title: High-sensitivity Gd(III) DEER with composite chirp pulses

Sep 2014 Contributed talk at the European federation of EPR meeting (EFEPR) in Marseilles, France, Title: Gd^{3+} DEER with chirp pulses

Jul 2014 Contributed talk at the EUROMAR Zürich, Switzerland, Title: Fourier-transform electron spin resonance with bandwidth-compensated chirp pulses

Jan 2013 **Poster award** at the EPR winter school at the Weizmann institute of science, Israel, Poster title: Adiabatic and fast passage ultra-wideband inversion in pulsed EPR

Languages

German and English (very good)

French (higher education entrance qualification)

Croatian and Spanish (basic verbal communciation)

Other Interests

Sports (Running, Cycling, Gymnastics)

Music (Electric guitar and recording techniques)

Traveling (6 months in South America from Feb 2011, including 5 weeks of English teaching; Russia, Greece, Ireland, Croatia, USA)

Zürich, June 1, 2016